



TUM School of Natural Sciences

DOCTORAL THESIS

---

**Novel technique to access the strong  
interaction in three-body systems  
and  
Re-evaluated cosmic ray antinuclei fluxes**

---

*Author:*  
Laura Šerkšnytė

*Supervisor:*  
Prof. Dr. Laura Fabbietti



*A thesis submitted in fulfillment of the requirements  
for the degree of Doctor of Natural Sciences  
in the  
TUM School of Natural Sciences*

April, 2023



To the most kind, intelligent and loving person which I am honoured to call my  
Grandmother.

You were and are my mother, my grandmother, my best friend.

You always supported me, allowed me to make mistakes and loved me  
unconditionally. I really believe that I am the luckiest person in the world to have  
you in my life.

Skiriu geriausiam, protingiausiam ir labiausiai mylinčiam žmogui, kurį turiu  
garbės vadinti močiute.

Tu buvai ir esi mano mama, močiutė ir geriausia draugė.

Tu visada mane palaikei, leidai man klysti ir besalygiškai mane mylėjai. Aš tikiu,  
kad esu laimingiausias žmogus pasaulyje, nes turiu savo gyvenime tave.





## TUM School of Natural Sciences

---

# **Novel technique to access the strong interaction in three-body systems and Re-evaluated cosmic ray antinuclei fluxes**

---

Laura Šerkšnytė

Vollständiger Abdruck der von der TUM School of Natural Sciences der  
Technischen Universität München zur Erlangung des akademischen Grades  
einer

Doktorin der Naturwissenschaften (Dr. rer. nat.)

genehmigten Dissertation.

Vorsitz: Prof. Dr. Andreas Weiler  
Prüfer\*innen der Dissertation: 1. Prof. Dr. Laura Fabbietti  
2. Prof. Dr. Stefan Schönert

Die Dissertation wurde am 05.05.2023 bei der Technischen Universität  
München eingereicht und durch die TUM School of Natural Sciences am  
21.06.2023 angenommen.



## Declaration of Authorship

I, Laura Šerkšnytė, declare that this thesis titled, "Novel technique to access the strong interaction in three-body systems and Re-evaluated cosmic ray antinuclei fluxes" and the work presented in it are my own. I confirm that:

- This work was done wholly or mainly while in candidature for a research degree at this University.
- I have not employed the services of an organization that provides dissertation supervisors in return for payment or that fulfills, in whole or in part, the obligations incumbent on me in connection with my dissertation.
- I have not submitted the dissertation, either in the present or a similar form, as part of another examination process.
- I have not yet been awarded the desired doctoral degree nor have I failed the last possible attempt to obtain the desired degree in a previous doctoral program.
- Where I have consulted the published work of others, this is always clearly attributed.
- Where I have quoted from the work of others, the source is always given. With the exception of such quotations, this thesis is entirely my own work.
- I have acknowledged all main sources of help.
- Where the thesis is based on work done by myself jointly with others, I have made clear exactly what was done by others and what I have contributed myself.

Signed:

---

Date:

---



# *Abstract*

Doctor of Philosophy

**Novel technique to access the strong interaction in three-body systems**

**and**

**Re-evaluated cosmic ray antinuclei fluxes**

by Laura Šerkšnytė

Two studies have been performed in this thesis: the measurement of strong interaction in three-body systems using the femtoscopy technique, and the estimations of cosmic ray antinuclei fluxes resulting from collisions between ordinary cosmic rays and the interstellar medium.

In the past decade, the femtoscopy technique has been utilized to measure hadronic interactions between particles that were previously difficult to access through experiments, including hadron pairs with multi-strangeness or charm. The distances between particles in pp collisions at the LHC are of the order of 1 fm providing perfect conditions to measure the strong interaction. The natural next step is to extend this technique to the three-hadron case. Three-baryon interactions, especially p-p-p and p-p- $\Lambda$ , are of great interest to nuclear and astrophysics, as they provide relevant input to better understand (hyper-)nuclei and the equation of state of dense systems. The latter is required to solve the hyperon puzzle, which aims to answer the question of which constituents make up the inner core of neutron stars. This thesis presents the first measurements of three-baryon correlations in non-bound systems. To achieve this goal, the femtoscopic technique was extended for the first time to the three-baryon case. The correlation functions of p-p-p and p-p- $\Lambda$  were studied in high-multiplicity pp collisions at  $\sqrt{s} = 13$  TeV, which were recorded with the ALICE detector at the LHC. The genuine three-body effects were studied using the Kubo's cumulant technique. A negative three-particle cumulant was measured for p-p-p triplets. The p-value extracted from the  $\chi^2$  test corresponds to a deviation of  $6.7\sigma$  from the assumption that only two-body correlations are present in the system. It was evaluated in the kinematic region corresponding to the low relative momenta of three particles in center-of-mass system, at values of the hypermomentum  $Q_3 < 0.4$  GeV/c. This result indicates the presence of genuine three-body effects. The measured p-p-p correlation function was also compared to the first preliminary calculations, which suggest that the observed cumulant is partially related to the antisymmetrization of the three-particle wave function. For the p-p- $\Lambda$  system, a positive cumulant was observed at low  $Q_3$ . The deviation from zero at  $Q_3 < 0.4$  GeV/c is  $0.8\sigma$ , suggesting that the data can be sufficiently well explained by assuming only two-body correlations in the system, within the current uncertainties. More conclusive results for both p-p-p and p-p- $\Lambda$  systems require a larger data sample, which is expected from the Run 3 data taking. To ensure that all events which include a collimated triplet are stored, a three-body software trigger was developed in this thesis.

Cosmic ray antinuclei fluxes are an important channel for indirect dark matter searches. Some dark matter models, such as weakly interacting massive particles, are expected to annihilate into ordinary matter, including antinuclei. The produced antinuclei then propagate in the Galaxy and can reach detectors at Earth. Measuring cosmic ray antinuclei also includes a background component stemming from ordinary cosmic ray collisions with interstellar medium. Nevertheless, the fluxes from different origins are expected to have different energy distributions, leading to a signal-to-background ratio that can reach several orders of magnitude at low antinuclei energies.

This thesis presents estimates of secondary cosmic ray antideuteron and antihelium-3 fluxes. The antinuclei source functions and inelastic cross-sections based on data-driven methods were implemented in GALPOP. The secondary antideuteron fluxes were studied in detail by employing different production models and propagation parameters to estimate relevant uncertainties in the field. The results showed that the dominant uncertainty at kinetic energies above 1 GeV/ $A$  is due to production, as different production models provide significantly different results. In the lower energy regime, the choice of propagation parameters in GALPROP also contributes significantly to the flux uncertainty. The antideuteron inelastic cross section with matter, based on recent ALICE measurements, was implemented for the first time in GALPROP, and the experimental uncertainty was propagated to the flux predictions. The results showed that this uncertainty is only 25% at low kinetic energies, constituting the smallest contribution to the total uncertainty. The obtained results were also used to estimate the Galaxy's transparency to the propagation of secondary cosmic ray antideuterons. It was found to increase from around 35% to 90%, depending on the kinetic energy per nucleon. Similar studies were performed for the secondary cosmic ray antihelium-3 nuclei. The transparency increases from around 20% to 90% with increasing energy. The results show that the Galaxy is very transparent to the cosmic ray antinuclei and thus such fluxes could indeed be measured by the dedicated detectors in the future. Additionally, the secondary fluxes obtained from this thesis were compared to those expected from dark matter annihilation, revealing a signal-to-background ratio of several orders of magnitude for both cosmic ray antideuterons and antihelium-3 if a dark matter mass assumption of  $m_\chi = 100$  GeV is made.

# Zusammenfassung

In dieser Dissertation wurden zwei Studien durchgeführt: Die Messung von starken Wechselwirkungen in Drei-Körper-Systemen mithilfe der Femtoskopie-Technik und die Abschätzungen von Antinukleonen-Flüssen aus kosmischer Strahlung, die aus Kollisionen zwischen gewöhnlichen kosmischen Strahlen und dem interstellaren Medium resultieren. In den letzten zehn Jahren wurde die Femtoskopie-Technik genutzt, um hadronische Wechselwirkungen zwischen Teilchen zu messen, die experimentell schwer zugänglich waren, darunter Hadronenpaare mit Multi-Strangeness oder Charm. Die Abstände zwischen den Teilchen in pp-Kollisionen am LHC betragen etwa 1 fm und bieten somit perfekte Bedingungen, um die starke Wechselwirkung zu untersuchen. Der natürliche nächste Schritt besteht darin, diese Technik auf Systeme mit drei Hadronen auszuweiten. Drei-Baryonen-Wechselwirkungen, insbesondere p-p-p und  $\Lambda$ -p-p, sind von großem Interesse für die Kern- und Astrophysik, da sie wesentlich zum besseren Verständnis von (Hyper-)Kernen und der Zustandsgleichung von dichten Systemen beitragen. Letztere ist erforderlich, um das Hyperonen-Rätsel zu lösen und damit die Frage zu beantworten, aus welchen Bestandteilen der innere Kern von Neutronensternen besteht. Diese Dissertation präsentiert die ersten Messungen von Drei-Baryonen-Korrelationen in nicht-gebundenen Systemen. Um dieses Ziel zu erreichen, wurde die Femtoskopie-Technik erstmals auf Systeme mit drei Baryonen erweitert. Die Korrelationsfunktionen von p-p-p und  $\Lambda$ -p-p wurden in pp-Kollisionen mit hoher Multiplizität bei  $\sqrt{s} = 13$  TeV untersucht, die mit dem ALICE-Detektor am LHC aufgezeichnet wurden. Die echten Drei-Körper-Effekte wurden mithilfe der Kubo-Kumulanten-Technik untersucht. Es wurde ein negativer Drei-Teilchen-Kumulant für p-p-p-Triplets gemessen. Der p-Wert, der aus dem  $\chi^2$ -Test extrahiert wurde, entspricht einer Abweichung von  $6,7\sigma$  von der Annahme, dass nur Zwei-Teilchen-Korrelationen im System vorhanden sind. Hierfür wurde der kinematische Bereich betrachtet, der niedrigen Relativimpulsen für die drei Teilchen im System entspricht, also Werten des Hyperimpulses  $Q_3 < 0,4 \text{ GeV}/c$ . Dieses Ergebnis zeigt das Auftreten von echten Drei-Teilchen-Effekten. Die gemessene p-p-p-Korrelationsfunktion wurde zudem mit ersten vorläufigen Berechnungen verglichen, die nahelegen, dass der beobachtete Kumulant teilweise mit der Antisymmetrisierung der Drei-Teilchen-Wellenfunktion zusammenhängt. Für das p-p- $\Lambda$ -System wurde bei niedrigem  $Q_3$  ein positiver Kumulant beobachtet. Die Abweichung von Null bei  $Q_3 < 0,4 \text{ GeV}/c$  beträgt  $0,8 \sigma$ , was darauf hindeutet, dass die Daten innerhalb der aktuellen Unsicherheiten ausreichend gut durch die Annahme von reinen Zwei-Teilchen-Korrelationen im System erklärt werden können. Aussagekräftigere Ergebnisse für beide Systeme, p-p-p und p-p- $\Lambda$ , erfordern eine größere Menge Daten, die im Rahmen der Run-3-Datenaufnahme erwartet wird. Um sicherzustellen, dass alle Ereignisse, welche ein kollimiertes Triplet beinhalten, gespeichert werden, wurde in dieser Arbeit ein Drei-Teilchen-Software-Trigger entwickelt.

Der Fluss von Antinukleonen in kosmischer Strahlung stellt einen wichtigen Kanal für die indirekte Suche nach Dunkler Materie dar. Durch einige Modelle der Dunklen Materie, wie zum Beispiel schwach wechselwirkender massereicher Teilchen, erwartet man, dass sie in gewöhnliche Materie, einschließlich Antinukleonen, zerfallen. Die produzierten Antinukleonen verbreiten sich dann in der Galaxie

und können Detektoren auf der Erde erreichen. Die Messung von kosmischen Antinukleonen beinhaltet auch eine Hintergrundkomponente, die aus Kollisionen gewöhnlicher kosmischer Strahlung mit dem interstellaren Medium stammt. Die Flüsse aus verschiedenen Quellen haben jedoch unterschiedliche Energieverteilungen, was zu einem Signal-Hintergrund-Verhältnis führt, das bei niedrigen Antinukleonenenergien mehrere Größenordnungen erreichen kann.

Diese Arbeit präsentiert Abschätzungen der Flüsse von sekundären Antideuteronen und Antihelium-3 in kosmischen Strahlen. Die Antinukleonen-Quellfunktionen und inelastischen Wirkungsquerschnitte, basierend auf datengetriebenen Methoden wurden in GALPROP implementiert. Die sekundären Antideuteron-Flüsse wurden eingehend untersucht, indem verschiedene Produktionsmodelle und Propagationsparameter verwendet wurden, um relevante Unsicherheiten in diesem Bereich abzuschätzen. Die Ergebnisse zeigen, dass die dominante Unsicherheit bei kinetischen Energien über 1 GeV/A auf die Produktion zurückzuführen ist, da verschiedene Produktionsmodelle signifikant unterschiedliche Ergebnisse liefern. Im niedrigen Energiebereich trägt auch die Wahl der Propagationsparameter in GALPROP wesentlich zur Unsicherheit der Flüsse bei. Der inelastische Wirkungsquerschnitt von Antideuteronen mit Materie, basierend auf jüngsten ALICE-Messungen, wurde erstmals in GALPROP implementiert, und die experimentelle Unsicherheit wurde auf die Flussvorhersagen übertragen. Die Ergebnisse zeigten, dass diese Unsicherheit bei niedrigen kinetischen Energien nur 25% beträgt und somit den geringsten Beitrag zur Gesamtunsicherheit darstellt. Die erhaltenen Ergebnisse wurden auch verwendet, um die Transparenz der Galaxie für die Propagation von sekundären kosmischen Antideuteronen abzuschätzen. Es wurde festgestellt, dass die Durchlässigkeit der Galaxie für Antideuteronen in sekundärer kosmischer Strahlung je nach kinetischer Energie pro Nukleon von etwa 35% auf 90% steigt. Ähnliche Studien wurden für Antihelium-3 in sekundärer kosmischer Strahlung durchgeführt. Die Durchlässigkeit nimmt mit steigender Energie von etwa 20% auf 90% zu. Die Ergebnisse zeigen, dass die Galaxie sehr durchlässig für Antinukleonen in kosmischer Strahlung ist und dass solche Flüsse in Zukunft tatsächlich von dedizierten Detektoren gemessen werden können. Zusätzlich wurden die sekundären Flüsse, die aus dieser Arbeit gewonnen wurden, mit denjenigen verglichen, die bei der Annihilation dunkler Materie erwartet werden. Dabei wurde ein Signal-Hintergrund-Verhältnis von mehreren Größenordnungen gefunden, sowohl für Antideuteronen als auch für Antihelium-3. Hierbei wurde eine Annahme für die dunkle Materie-Masse von  $m_\chi = 100 \text{ GeV}$  getroffen.

## *Acknowledgements*

Along the way to finishing this thesis, I had a team of brilliant and kind people who were always there for me. First of all, I want to thank my supervisor Prof. Laura Fabbietti. I applied for a Master's thesis with her, and she took me with open arms with my slightly strange and very complicated personality. While the last five years were sometimes bumpy, it was the best ride of my life. Laura believed in me from the moment we started working together and supported me with her brilliant physics ideas and being there as a friend when I needed it. I wouldn't have become a physicist without her. During the PhD, she often pushed me to be my best self but also gave me space when needed. Working in her group helped me grow exponentially as a scientist and I am extremely grateful to have had this opportunity to work on interesting and fulfilling physics projects.

Our group is like a family to me. I never felt so accepted and appreciated as I feel every day at work. Thus a huge thanks go to every single person in our group. When I started my PhD, Raffaele del Grande joined our group with his infinite love for physics. We always had some of the most interesting physics discussions together, and I feel fortunate to have had the opportunity to work with you. I am even luckier that we became really good friends. Your intelligence and knowledge of physics inspire me. I also had the opportunity to enjoy physics (and not only) discussions with Dimitar and Valentina - the other two femto postdocs. Thanks, Dimitar, for all the great morning coffee breaks and very emotional conversations we had. Valentina - you allowed me to not be the loudest person in the room for once in my life! Jokes aside, you are a great example that there are no rules on how a woman in physics has to look and behave. This is extremely important for future generations - so we can become great physicists without losing who we are.

When I started in the group, Cindy was one of the kindest and friendliest people to me. I thank you for this because sometimes I felt lonely, and you always asked how I was doing. However, with time I became very close with most of the people in the group. Emma - thanks for taking me to the metal concerts; sometimes I needed it much more than you knew. Bhawani - it was an honour to do PhD at the same time as you and become experimental physicists together! Also, thanks for the best memes ever. They always lightened up my day during our thesis writing. Stephan - as we both know, we only became friends after some time. Through the sleepless nights working on Christmas break and many conversations later, we grew to enjoy each other's company! Maximilian K. - our conversations make me feel less alien. Berkin - I am delighted to know you because your personality amazes me and there is no one else dancing with me every time we hear music. Huge thanks for finishing my unfinished painting for the thesis cover with computer magic! Daniel - I think you bring freshness to the femto group by seeing things (not only in physics) differently than the rest of us. Ante - we had a few fights, but I genuinely enjoy our conversations and am always happy to stop by your office to chat! Petra - a huge thanks for always being so nice and kind to all of us when we come with our paperwork problems. You always do your best to help, smile, and joke around, making our lives much easier. Anton - best Raffaelo cake ever. Finally, there are several other people whom I appreciate a lot but did not mention here explicitly - Chiara (you do things in your sparkly way, and it is refreshing), Maximilian H. (tough love never dies), Georgios (your kindness, calmness and general attitude are inspiring to me), Farid (it is always interesting to discuss with you complicated

topics in the world), Dima (I enjoy your blunt honestly a lot), Andi (we had this short conversation just before you left which changed my view of what can make people happy and I appreciate those 5 minutes more than you know), Verena (it was nice to do the Master thesis at the same time and stay friends after). While Thomas Pöschl is not in our group, he was one of my Master supervisors and a great one! The two people I left out on purpose - Marcel and Thomas - need separate thanks because we became very close friends. Marcel - even though we have known each other since I started working in the group, we became much closer once you started your PhD. The way you believe in me makes me believe in myself more. Your ridiculous jokes always improve my day, yet I enjoy our deep conversations even more. I am proud to call you my friend. Thomas - it is even silly to write something because you know without me telling. You are always there for me, and I try to always be there for you. You are like a brother to me, and I trust you completely. The two of you made the PhD journey and the office much more enjoyable!

While I was fortunate to work with this amazing group, I also made several good friends outside work since I came to Germany. Cesar - you were my first good friend in Munich, I enjoyed our late-night chats on the balcony and dancing nights. Marija - I always enjoyed cooking together and discussing life. We met when I was in a bit dark place, and you made me smile. Lea - I enjoyed the guilty pleasure of watching GNTM together! I am very happy we became so close friends while living together. A huge thanks for the empathy you showed me and my crazy work schedules. Luckily, my current flatmate Verena was also very kind and patient with me during the writing of this thesis. Astrid - it took a while for us to become close, but your openness and warmth inspire me. I always enjoy our honest conversations and appreciate the time we spend together. Two people, whom I met at CERN and not in Munich, are Jasmine and Aleksas. We became friends and shared our lives incredibly fast. You helped me through some very stressful moments, and the way you see me gives me strength and teaches me to believe in myself more.

I want to give a huge thanks to the people from my previous life in Lithuania. Every time I go back there, they make me feel at home, and also they make me feel grounded. First of all, my friend Milvydė. We have known each other since I was six - not all of it was pretty, but we always returned to each other. I appreciate our friendship, especially in the last five years. When we meet, we always laugh and have so much fun! Another person I have known for ages is Greta. Even though we don't chat often, I know you are there for me. I am very happy we have the chance to see each other grow and create our lives. Gytis - we always do our best to meet, whether it is in Munich or in a random village in the middle between Šiauliai and Panevėžys. I always feel much lighter after spending time with you, and your classical music playlist is why I managed to finish writing the Masters and PhD theses. And finally, my group of friends - Gentis - made me feel special yet accepted from our bachelor years up to now. Every time I go back to Lithuania, we meet, laugh, make fun of each other, complain, remember the glory days in Kamčiatka, and share the love for each other. I am extremely excited to see how our lives unravel and who we become. Two other friends also kept me grounded during these years - Aistė and Tomas. I am very happy to have met you all in my life.

A huge thanks go to my family. I already dedicated the thesis to my grandmother Dionyza, the most amazing person I have met in my entire life. I grew up with my dad Arūnas, grandma and grandpa Julius. I want to thank all of them for

the support and unconditional love they gave me through the years. I also want to thank my grandmother Broné who was always there for me too.

I came to Munich with 3061 Eur in my pocket for a two-year Master's and no plan. I want for once to thank the young me for having the courage and believing in myself to take this step. This was the moment that changed my entire life completely.



# Contents

<b>Declaration of Authorship</b>	<b>iii</b>
<b>Abstract</b>	<b>v</b>
<b>Zusammenfassung</b>	<b>vii</b>
<b>Acknowledgements</b>	<b>ix</b>
<b>Preface</b>	<b>1</b>
<b>1 Introduction: particles, interactions and very dense systems</b>	<b>3</b>
1.1 The Standard Model of Particle Physics and Quantum Chromodynamics	4
1.2 Baryon-baryon interaction . . . . .	8
1.2.1 Theory . . . . .	8
1.2.2 Available data . . . . .	10
1.3 Three-baryon interactions . . . . .	12
1.3.1 Three-nucleon interactions . . . . .	12
1.3.2 N-N- $\Lambda$ interactions . . . . .	15
1.4 Dense matter: neutron stars . . . . .	16
1.5 Two-particle femtoscopy . . . . .	19
1.5.1 Source function . . . . .	22
1.6 Extension to three-particle femtoscopy . . . . .	23
1.6.1 Three-particle correlation function . . . . .	23
1.6.2 Theory of three-particle correlation functions . . . . .	24
1.6.3 Cumulant method . . . . .	30
1.6.4 Projector method . . . . .	32
<b>2 ALICE - A Large Ion Collider Experiment</b>	<b>35</b>
2.1 Large Hadron Collider . . . . .	36
2.2 ALICE . . . . .	36
2.2.1 Triggering system . . . . .	38
2.2.2 Inner Tracking System . . . . .	39
2.2.3 Time Projection Chamber . . . . .	39
2.2.4 Time-of-Flight detector . . . . .	41
2.3 ALICE Upgrade: Run 3 . . . . .	42
2.4 Data reconstruction . . . . .	44
2.5 Event, track and V0 selection . . . . .	47
<b>3 Three-baryon correlations</b>	<b>55</b>
3.1 Correlation functions . . . . .	56
3.2 Statistical uncertainties . . . . .	60
3.3 Systematic uncertainties . . . . .	63
3.4 Measured correlation functions and Monte Carlo results . . . . .	64
3.5 Lower-order contributions . . . . .	64

3.6	Three-particle correlation functions and the total lower order contributions . . . . .	71
3.7	Correction for misidentified particles and feed-down . . . . .	73
3.8	Three-baryon Correlation Results . . . . .	76
3.8.1	Results: Cumulants . . . . .	76
3.8.2	Results: p-p-p correlation function and first theoretical predictions . . . . .	80
<b>4</b>	<b>Offline three-body triggers for Run 3</b>	<b>83</b>
4.1	Number of triplets expected in Run 3 . . . . .	83
4.2	Trigger results . . . . .	85
4.2.1	Benchmark: converted data . . . . .	86
4.2.2	Results: Run 3 data . . . . .	88
<b>5</b>	<b>Introduction to dark matter and cosmic ray antinuclei</b>	<b>97</b>
5.1	Dark matter . . . . .	98
5.1.1	Evidence for dark matter . . . . .	98
5.1.2	Dark matter candidates . . . . .	101
5.1.3	Searches for dark matter . . . . .	103
5.2	Cosmic rays . . . . .	108
5.2.1	Cosmic ray transport . . . . .	109
5.2.2	GALPROP . . . . .	112
5.3	Antinuclei studies at accelerators . . . . .	117
5.3.1	Light (anti)nuclei production . . . . .	117
	Simple coalescence model . . . . .	118
	Advanced coalescence model . . . . .	120
5.3.2	Inelastic interactions of antinuclei with matter . . . . .	121
<b>6</b>	<b>Secondary cosmic ray antideuteron and antihelium fluxes</b>	<b>125</b>
6.1	Source functions . . . . .	126
6.2	Inelastic cross sections . . . . .	129
6.3	Resulting antideuteron fluxes and transparency . . . . .	130
6.3.1	Discussion on the uncertainties . . . . .	134
6.4	Resulting antihelium fluxes and transparencies . . . . .	135
<b>7</b>	<b>Summary and outlook</b>	<b>137</b>
<b>A</b>	<b>Relevant Publications</b>	<b>141</b>

# List of Figures

1.1	Standard Model . . . . .	5
1.2	Strong interaction vertices . . . . .	6
1.3	Quark-quark interaction . . . . .	6
1.4	Running coupling constant . . . . .	7
1.5	Nucleon-nucleon potential . . . . .	9
1.6	Feynman Diagrams for $\chi$ EFT . . . . .	10
1.7	p- $\Lambda$ cross section . . . . .	11
1.8	Fujita-Miyazawa Force . . . . .	12
1.9	Nuclei binding energies . . . . .	13
1.10	Three-nucleon interactions in Illinois potentials . . . . .	14
1.11	Hypernuclei separation energies . . . . .	15
1.12	Particle number per baryon in neutron star and the EoS of a neutron star . . . . .	17
1.13	Separation energies obtained with two different parameterization of three-body potential . . . . .	18
1.14	Three-body effects to the EoS and NS . . . . .	19
1.15	Idea of femtoscopy . . . . .	20
1.16	p-p correlation function estimated with CATS . . . . .	22
1.17	Source size as a function of $m_T$ . . . . .	23
1.18	Three-particle Jacobi Coordinates . . . . .	24
1.19	Correlation function calculated for an antisymmetrized free plane wave and including strong interaction . . . . .	28
1.20	Correlation functions of three-protons including different interaction contributions . . . . .	29
1.21	Correlation functions of three-protons including interaction in $K=1,2$ channels . . . . .	30
1.22	Three-body correlation sketch . . . . .	31
1.23	Projector method validation with MC . . . . .	33
2.1	CERN Accelerators . . . . .	36
2.2	ALICE detector . . . . .	37
2.3	ALICE multiplicity . . . . .	38
2.4	ALICE ITS detector . . . . .	39
2.5	ALICE TPC . . . . .	40
2.6	Specific energy loss in ALICE TPC . . . . .	41
2.7	ALICE TOF . . . . .	42
2.8	Data reconstruction flow . . . . .	44
2.9	Reconstruction of primary vertex and V0 . . . . .	45
2.10	Proton identification via TPC and TOF . . . . .	49
2.11	Proton purity as a function of transverse momentum . . . . .	49
2.12	DCA template fits . . . . .	50
2.13	Invariant mass distributions for $\Lambda$ candidates . . . . .	52

2.14	Purity of $\Lambda$ candidates . . . . .	53
2.15	CPA template fits . . . . .	54
3.1	Track merging effect . . . . .	57
3.2	Close pair rejection effect to correlation functions . . . . .	57
3.3	Multiplicity re-weighting . . . . .	58
3.4	Particle and antiparticle same event comparison . . . . .	60
3.5	Particle and antiparticle correlation function comparison . . . . .	61
3.6	Sampled correlation function as a function of $Q_3$ . . . . .	62
3.7	Number of sampled correlation function entries as a function of $Q_3$ . . . . .	62
3.8	Comparison between the measured correlation functions and obtained with the PYTHIA 8 event generator . . . . .	65
3.9	$p$ - $p$ and $p$ - $\Lambda$ correlation functions . . . . .	66
3.10	Comparison of lower-order correlation functions obtained using the data-driven projector methods . . . . .	68
3.11	Comparison of total lower-order correlation functions obtained using the data-driven and projector methods . . . . .	69
3.12	$p$ - $\bar{p}$ correlation function . . . . .	70
3.13	$p$ - $\bar{p}$ correlation function with $Q_3$ selection . . . . .	70
3.14	Comparison of lower-order correlation functions obtained using the data-driven and projector methods . . . . .	71
3.15	Measured $p$ - $p$ - $p$ , $p$ - $p$ - $\Lambda$ and $p$ - $p$ - $\bar{p}$ three-particle correlation functions . . . . .	72
3.16	$p$ - $p$ - $p$ and $p$ - $p$ - $\bar{p}$ cumulants obtained with projector method . . . . .	77
3.17	$p$ - $p$ - $\Lambda$ cumulant obtained with projector method . . . . .	78
3.18	$p$ - $p$ - $p$ cumulant obtained using projector and data-driven methods . . . . .	79
3.19	$p$ - $p$ - $\Lambda$ cumulant obtained using projector and data-driven methods . . . . .	80
3.20	Feed-down corrections for $p$ - $p$ - $p$ correlation function . . . . .	81
3.21	Measured $p$ - $p$ - $p$ correlation function compared to theoretical predictions . . . . .	81
4.1	Multiplicity distribution expected in Run 3 . . . . .	84
4.2	Triplets per event as a function of multiplicity . . . . .	85
4.3	Trigger scheme . . . . .	85
4.4	O2Physics benchmark: Multiplicity . . . . .	87
4.5	O2Physics benchmark: Proton transverse momentum . . . . .	87
4.6	O2Physics benchmark: Same event distribution for $p$ - $p$ - $p$ . . . . .	88
4.7	Primary vertex position in Run 3 . . . . .	89
4.8	$n_{\sigma\text{TPC}}$ distributions of (anti)proton tracks in Run 3 . . . . .	90
4.9	TOF and combined $n_{\sigma}$ distributions of (anti)proton tracks in Run 3 . . . . .	91
4.10	Comparison of TPC PID Default values and customised . . . . .	91
4.11	Kinematic distributions of (anti)proton tracks in Run 3 . . . . .	92
4.12	DCA <sub>xy</sub> and DCA <sub>z</sub> distributions of (anti)proton tracks in Run 3 . . . . .	93
4.13	Kinematic and topological distributions of (anti) $\Lambda$ candidates in Run 3 . . . . .	94
4.14	Same event distributions for (anti) $p$ - $p$ - $p$ and (anti) $p$ - $p$ - $\Lambda$ triplets in Run 3 with trigger selections . . . . .	95
4.15	Same event distributions for (anti) $p$ - $p$ - $p$ and (anti) $p$ - $p$ - $\Lambda$ triplets in Run 3 with trigger selections (low $Q_3$ ) . . . . .	95
4.16	Trigger rejection factors . . . . .	95
5.1	Cosmic ray in the Galaxy . . . . .	98
5.2	Cosmic microwave background . . . . .	99

5.3	Rotation curve of the Milky Way . . . . .	100
5.4	Dark matter density profiles . . . . .	101
5.5	Dark matter candidates . . . . .	102
5.6	Dark matter annihilation diagrams . . . . .	103
5.7	Dark matter searches . . . . .	103
5.8	Dark matter exclusion plot from direct detections experiments . . . . .	104
5.9	Constrains from indirect dark matter searches . . . . .	104
5.10	Positron flux by AMS-02 . . . . .	105
5.11	Antiproton cosmic ray flux and limits on dark matter . . . . .	106
5.12	Antideuteron flux prediction . . . . .	107
5.13	Cosmic ray spectrum . . . . .	108
5.14	Galaxy sketch . . . . .	112
5.15	Hydrogen gas distribution in the Galaxy . . . . .	113
5.16	Different modelled cosmic ray fluxes compared to data . . . . .	115
5.17	Predictions of simple coalescence model compared to ALICE data . . . . .	119
5.18	Differential antinuclei production cross sections . . . . .	119
5.19	Predictions of advanced coalescence model compared to ALICE data . . . . .	121
5.20	Antideuteron inelastic cross sections . . . . .	122
5.21	Antihelium-3 inelastic cross sections . . . . .	123
6.1	Antideuteron total production cross sections and local source function . . . . .	126
6.2	Interpolation of antihelium-3 production cross section . . . . .	128
6.3	2-dimentional antideuteron source function . . . . .	128
6.4	Antinuclei inelastic cross sections on proton target . . . . .	129
6.5	Cosmic ray antideuteron fluxes . . . . .	131
6.6	Secondary cosmic ray antideuteron fluxes and corresponding uncertainties stemming from inelastic cross section . . . . .	132
6.7	Transparency of the Galaxy to the cosmic ray antideuteron propagation . . . . .	133
6.8	Comparison of cosmic ray antideuteron fluxes obtained employing different propagation parameters . . . . .	134
6.9	Systematic uncertainties for the choice of production and propagation models . . . . .	134
6.10	Cosmic ray antihelium-3 fluxes and transparencies . . . . .	136



# List of Tables

1.1	Ground-state binding energy of ${}^7\text{Li}$ nuclei . . . . .	15
2.1	Event cuts . . . . .	47
2.2	Proton cuts . . . . .	48
2.3	Lambda cuts . . . . .	51
3.1	Number of triplets for $Q_3 < 0.4 \text{ GeV}/c$ . . . . .	60
3.2	Variations of different selection criteria on the correlation functions . . . . .	63
3.3	$\lambda$ parameter values . . . . .	75
4.1	High-multiplicity event bins expected in Run 3 . . . . .	84
4.2	The trigger selection criteria applied in the benchmark . . . . .	87
4.3	Comparison of the trigger results obtained with AliPhysics and O2Physics . . . . .	88
4.4	Available Run 3 data . . . . .	89
4.5	Proton cuts (trigger) . . . . .	90
4.6	Lambda cuts (trigger) . . . . .	93
5.1	Propagation parameter values . . . . .	116



# Preface

While modern physics manages to explain many phenomena, there are still many unresolved mysteries. Observing our Galaxy and its constituents has been providing valuable input for the development of physics for centuries. However, it also poses some puzzles. This thesis tackles two of those by providing valuable input - the measurements of strong force between three baryons necessary to study the composition of neutron stars and the cosmic ray antinuclei flux calculations, which can be employed for indirect dark matter searches.

Neutron stars are some of the densest objects observed in the universe. They provide a unique environment, which cannot be obtained in laboratories on Earth. The measured mass to radii relation of neutron stars is directly related to the equation of state of dense matter. The densities in the inner core can be several times larger than the nuclear saturation density. Thus, the nucleon chemical potential can increase enough that it becomes energetically favourable to turn nucleons into hyperons. However, the plausibility of such a scenario is determined by the equation of state, which requires precise knowledge of the strong interaction between different hadron pairs and triplets at large densities. The first part of this thesis consists of developing a novel experimental technique to access three-body systems via femtoscopic measurements employing the pp collision data recorded by ALICE at the LHC. The triplets studied in this work are p-p-p and p-p- $\Lambda$ . While the method was successfully developed, a statistical sample larger than from the Run 2 data-taking period is needed to provide quantitative constraints on the three-body dynamics. For this purpose, a software trigger for Run 3 was developed in the scope of this thesis, ensuring that all collisions, which contain at least one triplet of interest, will be saved.

Neutron stars are born in supernova explosions of massive stars. The resulting supernova remnants are bound by the expanding shock wave. The shock waves are believed to accelerate the surrounding interstellar gas and thus produce cosmic rays in galaxies. Such cosmic rays are called primary and consist mainly of protons and helium-4, as these are the main constituents of interstellar gas. However, there also exist much rarer antimatter cosmic rays which are produced in ordinary cosmic ray collisions with the interstellar medium. Indeed, such secondary cosmic ray antinuclei are expected to be so rare that they provide an almost background-free probe for unknown physics processes, resulting in antinuclei production in our Galaxy. The second part of this thesis explores the cosmic ray antinuclei fluxes which can be employed for indirect dark matter searches. Some dark matter candidates, such as the weakly interacting massive particles, are expected to annihilate producing ordinary matter, including antinuclei. If the resulting cosmic ray antinuclei fluxes are much larger than the expected secondary fluxes, they can be employed as smoking gun signatures of dark matter. In this thesis, we study the secondary antideuteron and antihelium-3 fluxes and the related uncertainties. We included in the calculations, for the first time, data-driven estimates of the antinuclei inelastic cross sections with matter and obtained the transparency of our Galaxy to the

antinuclei cosmic rays.

This thesis consists of two different topics. It is structured in the following way - the introduction of each topic is followed by the analysis and results. The first chapter introduces the strong interaction, its relation to the equation of state of neutron stars and the femtoscopic technique employed in this work. The second chapter presents the ALICE detector and how the recorded data was used to select and identify hadrons of interest. The third chapter describes the analysis and results of the three-particle correlation studies. The fourth chapter discusses the development of the three-body trigger for the Run 3 data-taking period. The fifth chapter introduces the second topic - dark matter and cosmic ray antinuclei. The sixth chapter describes the corresponding work and results on cosmic ray antideuteron and antihelium-3 fluxes. Finally, the last chapter provides the summary and outlook for the work performed in this thesis.

## Chapter 1

# Introduction: particles, interactions and very dense systems

One of the remaining questions in nuclear physics is the dynamics of many-body systems. The first scattering experiments opened a new possibility to study the nucleon-nucleon interactions, and multiple theories were developed to evaluate the corresponding two-particle potentials. However, later studies of bound many body systems - such as nuclei and hypernuclei - resulted in disappointment. The binding energies of observed (hyper)nuclei could not be explained by employing only the well-constrained two-body potentials. There was an observed underbinding in nuclei [1] and overbinding in hypernuclei [2]. Furthermore, measurements of the neutron-rich nuclei showed that the existing two-body interaction potentials could not explain the position of the neutron drip line. This motivated the increasing theoretical interest in the many-body problem. From the theory side, Fujita and Miyazawa already proposed the genuine three-body interactions in 1956 [3]. They suggested that two pion exchange in the three-nucleon system can result in a  $\Delta(1956)$  resonance excitation. Nowadays, multiple phenomenological three-body potentials exist, as well as calculations from the  $\chi$ EFT and first attempts by lattice QCD. The available potentials could reproduce most experimental observables once fitted to the data. However, it has been shown that the existing data is insufficient to constrain the three-body interactions as the resulting potentials are strongly dependent on assumed two-body interactions and many-body effects in the nuclei. New experimental approaches are necessary to further the field of three-body interaction studies.

Such interactions are even more relevant for very dense systems, where distances between particles are very small. One such system in our universe is neutron stars. The densities at the inner core of neutron stars are expected to be several times higher than the nuclear saturation densities. At such high densities, depending on the interaction potentials of different particle species, it might become energetically favourable to introduce new degrees of freedom, such as strangeness. Indeed, there is an ongoing discussion on whether hyperons are present in neutron stars. The Equation of State must be calculated to answer this question, which can be directly related to the mass-to-radius relation of neutron stars. The latter can be measured for the observed neutron stars [4]. If the Equation of State is obtained assuming only two-body interactions and includes hyperons, only low-mass neutron stars could exist in our universe. However, the available measurements contradict this. A possible solution to such a problem is genuine three-body interactions which should play an important role at such high densities. Thus, the many-body problem in nuclear physics is interesting not only to describe such small systems as nuclei but also to such fascinating objects as neutron stars. The most interesting interactions

for both cases are the N–N–N and N–N– $\Lambda$  systems, where  $N$  is a nucleon.

In this thesis, we developed a method to measure the three-body interactions employing the femtoscopy technique. This Chapter introduces the available models and experimental data for the two- and three-baryon interactions. The neutron stars are discussed, and current state-of-the-art results on the Equation of State are presented. Finally, the two-body femtoscopy is introduced, and the extension to the three-baryon system is shown together with the first available calculations of the three-proton femtoscopic correlation function.

## 1.1 The Standard Model of Particle Physics and Quantum Chromodynamics

What is the world made of? The ancient Greek philosopher Empedocles suggested that the world is made of four primordial elements: fire, earth, air, and water. Now we know that all ordinary matter is made of elementary particles. The Standard Model is the state-of-the-art particle physics model describing the fundamental structure of matter, including the elementary particles and the interactions between them. The so-called fermions make up the matter, while bosons are the interaction carriers, as shown in Fig. 1.1. Fermions have a half-integer spin and are separated into two groups of six particles (and their six antiparticles): leptons and quarks, which manifest three generations. The lightest and most stable particles belong to the first generation. The second and third-generation particles are heavier and less stable but have the same charge and spin quantum numbers.

Leptons can interact via electromagnetic and weak forces. The lightest charged lepton is an electron with a mass of  $0.511 \text{ MeV}/c^2$ , and thus it is stable. The second and third-generation charged leptons are muon ( $\mu$ ) and tau ( $\tau$ ), respectively. The lightest neutral lepton is the electron neutrino, while the second and third-generation are muon and tau neutrinos. As these leptons are not electrically charged, they interact only weakly. Quarks, differently from the leptons, cannot be observed directly. They interact not only electromagnetically and weakly but also strongly. Each of the six quark flavours can come in three colours relevant to the strong interaction: red, green and blue. The antiparticles carry "anti-colours". Due to colour confinement, a property of the strong interaction explained in the next sub-Chapter, only colourless particles can be observed. The most common colourless objects consist either of three quarks with three different colours (baryons) or a quark-antiquark pair with a specific colour and its' anti-colour (mesons). The two most common and lightest baryons are protons and neutrons. A proton consists of uud quarks and a neutron of udd, where u corresponds to the up quark and d to the down quark. The lightest mesons - neutral pions - are made of  $u\bar{u}$  or  $d\bar{d}$  pairs. Indeed, the u and d quarks are the lightest quarks with masses  $2.2 \text{ MeV}/c^2$  and  $4.7 \text{ MeV}/c^2$ , respectively, and belong to the first generation. The second generation quark called strange ( $s$ ) has a mass of  $96 \text{ MeV}/c^2$ , comparable to the first generation quarks. Baryons with at least one strange quark are called hyperons, and the lightest of them is the  $\Lambda$  hadron. Another second-generation quark is the charm with a mass of  $1.28 \text{ GeV}/c^2$ . It is much heavier than the already mentioned up, down and strange quarks. Finally, the third-generation quarks top ( $t$ ) and bottom ( $b$ ) are the heaviest with the masses  $4.18 \text{ GeV}/c^2$  and  $173.1 \text{ GeV}/c^2$ , respectively. In this thesis, we will restrict ourselves to the particles made of up, down and strange quarks - protons and  $\Lambda$  hyperons. Bosons do not make up the matter but carry the interactions between the fermions.

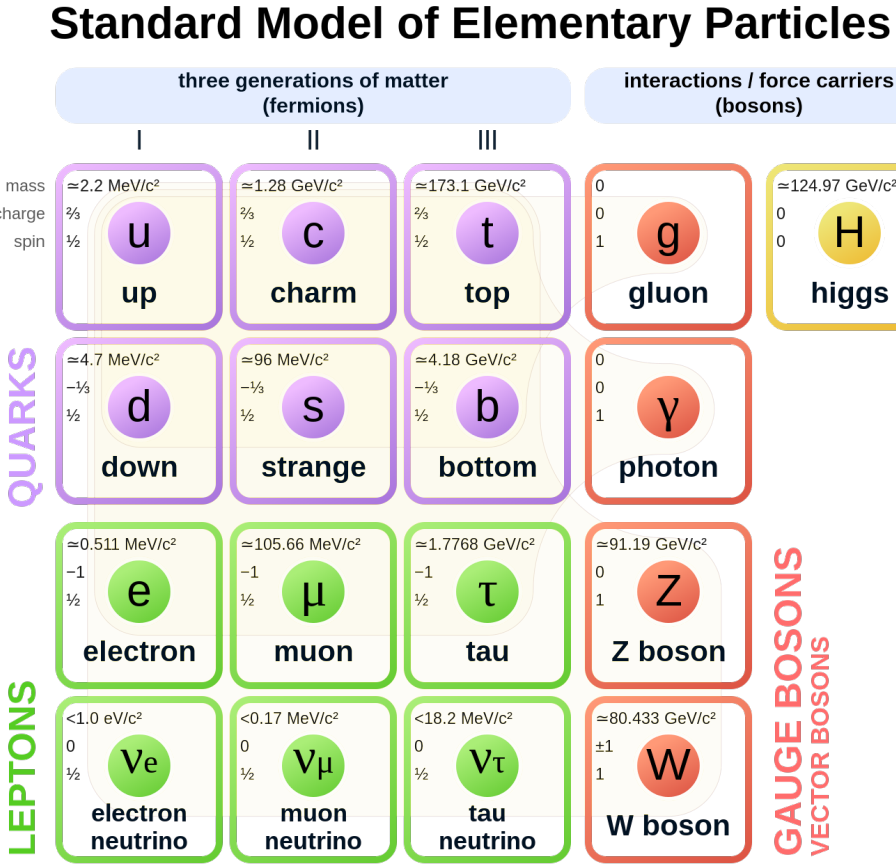


FIGURE 1.1: Representation of the Standard Model [5].

The heavy W and Z bosons, with masses of  $80.43 \text{ GeV}/c^2$  and  $91.19 \text{ GeV}/c^2$ , are responsible for the weak interaction which couples to all left-handed particles and right-handed antiparticles. The weak interaction also includes cross-generational quark coupling, such as  $s \rightarrow u + W^+$  vertex allowing  $\Lambda \rightarrow p + \pi^-$  decay. The photon carries the electromagnetic interaction and is mass-less. It couples only to electrically charged particles. The mass-less gluon is an exchange particle of the strong interaction, affecting only quarks as they carry the colour charge. There are, in total, eight gluons carrying different colour charges. The latest addition to the known bosons - the Higgs boson - was recently discovered by ATLAS and CMS experiments at the LHC [6, 7] with a mass of around  $125 \text{ GeV}/c^2$  providing one more successful test of the Standard Model.

The main interest of this thesis is the residual strong interaction between baryons; thus, it is helpful to introduce in more detail the strong interaction between elementary particles.

### Quantum Chromodynamics

Quantum Chromodynamics (QCD) is a theory describing the strong interaction between elementary particles. In QCD, colour plays the charge role; thus, quarks are the only fermions experiencing strong interaction. The mediators of the strong interaction are gluons, and the fundamental quark-gluon vertex is shown in the left panel of Fig. 1.2, corresponding to a process  $\text{quark} \rightarrow \text{quark} + \text{gluon}$ . The colour

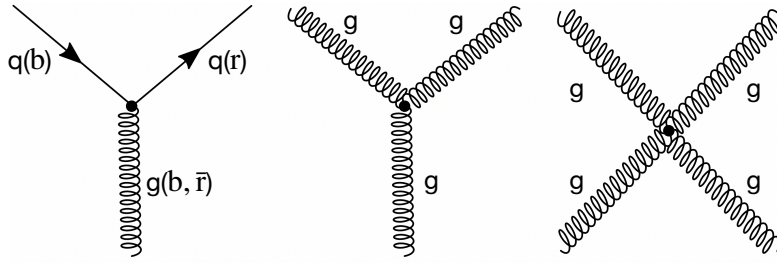


FIGURE 1.2: Fundamental vertices of strong interaction. Adapted from [8].

is conserved in the strong interaction; however, as shown in the Feynman diagram, the colour of the quark might change. A blue quark can become red if the gluon carries away the colour difference (blue and anti-red colours). Indeed, the gluons carry a combination of colour and anti-colour. This also means that they can couple with each other. The QCD allows two primitive gluon-gluon vertices: three-gluon and four-gluon, as shown in the middle and right panels of Fig. 1.2. These primitive vertices can be combined to represent more complicated processes. For example, the force between two quarks (responsible for binding quarks to form hadrons) can be described in the lowest order by the Feynman diagram shown in Fig. 1.3 and is mediated by the exchange of a gluon. The interaction strength depends on the number of vertices, as every vertex introduces a factor  $\alpha$  in the calculation of the scattering amplitude. In the case of the electrodynamics, the fine structure "constant"  $\alpha$  is  $\approx 1/137$  which **very** slightly increases when charges get closer<sup>1</sup>. This is a consequence of the vacuum polarisation, which partially screens the charge (like a charge is screened in a dielectric medium) and corresponds to loop diagrams. In the case of QCD, this is even more complicated as the "screening of the colour charge" includes simple loop diagrams and virtual gluon bubbles (based on three-gluon vertices). The former contribution results in "anti-screening" of the colour and is the dominant component - the coupling constant increases with the distance between the colour charges! The dependence of the so-called running coupling constant on the momentum transfer can be expressed in QCD as [9]

$$\alpha_s(|q^2|) = \frac{\alpha_s(\mu^2)}{1 + (\alpha_s(\mu^2)/12\pi)(11n - 2f)\ln(|q^2|/\mu^2)}, \quad (|q^2| > \mu^2), \quad (1.1)$$

where  $q$  is the momentum transfer of the interaction,  $n$  is the number of colours,  $f$  is the number of flavours and  $\mu$  is energy scale at which the  $\alpha_s(\mu^2)$  is evaluated. In the Standard Model, the numbers of colours and flavours are  $n = 3$  and  $f = 6$ , respectively, and the experimentally evaluated  $\alpha_s(m_Z)$  value at the Z boson mass scale is  $\approx 0.1179$  [10]. The  $\alpha_s$  dependence on the energy scale is shown in Fig. 1.4. The  $\alpha_s$

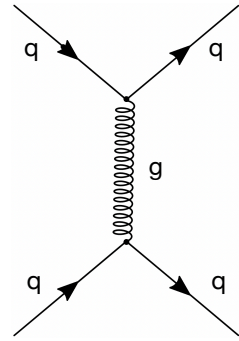


FIGURE 1.3: Quark-quark interaction mediated by an exchange of a gluon. Adapted from [8].

<sup>1</sup>The variation is tiny; however, it results in a detectable contribution to the Lamb shift in the hydrogen atom.

at large energy scales, corresponding to small distances, is very small, and particles are almost non-interacting. This phenomenon is known as asymptotic freedom. At such energy scales, perturbation theory can be employed to describe QCD processes and provide predictions. Due to very weak coupling at large densities, a transition to a deconfined state of matter is possible. Such a state is called quark-gluon plasma (QGP) and is actively studied at multiple accelerator facilities, including ALICE at the LHC [11, 12] and STAR at RHIC [13, 14]. On the other hand, the  $\alpha_s$  at low energy scales becomes larger and larger. If two quarks are being separated spatially, producing a  $q\bar{q}$  pair becomes more energetically favourable as the energy of the gluon field in between the interacting quarks becomes too large. Such an effect is known as confinement. Consequently, free quarks and gluons are not observed in nature, and only the colour singlets, corresponding to hadrons<sup>2</sup>, can be observed. As the quarks and gluons are strongly coupled in such a regime, the perturbation theory cannot be applied anymore. More quantitatively, such a regime starts at energy scales smaller than the so-called QCD scale  $\Lambda_{\text{QCD}}$ , around 200 MeV/c.

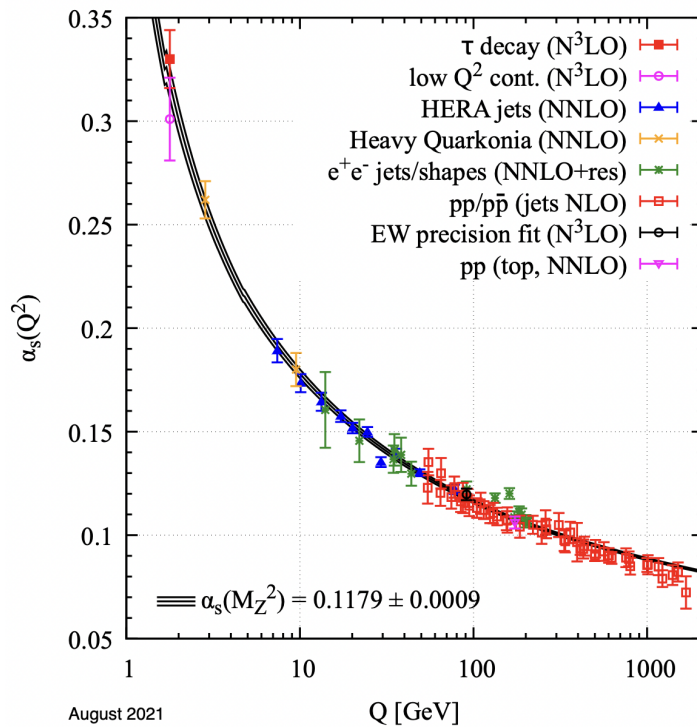


FIGURE 1.4: Summary of  $\alpha_s$  measurements as a function of the energy scale  $Q$  [10].

The strong interaction at the level of elementary particles can be described by a Lagrangian, which incorporates the fields of quarks and gluons. The Standard Model Lagrangian has global  $U(3) = U(1) \otimes SU(3)$  symmetry. Requiring the Lagrangian to be locally invariant under  $U(1)$  results in the derivation of electromagnetism. The requirement of local  $SU(3)$  symmetry is of interest for the strong interaction and results in the complete Lagrangian of chromodynamics

$$\mathcal{L} = [i\hbar c\bar{\psi}\gamma^\mu\partial_\mu\psi - mc^2\bar{\psi}\psi] - \frac{1}{16\pi}\mathbf{F}^{\mu\nu}\cdot\mathbf{F}_{\mu\nu} - (q\bar{\psi}\gamma^\mu\lambda\psi)\cdot\mathbf{A}_\mu, \quad (1.2)$$

<sup>2</sup>The self-interaction between gluons also allows colour singlet gluon balls.

where  $\psi$  corresponds to a three-component vector of Dirac spinors for the three colour quarks,  $A_\mu$  - vector gauge fields corresponding to the eight gluons and  $F^{\mu\nu}$  is also related to the gluon fields. The first component in Eq. 1.2 is the Lagrangian of free quarks. The second component accounts for the free gluon Lagrangian, including the gluon-gluon interaction via three and four gluon vertices. The third component describes the interaction of quarks and gluons, where  $\lambda$  has Gell-Mann matrices as components  $\lambda_1, \lambda_2, \dots, \lambda_8$ .

At high energy scales, the perturbative approaches can describe an interacting system. However, an analytical approach to the QCD has yet to be proposed at low energy scales. Numerical solutions of the QCD Lagrangians and effective field theories are applied to study processes at such energy regime. Describing the observable colour singlet states in nature - hadrons - from the principles of the QCD as bound states of quarks is a highly complicated task, but some efforts have been made towards this direction [15]. In this work, we are interested in the strong interaction between hadrons, for example, the p-p system. In the QCD, this corresponds to an interaction of six quarks which is a much too complicated task to solve analytically from the first principles. However, in the next Chapter, it will be shown that several methods exist to approach this problem. For example, nucleon-nucleon interactions are well understood and constrained by experiments.

## 1.2 Baryon-baryon interaction

The studies of the hadron-hadron residual strong interactions, especially nucleon-nucleon interactions, present one of the main problems in nuclear physics and provide a probe for the low-energy QCD. Effective models that describe such residual interactions consider nucleons as degrees of freedom. Indeed, the oldest nuclear force theory was proposed in 1935 [16] by Yukawa, which was long before the discovery that nucleons are made of quarks<sup>3</sup>. Yukawa described the strong interaction between nucleons as being mediated by a charged meson obeying Bose's statistics with a mass around 200 times the electron mass. While no such particle had yet been detected at the time, it has the same characteristics as charged pions. Several modern models are still based on the meson exchange principle, even though the potentials have become much more sophisticated.

### 1.2.1 Theory

The distance dependence of baryon-baryon interactions is generally divided into the so-called short, medium and long-range regions. A schematic view of the nucleon-nucleon potential is shown in Fig. 1.5. The long-range part is described in most models by One-Pion-Exchange potentials, as pions are the relevant degrees of freedom to describe the strong interaction between nucleons at such small energy scales. The medium-range part corresponds to the two-pion exchange and heavier meson exchanges. The short-range part is the most complicated, as quarks and gluons become relevant degrees of freedom. The repulsive core in nucleon-nucleon potential can be modelled, for example, by vector meson exchange [17]. The conventional phenomenological potentials are constructed based on these short-, medium- and large-range components and provide an excellent fit to the available data. One such

---

<sup>3</sup>The quantum field theory was already under development, used to describe electrodynamics.

potential for two-nucleon interaction is the Argonne  $v_{18}$  [18]. It models the long-range region as a one-pion exchange, and the contributions relevant to the intermediate and short-range regions are included via phenomenological parametrisations. This potential has 40 adjustable parameters and has  $\chi^2$  per datum of 1.09 for 4301 pp and np data in the range 0–350 MeV. However, such potentials are not very fundamental in the view of the QCD, as they do not use gluons and quarks as degrees of freedom. In general, there are several different quantitative approaches to obtain the baryon-baryon potentials. An extensive list and overview of available potentials for nucleon-nucleon interactions can be found in Ref. [19]. A good review of hyperon-nucleon systems is available in Ref. [20]. Here, we will discuss two approaches incorporating the knowledge from QCD: chiral effective field theory and lattice QCD.

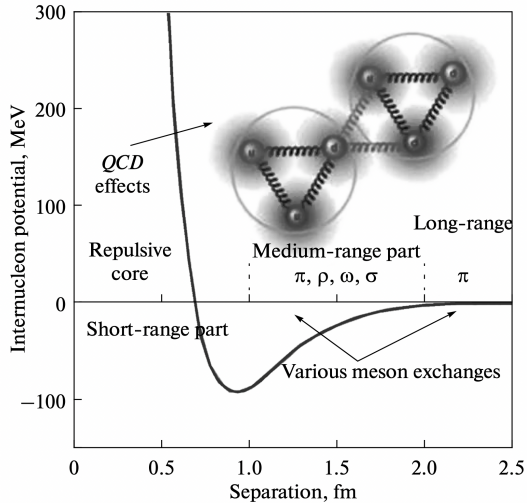


FIGURE 1.5: Sketch of nucleon-nucleon potential [19].

### Chiral effective field theory

Chiral Perturbation Theory is the effective theory of QCD introduced by Weinberg [21, 22] and we refer to it as chiral effective field theory ( $\chi$ EFT). Effective field theories exploit the separation of scales in a system. At a low energy scale, the relevant degrees of freedom are pions and nucleons, not quarks and gluons. Besides the pion exchange terms, the  $\chi$ EFT potentials include so-called contact terms, which parameterise the unresolved short-range nuclear interaction. The  $\chi$ EFT potentials are fitted to reproduce available scattering and (hyper)nuclei binding energy data for particle systems of interest.

The first step of the  $\chi$ EFT is to formulate the most general effective Lagrangian, which includes all possible terms and incorporates all symmetries and symmetry breakings, particularly the (broken) chiral symmetry, of the underlying theory. This is a significant difference from simple phenomenological models, where this strict relation to the underlying theory (in this case, QCD) is lost. In the second step, the obtained Lagrangian terms are ordered by their importance; thus, the process of interest can be calculated to the desired accuracy. The hierarchy of relevant contributions for nuclear forces is shown in Fig. 1.6.  $\chi$ EFT calculations naturally extend to the few-body systems (3N Force and 4N Force in Fig. 1.6). The effect of three-body interactions becomes evident only starting from the next-to-next-to-leading order (NNLO) accuracy. Such genuine three-body effects are necessary to reproduce observed binding energies of (hyper-)nuclei. They are also essential to the physics of neutron stars, as explained in the following Chapters. An excellent review with an introduction to  $\chi$ EFT can be found in Ref. [23]. For the state-of-the-art  $\chi$ EFT approach to describe p- $\Lambda$  interaction, refer to Refs. [24, 25].

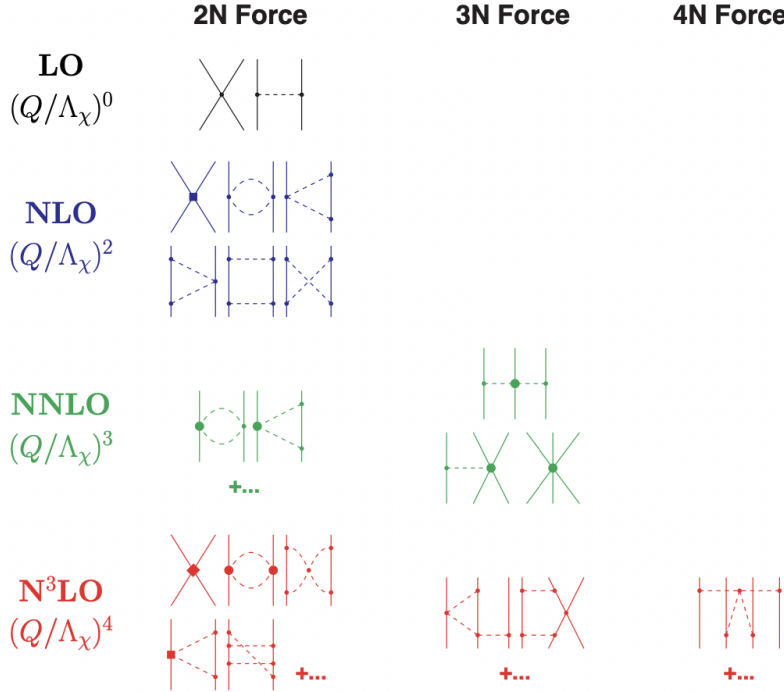


FIGURE 1.6: Hierarchy of interaction diagrams contributing to the nuclear force based on the Weinberg's power counting [23].

### Lattice QCD

Lattice QCD (LQCD) is a numerical approach to describe a quantum chromodynamical system from **first principles** with quarks and gluons as degrees of freedom using the Feynman path integral approach [26, 27]. It is a gauge invariant and non-perturbative calculation of QCD. The space and time are described as a four-dimensional lattice with spacing  $a$  and Euclidean time  $t$ . Same as in the case of the QCD, the only input parameters of LQCD are the coupling and the masses of the quarks. The state-of-the-art approaches can already perform the calculations at nearly physical quark masses ( $m_\pi=146$  GeV/ $c^2$ ) with lattice spacing  $a$  of the order of 0.1 fm and  $t/a$  of the order of 10 [28]. The LQCD can correctly predict masses of baryons [15], decay constants of  $D_s$  and  $D_s^*$  mesons [29], nucleon-hyperon correlation functions [30] and many other observables. The integrals in the LQCD are estimated employing Monte Carlo integration with the importance sampling, as the problem is too complicated for standard numerical integration methods. Two kinds of uncertainties contribute to the LQCD simulations: systematical and statistical. The latter is related to the importance sampling. The continuum limit ( $a$  size), infinite volume limit (number of points in the lattice) and the quark masses are some of the main systematic uncertainties. The latter arises because lattice calculations converge faster for heavy masses. Indeed, the LQCD simulations are usually performed with higher than physical masses of the light quarks, and final results are obtained by extrapolation.

#### 1.2.2 Available data

As explained previously, most baryon-baryon potentials are at least partially phenomenological and must be fitted to data. In this thesis, we are interested in p-p

and p- $\Lambda$  interactions. Traditionally, the interaction potentials for such baryon pairs have been fitted to scattering data, for example, to the phase shifts obtained via partial wave analysis. While the database for p-p scattering results is vast [31], the p- $\Lambda$  system is much less explored. A representative compilation of available scattering data in the  $\Lambda$ -p  $\rightarrow$   $\Lambda$ -p channel is shown in Fig. 1.7, where it is compared to two versions of  $\chi$ EFT potentials (red and blue bands) and phenomenological potentials (lines) [25]. The scattering data were obtained employing  $K^-$  meson beams which interacted with a thin target [32] or hydrogen gas [33] resulting in  $\Lambda$  hyperon production in direct ( $K^- + p \rightarrow \Lambda + X$ ) and secondary reactions, for example,  $\Sigma^0$  hyperon is produced in direct reaction  $K^- + p \rightarrow \Sigma^0 + X$  which then decays as  $\Sigma^0 \rightarrow \Lambda + \gamma$ . The produced  $\Lambda$  hadrons then interacted with the hydrogen gas in the bubble chamber, where the reactions were reconstructed. The data is very scarce, has significant uncertainties and is available only down to relative momentum of 130 GeV/c. At the high momentum part, a predicted coupling  $\Lambda N - \Sigma N$  is observed in the shown calculation. However, the available data could not resolve it (right panel).

The measurement of femtoscopic correlation functions improved the experimen-

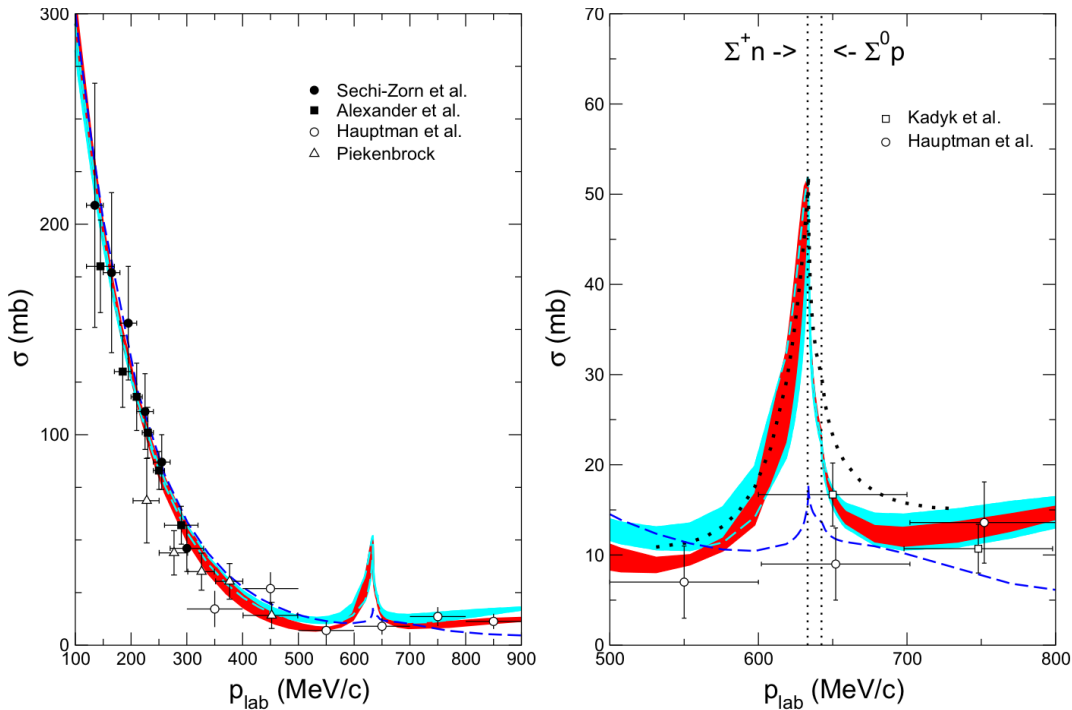


FIGURE 1.7: Scattering experiment cross sections for the  $\Lambda$ -p  $\rightarrow$   $\Lambda$ -p channel as a function of the momentum. The red and blue bands represent  $\chi$ EFT calculations, while the lines correspond to different phenomenological potentials. Figures taken from Ref. [25].

tal situation immensely. The goal of femtoscopy is to measure a particle pair correlation as a function of relative momentum in a pair rest frame which depends on the interaction potential between the two particles (for an extensive description, refer to Chapter 1.5). This method allowed the studies not only of p-p [34] and p- $\Lambda$  [35] systems, but also of many other hadrons pairs (p- $K^+$  and p- $K^-$  [36], p- $\Sigma^0$  [37],  $\Lambda$ - $\Lambda$  [38], p- $\Xi^-$  [39], p- $\Omega^-$  [30], p- $\phi$  [40] and baryon-antibaryon [41]). Some of these systems have never been measured before with traditional methods. The correlation functions of p-p, p- $\bar{p}$  and p- $\Lambda$  pairs are shown and discussed in detail in Chapter 3.5. Most importantly, these measurements provided unprecedented

precision data for these two systems down to relative momentum close to  $0 \text{ MeV}/c$ . In the case of the  $p\text{-}\Lambda$  pair, even the  $\Lambda N - \Sigma N$  coupling has been observed!

Finally, the interaction potentials can also be constrained to (hyper)nuclei data. However, the calculations of (hyper)nuclei properties require to account for many-body effects, including the genuine three-body interactions. Indeed, it has been shown that if only the two-particle interactions are included, it results in underbinding of the nuclei [1] and overbinding of the hypernuclei [2]. Thus the description of many-body systems requires the inclusion of the genuine three-body forces. The theoretical and experimental parts of the genuine three-body interactions are discussed in the next Chapter.

### 1.3 Three-baryon interactions

The first ideas of the three-body forces in atomic nuclei are almost 100 years old [42]. The long-range **three-nucleon** interaction was pioneered in 1956 by Fujita and Miyazawa [3], who described it as two pion exchange by extending the idea of Yukawa from two to three-body systems. Fujita and Miyazawa described the main contribution to this interaction coming from the excitation of  $\Delta(1232)$  resonance in the  $P_{33}$  partial wave of the pion-nucleon scattering amplitude, as shown in the left panel of Fig. 1.8. The contribution from S-wave also exists, but it is expected to be small [43]. The two-pion exchange results in attractive interaction at long distances [44]. However, as in the two-body case, the long-range part of the interaction is not enough to fully represent the three-body interactions. Thus often, a repulsive component was introduced for short-range interactions. For the three-body forces in the  $N\text{-}N\text{-}\Lambda$  system, the corresponding interaction component to the  $\Delta$  resonance in the three-nucleon system is the formation of virtual  $\Sigma$  hyperon as shown in the right panel of Fig. 1.8. A short review of some currently available studies of the three-baryon interactions and comparisons to available data is provided below. The main problem for phenomenological and  $\chi$ EFT approaches is that the extracted three-body potentials are constrained mainly to the hyper(nuclei) properties, which are significantly model-dependent observables and depend on the assumed two-body force. In the case of the three-nucleon system, the vast database from scattering experiments constrains the  $N\text{-}N$  potential rather precisely. However, for the hypernuclei description, the nucleon-hyperon potential is not that well constrained as, up to now, only the scarce scattering data have been used.

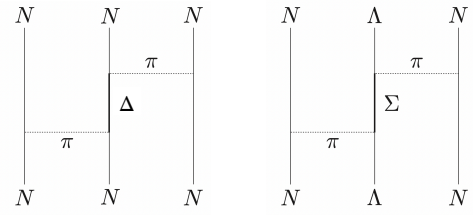


FIGURE 1.8: Fujita-Miyazawa three-nucleon force (left) and corresponding two pion exchange term in  $N\text{-}N\text{-}\Lambda$  system. Adapted from Refs. [43] and [2].

#### 1.3.1 Three-nucleon interactions

The calculations of nuclei binding energies, based on two-body potentials only, result in underbinding of the nuclei [1]. Another intriguing effect which cannot be

explained with the inclusion of only the two-body forces is the position of the neutron drip line. From light to medium mass nuclei, the limit of neutron-rich nuclei regularly evolves except for the anomaly in the oxygen isotopes. This thesis does not discuss this in detail; however, the newest results can be found in Ref. [45]. The way to resolve these issues is to account for the three-body interactions. The studies of nucleon-deuteron scattering experiments also showed that the three-body interactions are necessary to explain the data, which is also not discussed in detail here but can be found in Refs. [46, 47]. In the following, we discuss the status of the three-nucleon potentials from different approaches.

### Argonne $\nu_{18}$ (NN) + Illinois (NNN)

The Argonne  $\nu_{18}$  potential describes two-nucleon forces, as explained in the previous Chapter, and provides accurate fits to the scattering data. However, if used to determine the binding energies of nuclei in Quantum Monte Carlo (QMC) calculations (without additional NNN potential), they result in underbinding of nuclei [48]. This is shown in Fig. 1.9, where the binding energies for different nuclei are plotted for experimental values (green) and obtained using only Argonne  $\nu_{18}$  potential (blue). For all light nuclei, the calculations predict smaller binding energy than measured. The three-nucleon interaction can be described with several different potentials, for example, Urbana [49] and Illinois [50] series potentials. The Urbana series potentials include two-pion P-wave exchange (as shown in the left panel of Fig. 1.8) and a shorter-range phenomenological term. However, if the QMC calculations are performed using the Argonne  $\nu_{18}$  and Urbana IX potentials, only the binding energies of s-shell nuclei can be reproduced well, but not the p-shell light nuclei [48]. To address this problem, Illinois potentials were developed. In addition to the two Urbana

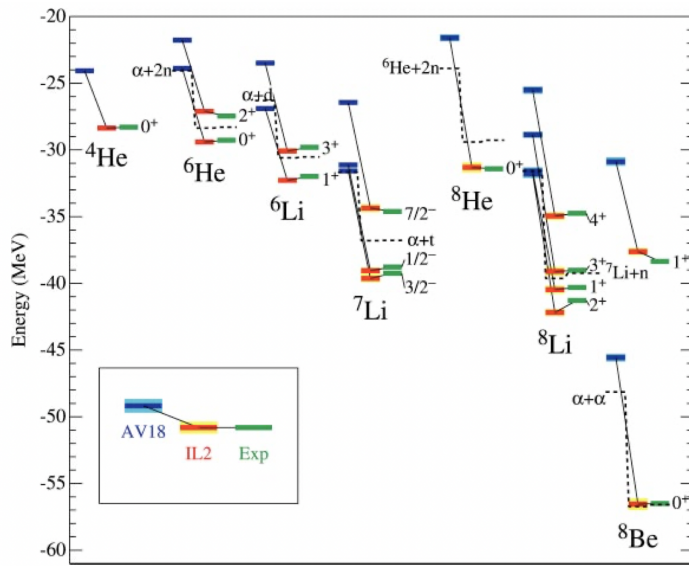


FIGURE 1.9: Binding energies for different nuclei [48]. The green line corresponds to the experimental value, the blue line to the result obtained using only Argonne  $\nu_{18}$  potential and the red line to the case where Illinois potential for three-body forces is included.

terms, it includes the S-wave contribution of the pion-nucleon scattering amplitude and a contribution from the three-pion exchange. The latter is implemented in a

simplified way in Illinois potentials, where only terms with the most significant contributions to this diagram are accounted for. The latter term is small and repulsive in s-shell nuclei but attractive in p-shell nuclei, which have isospin 3/2 triplets. This term is responsible for solving the p-shell problem observed with Urbana potential. All diagrams included in the Illinois potentials are shown in Fig. 1.10. The combination of Argonne  $\nu_{18}$  and Illinois II potentials in the QMC calculations (red box) results in a very good agreement with experimental values (green box) for both s-shell and p-shell nuclei as shown in Fig. 1.9.

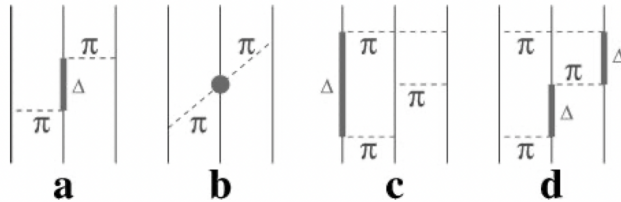


FIGURE 1.10: Three nucleon interactions included in Illinois potentials [48].

### Chiral effective field theories

The  $\chi$ EFT generates all interaction terms simultaneously, as explained in the previous Chapter on two-body interactions. This means that many-body interaction terms arise naturally, as shown in Fig. 1.6 at NNLO and higher orders for the  $\Delta$ -less  $\chi$ EFT. The  $\Delta$ -full  $\chi$ EFT includes an explicit  $\Delta$  isobar, and in such theory, the three-nucleon forces start already at the NLO term. It also changes the ordering of the two-body forces. Including  $\Delta$  isobar helps with the convergence of two-body and three-body forces at orders beyond NNNLO in  $\chi$ EFTs [23]. However, both versions of the theory lead to similar results if calculations up to NNLO are performed [51], as in the  $\Delta$ -less  $\chi$ EFT the effects due to the  $\Delta$  isobar are accounted for implicitly.

The  $\chi$ EFT with the inclusion of three-nucleon forces has been successfully applied in studies of light and medium-mass nuclei [1, 52–54]. It has been shown, for example, that to correctly describe the  $^7\text{Li}$  nuclei ground-state binding energy with *ab initio* no-core shell model, the inclusion of three-body forces in  $\chi$ EFT is necessary [1]. The same is observed for phenomenological models. The results obtained in Ref. [1] are summarised in Table 1.1. The second and third entries in the table correspond to the same model, but two different parameter sets describing the strength of the contact term for the three-nucleon force in the  $\chi$ EFT potential. These so-called strength constants were obtained in Ref. [1] by fitting the model to reproduce  $^3\text{H}$ , and  $^4\text{He}$  binding energies and two sets of parameters performed equally well. However, as shown in Table 1.1, they result in different values of the binding energy for  $^7\text{Li}$  nuclei. This is one example showing that determining three-body forces requires precise data, as different combinations of parameters might fit available data equally well. This has also been seen in studies of N-N- $\Lambda$  interactions, which will be discussed below.

### Lattice QCD

There are also first efforts towards the three-nucleon forces in LQCD. However, lattice simulations for nuclei are not yet realistic as they can be performed only for larger pion masses than the physical ones, and thus, we will not discuss these in detail. The state-of-the-art study of the three-nucleon forces on the lattice is published in Ref. [55].

Model	$E_{\text{gs}}$
NN only	34.6
w/ 3NF-A	38.0
w/ 3NF-B	36.7
AV18 only	31.6
AV18+Urbana IX	37.5
AV18+IL2	38.9
Expt.	39.2

TABLE 1.1: Ground-state binding energy of  ${}^7\text{Li}$  nuclei obtained using different interaction potentials. Table adapted from [1].

### 1.3.2 N-N- $\Lambda$ interactions

The measurements of hypernuclei, similarly to nuclei, showed that their binding energies could not be satisfactorily reproduced by the inclusion of two-body forces only, and it requires to account for the three-baryon N-N- $\Lambda$  interaction. However, in the case of hypernuclei, overbinding is observed [2]. Several approaches are available to describe the N-N- $\Lambda$  three-baryon potential.

#### Phenomenological approach

Similarly to the three-nucleon case, the N-N- $\Lambda$  interaction can be described by a two-pion exchange and an additional phenomenological term describing short-range contribution. Such potential was first introduced by Bodmer, Usmani, and

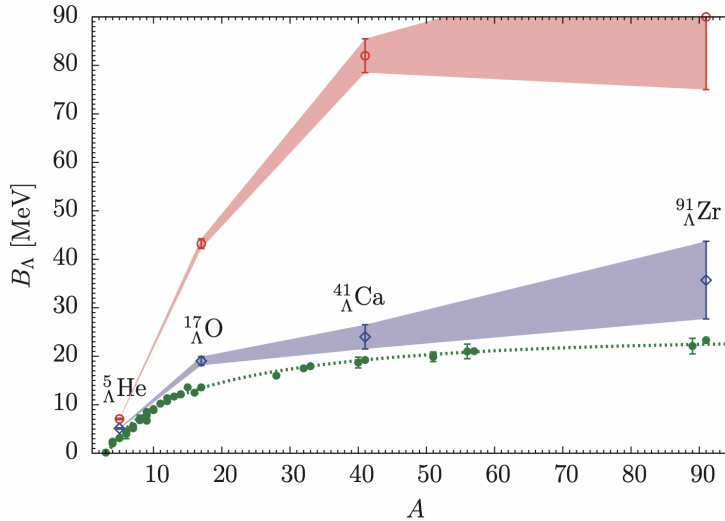


FIGURE 1.11: Hypernuclei separation energies as a function of the baryon number  $A$  [2]. The green points represent the available data, the red points - the separation energies obtained including only two-body interactions, and the blue points - with the inclusion of N-N- $\Lambda$  forces.

Carlson [56]. Usmani provided an updated version of phenomenological N-N- $\Lambda$  potential in 1995, where he also provided a parametrisation of parameters fitted to reproduce the  ${}^5\Lambda\text{He}$  and  ${}^{17}\Lambda\text{O}$  nuclei separation energies ( $B_\Lambda = B_{\text{nuc}} - B_{\text{hyp}}$ ) [57]. The

most modern version of the Usmani potential can be found in Ref. [58]. The effects of such three-body interactions on the hypernuclei description have been studied up to  $^{91}_{\Lambda}\text{Zr}$  nuclei in Ref. [2], where the auxiliary field diffusion Monte Carlo (AFDMC) model was used to solve many-body Schrödinger equation. The results of this study are shown in Fig. 1.11, where Argonne  $\nu'_4$  potential was used for the N-N interaction (which corresponds to a simplified version of Argonne  $\nu_{18}$ ) and for nucleon-hyperon and nucleon-nucleon-hyperon interactions, the Usmani potential is employed. The red points correspond to the calculation, where only two-body interactions are included. The obtained separation energies are too large compared to the data (green points). Including the three-body forces partially resolves this disagreement (blue curve). In a later study, Lonardoni et al. compare the equations of state<sup>4</sup> obtained using the Usmani potential discussed above [57] and a re-fitted parameterisation of this potential to reproduce better the binding energies of heavier hypernuclei [2]. Their study shows that although both potentials reproduce the data well, they result in entirely different Equations of State. Thus, again, more precise data is required.

### Other approaches

The  $\chi$ EFT has also progressed in the N-N- $\Lambda$  interactions by constructing effective density-dependent two-body potentials [59]. Also, a pionless EFT has been used to describe hypertriton [60]<sup>5</sup> (actually, such calculations are available also for nuclei [62, 63]). The lattice QCD also provides the first calculations for this channel; however, similarly to the nuclei case, they are performed at nonphysically high light quark masses [64].

## 1.4 Dense matter: neutron stars

The relevance of three-body forces increases with the increasing density of the system. Some of the densest objects in the universe are neutron stars which provide a bridge between nuclear physics and astrophysics. Neutron stars have been observed in a mass range of  $1\text{-}2 M_\odot$ , where  $M_\odot$  is the solar mass, and have a radius of around 10-12 km [4]. The structure of a neutron star consists of an atmosphere, outer crust, inner crust, outer core and inner core going from the outer part of the neutron star to its centre with an increasing density. While the composition of outer layers is rather well known [65], the inner core remains a mystery. In the following, we refer to the physics of the inner core of neutron stars as the physics of neutron stars. It was originally thought that neutron stars consist mainly of neutrons and are stable because the gravitational collapse is counteracted by the neutron degeneracy pressure, as neutrons are spin-1/2 particles. However, the fermionic nature of neutrons also means that the neutron chemical potential increases drastically with the increasing density of the system. Indeed, the densities of neutron stars might reach a few  $\rho_0$  (nuclear saturation density), and introducing new degrees of freedom might become energetically favourable. The chemical potential can be expressed as  $\mu_i(\rho) = M_i + U_i(\rho)$ , where  $M_i$  and  $U_i$  are the mass and the single-particle potential in nuclear matter composed of particle species  $i$ . It was proposed in 1960 that hyperons might appear in highly degenerate baryon gas at very high densities [66]. The microscopic and macroscopic properties of neutron

---

<sup>4</sup>More details in Chapter 1.4.

<sup>5</sup>We do not discuss pionless EFT in this thesis; however, a good review of both EFTs with and without explicit pions can be found in Ref. [61]

stars are related by the Tolman-Oppenheimer-Volkoff (TOV) [67–69] equations, which take as input the density dependence on the pressure of the system, also known as the nuclear Equation of State (EoS). The EoS depends on the neutron star’s composition and the interactions between its constituents. Every EoS thus results in a specific mass-to-radius relation of a neutron star. Thus EoSs, estimated by nuclear physicists, can be tested by comparing the result to the observed neutron star masses and radii. The assumption of pure neutron matter composition results in EoS, which could explain the observed very heavy neutron stars; however, hyperons are expected to appear in the system at high densities, as mentioned before. This would result in the softening of the EoS, and in some models, the predicted maximum possible mass of a neutron star is smaller than the observed  $2 M_{\odot}$  [70]. This is known as **hyperon puzzle**. The problem is very delicate, as to describe realistic EoS, the two and three-body interactions must be included, and the potentials constrained at nuclear densities must be extrapolated to the densities of neutron stars. The hyperon puzzle initiated decades lasting conquest for theorists to describe nucleon-hyperon potentials from first principles and for experimentalists to measure the nucleon-hyperon interactions, especially the three-body component. Enormous advancement in the experimental knowledge of nucleon-hyperon and hyperon-hyperon interactions was achieved in the last years by the femtoscopy technique [71]. Using nucleon-hyperon potentials, which agree with the femtoscopy measurements, a new EoS was obtained, and a corresponding mass-to-radius relation was estimated as shown in Fig. 1.12. The left panel shows particle number per baryon as a function of the energy density, where different lines correspond to different particle species. The right panel shows the mass-to-radius relation obtained for such EoS. Indeed, the heaviest neutron stars observed so far could be explained by such EoS.

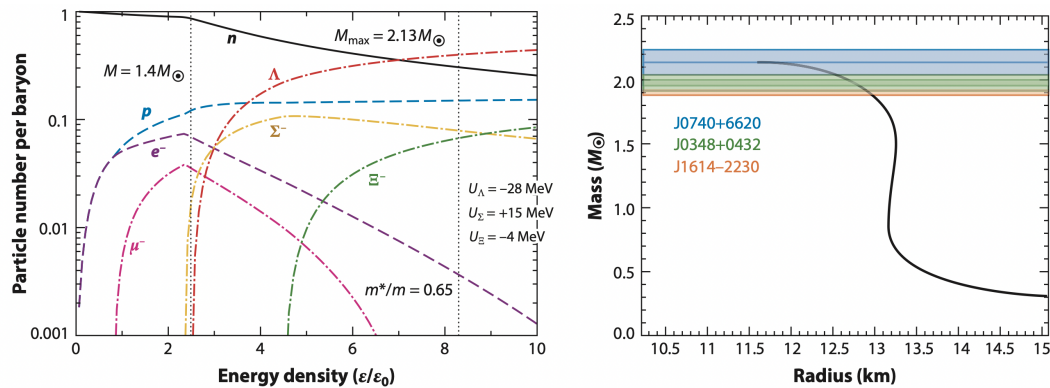


FIGURE 1.12: Left: Particle number per baryon as a function of energy density. Different lines correspond to different particle species. Right: Mass-to-radius relation corresponding to EoS used to obtain the result on the left panel. Figures taken from Ref. [71].

While this is an impressive result, some interaction potentials still need to be added to the EoSs estimated nowadays, and the problem of not well-constrained three-body forces still needs to be solved. Additionally, the uncertainties related to the measurements of interactions were not included in the discussed EoS study, which must be done to understand better the missing pieces required to solve the hyperon puzzle.

The effects of N-N- $\Lambda$  three-body forces on the EoS and mass-to-radius relation of

neutron stars have been studied in Ref. [72]. The authors used Argonne  $\nu_8'$  potential for N-N interactions, Urbana IX potential for N-N-N and a phenomenological potential adapted from [56] for N- $\Lambda$ . They tested two parameterizations of the phenomenological N-N- $\Lambda$  potential discussed in Chapter 1.3.2: the Usmani potential from 1995 fitted to reproduce  $^5_\Lambda$ He and  $^{17}_\Lambda$ O separation energies [57] (model I) and the updated parameterization of the Usmani potential studied by the authors explicitly in Ref. [73] which reproduces heavier hypernuclei better (model II).

The comparison of the hypernuclei separation energies obtained with the two parameterizations is shown in Fig. 1.13. The details of the study can be found in Ref. [73]. The green points correspond to the available data for separation energies of hypernuclei with nucleon number  $A$ . The blue diamonds show the results of calculations obtained, including only the two-body p- $\Lambda$  potential. The red diamonds correspond to the calculations including three-body interactions employing model I. These results are closely related to the study by the same authors in Ref. [2] and described in Chapter 1.3.2. The black triangles show results obtained using the updated parameters of the three-body potential referred to as model II. The latter reproduces better the separation energies for the shown hypernuclei; however, the predicted separation energies for  $A < 5$  hypernuclei are underestimated [73]. The values obtained employing model I for such nuclei agree with the data. The EoS with the three-body potential model I is shown as

the blue band on the left panel of Fig. 1.14. The green band represents the EoS obtained for pure neutron matter, while the EoS for neutron-hyperon matter, including only two-body N- $\Lambda$  forces, is shown as a red band. Indeed, as mentioned before, the EoS for pure neutron matter is rather steep, and the inclusion of the  $\Lambda$  hyperons softens it. The EoS, including the N-N- $\Lambda$  interaction, is stiffer than if only N- $\Lambda$  forces are accounted for, which suggests the repulsive nature of the included three-body potentials at high densities. The inset shows the densities at which the  $\Lambda$  hyperon appears in the system for the two models. The right panel of Fig. 1.14 shows mass-to-radius relations corresponding to the discussed EoSs. The pure neutron matter could explain the  $2 M_\odot$  neutron stars; however, the EoS including  $\Lambda$  hyperons but obtained using only N- $\Lambda$  interactions could explain only very light neutron stars. Including the N-N- $\Lambda$  interaction via model I results in heavier possible neutron stars; however, the maximum possible mass reaches only  $1.36 M_\odot$ . The dashed-dotted black curve represents the mass-to-radius relation obtained with EoS with N-N- $\Lambda$  included via model II. In this model, the repulsion of N-N- $\Lambda$  interaction would be so high that the  $\Lambda$  hyperon would not appear in the system at all, at tested densities.

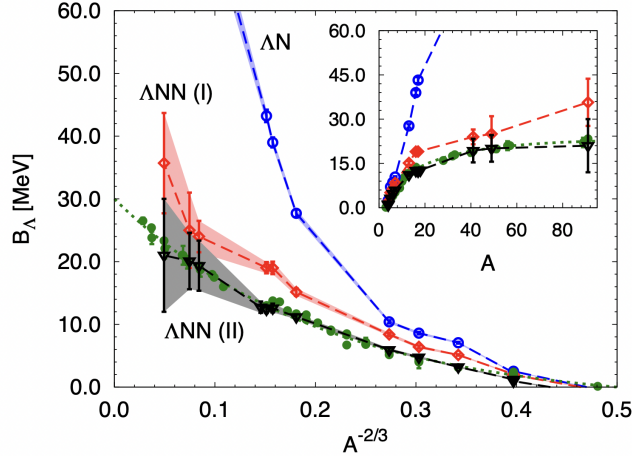


FIGURE 1.13: Separation energies obtained with two different parameterizations of the three-body potential [73]. The green circles correspond to the available data for hypernuclei separation energies. The empty blue circles correspond to the calculations including only the two-body p- $\Lambda$  potential. The red diamonds and black triangles correspond to the calculations including the three-body p-p- $\Lambda$  potential employing models I and II, respectively.

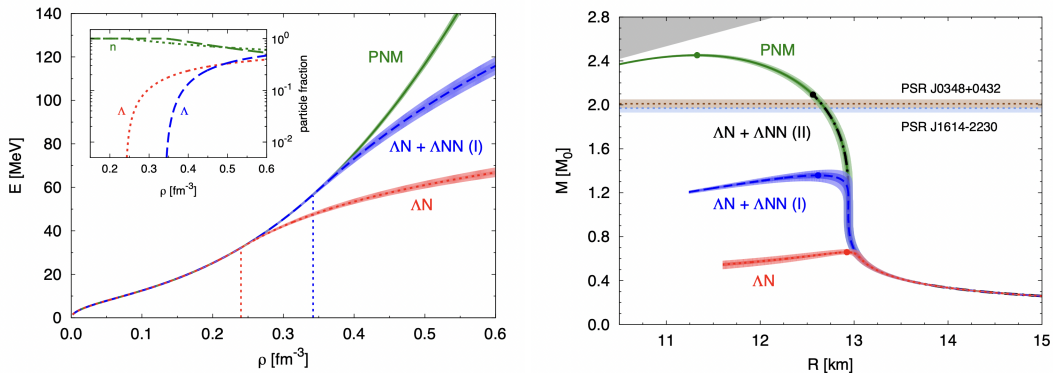


FIGURE 1.14: Left: Equation of state as a function of system density for pure neutron matter (green band), neutron-hyperon matter with only two-body interactions (red band) and including N-N- $\Lambda$  potential (blue band). Right: Mass-to-radius relations corresponding to these EoS. Figures taken from Ref. [72].

Thus, EoS based on model II could explain the  $2 M_\odot$  neutron stars, as shown in the figure. These results are significant, as employing two different parameterizations of the phenomenological three-body N-N- $\Lambda$  potential results in completely different EoSs, even though both models can explain the available hypernuclei data<sup>6</sup>. This is a prime example that fully understanding N-N- $\Lambda$  interaction requires additional data. The hyperon puzzle also requires an understanding of the interactions at high densities. Thus experimental constraints from high-density or small inter-particle distance systems are in high demand.

The first attempt to address the hyperon puzzle and three-body interactions using  $\chi$ EFT was recently published [59]. The authors showed that within  $\chi$ EFT framework, it is, indeed, *possible* for the three-body N-N- $\Lambda$  interactions to develop sufficient repulsion to suppress the appearance of  $\Lambda$  hyperons in the system. However, in this study, the three-body potential is also not well constrained, allowing a wide parameter set range. The results were obtained by *choosing* parameter set, which is compatible with hypernuclei data but could also result in enough repulsion to resolve the hyperon puzzle. This again proves the necessity for the new experimental constraints for the three body N-N- $\Lambda$  systems.

The first part of this thesis aims to develop a new method to access three-body systems down to small inter-particle distances of around 1 fm based on the femtoscopy technique.

## 1.5 Two-particle femtoscopy

The setup of scattering experiments to study the two-particle interactions requires a beam or a target made of particles of interest. Such setup can be easily achievable for a p-p system and a vast database is available. However, even for such strangeness S=-1 system as p- $\Lambda$  this becomes complicated, and not so many data points are available as shown in Chapter 1.2.2. An alternative experimental approach was necessary to advance the field of nuclear physics.

Femtoscopy is a technique which relates the two-particle correlation in momentum-space to the Final State Interaction (FSI) and the particle emission region. In the early

<sup>6</sup>Model I reproduces well light hypernuclei ( $A < 5$ ) and model II reproduces well heavier hypernuclei, as explained in the text.

days, the femtoscopy technique was used to measure hadron pairs, for which interaction is very well known, aiming to constrain the particle emission source in ultra-relativistic heavy ion collisions. An excellent review concerning such application of femtoscopy can be found in Ref. [74]. However, in the last decade, the paradigm of femtoscopy was inverted. The femtoscopic correlations are now being measured in systems of known size<sup>7</sup> to access the information about the FSI. Such an approach is also known as *non-traditional femtoscopy*. A fantastic chronological overview of the evolution of femtoscopic studies can be found in the thesis of my colleague Dimitar [75], which also serves as a very educationally written introduction to the two-particle femtoscopy. While the method of non-traditional femtoscopy is relatively new, it is very well established [71], and I will refer to it just as femtoscopy in the following.

The idea of femtoscopy is that if particles are produced in a collision close in phase-space, they might experience the FSI, and their momenta become correlated as shown in Fig. 1.15. The two-particle momentum correlation function [74, 76] is

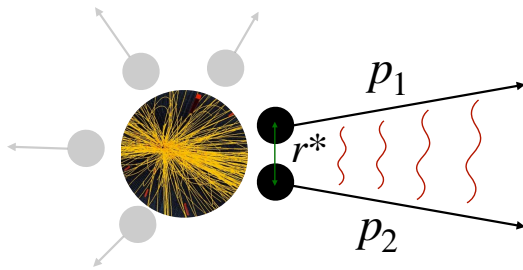


FIGURE 1.15: Femtoscopic picture of analysed particle pair.

defined as the probability of simultaneously finding two particles with momenta  $\mathbf{p}_1$  and  $\mathbf{p}_2$  divided by the single particle probabilities

$$C(\mathbf{p}_1, \mathbf{p}_2) \equiv \frac{P(\mathbf{p}_1, \mathbf{p}_2)}{P(\mathbf{p}_1)P(\mathbf{p}_2)}, \quad (1.3)$$

where these probabilities are proportional to the inclusive Lorentz-invariant spectra  $P(\mathbf{p}_1, \mathbf{p}_2) \propto E_1 E_2 \frac{d^6 N}{d^3 \mathbf{p}_1 d^3 \mathbf{p}_2}$  and  $P(\mathbf{p}_i) \propto E_i \frac{d^3 N_i}{d^3 \mathbf{p}_i}$ . Experimentally, the femtoscopic correlation function is described as

$$C(\mathbf{p}_1, \mathbf{p}_2) = C(k^*) = \mathcal{N} \frac{N_s(k^*)}{N_m(k^*)}, \quad (1.4)$$

where  $\mathbf{p}_i$  is the momentum of  $i$ th particle,  $N_s$  and  $N_m$  are the same and mixed event distribution,  $k^*$  is the relative momentum in pair rest frame  $k^* = |\mathbf{p}_1^* - \mathbf{p}_2^*|/2$  and  $\mathcal{N}$  is a normalisation constant. The same event distribution is obtained by creating all possible combinations of two particles in one event. In comparison, the mixed event distribution is obtained by taking the two particles from two different effects. While the mixed event does not include FSI effects, it accounts for the phase space available in the collision. From the theory side, the correlation function can be expressed via the Koonin-Pratt relation as [77, 78]

$$C(\mathbf{k}^*) = \int d^3 r^* S(r^*) |\psi(\mathbf{r}^*, \mathbf{k}^*)|^2, \quad (1.5)$$

<sup>7</sup>This will be explained in Chapter 1.5.1.

where  $S(r^*)$  corresponds to the distribution of the relative distances of particle pairs in the pair rest frame (PRF, denoted by the  $*$ ) — the so-called source function and  $\psi(\mathbf{r}^*, \mathbf{k}^*)$  is the wave function of the particle pair relative motion. The wave function generally depends on all possible interaction terms: the quantum statistics, the Coulomb interaction, and the residual strong interaction between hadrons. If no FSI is present for the given particle pair, the correlation function would be equal to unity. If particles of interest are fermions, their relative wave function must be antisymmetrised, resulting in depletion of the correlation function. The opposite is true for a boson pair. Such an effect strongly depends on the relative distance between the particles. The Coulomb interaction for the opposite-charged particle pair is attractive and thus results in a correlation function above unity, and the opposite effect is observed for the same-charged particle pair. As Coulomb interaction is long-range, its effects on the correlation functions are not strongly dependent on the relative distance between the particles. Finally, how the correlation function is affected by the strong interaction depends on its potential. The goal of femtoscopic studies is constraining the relative wave function of the pair and, thus, the potential between the two particles. One needs a method to calculate the relative wave function for a given potential to model a correlation function. A simplification to such a task was proposed by Lednický and Lyuboshits [76]. Their model provides an analytical form of correlation function related to the asymptotic solution of the wave function for elastic interaction obtained employing effective range expansion from scattering theory. Such wave function solution can be written as a sum of the incoming free wave and a modified outgoing spherical wave as

$$\psi(\mathbf{k}^*, \mathbf{r}^*) = e^{i\mathbf{k}^* \cdot \mathbf{r}^*} + f(k^*) \frac{e^{ik^* r^*}}{r^*}, \quad (1.6)$$

where the scattering amplitude for S-wave is given as

$$f_S(k^*) \approx \left( \frac{1}{f_0} + \frac{1}{2} d_0 k^{*2} - ik^* \right)^{-1}. \quad (1.7)$$

Here,  $f_0$  is the scattering length, and  $d_0$  is the effective range. Using this approximation, Eq. 1.5 can be solved, assuming a static and spherically symmetric source function described by a Gaussian function of width  $r_0$ . This would result in the Lednický and Lyuboshits formula. However, in this thesis, we will talk about p-p collisions, which have source sizes of around 1-2 fm, and an entirely asymptotic approximation would not satisfactorily describe the data. For this purpose, Lednický provided an improved formula with a correction factor  $\left(1 - \frac{d_0^S}{2\sqrt{\pi}r_0}\right)$

$$\begin{aligned} C(k^*) &= 1 + \frac{1}{2} \left| \frac{f_S(k^*)}{r_0} \right|^2 \left( 1 - \frac{d_0^S}{2\sqrt{\pi}r_0} \right) \\ &\quad + \frac{2\Re f_S(k^*)}{\sqrt{\pi}r_0} F_1(2k^*r_0) - \frac{\Im f_S(k^*)}{r_0} F_2(2k^*r_0), \end{aligned} \quad (1.8)$$

where  $F_1(2k^*r_0)$  and  $F_2(2k^*r_0)$  are analytical functions of the form

$$F_1(z) = \frac{e^{-z^2}}{z} \int_0^z e^{x^2} dx \quad (1.9)$$

and

$$F_2(z) = \frac{1}{z} \left( 1 - e^{-z^2} \right). \quad (1.10)$$

However, this approximation is not precise for very small distances, accounts only for s-wave, and assumes that interacting particles are point-like and thus could not be employed for such correlations as p-d.

An approach to estimate the integral shown in Eq. 1.5 without an asymptotic approximation would be preferred for small collision systems. Such a tool, called the "Correlation Analysis Tool using the Schrödinger equation" (CATS) [79], was developed by the previously mentioned colleague of mine, Dimitar. The CATS framework numerically solves this integral for a given source and wave functions. CATS also includes a Schrödinger solver for the cases when the wave function is unavailable, but interaction can be expressed as a real local potential  $V(r)$ . In such a case, the wave function is obtained by solving the Schrödinger equation, and then the correlation function can be computed. The in detail description of CATS is provided in Refs. [75, 79].

An exemplary correlation function obtained with CATS is shown in Fig. 1.16 for a p-p pair for a Gaussian source with  $r_0$  value of 1.25 fm. The different dashed and dashed-dotted lines represent contributions from the effect of the quantum statistics (below unity, as protons are fermions and the correlation function thus goes to 0.5 at  $k^* = 0 \text{ MeV}/c$ ), Coulomb interaction (below unity and goes towards 0) and strong interaction (goes above unity). The solid line represents the correlation function when all the interactions are included in the calculation. Here, the Aronne  $\nu_{18}$  potential is used for the strong interaction.

Some of the already measured two-body correlation functions are shown and discussed in Chapter 3.5. Before moving to the three-particle correlations, the source function must be discussed.

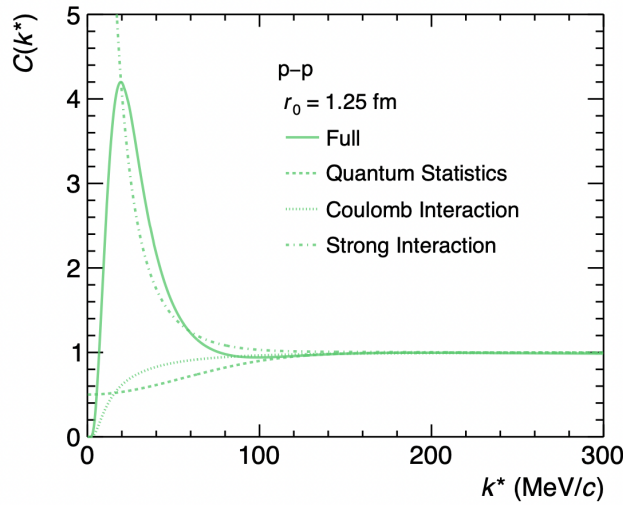


FIGURE 1.16: p-p correlation function estimated with CATS [80]. Details provided in text.

### 1.5.1 Source function

The particle pair emission source for different baryon pairs has been shown to be universal in high-energy pp collisions at ALICE [79]. It was achieved by modelling the source as a sum of a Gaussian core, the same for all baryons pairs, and a contribution from strong resonance decays. The Gaussian core is parametrised as

$$S(r) = \frac{1}{(4\pi r_{core}^2)^{3/2}} \exp\left(-\frac{r^2}{4r_{core}^2}\right), \quad (1.11)$$

where  $r_{core}$  is the so-called source size and  $r$  is the relative distance between particles. The short-lived strong resonance contribution is estimated by employing the statistical hadronisation model for resonance yields and the EPOS event generator for the kinematics of produced resonances. Thus the only free parameter in the model

is  $r_{\text{core}}$ . The resonance contribution is added to the Gaussian core. It has been shown that the obtained source function can be fitted with another Gaussian function resulting in an effective source radius  $r_0$ . Such source model was fitted to the measured p-p and p- $\Lambda$  correlation functions. Both systems have the same  $r_{\text{core}}$  value, as shown in Fig. 1.17, suggesting a universal source. Indeed, this source was successfully applied in later studies to estimate correlation functions for different hadron pairs.

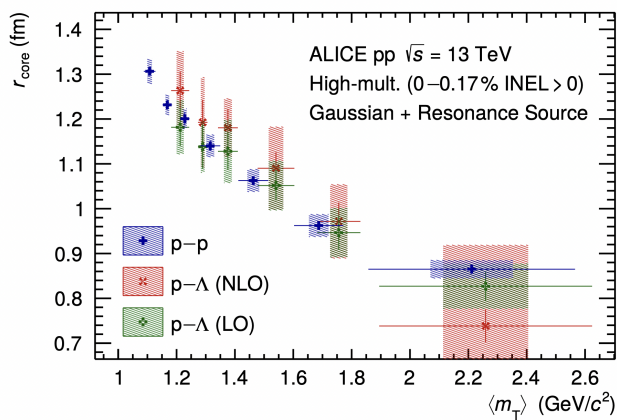


FIGURE 1.17: Source size as a function of transverse mass [79].

## 1.6 Extension to three-particle femtoscopy

The natural next step in the femtoscopy studies is extending it to the three-body case. Pairwise interactions and genuine three-body effects can induce momentum correlations in a three-body system. In this Chapter, we discuss the basis of the three-particle correlation functions and how we can use the cumulant method to subtract the lower-order contributions and inspect if any genuine three-body effects are present in the system. We will also present the projector method to calculate lower-order contributions to the three-body system for known two-body correlation functions.

### 1.6.1 Three-particle correlation function

The two-body correlation function can be generalised to obtain the three-body correlation function. The Eq. 1.3 then becomes

$$C(\mathbf{p}_1, \mathbf{p}_2, \mathbf{p}_3) \equiv \frac{P(\mathbf{p}_1, \mathbf{p}_2, \mathbf{p}_3)}{P(\mathbf{p}_1)P(\mathbf{p}_2)P(\mathbf{p}_3)}, \quad (1.12)$$

and the experimental expression is

$$C(\mathbf{p}_1, \mathbf{p}_2, \mathbf{p}_3) = C(Q_3) = \mathcal{N} \frac{N_s(Q_3)}{N_m(Q_3)}. \quad (1.13)$$

In analogy to the two-body case, the numerator is obtained by building all possible combinations of three particles of interest (triplets) in an event. In contrast, the denominator is obtained by combining three particles from three different events. The Lorentz-invariant variable  $Q_3$  is defined in [81] as

$$Q_3 = \sqrt{-q_{12}^2 - q_{23}^2 - q_{31}^2}, \quad (1.14)$$

where  $q_{ij}$  is the norm of the four-vector [74]

$$q_{ij}^\mu = (p_i - p_j)^\mu - \frac{(p_i - p_j) \cdot P_{ij}}{P_{ij}^2} P_{ij}^\mu, \quad P_{ij} \equiv p_i + p_j, \quad (1.15)$$

which can be rewritten as

$$q_{ij}^\mu = \frac{2 m_j}{m_i + m_j} p_i^\mu - \frac{2 m_i}{m_i + m_j} p_j^\mu. \quad (1.16)$$

Here  $m_i$  and  $m_j$  are the particle  $i$  and  $j$  masses,  $p_i^\mu$  and  $p_j^\mu$  are the particle four momenta, while  $q_{ij}^\mu$  is the relative four-momentum of the pair  $ij$ . In the case of same mass particles, the term  $\frac{(p_i - p_j) \cdot P_{ij}}{P_{ij}^2} P_{ij}^\mu$  becomes 0. In the non-relativistic case  $q_{ij}^2 = -4k_{ij}^{*2}$ , where  $k_{ij}^*$  is the relative momentum of the  $ij$  pair in the PRF. The theoretical correlation function is introduced in the next Chapter, together with one specific theoretical prediction by Alejandro Kievsky.

### 1.6.2 Theory of three-particle correlation functions

The most general form of the relation between the three-body correlation function and the source and the wave function can be written following Eq. 1.5 as

$$C_3(\mathbf{p}_1, \mathbf{p}_2, \mathbf{p}_3) = \int \int \int S_3(\mathbf{r}_1, \mathbf{r}_2, \mathbf{r}_3) |\Psi(\mathbf{r}_1, \mathbf{r}_2, \mathbf{r}_3, \mathbf{p}_1, \mathbf{p}_2, \mathbf{p}_3)|^2 d^3\mathbf{r}_1 d^3\mathbf{r}_2 d^3\mathbf{r}_3, \quad (1.17)$$

where  $\mathbf{r}_1$ ,  $\mathbf{r}_2$  and  $\mathbf{r}_3$  are the coordinates of the three particles,  $\mathbf{p}_1$ ,  $\mathbf{p}_2$  and  $\mathbf{p}_3$  are the corresponding conjugate momenta,  $S_3(\mathbf{r}_1, \mathbf{r}_2, \mathbf{r}_3)$  is the three-body source function and  $\Psi(\mathbf{r}_1, \mathbf{r}_2, \mathbf{r}_3, \mathbf{p}_1, \mathbf{p}_2, \mathbf{p}_3)$  is the three-body wave function. The calculations of two-body and many-body systems are often performed in the centre-of-mass of the  $A$ -body reference frame, and the spatial configuration of the  $A$ -body system can be sufficiently described by  $N=A-1$  vectors. The latter can be constructed using a linear combination of the  $\mathbf{r}_i$  vectors. One possible choice is the Jacobi coordinates that are defined such that the total kinetic energy of the system can be separated into two parts: the centre-of-mass movement and the relative movement between particles.

The general form of Jacobi vectors for a system of  $N+1$  particles of different masses is the following

$$\mathbf{x}_{N-j+1} = \sqrt{\frac{2m_{j+1}M_j}{(m_{j+1} + M_j)m}} [\mathbf{r}_{j+1} - \mathbf{X}_j], \quad j = 1, \dots, N, \quad (1.18)$$

where

$$M_j = \sum_{i=1}^j m_i, \quad \mathbf{X}_j = \frac{1}{M_j} \sum_{i=1}^j m_i \mathbf{r}_i, \quad (1.19)$$

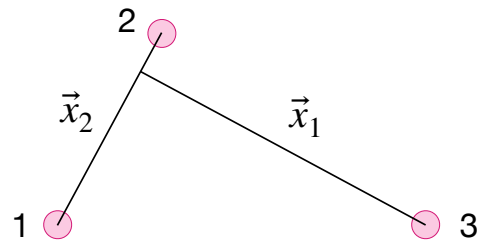


FIGURE 1.18: The Jacobi coordinates for a three-particle system. One possible particle permutation is shown.

and  $m_i$  is the mass of the  $i$ th particle. For a system of three identical mass particles, this results in

$$\begin{cases} \mathbf{x}_2 = \mathbf{r}_j - \mathbf{r}_i, \\ \mathbf{x}_1 = \frac{2}{\sqrt{3}} \left( \mathbf{r}_k - \frac{\mathbf{r}_i + \mathbf{r}_j}{2} \right). \end{cases} \quad (1.20)$$

The ordering of  $i, j, k$  indices corresponds to different particle permutations. The case of the permutation  $i,j,k \rightarrow 1,2,3$  is shown in Fig. 1.18. The Hamiltonian for such a system can be written as

$$H = T + V = T_{CM} - \frac{\hbar^2}{m} (\nabla_{x_1}^2 + \nabla_{x_2}^2) + \sum_{i < j} V(i, j) + \sum_{i < j < k} W(i, j, k), \quad (1.21)$$

where  $T_{CM}$  corresponds to the kinetic energy associated with the centre-of-mass movement,  $\frac{\hbar^2}{m} (\nabla_{x_1}^2 + \nabla_{x_2}^2)$  is the kinetic energy operator for the relative particle movement and  $\sum_{i < j} V(i, j)$  and  $\sum_{i < j < k} W(i, j, k)$  are the two- and three-body interaction potentials.

Different methods have been applied to study the few-body bound and scattering states. For example, Faddeev equations [82, 83], quantum Monte-Carlo methods [84] or the Kohn variational principle [85] can be used to study three-body systems. However, these methods have yet to be applied to study correlation functions. Recently, a new development towards this direction has been carried out by Alejandro Kievsky, who employed the Hyperspherical Harmonics (HH) method [86] to obtain the preliminary results for the p-p-p wave function and the corresponding correlation function. The calculations introduced in this Chapter and corresponding figures show preliminary results from Alejandro's calculations.

The three-nucleon wave function can be expressed as a sum of Faddeev-like amplitudes [86]

$$\Psi = \sum_{p=1}^3 \psi \left( \mathbf{x}_1^{(p)}, \mathbf{x}_2^{(p)} \right), \quad (1.22)$$

where the index  $(p)$  indicates the  $p$ th even permutation and  $\psi \left( \mathbf{x}_1^{(p)}, \mathbf{x}_2^{(p)} \right)$  amplitudes are antisymmetric, by construction, to the exchange of  $i$ th and  $j$ th particles. The three-body plane wave can be expanded employing the HH orthogonal basis as follows

$$\Psi_s^0 = \frac{(2\pi)^3}{(Q\rho)^2} \sum_{Jj_z} \sum_{[K]} i^K J_{K+2}(Q\rho) \mathcal{Y}_{[K]}^{LSJj_z}(\Omega) \mathcal{Y}_{[K]}^{LSJj_z,*}(\hat{Q}), \quad (1.23)$$

where  $\rho = (\mathbf{x}_1^2 + \mathbf{x}_2^2)^{1/2}$  is the hyperradius and  $Q = (\mathbf{k}_1^2 + \mathbf{k}_2^2)^{1/2}$  is the hypermomentum with  $\mathbf{k}_1$  and  $\mathbf{k}_2$  being the conjugate momenta of  $\mathbf{x}_1$  and  $\mathbf{x}_2$ , respectively. The full set of hyperspherical coordinates consists of  $\rho$  and  $\Omega$ , where  $\Omega$  is the set of angular variables  $\phi, \hat{x}, \hat{y}$ . The hyperradius and hypermomentum do not depend on the specific particle permutation used to construct the Jacobi vectors. The hypermomentum  $Q$  is related to the experimental observable  $Q_3$  by a constant  $\sqrt{6}$  for three identical mass particles. The  $J_{K+2}(Q\rho)$  are the Bessel functions of the first kind and the  $\mathcal{Y}_{[K]}^{LSJj_z}(\Omega)$  correspond to the HH functions  $\mathcal{Y}_{[K]}(\Omega)$  coupled to the spin functions  $\chi_{SS_z}^{S_{12}}$  for a given total angular momentum  $J$ , spin  $S$  and orbital angular momentum  $L$ . The HH functions  $\mathcal{Y}_{[K]}(\Omega)$  of order  $K$  are the generalisation of spherical harmonic functions to the three-body problem. The symbol  $[K]$  stands for a specific set of

quantum numbers  $[K] \equiv \{\ell_1, \ell_2, m_1, m_1, n_2\}$ , where  $\ell_1$  and  $m_1$  are the angular momentum and projection of the angular momentum on the z-axis associated with the spherical harmonic functions and correspond to the pair of particles 1 and 2, while  $\ell_2$  and  $m_2$  are related to the particle 3 and the centre of mass of particles 1 and 2. The quantum number  $n_2$  defines the degree of the hyperspherical polynomial included in  $\mathcal{Y}_{[K]}^{LSJJ_z}(\Omega)$ . A specific grand angular quantum number involved in the calculations is  $K = \ell_1 + \ell_2 + 2n_2$ . One grand angular quantum number  $K$  case may include more than one specific set of quantum numbers  $[K]$ . To obtain the correlation function, the norm of the wave function is of interest which has a much simpler form due to the properties of the HH functions. The norm of the shown free plane wave is

$$|\Psi_s^0|^2 = \frac{c}{N_S} \frac{2^6}{(Q\rho)^4} \sum_K J_{K+2}^2(Q\rho) N_{ST}(K), \quad (1.24)$$

where  $c$  is chosen such that  $|\Psi_s^0|^2 \rightarrow 1$  as  $x = Q\rho \rightarrow \infty$ ,  $N_S$  is the number of spin states and finally the  $N_{ST}(K)$  is the number of states depending on the grand angular quantum number  $K$ . For the three-nucleon case, there are eight spin states. For each value of the  $[K]$ , the HH functions can be symmetric, mixed or antisymmetric, while the final three-proton wave function must be antisymmetric. As introduced previously, the wave function is represented by the HH functions coupled to spin functions. The spin vector of the three-proton system can be either of mixed symmetry ( $S=1/2$ ) or symmetric ( $S=3/2$ ). Thus, only mixed and antisymmetric HH functions can be included to obtain the antisymmetric wave function. The two mixed symmetry spin states combined with two mixed HH functions result in an antisymmetric state. Also, the symmetric spin state, in combination with the antisymmetric HH function, provides an antisymmetric state. The final number of  $N_{ST}(K)$  states for generic  $[K]$  values can be estimated using a numerical algorithm, taking into account these considerations for antisymmetrisation. For the specific case of the three-proton system, the normalisation constant  $c$  equals 6. Finally, to estimate a correlation function, the source must also be expressed as a function of hyperradius. The hyperspherical source for three particles used in the calculation is defined as

$$S_{123} = \frac{1}{\pi^3 \rho_0^6} e^{-(\rho/\rho_0)^2}, \quad (1.25)$$

with  $\rho_0$  being a free parameter which must be defined experimentally and corresponds to the  $r_{core}$  parameter in two-particle femtoscopy shown in Eq. 1.11. As mentioned before, the hyperradius is defined as  $\rho = (x_1^2 + x_2^2)^{1/2}$ . The visual representation of  $x_i$  is shown in Fig. 1.18, and  $x_2$  corresponds to the relative distance between one of the pairs in the triplet and thus is related to the  $r$  in Eq. 1.11 of the two-particle source. The latter is obtained if single particle sources are assumed to be Gaussian. While the motivation for a Gaussian source for the three-particle system is the same, it remains to be confirmed to be valid.

The source function must be normalised such that

$$\int S_{123} \rho^5 d\rho d\Omega = 1. \quad (1.26)$$

Then the correlation function can be defined as

$$C_{123}(Q) = \int \rho^5 d\rho d\Omega S_{123} |\Psi_s|^2. \quad (1.27)$$

For the previously discussed free wave function, this becomes

$$C_{123}(Q) = \int \rho^5 d\rho d\Omega S_{123} |\Psi_s|^2 = \frac{6}{8} \frac{2^6}{(Q\rho)^4} \frac{1}{\rho_0^6} \int \rho^5 d\rho e^{-(\rho/\rho_0)^2} \sum_K J_{K+2}^2(Q\rho) N_{ST}(K), \quad (1.28)$$

which is the final result after integration on hyperangles. The resulting correlation function for different values of  $\rho_0$  is shown in the upper panel of Fig. 1.19. A correlation function of a nucleon triplet is shown considering only the antisymmetrisation of the wave function. The smaller the assumed particle source size, the further the correlation function is from unity. This is expected, as a small source size implies that more particle triplets are produced at small relative distances. Therefore, the effect of the antisymmetrisation in the calculation becomes dominant. The next step is to introduce interactions between particles. The inclusion of the strong interaction in the lowest partial waves modifies the wave function, which results in the following norm

$$|\Psi_s|^2 = |\Psi_s^0|^2 + \frac{6}{8} \frac{2^6}{(Q\rho)^4} \sum_{[K]}^{[K]_{\max}} [u_{[K]}^2(Q\rho) - J_{K+2}^2(Q\rho)] N_{ST}(K), \quad (1.29)$$

where  $u_{[K]}$  corresponds to the reduced wave function with asymptotic behaviour

$$u_{[K]} \rightarrow J_{K+2}(Q\rho) + T_{[K]} \mathcal{O}_{[K]}(Q\rho), \quad (1.30)$$

where  $T_{[K]}$  is the T-matrix for quantum number set  $[K]$  and the outgoing wave function  $\mathcal{O}_{[K]}(Q\rho)$ . The T-matrix in the following calculations is obtained by employing a Gaussian potential in spin  $S = 0$  state with a parametrisation chosen to reproduce the known p-p interaction scattering parameters. Thus these calculations do not yet include the three-body potential. The Eq. 1.27 can be used to calculate the correlation function corresponding to the different contributions. The resulting correlation functions are shown in the lower panel of Fig. 1.19 for a source hyperradius  $\rho_0$  of 2 fm. The red curve shows the correlation function calculated using a three-particle properly antisymmetrised free plane wave; the black curve - using the free wave function but including only the grand angular quantum number  $K=1$  case; the green curve - using a wave function with the strong interaction but including only  $K=1$  case and, finally, the blue curve represents the total correlation function if the interaction is included for  $K=1$  case and the rest of the states are included as free waves. In the specific case of three protons, the  $K=1$  grand angular quantum number includes several configurations of quantum numbers. The HH functions for  $K=1$  have only mixed symmetry; thus, only the mixed symmetry spin state  $S=1/2$  is allowed to obtain antisymmetric final wave function.<sup>8</sup> As  $K = \ell_1 + \ell_2 + 2n_2$ , the only allowed configurations of the quantum numbers  $[\ell_1, \ell_2, n_2]$  are  $[1,0,0]$  and  $[0,1,0]$ , which result in the allowed orbital angular momentum  $L = 1$  and the total angular momentum states  $J=1/2$  and  $J=3/2$ . In the following, such states will be referred to as  $K=1$  channel. These results still need to include the Coulomb interaction, which is necessary to describe a three-proton system. The Coulomb potential for a many-body system is expressed as

$$V_{\text{Coul}} = \sum_{i < j} \frac{e^2}{r_{ij}}. \quad (1.31)$$

The asymptotic solution of the Schrödinger equation for three charged particles

---

<sup>8</sup>However, the antisymmetric HH functions start to exist at  $K=2$  and thus for such channel the symmetric spin state  $S=3/2$  would be allowed.

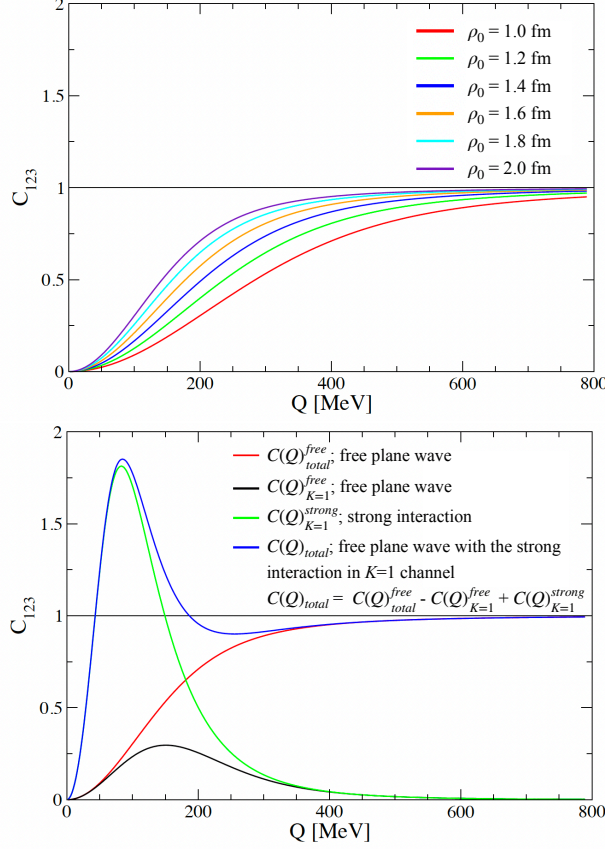


FIGURE 1.19: Upper panel: Three-nucleon correlation function for an antisymmetrised free plane wave for different source parameter values  $\rho_0$ . Lower panel: Correlation functions obtained considering only the  $\rho_0=2$  fm. The red curve corresponds to the total correlation function obtained using free plane waves; the black line - correlation function only for  $K=1$  channel obtained using free plane waves; the green line - correlation function only for  $K=1$  channel obtained including the strong interaction, as explained in the text; blue line - total correlation function obtained including the strong interaction in  $K=1$  channel and using free plane wave for the rest of the contributions. Provided by Alejandro Kievsky in private communication.

is not known, but the effect of Coulomb interaction on the correlation function can be approximately studied by employing an average force over the hyperangles assuming hyperradial form as

$$V_C(\rho) = \frac{1}{\pi^3} \int d\Omega \sum_{i < j} \frac{e^2}{r_{ij}} = \frac{16}{\pi} \frac{e^2}{\rho}. \quad (1.32)$$

For such case, the norm of the free scattering wave function, including Coulomb interaction, becomes

$$|\Psi_s^0|^2 = \frac{1}{C_{3/2}^2} \frac{1}{(Q\rho)^5} \sum_K F_{K+3/2}^2(\eta, Q\rho) N_{ST}(K), \quad (1.33)$$

where  $C_{3/2}$  is a Coulomb factor equal to  $\sqrt{8\pi}/32$  and  $F_{K+3/2}$  is a regular Coulomb function. Here, as previously,  $N_{ST}(K)$  is the number of states. The upper panel of

Fig. 1.20 shows the correlation function calculated using different wave functions for a source radius of 2 fm. The red curve represents the correlation function ob-

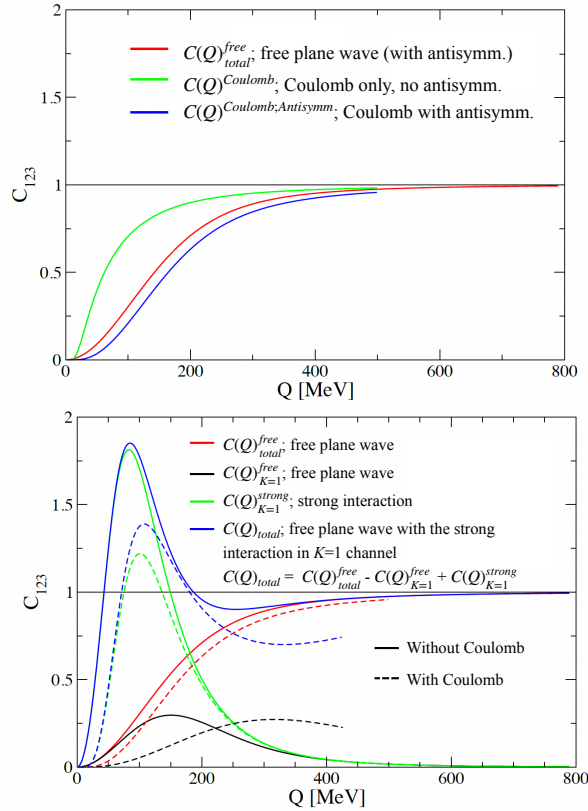


FIGURE 1.20: Correlation functions calculated using different wave function assumptions. Details are provided in the text. Upper panel: Study of the effects of antisymmetrisation and Coulomb interaction. Lower: Final results for correlation function if antisymmetrised wave function is used accounting for Coulomb interaction (dashed line) and not (solid line). Both figures show results for a source parameter  $\rho_0=2$  fm. Provided by Alejandro Kievsky in private communication.

tained using the antisymmetrised free plane wave. The green curve shows the correlation function calculated using a wave function without antisymmetrisation (all HH functions are allowed, thus resulting in a different number of states  $N_{ST}(K)$ ) but including Coulomb interaction. The blue curve represents the correlation function calculated using the antisymmetrised wave function and including the Coulomb force. The Coulomb interaction provides more repulsion between the protons and thus brings the correlation function to lower values. Finally, the norm of an antisymmetrised wave function, including both the strong and Coulomb interactions, can be written as a combination of the above-shown expressions

$$|\Psi_s|^2 = |\Psi_s^0|^2 + \frac{1}{C_{3/2}^2(0)} \frac{6}{8} \frac{1}{(Q\rho)^5} \sum_{[K]}^{[K]_{\max}} \left[ u_{[K]}^2(Q\rho) - F_{K+3/2}^2(Q\rho) \right] N_{ST}(K). \quad (1.34)$$

The resulting correlation function is shown in the lower panel of Fig. 1.20 together with different contributions. The solid lines correspond to results shown in the lower panel of Fig. 1.19, while the dashed line shows how such correlation functions change if the Coulomb interaction is taken into account. Thus the blue dashed

line represents the preliminary calculation of how the correlation function of a three-proton system should look when the interaction is included only in the  $K = 1$  channel and only the two-body nuclear interaction potential is included. Finally, the upper and lower panels in Fig. 1.21 show the result if the interaction is also included in  $K=2$  channel for a source radius of 1.5 fm (upper) and 2 fm (lower). As mentioned

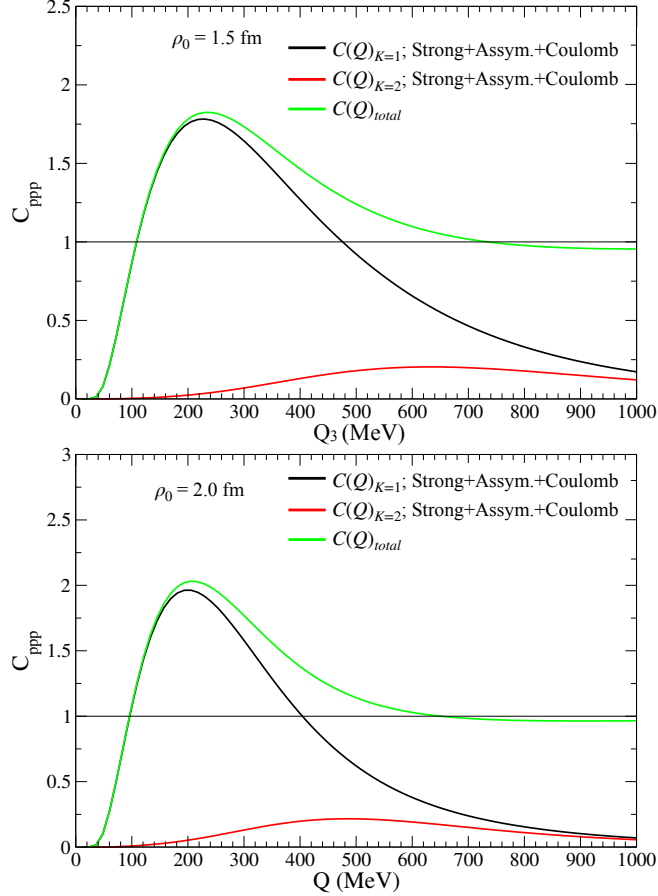


FIGURE 1.21: Correlation functions calculated for a hypersource radius  $\rho_0=1.5$  fm (upper panel) and  $\rho_0=2$  fm (lower panel) shown as a function of  $Q_3$ . The green curve represents the total correlation function calculated using an antisymmetrised wave function, including the Coulomb interaction and the strong interaction in  $K=1,2$  channels. Black and red curves correspond to the correlation functions obtained specifically for  $K=1$  and  $K=2$  channels, respectively. Provided by Alejandro Kievsky in private communication.

before, these calculations are only preliminary. The parts requiring improvement are the inclusion of the interaction for higher grand angular quantum number states, calculation of the T-matrix assuming realistic two-body potential and inclusion of the three-body potential, and improvement in Coulomb interaction, which is now approximated by hyperradial form. These results are the first-ever attempt to calculate a three-body correlation function, and we thank Alejandro Kievsky again for providing the calculations and collaborating with us.

### 1.6.3 Cumulant method

The three-particle correlation function  $C(\mathbf{p}_1, \mathbf{p}_2, \mathbf{p}_3)$  includes all possible contributions as shown in Fig. 1.22: the three pairwise correlations and a genuine three-body

correlation. As the calculations are still preliminary and require further improvements, we exploited the Kubo's cumulant method [87] to study the sensitivity of the measured correlation functions to possible three-body effects. Kubo's cumulant method is widely used in flow analyses, which helps better understand the quark-gluon plasma produced in heavy ion collisions [88–91].

Given random variables  $X_i$ , the cumulant for a triplet is defined as

$$\begin{aligned} \langle X_1 X_2 X_3 \rangle_c &= \langle X_1 X_2 X_3 \rangle \\ &\quad - \{ \langle X_1 X_2 \rangle \langle X_3 \rangle + \langle X_2 X_3 \rangle \langle X_1 \rangle + \langle X_3 X_1 \rangle \langle X_2 \rangle \} \\ &\quad + 2 \langle X_1 \rangle \langle X_2 \rangle \langle X_3 \rangle, \end{aligned} \quad (1.35)$$

where  $\langle X_i \rangle$  is the expectation value of the variable  $X_i$  and  $\langle X_i X_j \rangle$ ,  $\langle X_i X_j X_k \rangle$  are the two- and three-variable joint moments. The Theorem I from [87] is the most

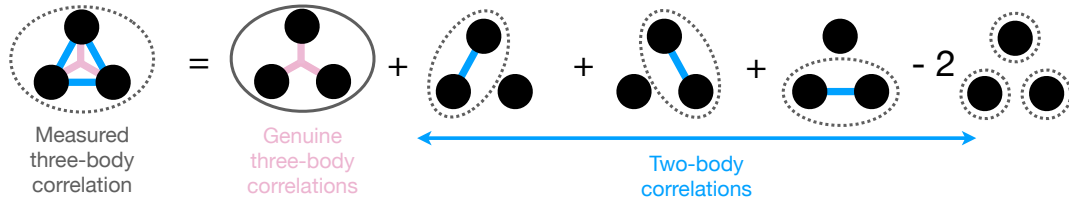


FIGURE 1.22: Sketch of all correlations contributing to the three-particle correlation function following femtoscopic cumulant formalism.

important for our femtoscopic studies:

*A cumulant,*

$$\kappa(X_i X_j \dots) \equiv \langle X_i X_j \dots \rangle_c$$

*is zero if the elements  $X_i, X_j, \dots$  are divided into two or more statistically independent groups.*

The cumulant method can be applied to the Eq. 1.13 numerator, which contains the correlated particles. The three-particle femtoscopic cumulant  $c_3$  is defined as such expression normalised to the uncorrelated triplet distribution as

$$\begin{aligned} c_3(\mathbf{p}_1, \mathbf{p}_2, \mathbf{p}_3) &= [N_3(\mathbf{p}_1, \mathbf{p}_2, \mathbf{p}_3) \\ &\quad - N_2(\mathbf{p}_1, \mathbf{p}_2) N_1(\mathbf{p}_3) - N_2(\mathbf{p}_2, \mathbf{p}_3) N_1(\mathbf{p}_1) - N_2(\mathbf{p}_3, \mathbf{p}_1) N_1(\mathbf{p}_2) \\ &\quad + 2N_1(\mathbf{p}_1) N_1(\mathbf{p}_2) N_1(\mathbf{p}_3)] / N_1(\mathbf{p}_1) N_1(\mathbf{p}_2) N_1(\mathbf{p}_3), \end{aligned} \quad (1.36)$$

where  $N_3(\mathbf{p}_1, \mathbf{p}_2, \mathbf{p}_3)$  and  $N_2(\mathbf{p}_i, \mathbf{p}_j)$  are the same-event three- and two-particle momentum distributions;  $N_1(\mathbf{p}_i)$  is the single-particle momentum distribution; the product terms  $N_2(\mathbf{p}_i, \mathbf{p}_j) N_1(\mathbf{p}_k)$  and  $N_1(\mathbf{p}_i) N_1(\mathbf{p}_j) N_1(\mathbf{p}_k)$  indicate the mixed event distributions. This can be further rewritten as

$$c_3(\mathbf{p}_1, \mathbf{p}_2, \mathbf{p}_3) = C(\mathbf{p}_1, \mathbf{p}_2, \mathbf{p}_3) - C([\mathbf{p}_1, \mathbf{p}_2], \mathbf{p}_3) - C([\mathbf{p}_2, \mathbf{p}_3], \mathbf{p}_1) - C([\mathbf{p}_3, \mathbf{p}_1], \mathbf{p}_2) + 2. \quad (1.37)$$

This method has already been successfully applied within the ALICE Collaboration to study the possibility of coherent pion production by measuring three-pion femtoscopic cumulants in Refs. [81, 92]. Following Theorem I, the observation of  $c_3(\mathbf{p}_1, \mathbf{p}_2, \mathbf{p}_3) = 0$  indicates the absence of genuine three-body correlations. The non-vanishing values of  $c_3$  can be obtained only in the presence of the genuine three-body effects.

The three-particle correlation function can be expressed using only lower-order contributions in the absence of the genuine three-body effects as follows

$$C^{\text{two-body}}(\mathbf{p}_1, \mathbf{p}_2, \mathbf{p}_3) = C([\mathbf{p}_1, \mathbf{p}_2], \mathbf{p}_3) + C([\mathbf{p}_2, \mathbf{p}_3], \mathbf{p}_1) + C([\mathbf{p}_3, \mathbf{p}_1], \mathbf{p}_2) - 2. \quad (1.38)$$

In Eq. 1.38,  $C([\mathbf{p}_i, \mathbf{p}_j], \mathbf{p}_k)$  term corresponds to two interacting particles and one spectator. Such contribution can be evaluated with a data-driven or newly developed projector method. Based on the data-driven method, the lower order contributions are built by combining particles  $i$  and  $j$  from the same event with particle  $k$  from another event to obtain the numerator  $N_2(\mathbf{p}_i, \mathbf{p}_j)N_1(\mathbf{p}_k)$  of the correlation function while the denominator  $N_1(\mathbf{p}_1)N_1(\mathbf{p}_2)N_1(\mathbf{p}_3)$  is estimated using three particles from three different events. The shortcoming of the data-driven method is the statistical uncertainty which depends on how many mixed events are used to obtain the numerator. Computation expenses limit this number of events. Luckily, the projector method, described in the next Chapter, does not have such limitations.

#### 1.6.4 Projector method

The projector method was developed in our group by Raffaele Del Grande; I contributed mostly to the initial calculation codes and simulations. The performed study was published in EPJC [93], showing an in-detail derivation of the method.

The goal of the projector method is to estimate the correlation function  $C([\mathbf{p}_i, \mathbf{p}_j], \mathbf{p}_k)$ , where only particles  $i$  and  $j$  are interacting and this interaction is known either from theory or from experiments. In the case of only two interacting particles, the three-body Hamiltonian, shown in Eq. 1.21, becomes much simpler and reads as

$$H = H_{CM} + H_1 + H_2 = T_{CM} - \frac{\hbar^2}{m} \nabla_{x_1}^2 + \left( \frac{-\hbar^2}{m} \nabla_{x_2}^2 + V(i, j) \right), \quad (1.39)$$

where all three Hamiltonian operators commute. In such a case, the total wave function of the system can be factorised. The wave functions can be obtained by solving stationary Schrödinger equations for  $H_{CM}$ ,  $H_1$  and  $H_2$  Hamiltonians. The solution for both  $H_{CM}$  and  $H_1$  cases are free plane waves, while the solution for  $H_2$  depends on the assumed two-body interaction. This leads to a correlation function which depends only on the wave function for the particles  $i$  and  $j$ . Such wave function is directly related to the correlation function between interacting particles, and thus the total correlation function of the three-particle system can be expressed as

$$C_3(Q_3) = \int_0^{\sqrt{\frac{\gamma}{\alpha\gamma-\beta^2}} Q_3} C_2(k_1) W(k_1, Q_3) dk_1. \quad (1.40)$$

This relation projects the two-body correlation function  $C_2(k_1)$  between particles 1 and 2 on the three-body hyper-momentum  $Q_3$ . The coefficients are expressed as

$$\alpha = \frac{4 m_3^2}{(m_1 + m_3)^2} + \frac{4 m_3^2}{(m_2 + m_3)^2} + 4, \quad (1.41)$$

$$\beta = \frac{4 m_3 (m_1 + m_2 + m_3)}{m_1 + m_2} \left[ \frac{m_2}{(m_2 + m_3)^2} - \frac{m_1}{(m_1 + m_3)^2} \right], \quad (1.42)$$

$$\gamma = \frac{4 (m_1 + m_2 + m_3)^2}{(m_1 + m_2)^2} \left[ \frac{m_1^2}{(m_1 + m_3)^2} + \frac{m_2^2}{(m_2 + m_3)^2} \right], \quad (1.43)$$

where  $m_i$  corresponds to the mass of  $i$ th particle. The analytical form of projector function  $W(k_1, Q_3)$  then is

$$W(k_1, Q_3) = \frac{16(\alpha\gamma - \beta^2)^{3/2}k_1^2}{\pi Q_3^4 \gamma^2} \sqrt{\gamma Q_3^2 - (\alpha\gamma - \beta^2)k_1^2} \quad (1.44)$$

The projector method essentially takes the known two interacting particle correlation function and projects it from  $k^*$  space to  $Q_3$  by accounting for the allowed phase space of the third particle, depending on its mass.

We tested the projector method using a Toy MC [93]. We simulated p–p– $\Lambda$  triplets by sampling the components of the single hadron momentum from uniform distributions  $U(\mathbf{p}) = U(p_x)U(p_y)U(p_z)$  for free hadrons. To validate the projector method, we assumed that one pair in the triplet might interact, specifically one of the p– $\Lambda$  pairs, while the second proton remains a spectator. A joint distribution was used to account for the possible interaction resulting in total probability density function  $f(\mathbf{p}_1, \mathbf{p}_2, \mathbf{p}_3) = qU(\mathbf{p}_1)U(\mathbf{p}_2)U(\mathbf{p}_3) + pf_2(\mathbf{p}_1, \mathbf{p}_2)U(\mathbf{p}_3)$ , where the first term corresponds to a three free hadron system and the second term corresponds to the two interacting hadrons and one spectator. Here,  $f_2(\mathbf{p}_1, \mathbf{p}_2)$  is a Gaussian distribution with a standard deviation  $\sigma$  and the parameters  $q$  and  $p$  corresponds to the weights of the two sub-samples. The values of  $\sigma, q, p$  were fitted so that the

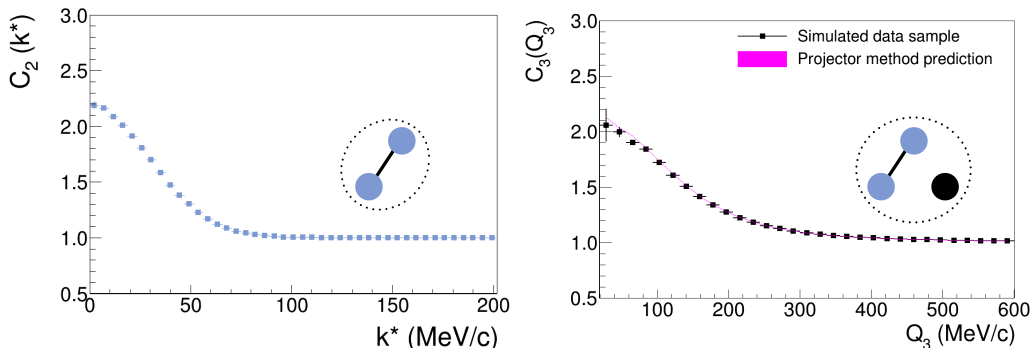


FIGURE 1.23: Projector method validation with Toy MC model [93]. Left: Two-particle p– $\Lambda$  correlation function for the simulated sample as a function of the relative momentum in the centre-of-mass system of the interacting pair. Right: Three-particle correlation function for the simulated sample obtained with the data-driven method (black squares) and the projector method (pink line). The vertical lines on the black squares correspond to the statistical uncertainty dependent on the simulated sample size.

p– $\Lambda$  correlation function obtained from the simulated sample would reproduce the correlation function estimated for a spin-0 p– $\Lambda$  interaction calculated within  $\chi$ EFT framework at NLO given in Ref. [24]. The correlation function obtained for the interacting p– $\Lambda$  pair from the simulated sample is shown in the left panel of Fig. 1.23 as a function of the relative momentum between the two baryons in the pair rest frame. The three-body correlation function from the simulated triplet sample can also be estimated using the data-driven method, shown as the black squares in the right panel of Fig. 1.23. Finally, the projector method was used to estimate the three-body correlation function by employing the Eq. 1.40 and using the two-particle correlation function shown in the left panel of Fig. 1.23 as  $C_2(k_1)$  term in Eq. 1.40. The correlation function obtained with the projector method reproduces well the one obtained with the data-driven approach. While the projector method was validated with the

Toy MC studies, it must also be validated with data. In this thesis, we will show the first comparison of the projector method to the data-driven approach based on experimental data, which was included in our paper accepted by EPJA [94].

## Chapter 2

# ALICE - A Large Ion Collider Experiment

The European Organization for Nuclear Research, also known as CERN, was established in 1954 and has since been one of the leading scientific centres in the world. Some of the most significant achievements made by the experiments at CERN are the discoveries of the W and Z bosons [95], the direct CP violation [96–99], and many others, including the recent discovery of the Higgs boson [6, 7]. As of 2022, CERN hosts 11 active machines, including the Large-Hadron-Collider (LHC) - the world's largest and most powerful particle collider. The LHC aims to tackle fundamental questions such as the origin of mass, dark matter, and dark energy, why there is a matter-antimatter asymmetry in the universe, and the properties of QGP. During the two data-taking campaigns so far, the LHC experiments managed not only to answer some of these questions (and are still investigating the others) but also found new ways of using the data to study physics questions that were not in the original scope.

The four biggest experiments at the LHC are ALICE (A Large Ion Collider Experiment), ATLAS (formerly known as A Toroidal LHC Apparatus), CMS (Compact Muon Solenoid), and LHCb (The Large Hadron Collider beauty). This thesis focuses on the ALICE detector, initially built to tackle the questions regarding QGP created in ultra-relativistic heavy-ion collisions and the following hadronisation processes. The QGP is a new state of matter composed only of deconfined quarks and gluons. The evolution of the QGP can be described with relativistic viscous hydrodynamic simulations, which predict that it will expand due to its pressure [100]. To test the current understanding of the QGP and the available models for initial conditions, the hydrodynamic expansion and hadronisation, probes such as flow [11, 12, 101, 102], tagged and un-tagged jets [103–105], the production of different particle species [106–108], and others are studied. Accessing the properties of the matter created in ion-ion (A-A) collisions requires a good understanding of the underlying dynamics of collisions. The data of proton-proton (pp) and proton-ion (p-A) collisions provides both such reference and an environment to study fundamental physics. All these measurements require excellent particle identification (PID) capabilities, which is one of the main advantages of the ALICE detector. The ability to identify different hadrons and (anti-)nuclei was also used for a large number of measurements unrelated to studies of the QGP: the inelastic cross section measurements of antinuclei using the detector material as a target [109, 110], the lifetime and separation energy of hypertriton [111], measurements of the strong interaction between different hadron pairs [30, 34, 36–41], and others.

The LHC accelerator and the ALICE detector are described in the following Chapter, together with the selections for events and single particles applied in this thesis.

## 2.1 Large Hadron Collider

The CERN accelerator complex consists of several accelerator rings and linear accelerators, as shown in Fig. 2.1. The largest accelerator is the LHC, a two-ring-superconducting-hadron accelerator and collider installed in the existing 26.7 km tunnel originally constructed for CERN’s Large Electron-Positron (LEP) machine [112]. It was designed to reach maximum centre-of-mass collision energy  $\sqrt{s}=14$  TeV in pp collisions. However, the maximum energy reached in Run 1 was  $\sqrt{s}=8$  TeV because of safety precautions after an incident in one of the main dipole circuits during the first commissioning in 2008 [113]. During the first LHC Long Shutdown after Run 1, the accelerator was upgraded to ensure it could operate at higher energies, and indeed, the maximum operating centre-of-mass collision energy was increased to  $\sqrt{s}=13$  TeV during Run 2.

Protons injected in the LHC ring are already accelerated to an energy of 450 GeV by the LHC injector chain, consisting of the linear accelerator called LINAC 2, Proton Synchrotron Booster (PSB), Proton Synchrotron (PS) and Super Proton Synchrotron (SPS) [114]. When the bunches finally collide at the LHC interaction points (IP), the detectors measure the produced particles at these IPs.

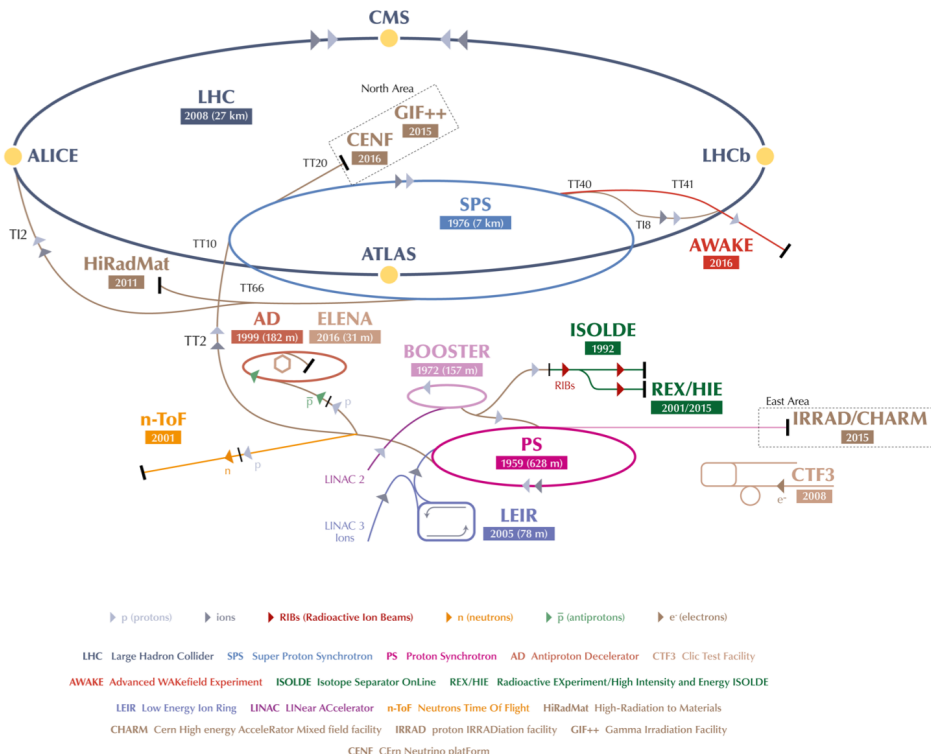


FIGURE 2.1: CERN accelerator complex [115].

## 2.2 ALICE

The ALICE detector, located at the interaction point IP2 of the LHC, has dimensions of  $16 \times 16 \times 26$  m<sup>3</sup> and weighs around 10000 tons. Besides excellent particle identification capabilities, the detector has a low transverse momentum threshold  $p_T^{min} \approx 0.15$  GeV/c to identify particles and high detector granularity [116], which makes ALICE the perfect detector to perform measurements of small relative momenta below 100 MeV/c. In Run 2, this is achieved by the 19 ALICE sub-detector

systems, which can be separated into three main categories: central-barrel detectors, forward detectors, and the MUON spectrometer. A schematic view of the ALICE machine is shown in Fig. 2.2. The in-detail description of the detector can be found in Refs. [116–119].

The central-barrel detectors are embedded in the L3 solenoid magnet and thus immersed in a homogeneous 0.5 T magnetic field parallel to the beam direction. The Inner Tracking System (ITS), Time Projection Chamber (TPC), Transition Radiation Detector (TRD), Time Of Flight (TOF), Photon Spectrometer (PHOS), Electromagnetic Calorimeter (EMCal), Di-jet Calorimeter (DCal) and High Momentum Particle Identification Detector (HMPID) belong to this category.

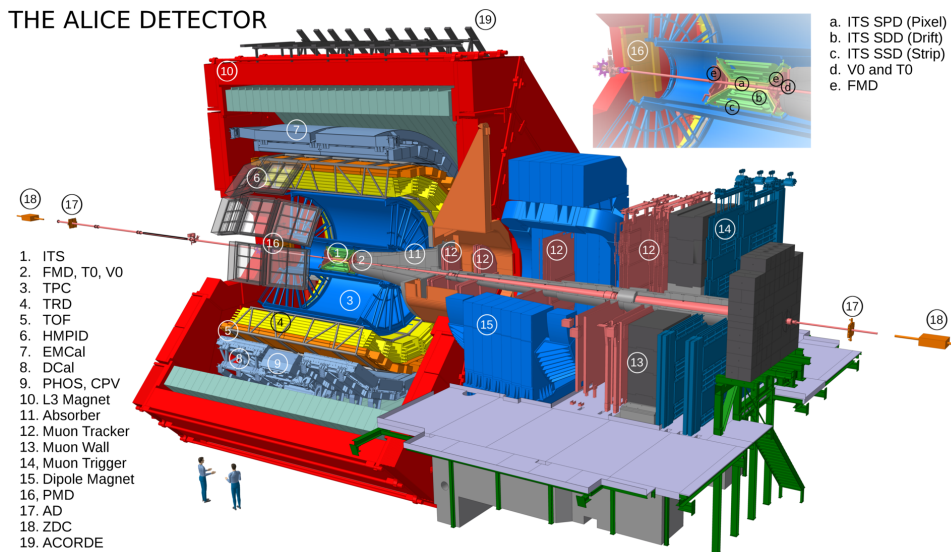


FIGURE 2.2: ALICE detector system during the LHC Run 2 period [120]. The inset shows a zoomed view of the sub-systems located around the nominal interaction point.

The ITS and TPC are the main detectors used for charged particle tracking, while particle identification can be achieved using TPC information at low momenta (around  $p < 1 \text{ GeV}/c$  for protons) and TOF at intermediate momenta (around  $p < 4 \text{ GeV}/c$  for protons). ITS is also responsible for primary and secondary vertex reconstruction and can be used for particle identification. The rest of the central-barrel detectors have a specific purpose as well: the TRD allows for pion/electron separation, the EMCal and the DCal are optimised for the studies of jet physics, the PHOS - for soft photon studies, and the HMPID extends the PID capabilities to larger  $p_T$  values. The relatively low magnetic field inside the detector results in the possibility of measuring very low  $p_T^{\min}$  particles.

The Photon Multiplicity Detector (PMD), Forward Multiplicity Detector (FMD), V0 detector, T0 detector, and Zero Degree Calorimeter (ZDC) belong to the forward detector category. The PMD and FMD measure photons and charged particles in the forward direction, respectively, while the ZDC counts spectator nucleons. The V0 and T0 detectors are responsible for the triggering and event characterisation. The muon spectrometer measures heavy-quark vector-meson resonances and light vector mesons via  $\mu^+ \mu^-$  decay.

The detector systems relevant to this work will be described in the following Chapters.

### 2.2.1 Triggering system

ALICE had a two-layer trigger system in Run 2 [121]: a low-level hardware trigger called Central Trigger Processor (CTP) and a purely software-based trigger called High-Level Trigger (HLT). The CTP has three main trigger levels, classified by the time needed to receive trigger signals from the detectors. The first two trigger levels decide the start of the event data buffering in the detector front-end electronics. The last level decision is responsible for triggering the sending of the recorded data to the HLT and the Data Acquisition (DAQ) systems or, if an event is rejected, the discarding of the obtained digital and analogue information [116].

The CTP trigger logic can receive a total of up to 60 detector signals which are combined to obtain multiple trigger classes [116]. The simplest triggers - the Minimum-Bias (MB) triggers - aim to trigger on *all* inelastic interactions occurring in the detector. Thus MB triggers are expected to introduce the most negligible bias to the physics of recorded event samples and have high rates. The so-called rare triggers have much lower rates as they look for rare signals, such as High-Multiplicity (HM) events for pp collisions, charged or neutral jets in an event, and other signals. Usually, all triggers - minimum bias and rare - are recorded. However, there is a limit on the total allowed rate imposed by the maximum data bandwidth (ALICE was designed to have 1.25 GB/s bandwidth to data archiving for heavy-ion collisions, and this was further improved during Long Shutdown 1 [121]), which can be recorded on the disk and tape. Only rare triggers are accepted if temporary memory and disk buffers use increases over a predefined limit. If the usage goes down - all triggers are accepted again. Such prioritisation prevents a situation in which rare events are triggered but cannot be stored and thus are lost. This inspired Run 3 to have specific offline software triggers for different physics purposes. The development of such a trigger for the three-particle femtoscopy is part of this thesis and is described in Chapter 4.

Returning to Run 2, the femtoscopy studies performed in this work require either 3 protons (or their antiparticle triplet) or two protons and one  $\Lambda$  hyperon (or their antiparticle triplet), which are more likely to be found in HM events. Another reason to use the HM data is the observed strangeness enhancement in such collisions compared to MB [122] as it increases the probability of observing p-p- $\Lambda$  and  $\bar{p}$ - $\bar{p}$ - $\bar{\Lambda}$  triplets. The HM trigger used in this analysis is called *kHigh-MultV0*, and the decision is made accordingly to the signal received from the V0 detector, which works as a proxy for the charged particle multiplicity traversing the detector.

The V0 detector consists of two

plastic scintillator arrays. The so-called V0A detector is located 3.4 m from the interaction point and covers the pseudorapidity range of  $2.8 < \eta < 5.1$  while V0C is

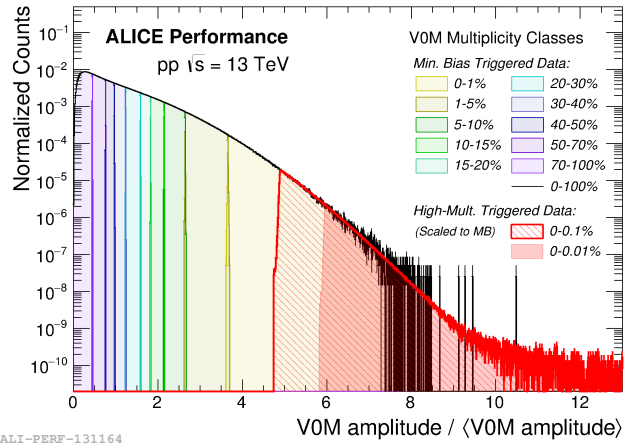


FIGURE 2.3: Distribution of the event multiplicity, estimated as the multiples of average V0M amplitude in MB events [120]. The legend indicates that the shaded red area shows the HM-triggered data.

on the opposite side, located -0.9 m from the interaction point and covers the pseudorapidity region  $-3.75 < \eta < -1.7$ .<sup>1</sup> The V0 detector provides a trigger signal input required for HM and MB triggers. The commonly used MB trigger is V0AND which requires coincidental hits in both V0A and V0C synchronous with the LHC bunch crossing time. The sum of the measured signal amplitudes in the two detectors is V0M. Additionally to the MB conditions, the HM trigger requires the V0M to be larger than a threshold, defined as multiples of the average V0M measured in MB events  $N < V0M$ , where  $N$  typically was set to around 5. The selected HM events correspond to the highest 0.17% multiplicity interval with respect to all inelastic collisions with at least one measured charged particle within  $|\eta| < 1$  ( $\text{INEL} > 0$ ) as shown in Fig. 2.3.

### 2.2.2 Inner Tracking System

The ITS is the innermost central-barrel detector of the ALICE, as shown in Fig. 2.2, designed for high-precision tracking and vertex reconstruction close to the interaction point. The ITS can measure low-momentum particles with transverse momenta down to  $0.1 \text{ GeV}/c$  and, in general, improve the resolution of position, angle, and momentum estimation for tracks reconstructed using TPC information. The ITS consists of six cylindrical layers of lightweight silicon detectors surrounding the beam pipe at radii of 3.9 to 43 cm [124]. The schematic view of these layers is shown in Fig. 2.4. The two inner layers hold high-granularity Silicon Pixel Detectors (SPD) and reach a spatial resolution of  $12 \mu\text{m}$  and  $100 \mu\text{m}$  in  $r\phi$  and  $z$  directions, respectively [123]. The two intermediate layers consist of Silicon Drift Detectors (SDD) and achieve a precision of  $35 \mu\text{m}$  in  $r\phi$  and  $25 \mu\text{m}$  in  $z$  directions. The two outer layers of the ITS are crucial for ITS-TPC matching. They are composed of Silicon Strip Detectors (SSDs) and provide a resolution of  $27 \mu\text{m}$  in  $r\phi$  and  $830 \mu\text{m}$  in  $z$  directions. The high spatial resolution of all layers results in the possibility of localising the position of the collision, the so-called Primary Vertex (PV), with a precision of less than  $100 \mu\text{m}$  and in identifying the secondary vertices of heavy flavour and hyperon decays.

### 2.2.3 Time Projection Chamber

The TPC is one of the main particle tracking and identification systems in ALICE. As it surrounds the ITS and is aligned with the LHC beams, the TPC sits parallel to the magnetic field provided by the L3 solenoidal magnet, as shown on the right panel in Fig. 2.5. The TPC is a large hollow cylinder with an inner radius of the active volume of 0.85 m, an outer radius of 2.5 m, and a length of 5 m. The cylinder was

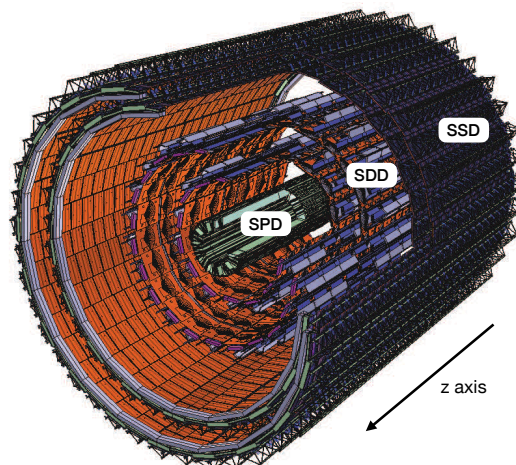


FIGURE 2.4: Schematics of the Inner Tracking System. The figure adapted from [123].

<sup>1</sup>Pseudorapidity ( $\eta$ ) expresses angles with respect to the beam axis and is defined as  $\eta = -\ln(\tan \frac{\theta}{2})$ .  $\eta = 0$  describes the direction perpendicular to the beam axis.

filled with a mixture of Ar-CO<sub>2</sub> (90:10) gas at atmospheric pressure in 2016 and 2018, while in 2017, it was filled with Ne-CO<sub>2</sub>-N<sub>2</sub> (90:10:5) mixture. The drift volume of TPC is divided into two parts by the conducting high voltage electrode placed in the centre of the detector, as shown in both panels of Fig. 2.5. Together with the inner and outer field cages, it provides a uniform electric field parallel to the axis of the cylinder. The charged particles traversing the detector ionise the gas in the active volume, creating ionisation electrons and ions. The latter drift in the electric field towards the central electrode, while the electrons go to the two endplates, where the readout chambers are installed. However, the total yield of ionisation electrons is too low to obtain a detectable signal. Thus the charge amplification is achieved, and the signal is detected by employing the Multi-Wire Proportional Chambers (MWPC) combined with cathode pad readout [125].

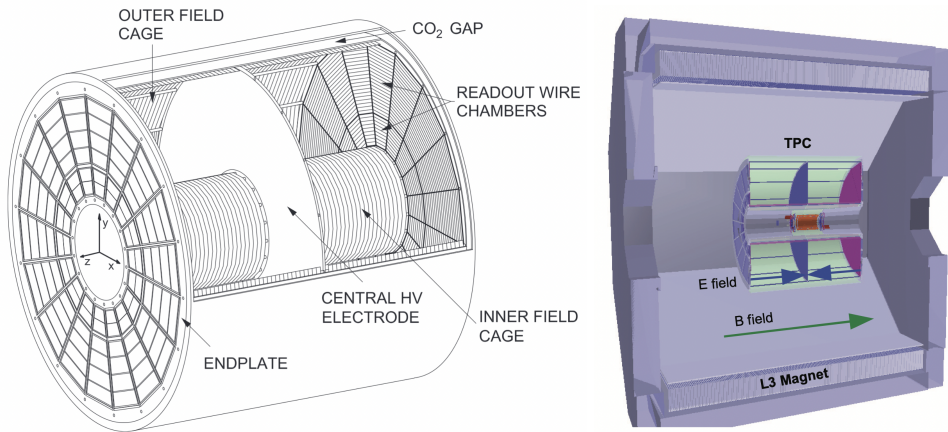


FIGURE 2.5: Left: Schematics of the Time Projection Chamber cage [126]. Right: TPC position in the L3 Magnet is shown together with the direction of electric and magnetic fields [127].

The precisely measured positions where the electrons hit the detector are used to reconstruct the particle trajectory projected on the transverse plane. If combined with additional information about when the electrons reached the endplate, the  $z$  position can be reconstructed and a three-dimensional track defined. The maximum number of measured space points for a track is 159. The measured amplitude of the signal is also used to estimate how much energy the ionising particle lost in the TPC, allowing us to perform particle identification. The reconstructed tracks are used to calculate the momentum of the particle employing the fact that the curvature radius  $r$  of the particle trajectory in a magnetic field  $B$ , the electric charge of the particle  $ze$  (where  $e$  is the elementary charge) and the momentum of the particle  $p$  as  $r = p/(Bze)$ . Once the momentum is known, the particle's specific energy loss per unit distance ( $dE/dx$ ) in the TPC gas is used for particle identification. The average  $dE/dx$  can be calculated using the Bethe-Bloch equation

$$\left\langle \frac{dE}{dx} \right\rangle = \frac{4\pi N e^4}{mc^2} \frac{z^2}{\beta^2} \left[ \ln \left( \frac{2mc^2}{I} \frac{\beta^2}{1-\beta^2} \right) - \beta^2 - \frac{\delta(\beta)}{2} \right]. \quad (2.1)$$

The energy loss depends on the traversed material ( $N$  is the number density of electrons,  $mc^2$  is the rest energy of the electron,  $I$  is the mean excitation energy of an atom) and, most importantly, the charge  $z$  (in multiples of elementary charge) and velocity  $\beta$  of the particle. A density effect that leads to the shielding of the electric field of the incident particle by the electric polarisation of the medium is accounted

for in the term  $\delta(\beta)$ . The variables of the particle of interest are shown in Eq. 2.1 in pink. As mentioned before, the TPC tracking provides the particle's momentum. The Bethe-Bloch equation does not depend on the mass, only on the velocity of the traversing particle, which means that different particle species with the same momenta will lose a different amount of energy in the TPC gas as they have different velocities. The energy loss is more significant for slower particles, and thus for the same momenta, the heavier of the two particles will lose more energy, as shown in Fig. 2.6. The bands correspond to different particle species, and the width of the band depends on the resolution of the TPC. The lines shown in the figure correspond not directly to the Bethe-Bloch calculation but to a parametrisation function proposed by the ALEPH collaboration [128]

$$f(\beta\gamma) = \frac{P_1}{\beta^{P_4}} \cdot \left\{ P_2 - \beta^{P_4} - \ln \left[ P_3 + \frac{1}{(\beta\gamma)^{P_5}} \right] \right\}. \quad (2.2)$$

The parameters  $P_{1-5}$ , shown in pink, are fitted to the data. The particle identification is performed by comparing measured particle energy loss to the expectation value for different particle species. The agreement with the hypothesis for specific species is expressed in multiples of standard deviations  $n\sigma$ . As seen in Fig. 2.6, the TPC is good at PID for low momentum particles, where the different species bands are well separated. However, the bands merge with increasing momentum. The PID is performed by combining the TPC and TOF information for higher momentum particles to achieve good particle purity. The selection criteria applied in our analysis are shown in detail in Chapter 2.5.

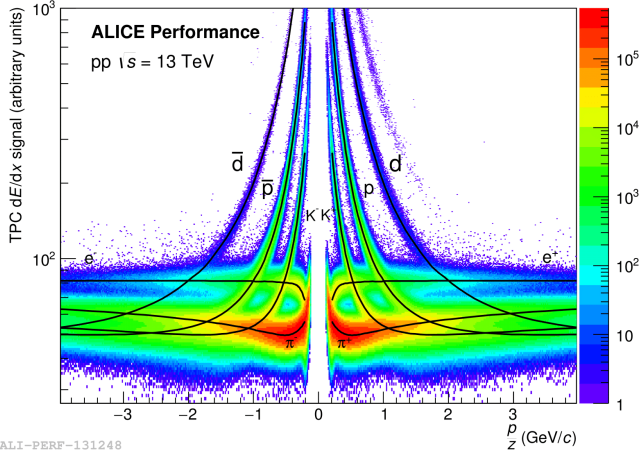


FIGURE 2.6: Specific energy loss in the TPC measured as a function of the momentum over charge in pp collisions at  $\sqrt{s}=13$  TeV [120].

#### 2.2.4 Time-of-Flight detector

The Time-of-Flight detector [129] provides a complementary way to identify particles and extends the PID capabilities of ALICE to the intermediate momentum range. TOF measures the time the particle hits the detector and provides the velocity if combined with the known time of the collision and the distance travelled. If particle velocity and momentum are known, one can estimate the particle's mass using the equation  $m = p\sqrt{\beta^{-2} - 1}$ . However, the particle momentum must be known from another detector.

To identify the different particle species, one can plot the measured particle velocity as a function of the momentum, and various particle species will fall into different bands, as shown in Fig. 2.7. Compared to the TPC, the TOF detector can identify higher momentum particles as the different species bands are separated up to high momentum.

TOF is the outer detector in the central barrel, positioned at radii between 370 cm and 399 cm from the beam axis. Very low momentum particles might get absorbed on their way from the interaction point to the active detector region as they have to traverse rather large transverse distances. This, together with the bending of the particles induced by the magnetic field, causes a rigidity cut-off at about 300 MeV/c. Thus, our analysis uses only the TPC to identify particles with momentum  $p < 0.75 \text{ GeV}/c$ .

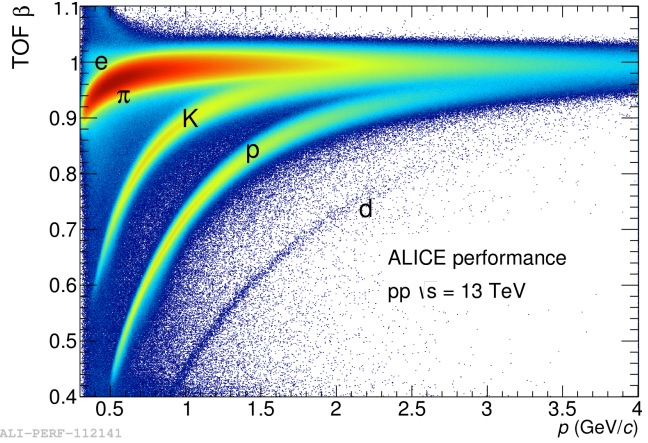


FIGURE 2.7: Velocity measured by TOF as a function of the momentum in pp collisions at  $\sqrt{s}=13 \text{ TeV}$  [120].

## 2.3 ALICE Upgrade: Run 3

As shown in Chapter 3.8, the three-baryon femtoscopic analysis of Run 2 data demonstrates that the three-particle correlations are accessible with ALICE measurement. However, a much higher statistical sample is required to provide quantitative information on the genuine three-baryon interactions. One of the main objectives of LS2 was to improve the readout rate to accommodate the increased interaction rate during the Run 3 of the LHC, which will result in a much higher number of recorded events. In the following, the main ALICE upgrades done during LS2 are presented and the motivation for offline software triggers to record all events with triplets of interest is introduced.

The collision rates read out by the ALICE detector during LHC Runs 1 and 2 were up to 8 and 200 kHz for Pb-Pb and pp collisions, respectively. During the LS2 at the LHC, the ALICE detector received upgrades to record the data at collision rates of 50 kHz for Pb-Pb and 0.5 to 1.0 MHz for pp collisions.

In Run 2, the ITS consisted of silicon detectors and had a limitation of 1 kHz readout rate. It has been replaced by ITS2 based on seven layers of ALPIDE monolithic active pixel sensors (MAPS) representing the largest-scale application of MAPS in a high-energy physics experiment. The main goals of the ITS upgrade were the increased readout rate and the improved precision of the reconstruction of the PV and the decay vertices. The improved precision has been achieved by moving the innermost detector layer closer to the interaction point from 39 mm to 22.4 mm, which was possible due to an implementation of a new beam pipe with a reduced outer radius. Also, the pixel granularity for all ITS layers was increased and an additional layer was added in the inner barrel. The material budget was significantly reduced for the innermost layers to improve the detection of low- $p_T$  particles. The ALPIDE technology also allows for readout rates of 50 and 400 kHz for Pb-Pb and pp collisions, respectively. The development and main test results related to the ALPIDE technology can be found in Ref. [130].

The TPC detector was based on MWPC in Run 2, as described in the previous Chapter and shown in Fig. 2.5. One of the shortcomings of such a system was the active

gating required to deal with the ion backflow into the drift region, which limited the readout rate for Pb-Pb collisions to about 700 Hz. Due to the increased interaction rate and the requirements of the ALICE physics program for Runs 3 and 4, the TPC had to be upgraded to operate in continuous readout. This was achieved by employing readout chambers based on the Gas Electron Multiplier (GEM) foils. Such technology reduces the ion backflow so that the space charge distortions can be corrected for the required interaction rate of 50 kHz for Pb-Pb collisions. This is extremely impressive as the expected number of events contributing to the space charge distortions at such interaction rate is around  $10^4$  [131] (estimated for the ion drift time of 214 ms required to travel from the readout plane to the central electrode). The TPC upgrade is described in detail in Refs. [126, 132]. During my PhD, I contributed to the development of the online quality control system for TPC.

Besides these two major ITS and TPC upgrades, the readout electronics of most of the other sub-detector systems were improved. Several other detectors were further upgraded and installed; however, they are not used in the analysis reported in this thesis and thus are not mentioned. The full LS2 upgrade is in detail described in a recent ALICE publication [131].

The increased interaction and readout rates also require a new way of processing and storing the data. For Runs 3 and 4, the ALICE computing model is oriented at maximal compression of the data volume, which is read from the detector synchronously with the data taking. The upgraded system supports both continuous and triggered (by hardware) readouts. The latter is required for commissioning and calibration runs and legacy sub-systems that were not upgraded for the continuous readout. The reconstruction of the events consists of synchronous and asynchronous steps. The first runs at the time of data taking, while the second takes place afterwards and can be performed several times until the required quality of reconstructed data is achieved. The main goals of synchronous reconstruction are reducing the data rate from the TPC and extracting the calibration data. The full TPC reconstruction is required to compress the data to be stored, as the TPC makes up most of the raw data volume in ALICE. The compression is performed by rejecting clusters associated with or in the proximity of the background tracks, storing the cluster information in integer and floating point formats with a number of bits corresponding to the intrinsic TPC resolution, and storing raw coordinates of hits in respect to the extrapolated tracks. The reconstruction of data from other sub-detector systems runs in parallel to the TPC reconstruction. The calibration algorithms also run during the synchronous reconstruction and the acquired information is stored; however, the final calibration constants are obtained in four to six weeks during the asynchronous reconstruction passes. The calibrations are extremely relevant for the TPC, where the space charge distortions can reach up to 10 cm. During the asynchronous reconstruction, the tracks are obtained by combining information from all available detectors; primary vertices are located; secondary vertices and cascades are identified. The general algorithms to obtain such reconstructed entities are introduced in the next Chapter.

While all Pb-Pb events will be stored, the number of pp collisions at the  $\sqrt{s} = 13.6$  TeV must be reduced by a factor of 1000 because of storage space limitations. Offline software triggers, which run after the asynchronous reconstruction and select events relevant to physics analyses, achieve this. Every physics working group in ALICE is allowed to have several triggers for which the total rejection factor is 10000. We developed four three-body triggers for the three-baryon interaction studies (ppp, pp $\Lambda$ , p $\Lambda\Lambda$ ,  $\Lambda\Lambda\Lambda$ ) and two two-body triggers, including deuteron in the pair (pd and Ad). The three-body triggers I developed and relevant to this analysis are presented

in Chapter 4.

## 2.4 Data reconstruction

While the detector system is the most crucial component of any experiment, the measured data must also be reconstructed and calibrated, for which specific procedures and software must be developed. The data preparation flow in ALICE is shown in Fig. 2.8. The calibration process is required for all steps before and including the tracking. The final reconstructed data is stored in so-called *Event Summary Data* (ESD) files which are the largest of the available data formats in ALICE and store the most detailed information about the collisions. The first step of the reconstruction is clusterisation which is performed for all detectors separately. When a particle crosses a specific detector, it fires multiple cells, and this information corresponds to raw data. However, for data reconstruction, one such particle hit is interesting as an entity; thus, the fired cells are combined into a cluster for each hit. Such clusters are characterised by position, signal amplitude, shape, and other quantities. They are used as input for tracking algorithms for ITS, TPC, and TRD, but other detectors also use clustering.

The initial point of the collision is required as an anchor point to use the clusters for the track reconstruction. Thus, the primary vertex reconstruction occurs next. At this stage, it is based solely on the SPD information. First, tracklets are formed from pairs of clusters, as shown in the left panel of Fig. 2.9. The primary vertex is then reconstructed by searching for the overlap region of all tracklets. The tracklets not pointing to this vertex are assumed to be pile-up and rejected (grey dotted lines). As a default approach, a 3D vertex is reconstructed in pp collisions. However, in the case of low multiplicity events, a z-vertex-only reconstruction algorithm can be used.

Once the primary vertex is known, the tracking algorithms can be employed. The tracking is performed by combining all available detector information, and the reconstruction method, based on the Kalman filter, is described in detail in Ref. [133]. In the first phase, the track is reconstructed starting from the outer TPC layer inwards until the inner radius of the TPC is reached. The tracks can be reconstructed without the ITS clusters but still constrained to SPD vertex, which results in so-called *TPC-only tracks*. However, the complete reconstruction procedure propagates the track further using the ITS clusters. In the second phase, the backpropagation is performed, starting with the reconstructed primary vertex at the ITS to the outer layer of TPC using the clusters found in the previous phase but extending the track to include the outer detectors such as TRD, TOF, HMPID, EMCAL, PHOS. In the final phase, the re-fit employs inwards propagation, including clusters from all detectors associated with the track in the previous step. Tracks reconstructed in the TPC and prolonged to the ITS with successful re-fit are called *global tracks*. Such tracks are used to constrain again the primary vertex,

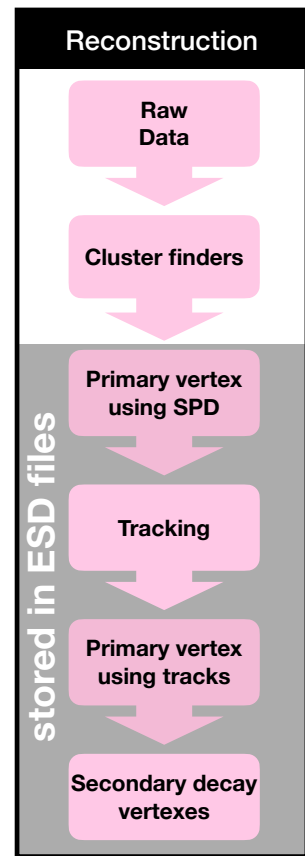


FIGURE 2.8: Data reconstruction flow in ALICE.

which provides better resolution than the SPD method but has lower efficiency at low multiplicities. Additionally, pile-up tagging via multiple reconstructed vertices is possible.

Once the event and the tracks are reconstructed, the secondary vertices from weak

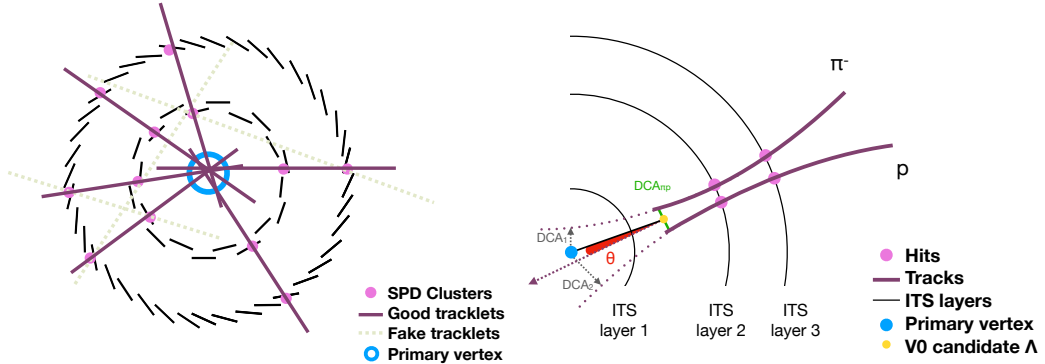


FIGURE 2.9: Left: Illustration of the primary vertex finding algorithm using SPD clusters. Right: An explanatory sketch of V0 Reconstruction and selection. A detailed explanation is provided in the text.

decays of long-lived hadrons and photon conversions are identified. The reconstructed decay, when two un-like sign particles are produced, is called *V0 candidate* ( $K_s^0 \rightarrow \pi^+ + \pi^-$ ;  $\Lambda \rightarrow p + \pi^-$ ;  $\gamma \rightarrow e^+ + e^-$ ). Reconstructed decay into an uncharged particle which decays further into un-like sign particle pair is called *cascade candidates* ( $\Xi^- \rightarrow \Lambda + \pi^- \rightarrow p + \pi^- + \pi^-$ ). The reconstruction of cascades is based on first reconstructing the V0 candidate and then creating combinations with track candidates. However, in this thesis, only the  $\Lambda$  particles are of interest, and thus only the V0 reconstruction is discussed in detail.

The secondary (daughter) tracks are produced at the decay vertex. They do not point to the primary vertex as shown in the right panel of Fig. 2.9 by the extrapolated tracks (grey dotted lines). The distance of the closest approach (DCA, shown as grey dotted arrows) of a track to the primary vertex is thus used to select secondary tracks. The combinations of such un-like sign secondary tracks provide the V0 candidates (denoted as a yellow dot). However, such simple requirements significantly contaminate the reconstructed V0 sample. Additional topological selections are thus required. As the secondary tracks are produced in the decay, the distance of the closest approach between them is expected to be small, and the  $DCA_{p\pi}$  (solid green line) of the tracks at the secondary vertex is used as one of the selection criteria. The reconstructed V0 candidate is expected to point to the primary vertex where it was produced. This can be imposed by requiring a large cosinus-pointing-angle (red  $\theta$  angle in the right panel of Fig. 2.9) defined as the cosinus of the angle between the reconstructed momentum vector of V0 and the vector pointing from V0 vertex to the primary vertex. The best invariant mass resolution of V0 candidates is achieved during so-called *on-the-fly* reconstruction as the cluster information is used. However, it is performed only once during the reconstruction of events and cannot be re-run at the analysis level if different selection criteria are required. For this purpose, the *offline* reconstruction is available, where the track information stored in the ESD files is used. This work employs the second method. However, not using the raw cluster information results in a worse resolution of reconstructed candidates.

As shown in Fig. 2.8, only the information about reconstructed entities is stored in ESD (no raw cluster information). Nevertheless, the ESD files are still extensive and

resource intensive. The physics analyses are performed on so-called *Analysis Object Data* (AOD) files instead, which store only observables relevant for physics (momentum, charge, etc.), the topological information about tracks (for example, DCA) and the quantities relevant to estimate track quality (number of clusters in TPC, etc.). Further filtering can reduce the file size and the time needed for analysis by storing only information relevant to specific analysis. The resulting files are called *NanoAODs*, and in this work, we use NanoAODs filtered specifically for femtoscopic analysis.

## Simulations

The Monte-Carlo (MC) simulations are needed to understand better the detector, the possible detector effects on specific analyses, and even the final results. Full-scale MC simulations start with an event generator that simulates collisions and creates a list of produced particles and their kinematic information. The ALICE MC framework is modular and thus allows one to choose among many different event generators depending on the collision system and physics required. Some of the possibilities include PYTHIA [134], DPMJET [135] and HIJING [136]. For pp collisions analysed in this work, the PYTHIA 8 event generator is used (Monash 2013 Tune). The PYTHIA 8 simulation starts from a hard scattering of two partons, one from each of the colliding protons, resulting in a few particles and possible production of short-lived resonances which decay to normal particles [137]. The initial and final state radiation of additional particles (partons, photons, and others) is included in further steps. The interactions between partons from initial protons (not considered in the first step) can also occur. Such a process is called multiple-parton interactions. After, the produced QCD partons are confined by the strong interaction to colour-singlet systems, called strings, while the leftover partons from initial colliding particles are combined to beam remnants. The strings fragment into hadrons following the Lund model [138]. At the level of produced hadrons, the quantum statistics rules are applied to the identical close in phase-space particles resulting in enhancements (for hadrons following Bose-Einstein statistics - integer-spin particles) or suppressions (for hadrons following Fermi-Dirac statistics - half-integer-spin particles). Finally, the unstable hadrons decay until only stable particles remain. In these stages, the rescattering, reannihilation, or recombination processes might occur in densely populated regions of the phase space. Summarising, PYTHIA 8 takes care of the underlying event physics, however, it does not include any final state interactions for final produced particles. This is relevant for femtoscopic studies, as such simulations can be used to study non-femtoscopic correlations resulting from the hard scattering at the parton level and energy and momentum conservation for hadrons. Such effects in the underlying event go under the name of minijets [41], which are the consequence of the hard scatterings at the parton level.

The produced particles employing any event generator must be propagated in an ALICE detector simulation which is done by employing the GEANT 3 [139] code. It simulates how the traversing particles interact with the detector material and the corresponding deposit energy. The customised version of the GEANT 3 for the ALICE experiment provides a very detailed description of the sub-detectors, where the material budget calibrated by electromagnetic and hadronic probes [116, 140] is known within uncertainty of 5%. Additionally, the ALICE offline framework Ali-ROOT, based on the ROOT software, is employed. The latter provides simulations of the signal formation and processing, allowing us to infer the expected output of the detector's front-end electronics. Finally, when all these steps are performed,

the resulting MC data is processed and reconstructed precisely like the real data. The simulation also includes a dedicated high-multiplicity selection to mimic the V0 high-multiplicity trigger in the real data. Such detailed simulations of events and the resulting particle propagation in the detector are used to determine the detector's resolution and the purity of identified charged particles and can even be used for template fits to obtain the fractions of secondary and primary particles. The procedures of estimating the purity and performing template fits are described in Chapter 2.5.

## 2.5 Event, track and V0 selection

The goal of femtoscopic correlation measurements is to study the strong short-range interaction among hadrons with different quark content. As shown in Fig. 1.17, we are primarily interested in hadron pairs with inter-particle distance below 2 fm as this is the region where the strong interaction strength is more pronounced. While ALICE measures pp, p–Pb, and Pb–Pb colliding systems, pp collisions are the most interesting for this kind of study as the resulting particle source has the smallest size and thus provides a data sample with an enhanced number of strongly interacting pairs and triplets. As explained in Chapter 2.2.1, we use the pp collisions with a centre-of-mass energy  $\sqrt{s}=13$  TeV selected with the HM trigger as high-multiplicity events have enhanced strangeness production and higher probability to find triplets of interest. To further ensure the quality of the selected events, some standard selection criteria are applied, as shown in Table 2.1. The default physics selection rejects poor-quality events and background events from the proton beam collisions with either the beam pipe material or the residual gas. Additionally, the events must pass some essential quality assessment criteria, which is enforced by requiring *check* flag for incomplete data acquisition (DAQ) in AliRoot.

Selection criterion	Value
Trigger	kHighMultV0
Physics selection	default
Incomplete DAQ	check
$z$ vertex	$ vtx_z  < 10$ cm
Contributors to track vertex	$N_{\text{contrib,track}} > 1$
Contributors to SPD vertex	$N_{\text{contrib,SPD}} > 0$
Distance between track and SPD vertex	$d_{\text{vtx,track-SPD}} < 0.5$ cm
SPD vertex $z$ resolution	$\sigma_{\text{SPD},z} < 0.25$ cm
Pile-up rejection	<code>AliEvent::IsPileUpFromSPD()</code> <code>AliEventUtils::IsSPDClusterVsTrackletBG()</code>

TABLE 2.1: Event selection criteria.

If the selected events have the primary vertex reconstructed using SPD tracklets and a vertex obtained using reconstructed global tracks, the distance between the two vertices in the  $z$ -axis must be less than 5 mm. Pile-up events are rejected by requiring only one primary vertex to be reconstructed in the SPD. To ensure the detector coverage is uniform, the primary vertex position from the centre of the detector in the  $z$ -axis must be less than 10 cm.

## Reconstructed proton candidates

Once the event is selected, protons and  $\Lambda$  hyperons are selected. The particle and antiparticle selection is identical; thus, we explicitly refer only to particles in the following. The selection criteria are summarised in Table 2.2. In this analysis, the TPC-only tracks are used for kinematic information. The topological information is obtained from the corresponding global tracks because they have a better spatial resolution. This results in a requirement that only TPC-only tracks with a corresponding global track are selected. Only protons in the pseudorapidity

Selection criterion	Value
Pseudorapidity	$ \eta  < 0.8$
Transverse momentum	$0.5 \leq p_T \leq 4.05 \text{ GeV}/c$
TPC cluster	$n_{\text{TPC}} > 80$
Crossed TPC pad rows	$n_{\text{crossed}} > 70$ (out of 159)
Findable TPC clusters	$n_{\text{crossed}} / n_{\text{findable}} > 0.83$
Tracks with shared TPC clusters	rejected
Distance of closest approach $x/y$	$ DCA_{xy}  < 0.1 \text{ cm}$
Distance of closest approach $z$	$ DCA_z  < 0.2 \text{ cm}$
Particle identification	$ n_{\sigma,\text{TPC}}  < 3$ for $p < 0.75 \text{ GeV}/c$ $n_{\sigma,\text{combined}} < 3$ for $p \geq 0.75 \text{ GeV}/c$

TABLE 2.2: Proton selection criteria.

region  $|\eta| < 0.8$  are analysed. To ensure a high track quality, a sufficiently large number of TPC clusters per track  $n_{\text{TPC}}$ , crossed TPC pad rows  $n_{\text{crossed}}$  and the fraction of findable TPC clusters  $n_{\text{crossed}} / n_{\text{findable}}$  are required, and tracks with shared clusters are rejected. Only primary protons are of interest in femtoscopy studies. Thus secondary protons from weakly decaying particles are rejected by requiring the extrapolated trajectory to be close to the primary vertex (small  $DCA_{XY}$  and  $DCA_Z$  values). Finally, the low-momentum proton sample is contaminated with the particles resulting from interactions with the detector material. Only tracks with transverse momentum higher than  $0.5 \text{ GeV}/c$  are selected to minimise this contribution. As described in previous Chapters, particle identification is performed using TPC and TOF information. At low momentum  $p < 0.75 \text{ GeV}/c$ , where particles have a small probability of reaching the TOF detector, and the TPC detector provides excellent PID, only the requirement of the  $n_{\sigma,\text{TPC}}$  smaller than 3 is applied. However, at a momentum larger than  $0.75 \text{ GeV}/c$ , the TPC cannot efficiently separate protons from other particle species as the specific energy loss in the TPC gas becomes very similar (as shown in Fig 2.6). Within this momentum range, the combined PID from the TPC and the TOF detectors is used, and the condition  $n_{\sigma,\text{combined}} = \sqrt{n_{\sigma,\text{TPC}}^2 + n_{\sigma,\text{TOF}}^2} < 3$  is required. This results in a sharp decrease of the number of candidates at the threshold momentum visible in the left panel of Fig. 2.10, where the distribution of  $n_{\sigma,\text{TPC}}$  as a function of the candidate momentum is depicted. A very clean peak centred at  $n_{\sigma} = 0$  is observed for protons. The absence of additional peak structures means misidentified particles do not contaminate the sample.

The purity of candidates is studied employing Monte Carlo (MC) simulations. As explained in Chapter 2.4, the MC simulations that we use are based on PHOTON 8 for event generation and GEANT 3 for the simulation of the detector response. The

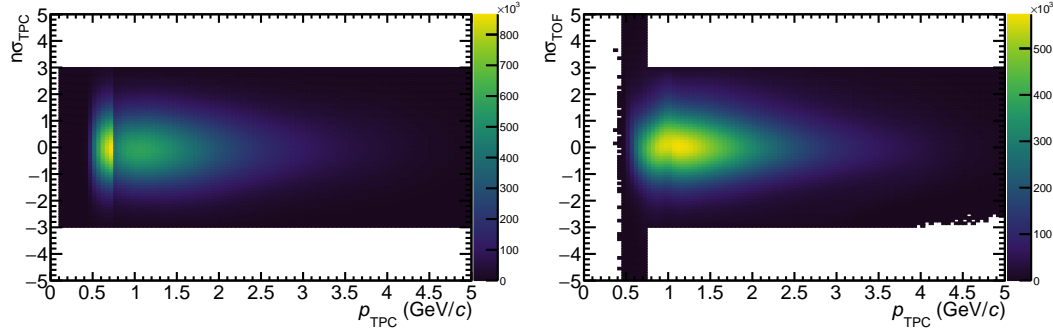


FIGURE 2.10:  $n\sigma_{\text{TPC}}$  (left) and  $n\sigma_{\text{TOF}}$  (right) distributions as a function of the transverse momentum of selected proton candidates.

purity is defined as the ratio of the number of reconstructed true protons produced by the generator and the number of all candidates identified as protons as a function of the reconstructed transverse momentum. The purity obtained for the selected proton candidates is shown in the left panel of Fig. 2.11 as a function of transverse momentum. It decreases with increasing transverse momentum. Thus only tracks with transverse momentum less than  $4.05 \text{ GeV}/c$ , which is the limit at which the purity becomes smaller than 80%, pass the selections. The right panel of Fig. 2.11 shows the proton distribution as a function of transverse momentum. The number of selected tracks decreases with increasing  $p_{\text{T}}$  value, meaning that most of the selected sample is in a very high purity region of  $p_{\text{T}}$ . Indeed, the weighted average purity of the identified protons is 0.98. The same purity is obtained for antiprotons.

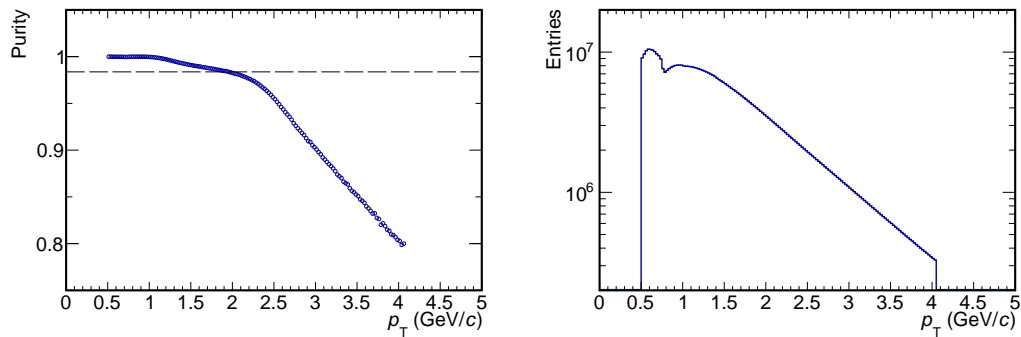


FIGURE 2.11: Left: Proton purity as a function of transverse momentum obtained using MC. Right: Track distribution as a function of transverse momentum for data.

While the proton sample has high purity, it includes primary and secondary protons stemming from weak decays of strange baryons and interactions in the detector material. The latter are produced far away from the interaction point and can not undergo final state interactions, which act up to distances of 100 fm, with other hadrons produced in the collision. Thus particle pairs formed with at least one such proton do not carry information about the strong interaction and result in a decrease of the correlation signal in femtoscopy studies. In contrast, the secondary protons from weak decays may induce additional correlation signals as they carry the information about the interactions of their mother particle with the other hadron building a

pair. All these effects must be considered, and the genuine correlation among correctly identified primary particles must be extracted. The detailed description of the required procedure is in Chapter 3.7. At this point, it is essential to know that to account for such effects, we need to know not only the proton purity but also the fractions of protons from different origins.

To estimate the contributions of the different sources, an observable with sensitivity to the origin of the protons is required. The protons from weak decays are formed at distances of several centimetres w.r.t the collision point. The protons from the material are produced even further from the primary vertex. This results in different DCA distributions for the different protons. While the proton origin cannot

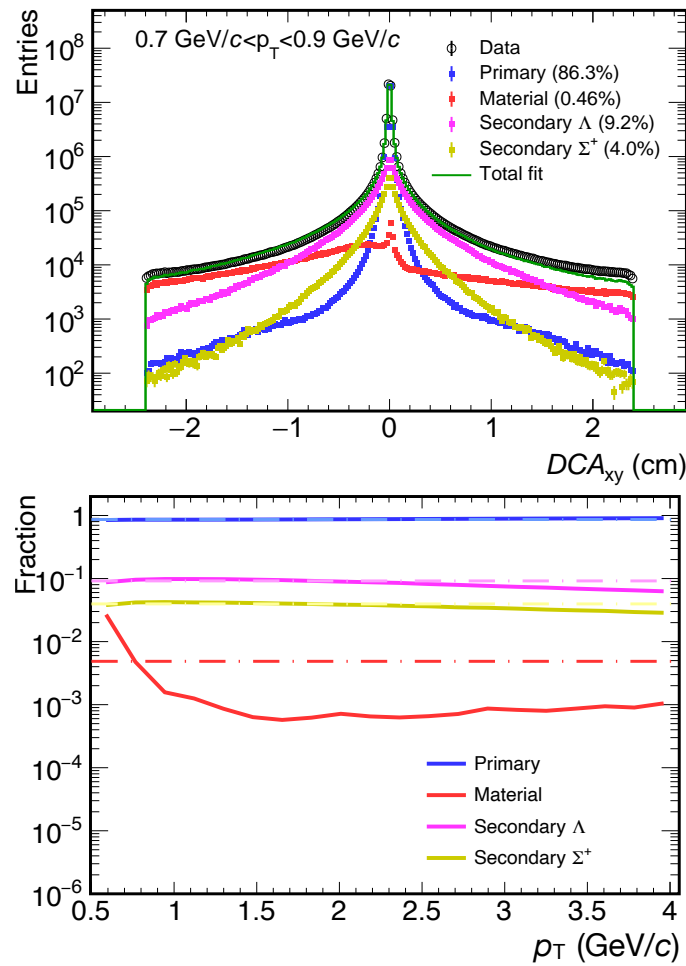


FIGURE 2.12: Upper panel: Proton template fits for one  $p_{\text{T}}$  bin. Lower panel: Fractions as a function of  $p_{\text{T}}$ . Solid lines represent the resulting primary, secondary, and material proton origin fractions.

be told on a particle-by-particle basis, the fractions of primary, secondary, and so-called material protons can be estimated. The shapes of the DCA distributions for different protons are obtained from simulations because in MC one can select particles from specific origins. Such MC distributions can be used as templates to fit the recorded experimental distributions, assuming that the total data sample is the sum of all DCA templates weighted by the fraction of how many such protons are in the sample. Such template fit is shown in the upper panel of Fig. 2.12. The different coloured squares represent the templates obtained from MC, the empty circles corresponds to the data, and the green line shows the total fit. This procedure is

done separately for all transverse momentum bins, and the extracted fractions are shown in the lower panel of Fig. 2.12 as a function of  $p_T$  by solid lines. The fractions shown here are obtained not from the entire sample shown in the upper panel but only for the  $|DCA_{xy}| < 0.1$  cm, as this is the applied selection criteria in the analysis. The dash-dotted lines represent the  $p_T$  weighted averages. The final average fractions for protons and antiprotons are around 86.8 % of primaries, 9.3 % secondaries from  $\Lambda$  decay, 4 % secondaries from  $\Sigma^+$  decays, and a negligible amount of material protons.

### Reconstructed $\Lambda$ hyperon candidates

Finally, we need to select the  $\Lambda$  candidates. A detailed explanation of most of the topological variables used for the V0 selection was provided in Chapter 2.4 while the values specific for this analysis are shown in Table 2.3. However, additional selection criteria are needed to improve the purity of the  $\Lambda$  candidate sample. Similarly to primary protons, the requirements on the pseudorapidity region and the number of TPC clusters are applied for the daughter tracks. The daughters are identified using only TPC information and with a much looser  $n_{\sigma,TPC}$  limit of 5. Tracks selected as secondary do not point to the primary vertex. Thus no higher DCA limit is applied, which introduces particles stemming from out-of-bunch pile-up events (further pp collisions that occur within the integration time of the detector) to the sample. The requirement to have an associated hit in the ITS SPD or SSD or the TOF timing is imposed to prevent this. These fast detectors allow us to differentiate tracks produced at different times. To enhance the purity of resulting reconstructed  $\Lambda$  candidates, a selection on the radial distance of the secondary vertex to the primary vertex is applied together with the requirement of  $\Lambda$  transverse momentum to be higher than 0.3 GeV/c. Finally, only V0 candidates with a reconstructed in-

Selection criterion	Value
<i>Daughter track selection criteria</i>	
Pseudorapidity	$ \eta  < 0.8$
TPC cluster	$n_{TPC} > 70$
Distance of closest approach	$DCA > 0.05$ cm
Particle identification	$ n_{\sigma,TPC}  < 5$
Out-of-bunch pile-up removal	Hit in ITS SPD or SSD or TOF timing
<i>V<sup>0</sup> selection criteria</i>	
Transverse momentum	$p_T > 0.3$ GeV/c
decay vertex	$ i_{vertex_\Lambda}  < 100$ cm, $i=x,y,z$
Transverse radius of the decay vertex $r_{xy}$	$0.2 < r_{xy} < 100$ cm
DCA of the daughter tracks at the decay vertex	$DCA( p, \pi ) < 1.5$ cm
Pointing angle $\alpha$	$\cos \alpha > 0.99$
K <sup>0</sup> rejection selection	$0.48 < M_{\pi^+\pi^-} < 0.515$ GeV/c <sup>2</sup> $ M_{p\pi} - M_{\Lambda,PDG}  < 4$ MeV/c <sup>2</sup>

TABLE 2.3:  $\Lambda$  selection criteria.

variant mass corresponding to the nominal  $\Lambda$  mass 1115.66 MeV/c<sup>2</sup> are selected, allowing a spread of  $\pm 4$  MeV/c<sup>2</sup>. As the daughter particle PID requirement is

loose, the  $\Lambda$  sample is contaminated by the  $K_s^0$  mesons. V0s with the invariant mass  $0.48 \text{ GeV}/c^2 < M_{\pi^+\pi^-} < 0.515 \text{ GeV}/c^2$  under the hypothesis of a  $\pi^+\pi^-$  are rejected to reduce such background.

The purity of  $\Lambda$  candidates can be estimated directly from the data by looking at the invariant mass distributions and fitting them with two functions, one corresponding to the signal and one to the background. The invariant mass distribution of the reconstructed  $\Lambda$  candidates strongly depends on the detector resolution and can usually be described with a Gaussian function. However, the shape of the  $\Lambda$  peak might be more complicated as the resolution of the reconstructed candidates depends on several factors. It has been observed experimentally that it can be better fitted with a sum of two Gaussian functions [35]. The background contribution can be described sufficiently well with a second-order polynomial. The purity is estimated separately for all  $p_T$  bins, and the resulting fits are shown in Fig. 2.13. The upper panels in Fig. 2.14 show the obtained purities for  $\Lambda$  (left panel) and  $\bar{\Lambda}$  (right panel) candidates. While the invariant mass fits work perfectly well in the  $p_T$  bins, it is unclear which of these transverse momentum regions contributes the most to the actual p-p- $\Lambda$  correlation function. To test this, we performed the same invariant mass fitting procedure in  $Q_3$  bins. As the data sample of triplets at low  $Q_3$  is extremely small, the mixed-event sample was fitted. The lowest  $Q_3$  bins still have extremely small counts, and the fits in the first few bins are not of high quality.

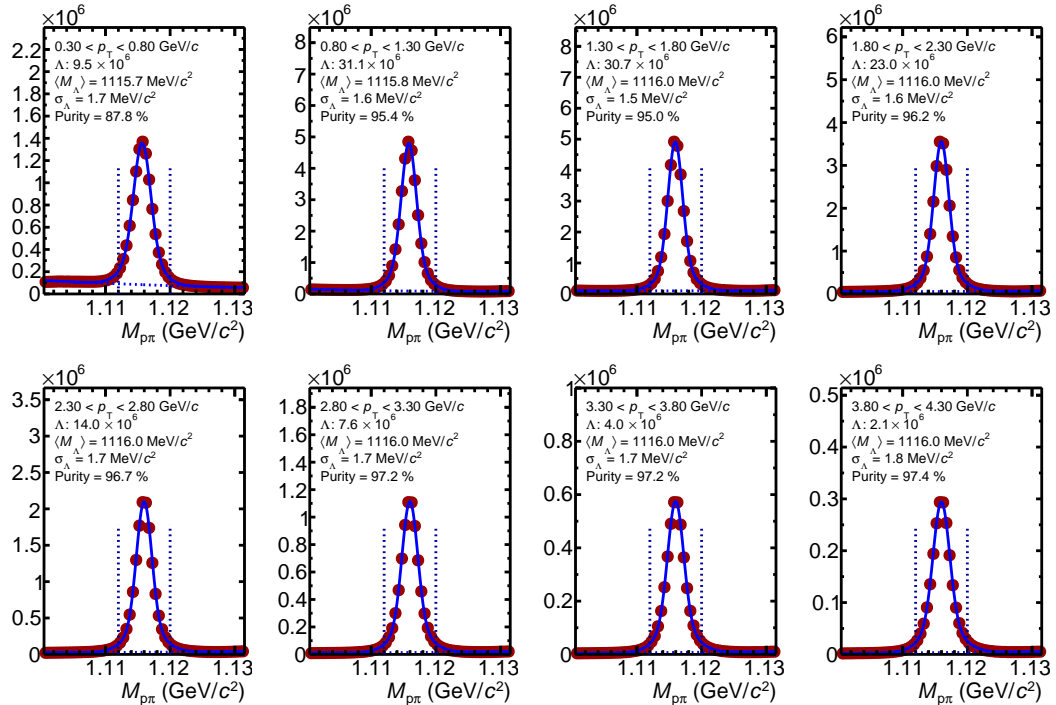


FIGURE 2.13:  $\Lambda$  invariant mass fits used to extract the purity. The different panels show fits for different  $p_T$  bins.

However, the purities obtained as a function of  $Q_3$  are very similar to the purities extracted for different  $p_T$  bins, as is shown in the lower panel of Fig. 2.14.

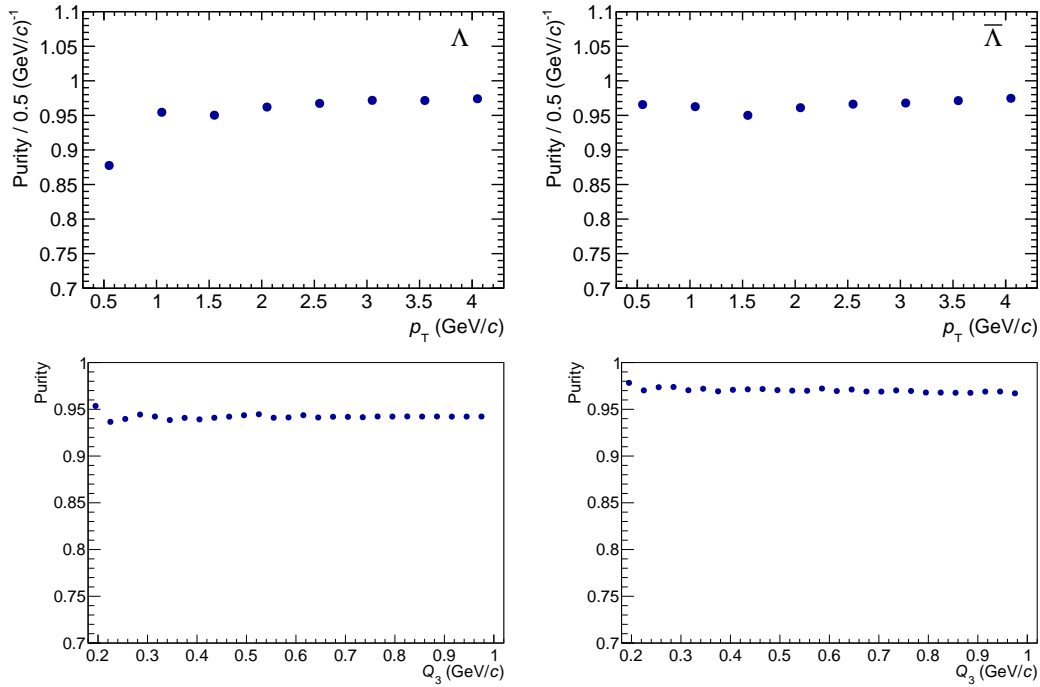


FIGURE 2.14: Upper panels:  $\Lambda$  (left) and  $\bar{\Lambda}$  (right) candidate purity as a function of the transverse momentum. Lower panels:  $\Lambda$  (left) and  $\bar{\Lambda}$  (right) candidate purity as a function of the Lorentz invariant hyper-momentum.

The  $\Lambda$  purity seems to be, on average lower than  $\bar{\Lambda}$  purity which the contamination can partially explain from secondaries (also visible in the first  $p_T$  bin for the  $\Lambda$  candidates). The weighted average purity of  $\Lambda$  is around 94.27%, while for the antihyperon, it is 96.87%.

As in the case of the protons, the  $\Lambda$  candidate sample is pure, but not all particles are primaries. The fractions of primary, secondary, and material  $\Lambda$  candidates can be obtained similarly as for protons by performing template fits of topological observable. The CPA can differentiate the  $\Lambda$  candidates as this observable depends on where the particle was produced - whether the reconstructed momentum points to the primary vertex. The MC simulations are again employed to obtain the template distributions of the CPA for  $\Lambda$  particles from different origins and then fitted to the data to obtain the fractions. The obtained results are shown in Fig. 2.15. The possible feed-down to  $\Lambda$  hyperons consists of  $\Sigma^0 \rightarrow \Lambda\gamma$ ,  $\Xi^- \rightarrow \Lambda\pi^-$  and  $\Xi^0 \rightarrow \Lambda\pi^0$  decays. Because of the very short lifetime of the  $\Sigma^0$ , the  $\Lambda$  coming from its decay can not be experimentally differentiated from the sample of primaries. The expected ratio of produced  $\Sigma^0$  and  $\Lambda$  particles in high energy collisions is 1/3 based on predictions from the isospin symmetry and a measurement of the corresponding production ratios [141]. Thus, the primary  $\Lambda$  particles contribute on average to about 58.5% of the total yield, while about 19.5% of the sample is  $\Lambda$  hyperons from the electromagnetic decays of  $\Sigma^0$ . The secondaries which can be differentiated by CPA are from weak  $\Xi$  decays:  $\Xi^-$  and  $\Xi^0$  contribute about 11 % each to the yield of  $\Lambda$  hyperons. The contributions of fakes and material particles are negligible.

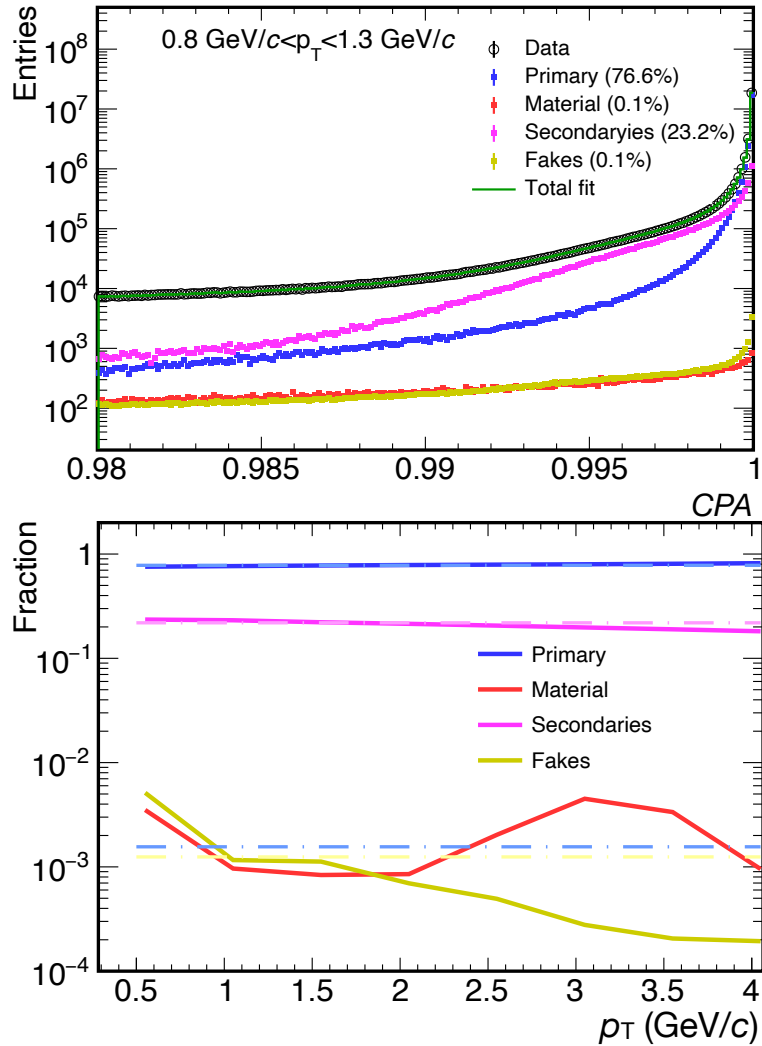


FIGURE 2.15: Upper panel:  $\Lambda$  template fits of cosine pointing angle for one  $p_T$  bin. Lower panel: Fractions as a function of  $p_T$ . Solid lines represent the resulting primary, secondary, fake, and material  $\Lambda$  origin fractions.

## Chapter 3

# Three-baryon correlations

The final state interactions are imprinted in the measured particle momenta correlations among three particles produced in the same event ( $N_s(Q_3)$ ). To obtain a correlation function  $C(Q_3)$ , also a reference sample of non-interacting particles ( $N_m(Q_3)$ ) is required

$$C(Q_3) = \mathcal{N} \frac{N_s(Q_3)}{N_m(Q_3)}, \quad (3.1)$$

where  $\mathcal{N}$  is a normalisation constant chosen such that in the region of large  $Q_3$ , the correlation function is equal to 1 since for large  $Q_3$  no signal from final state interactions is observed. In this work, all correlation functions are normalised at the region  $1.0 \text{ GeV}/c < Q_3 < 1.2 \text{ GeV}/c$ . The same event sample is built by considering all possible combinations of particle triplets in a single event. The most common method used to estimate the reference sample where no interaction occurs is the mixed event technique, and it consists of considering particles taken from different collisions. This technique has been successfully applied in femtoscopy [74] and other studies such as angular correlation measurements [142]. Particles combined to form a mixed event triplet should be produced in similar events. To ensure this, particles are mixed only if the parent collisions have similar multiplicity and vertex position on the z-axis. The first condition is required to have similar track acceptance in the detector, while the second condition helps to constrain event shapes and produced particle momentum spectra. The obtained mixed event triplets undergo identical triplet selections as the same event triplets. Once the same and mixed event samples are obtained, the correlation function can be evaluated, and the systematic and statistical uncertainties can be studied. At the moment of this analysis, no theoretical predictions for three-particle correlation functions were available. Thus, as explained in Chapter 1.6.3, the Kubo's cumulant method was employed, which allows us to study if any three-body effects are present in the system - may it be the genuine three-body strong interaction or Quantum Statistics effects for three identical particles or other. The cumulant method requires the measured three-body correlation function and lower-order correlation functions, which describe a system of two interacting particles and one spectator. A data-driven method based on event mixing has been previously used in the field [81], where two particles in the numerator of Eq. 3.1 are taken from the same event and one from another event. A projector method has been developed to ensure that such a technique reasonably describes the lower-order contributions. In this thesis, both methods are employed. The correlation functions were measured for p-p-p, (p-p)-p, p-p- $\Lambda$ , (p-p)- $\Lambda$ , p-(p- $\Lambda$ ), p-p- $\bar{p}$ , (p-p)- $\bar{p}$ , p-(p- $\bar{p}$ ) triplets. The notation (X-Y)-Z, where X, Y, and Z are particle species, is used for correlation function where X and Y interact, but Z is only a spectator. We are primarily interested in p-p-p and p-p- $\Lambda$  systems, while the p-p- $\bar{p}$  measurements were performed as a mixed proton charge cross-check. Finally, Alejandro Kievsky

performed preliminary calculations of the p-p-p correlation functions employing the Hyperspherical Harmonics method [86], which will be compared to the obtained results in the next Chapter and was introduced in Chapter 1.6.2.

### 3.1 Correlation functions

The selections of particle triplets and the re-weighting procedure to account for different multiplicity distributions in same and mixed event triplets are discussed first. The raw correlation functions before and after these steps will be presented. Finally, the correlation functions obtained with all selections and multiplicity re-weighting will be shown.

#### Triplet selections

The experimentally measured correlation function can be contaminated by non-femtoscopic correlations resulting from the particle candidate reconstruction and detector effects.

If one compares Tables 2.2 and 2.3, it is obvious that the requirements for primary and secondary tracks have some overlap. This can lead to a situation where the same track is reconstructed as a primary proton but also is used in a V0 reconstruction as a daughter particle. If the same event distribution is built by combining such proton and  $\Lambda$  hyperons, self-correlations appear in the measured correlation function. The pair cleaning is performed before creating the triplets to suppress such cases. All possible combinations of a primary proton and a  $\Lambda$  hyperon are created on an event-by-event basis. If the same track is used as a primary and secondary particle, the corresponding  $\Lambda$  particle is deleted from the list. Only  $\sim 0.6\%$  of all events have one such pair, and the penalty factor for every other pair is  $\sim 100$ . All combinations of  $\Lambda$  hyperons in an event are also created. If two  $\Lambda$ s are reconstructed using the same daughter track, only the  $\Lambda$  with the smaller pointing angle to the primary vertex is used for the triplet creation. Only  $\sim 0.065\%$  of all events are affected. Every additional pair in the event has a penalty factor  $\sim 100$ .

The limited tracking resolution can also induce unwanted correlations in the relative momentum of particle triplets. If two particles are produced close to each other, they might be reconstructed as a single track, which results in a depletion of particle pairs in a  $\Delta\phi$ - $\Delta\eta$  plane at small values as it is visible in the left panel of Fig. 3.1. However, this does not affect the mixed event sample, as shown in the right panel of Fig. 3.1. The effect is present not only in cases when two primary protons are produced (which is shown in Fig. 3.1) but also if a proton is produced together with a  $\Lambda$  hyperon where the primary proton and a secondary proton coming from  $\Lambda$  decay can be indistinguishable to the tracking algorithm. To avoid this, the triplets in which at least one p-p pair, either composed of two primary protons or a primary combined with a secondary proton, fulfils the following condition are not used

$$(\eta_1 - \eta_2)^2 + (\phi_1 - \phi_2)^2 < (0.017)^2. \quad (3.2)$$

The cut is applied on the  $\Delta\phi - \Delta\eta$  distribution obtained as an average over nine different radii in the TPC ( $r_{TPC} = 85\text{ cm}, 105\text{ cm}, 125\text{ cm}, 145\text{ cm}, 165\text{ cm}, 185\text{ cm}, 205\text{ cm}, 225\text{ cm}$  and  $245\text{ cm}$ ) in case of both same and mixed event samples. This selection criterion is included in the systematic variations defined in Chapter 3.3 by increasing the radius of the circumference if Fig. 3.1 from 0.017 to 0.019.

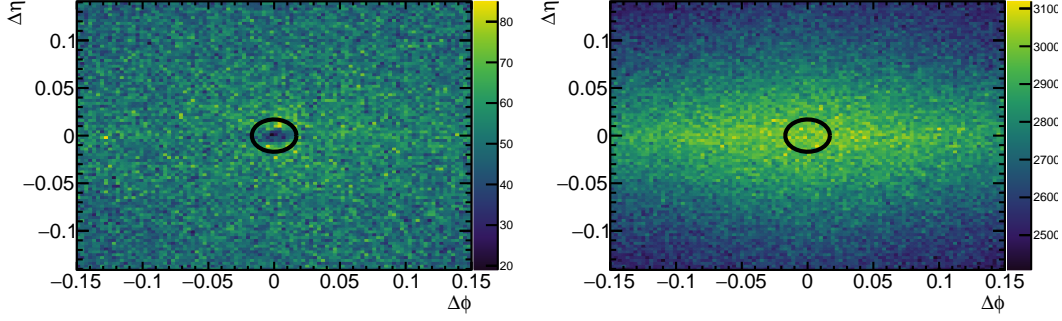


FIGURE 3.1:  $\Delta\phi$ - $\Delta\eta$  distributions of p-p pairs for the same event (left) and mixed event (right) samples obtained using MC data. The black circle shows the performed selection.

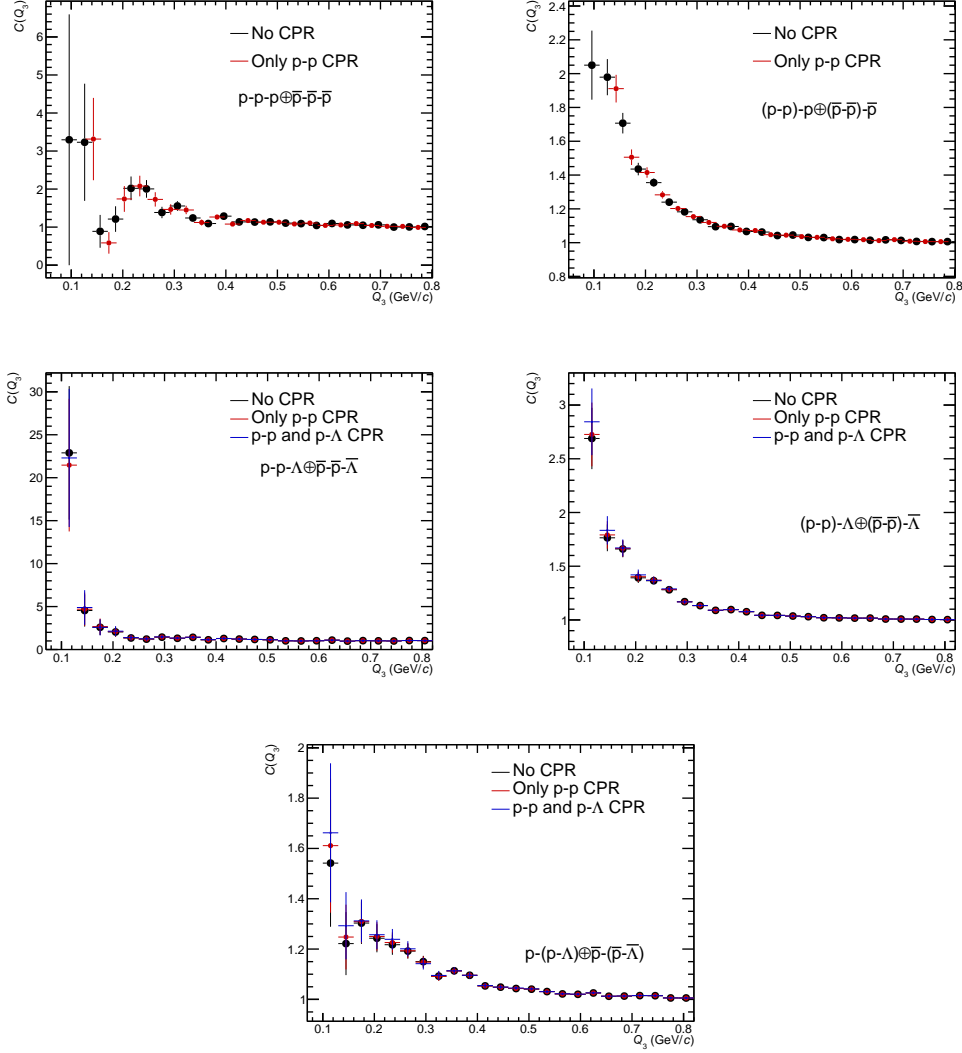


FIGURE 3.2: Raw correlation functions obtained with and without the close pair rejection (CPR).

The correlation functions were estimated with and without the selection to test if there are any unexpected effects in the case of three-body femtoscopy. The

comparison is shown in Fig. 3.2<sup>1</sup>. Here, the particle and antiparticle samples are added to obtain the total correlation functions as explained later in Chapter 3.5. It is clear that the selection does not change the underlying shape of the correlation functions and shows only slight variation in the bin-by-bin values as previously observed in two-particle femtoscopic studies by ALICE.

## Multiplicity re-weighting

The underlying event shape affects the particle momenta and thus can influence the correlation function. As mentioned, this implies that the event mixing must be per-

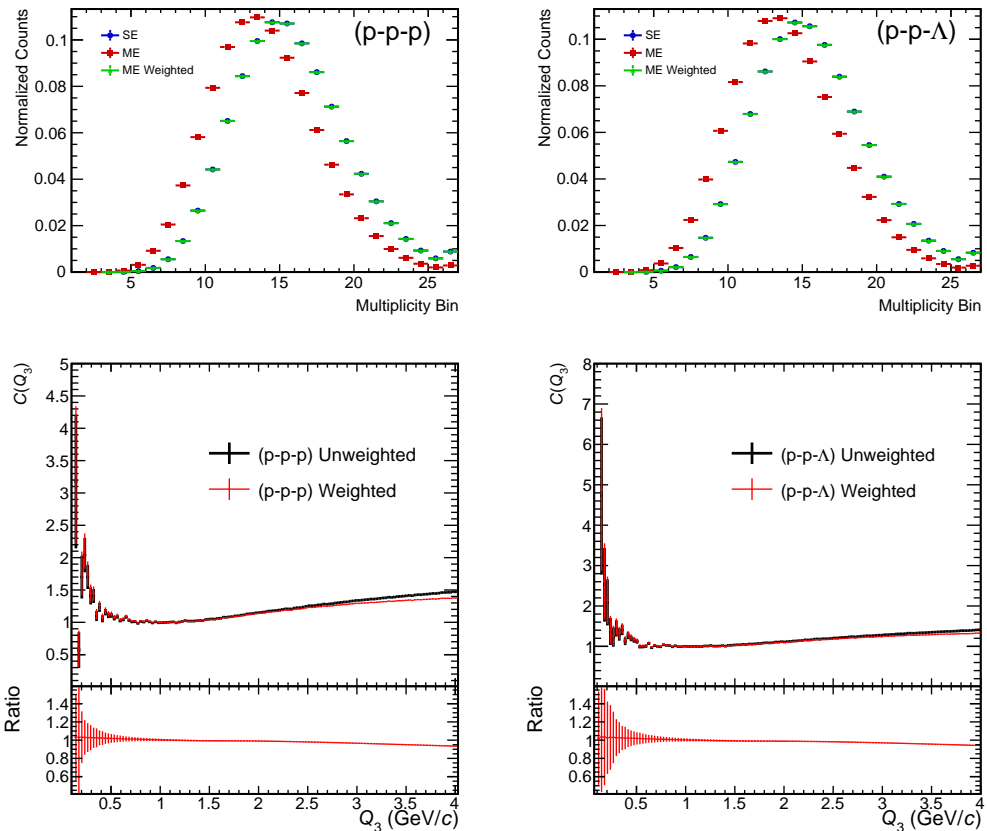


FIGURE 3.3: Upper figures: Same (blue) and mixed (red) event distributions as a function of multiplicity for p-p-p (left panel) and p-p- $\Lambda$  (right panel) triplets. The green data points show the re-weighted mixed event distribution. Lower figures: Correlation functions obtained with (red) and without (black) re-weighting of mixed event sample for p-p-p (left figure) and p-p- $\Lambda$  (right figure) triplets (upper panel) and their ratio (lower panel).

formed only between events with similar multiplicity. It is also essential to check if the same and mixed event triplets have identical multiplicity distributions. Indeed, as shown in the upper panels of Fig. 3.3, the same event (blue) and mixed event (red) triplet distributions as a function of multiplicity are not the same. A re-weighting of

<sup>1</sup>The shown correlation functions are not the final result of this work but just a check and were obtained using a small number of events for event mixing (10). This is also true for the other figures, where different effects are analysed. The final results are shown in Chapter 3.4.

the mixed event sample is performed to avoid such bias in the final result. First, the mixed event triplets are measured as a function of  $Q_3$  and multiplicity. Then every multiplicity bin is re-weighted to have the same statistical weight as in the case of the same event. After this procedure, the same and mixed event triplet distributions are identical as a function of multiplicity as shown in upper panels of Fig. 3.3 (re-weighted distribution is depicted in green symbols). The results here are shown only for p-p-p and p-p- $\Lambda$  triplets. However, the same procedure is performed on all measured systems. The effect of the mixed event re-weighting for correlation functions is shown in the lower panels of Fig. 3.3. In two-body femtoscopy, it was observed that the multiplicity re-weighting only slightly affects the low relative momenta region and mainly changes the correlation shape at high relative momenta. In the case of three-body femtoscopy, the effect is also most predominant at high  $Q_3$ .

### Particle and antiparticle triplets

Finally, we can look in detail at the obtained triplet distributions and the correlation functions. The number of triplets in the nominator of Eq. 3.1 for p-p-p and p-p- $\Lambda$  systems does not depend on the number of events used for event mixing, as all three particles are taken from the same event. However, for (p-p)-p, (p-p)- $\Lambda$  and p-(p- $\Lambda$ ) triplets, the numerator sample is obtained by taking two particles from the same event and the third particle from a different event. In such a case, the statistical uncertainty of the correlation functions strongly depends on the chosen number of events used for mixing. This number also cannot be chosen to be large because it becomes computationally too expensive to perform the analysis. All correlation functions, except p-(p- $\Lambda$ ), were obtained using 30 events for event mixing in this work. Forming p-(p- $\Lambda$ ) triplet requires having p- $\Lambda$  pairs in the same event, which is less probable than the p-p pair requiring a higher number of events for mixing, which was chosen to be 100. The same is true for the antiparticle triplets. The resulting numbers of triplets in the low  $Q_3 < 0.4$  GeV/c region, which is expected to be sensitive to the two- and three-particle interactions, are shown in Table 3.1. The denominator for all triplets is obtained using the same number of events for mixing as for the numerator. The number of triplets for three-correlated particles is small. The counts of the same event triplets for particle and antiparticle systems as a function of  $Q_3$  are shown in Fig. 3.4. On the left panel, the distributions are shown for p-p-p (blue) and  $\bar{p}$ - $\bar{p}$ - $\bar{p}$  (red) systems. Five triplets are obtained for both particles and antiparticles in the first bin. The second bin has only two entries for particles and three for antiparticles. The third bin has 13 entries for particles and 16 entries for antiparticles. In the case of p-p- $\Lambda$  triplets, the first four bins have less than ten entries each for particles and antiparticles.

The final state interactions in the case of particle and antiparticle triplets are expected to be the same. It was also shown in Chapter 2.5, that proton and antiproton purities are the same, while for  $\Lambda$  particle and antiparticle, they are very similar. Thus it is convenient to add the two samples to obtain the final correlation function, as it increases the statistical significance of the result. However, it must be first confirmed that the measured particle and antiparticle correlation functions are in good agreement, as expected.

The particle and antiparticle correlation functions are compared in Fig. 3.3. In all five cases, the overall shape is in good agreement between particle and antiparticle correlation functions. More considerable disagreements on a bin-by-bin basis are visible at the low  $Q_3$  region. However, as mentioned above, the low  $Q_3$  bins have a

very small number of entries, and the differences between particles and antiparticles can be interpreted as statistical fluctuation.

Pair	Number of triplets at $Q_3 < 0.4 \text{ GeV}/c$
p-p-p	600
$\bar{p} - \bar{p} - \bar{p}$	378
(p-p)-p	$1.46 \times 10^5$
$(\bar{p} - \bar{p}) - \bar{p}$	$1.04 \times 10^5$
p-p- $\Lambda$	296
$\bar{p} - \bar{p} - \bar{\Lambda}$	177
(p-p)- $\Lambda$	$7.19 \times 10^4$
$(\bar{p} - \bar{p}) - \bar{\Lambda}$	$5.07 \times 10^4$
p-(p- $\Lambda$ )	$1.057 \times 10^5$
$\bar{p} - (\bar{p} - \bar{\Lambda})$	$7.7 \times 10^4$

TABLE 3.1: Number of triplets for  $Q_3 < 0.4 \text{ GeV}/c$ .

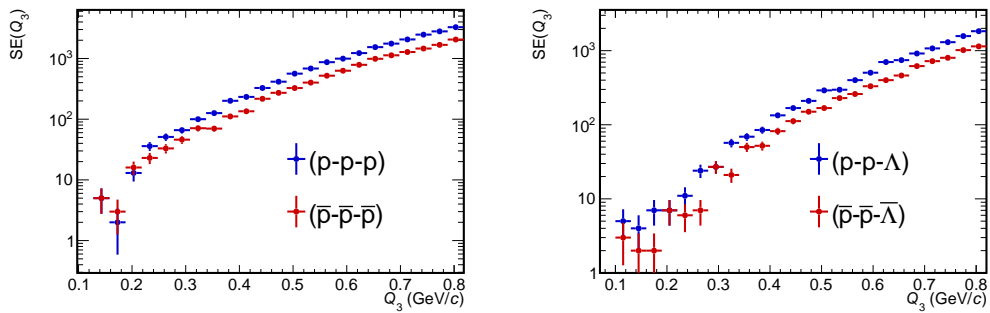


FIGURE 3.4: The number of counts in the same event distribution for particles (blue) and antiparticles (red).

In order to build the final three-particle correlation functions, particle and antiparticle distributions are combined as

$$C(Q_3) = \frac{N_{same,total}(Q_3)}{N_{mixed,total}(Q_3)} = \frac{N_{same,particles}(Q_3) + N_{same,antiparticles}(Q_3)}{N_{mixed,particles}(Q_3) + N_{mixed,antiparticles}(Q_3)}.$$

In the following, p-p-p refers to  $p-p-p \oplus \bar{p} - \bar{p} - \bar{p}$  and p-p- $\Lambda$  refers to  $p-p-\Lambda \oplus \bar{p} - \bar{p} - \bar{\Lambda}$  and so on.

## 3.2 Statistical uncertainties

The probability of recording a particular number of counts in an experiment for a given mean expected number of counts follows a Poisson distribution [143]. In the case of a large number of counts, the Poisson distribution can be approximated using a Gaussian distribution. The statistical uncertainty then can be assumed to be symmetrical and equal to the  $\sqrt{N}$ , where  $N$  is the number of counts. However, in the case of small counts per bin, it is more accurate to evaluate the error by considering the asymmetry of the distribution. In such a case, using alternative methods to estimate statistical uncertainties becomes useful. In this work, we chose to estimate

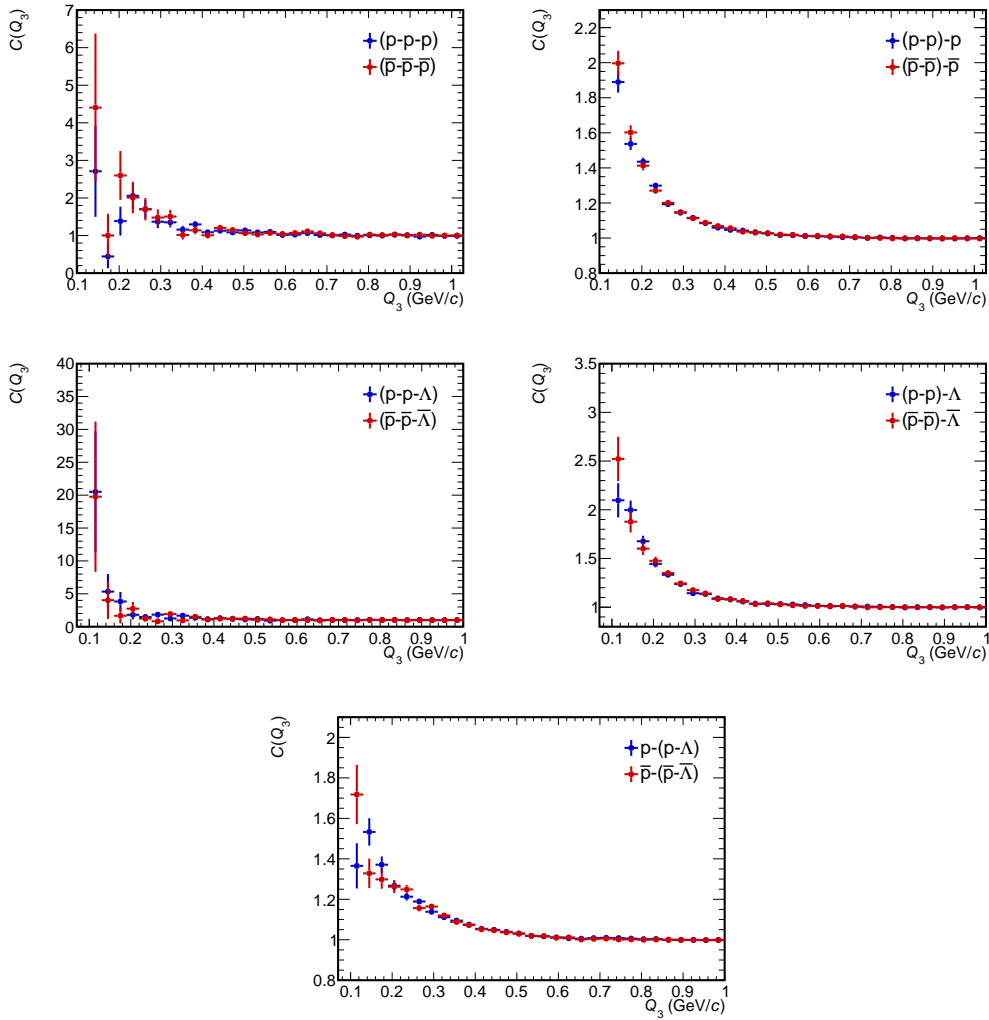


FIGURE 3.5: The correlation functions obtained for particles (blue) and antiparticles (red).

the statistical uncertainties of the correlation functions by employing a bootstrap procedure. The following steps were taken to obtain the final uncertainties:

1. The same and mixed event triplet counts are sampled accordingly to a Poisson distribution using the measured triplet count as the expectation value. Here, the measured triplet counts are the sum of particle and antiparticle triplets.
2. The correlation function is calculated as  $C(Q_3) = \mathcal{N}(Q_3)N_{SE}(Q_3)/N_{ME}(Q_3)$ , where the counts are sampled in the previous step and  $\mathcal{N}(Q_3)$  is a normalisation function which includes the standard correlation function normalisation to 1 and the re-weighting due to the different multiplicity distribution in the same and mixed event (explanation in Chapter 3.1). This normalisation is obtained from the standard analysis, where correlation functions are estimated as described in previous Chapters. After repeating this step for all bins  $10^6$  times, the 2D distribution shown in Fig. 3.6 is obtained for the p-p-p triplet. The same bootstrap method was employed for all correlation functions.
3. The final correlation function is then obtained by using the mean of the sampled  $C(Q_3)$  distribution at one  $Q_3$  bin as the correlation function value, and

the 68% central confidence interval is shown as the statistical uncertainty. The correlation function estimated in such a way perfectly agrees with the correlation function obtained using measured yields with differences smaller than 0.5% per bin.

4. The cumulants are calculated using the mean and uncertainty values mentioned above.

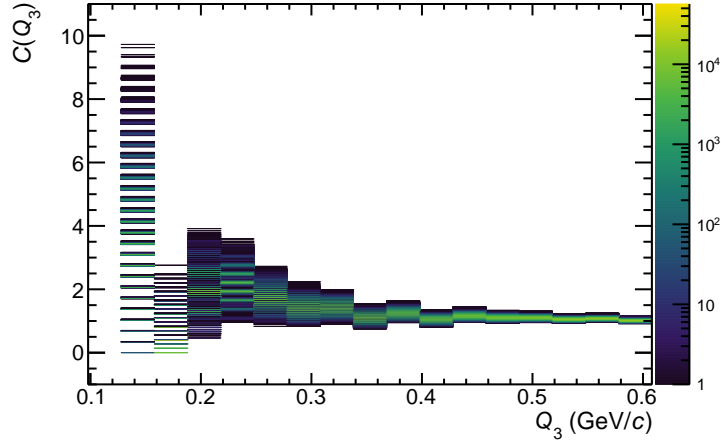


FIGURE 3.6: Sampled correlation function as a function of  $Q_3$ .

The distribution shown in Figure 3.6 shows the result obtained using the described bootstrap method for p-p-p triplets. Figure 3.7 shows results for the second (left panel) and the seventh (right panel) bins. The total distribution consists of many Gaussian-looking distributions. The  $C(Q_3)$  value, at which the distributions are centred, correspond to a specific value of same event counts as these are discrete numbers. The width of these distributions depends on the mixed event counts.

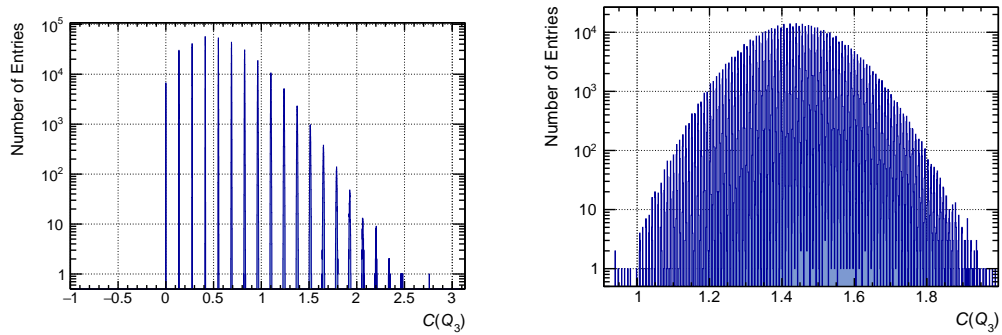


FIGURE 3.7: The number of sampled entries as a function of  $Q_3$ . The left panel shows results for the second bin and the right panel for the seventh bin.

### 3.3 Systematic uncertainties

Systematic uncertainties should account for all uncertainties not included in the statistical uncertainties. For example, a measurement with a ruler can depend on the room temperature, as the ruler might contract or expand at different temperatures. In experimental particle physics, treating the systematic uncertainties can pose a challenge as there is no single correct approach. The systematic effects in high-energy physics include integrated luminosity, geometrical acceptance, reconstruction efficiency, trigger efficiency, etc. However, the correlation function does not depend on luminosity. Acceptance and efficiency effects for single particles mostly cancel out in the same and mixed event triplet ratio. The high-multiplicity trigger used in this analysis biases the event selections, which should affect only the source size of the produced particles, which is usually accounted for in the modelling of the correlation function. Additional biases might be introduced by the selection criteria applied to the tracks and V0s. Such systematic uncertainties of experimental data can be estimated by varying the selection criteria. It resembles the situation of making multiple measurements with slightly different setups. In this work, we evaluated the systematic uncertainties of correlation functions by performing simultaneous variations of the selection criteria for tracks, V0s and the close pair rejection requirement. The latter is defined in Eq. 3.2. The standard value 0.017 is varied by +10 %. As changing the default rejection value by -10 % would accept the triplets affected by the track merging, such variation is not performed. The track and V0 selection variations for systematic uncertainties are shown in Table 3.2 and are standard in femtoscopic studies of protons and  $\Lambda$  hyperons [35]. To account for the correlations between the systematic uncertainties, the described variations are combined to form 44 sets in which at least one selection criteria is varied. The same and mixed event triplet distributions are obtained for all 44 sets of varied selection criteria. However, only sets for which the obtained number of the same event triplets in the kinematic region  $Q_3 < 0.4 \text{ GeV}/c$  is varied by less than 10% with respect to the standard selection are used to estimate systematic uncertainties.

Variable	Default	Variation
$p_T$ proton ( $\text{GeV} c_0^{-1}$ )	0.5	0.4, 0.6
$ \eta $ proton	0.8	0.77, 0.85
$n_\sigma$ proton	3	2.5, 3.5
$n_{\text{Cluster}}$ proton	80	70, 90
$\cos(\alpha)$ $V^0$	0.99	0.995
$n_\sigma$ $V^0$ daughter	5	4
$n_{\text{Cluster}}$ $V^0$ daughter	70	80
$ \eta $ $V^0$	0.8	0.77, 0.83
DCA( $ p, \pi $ ) (cm)	1.5	1.2
DCA (cm)	0.05	0.06

TABLE 3.2: Variations of different selection criteria on the correlation functions.

The normalisation region of the correlation function is also considered a systematic uncertainty in the femtoscopic analysis. The standard normalisation region is  $1.0 \text{ GeV}/c < Q_3 < 1.2 \text{ GeV}/c$ . Varying the normalisation region by  $\pm 0.1 \text{ GeV}/c$  does not strongly affect the measured correlation functions (maximum obtained variation was 1% per bin); thus, this variation is not included in the systematic uncertainties. The mixing procedure was performed using all events. However, the events with

at least one triplet of interest might have a different underlying event that could cause unwanted changes in the momentum spectrum of single particles. A test was performed by estimating correlation functions where only events with at least one triplet of interest were used for the event mixing. The obtained correlation functions have a maximum of a few percent differences, but no systematic behaviour was observed. It is impossible to differentiate if any effect is present within the current statistical uncertainties. The different selection of the mixed event sample is not considered in the final systematics.

### 3.4 Measured correlation functions and Monte Carlo results

The final correlation function results for the p–p–p, p–p– $\Lambda$ , (p–p)–p, (p–p)– $\Lambda$  and p–(p– $\Lambda$ ) triplets are shown in Fig. 3.8 as green markers together with statistical (vertical lines) and systematic (boxes) uncertainties. These results were submitted to EPJA and are already accepted, yet not published. However, the final version of the paper can be found in Ref. [144]. The in-depth discussion of the measured correlation functions will follow in the next Chapters, where the correlation functions are compared to the lower-order contributions. Before drawing any conclusions about the final state interactions, we must ensure that no other correlations are involved in the three-particle system and that no detector effects remain. This can be done by performing the same analysis described in this work but on MC data. As explained in Chapter 2.4, the MC data used in this work is based on generating the events in PYTHIA 8 and then propagating the resulting particles in GEANT 3 which describes the ALICE detector. PYTHIA 8 accounts for effects such as minijets while GEANT 3 accounts for the possible detector effects. Neither two- nor three-particle FSIs are included in the event generator. Thus, the correlation functions at low  $Q_3$  region are expected to be equal to unity in MC if no minijet or detector effects are present. The obtained correlation functions for analysed MC are shown as black squares in Fig. 3.8. The statistical sample of triplets in MC is considerably smaller than in the measured data, as is visible from the statistical uncertainties. In the case of p–p– $\Lambda$ , the second bin has no entries in the same event sample, and thus the correlation function is shown as equal to 0 with no uncertainty.

All simulated correlation functions are consistent within the uncertainties with unity for the entire  $Q_3 < 0.8 \text{ GeV}/c$  range. This shows that no additional correlations caused by the minijets or detector effect are present in the measured systems.

The measured correlation functions are discussed in the next Chapters.

### 3.5 Lower-order contributions

At the time of this analysis, no theoretical predictions were available for the three-particle correlation functions. Thus, to conclude on three-body effects in the measured correlation functions, we employed Kubo's cumulant method [145]. As explained in Chapter 1.6.3, it allows us to estimate the lower-order contributions which account for the two-particle interactions in the three-particle system as

$$C^{\text{two-body}}(Q_3) = C_{12}(Q_3) + C_{23}(Q_3) + C_{31}(Q_3) - 2 , \quad (3.3)$$

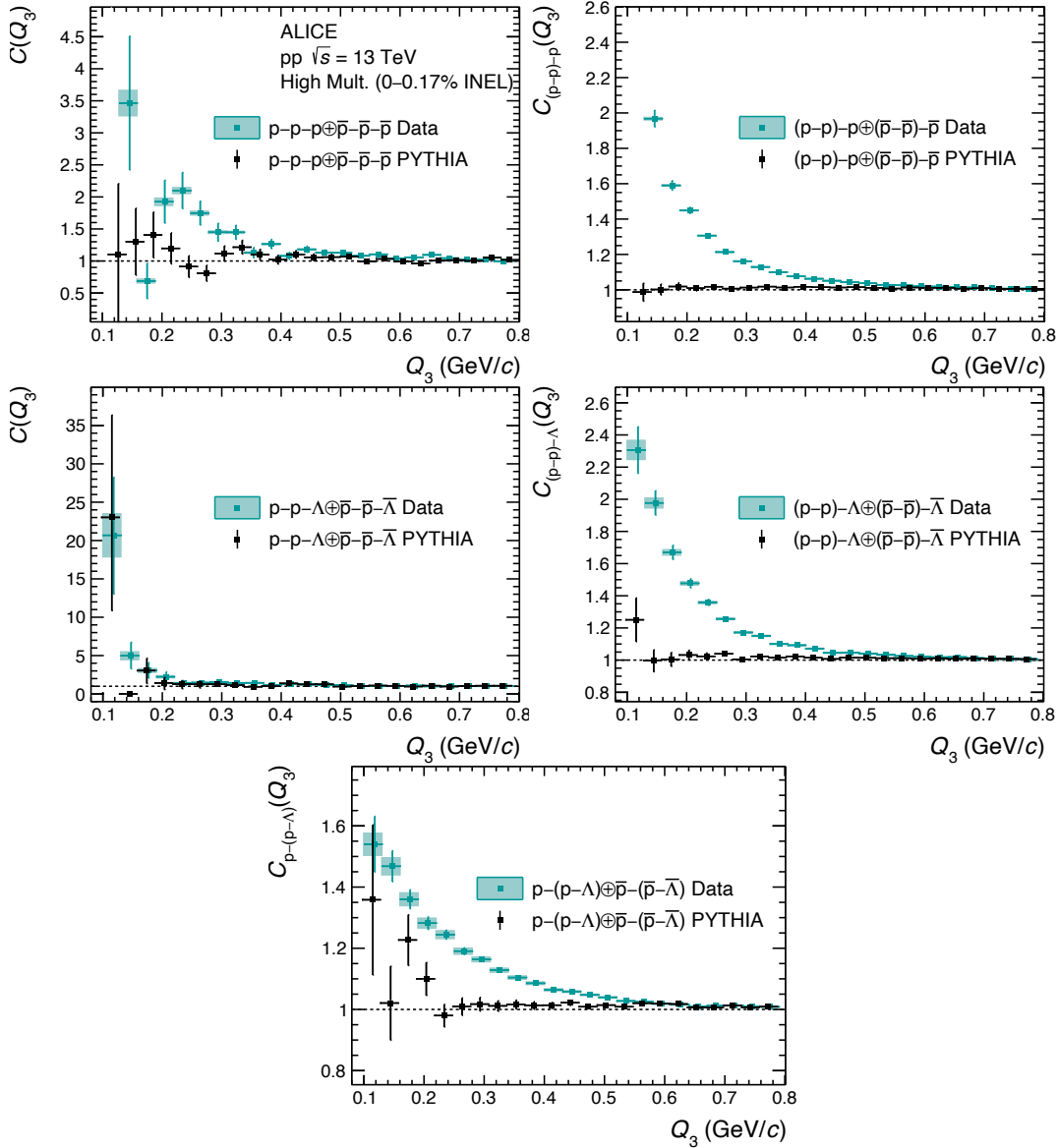


FIGURE 3.8: Comparison between the measured correlation functions (green) and obtained with the PYTHIA 8 event generator (black).

where  $C_{ij}(Q_3)$  is the correlation function between particles  $i$  and  $j$  projected in the three-particle system. **Such a lower-order estimate does not include any three-body effects.** In case of p-p-p system, the Eq. 3.3 can be rewritten as

$$C_{p-p-p}^{\text{two-body}}(Q_3) = 3 C_{(p-p)-p}(Q_3) - 2, \quad (3.4)$$

and in the case of p-p- $\Lambda$ , we have

$$C_{p-p-\Lambda}^{\text{two-body}}(Q_3) = C_{(p-p)-\Lambda}(Q_3) + 2 C_{p-(p-\Lambda)}(Q_3) - 2. \quad (3.5)$$

The correlation functions on the right-hand side of these equations can either be obtained with the data-driven method or the projector method, as explained in Chapter 1.6.3. These correlation functions, obtained using the data-driven method, were already shown in Fig. 3.8. The projector method allows estimating these functions

by calculating the following integral

$$C_{ij}(Q_3) = \int C(k_{ij}^*) W_{ijl}(k_{ij}^*, Q_3) dk_{ij}^*, \quad (3.6)$$

where  $W_{ijl}(k_{ij}^*, Q_3)$  is the projector function, described in detail in Chapter 1.6.4, which depends on the masses of the  $i, j, l$  particles, and  $C(k_{ij}^*)$  is the correlation function for  $i - j$  particle pair.

To estimate the (p-p)-p and (p-p)- $\Lambda$  correlation functions, the p-p correlation function is required, and it can be evaluated theoretically or experimentally. However, we aim to subtract the projected correlation functions from the measured three-body correlation function. This requires the projector method to account for the momentum resolution of the ALICE detector and to have the same feed-down and misidentification contributions. The most straightforward way is to use the measured two-body correlation functions, which already include all possible effects. In this work, we use the correlation function published by ALICE in Ref. [37] and shown in the upper sub-figure of Fig. 3.9. This p-p study used the same data set analysed in this thesis. The measured p-p correlation function was modelled using CATS taking into account the Coulomb and the strong interactions and the quantum statistics. The Argonne  $v_{18}$  [18] potential in S, P and D waves was used as input for the strong interaction component. The Argonne  $v_{18}$  potential is well constrained by the abundant N-N scattering data; thus, it is expected that the modelled correlation function should also reproduce the femtoscopic data well. The measured correlation function shows the attractive nature of the p-p strong interaction with a repulsive core visible in the inset of the discussed figure. At a low  $k^*$  region, the Coulomb repulsion and Pauli blocking become apparent. Indeed, a good agreement between the data and the model was observed, as expected.

To estimate the p-(p- $\Lambda$ ) correlation function using the projector method, the measured p- $\Lambda$  correlation function is required. In this work, we use the correlation function published by ALICE in Ref. [35] and shown in the lower sub-figure

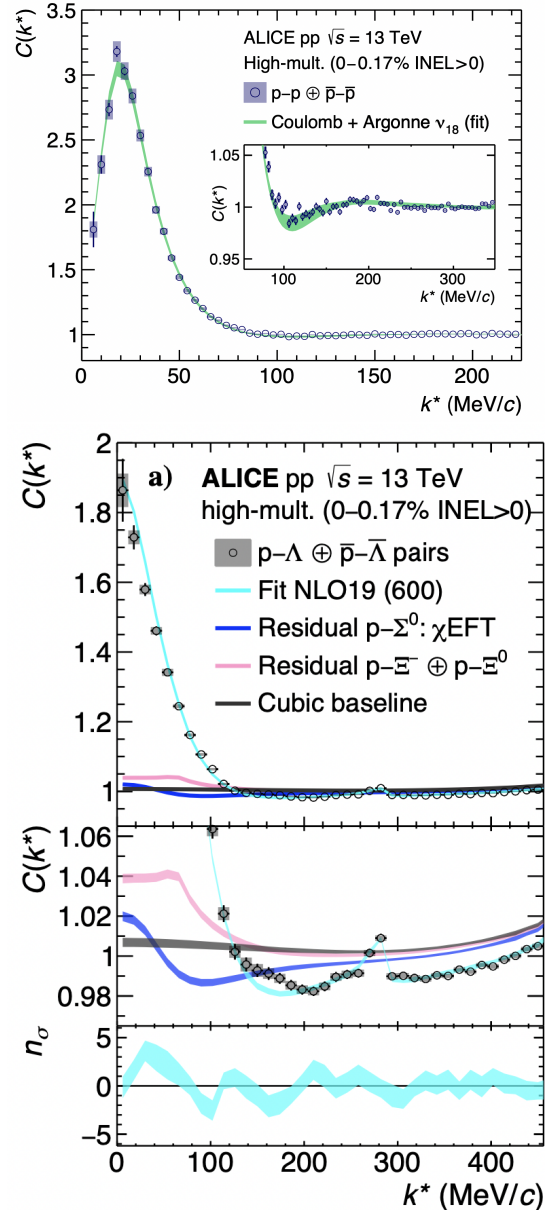


FIGURE 3.9: Two-body correlation functions for p-p [37] and p- $\Lambda$  [35] system.

of Fig. 3.9. The p– $\Lambda$  system was modelled employing CATS, and the NLO19  $\chi$ EFT potential [25] obtained with a cut-off parameter of 600 MeV.<sup>2</sup> Such a state-of-the-art p– $\Lambda$  potential has been successfully used to reproduce the available scattering data and the hypernuclei measurements. The measured correlation function shows the attractive nature of the strong interaction of the p– $\Lambda$ . As  $\Lambda$  hyperon has no electric charge, the Coulomb interaction is absent in the system. This correlation function represents the first experimental observation of the  $N\Sigma \rightarrow N\Lambda$  coupled channel in p– $\Lambda$  system and is the most precise data of p– $\Lambda$  system down to zero momentum. The theoretical correlation function, shown in the lower sub-figure of Fig. 3.9 as a cyan band, was obtained by employing the  $\chi$ EFT to describe also the p– $\Sigma^0$  strong interaction. The total agreement between the modelled correlation function and the data was estimated to be  $3.7\sigma$ . If negligible FSI are assumed for the p– $\Sigma^0$  system, the agreement improves to  $1.6\sigma$ .

Once these measured two-body correlation functions are inserted in Eqs. 3.4 and 3.5, the lower-order contributions  $C_{ij}(Q_3)$  can be evaluated. The obtained results are shown in Fig. 3.10 (grey band) together with the lower order contributions obtained using the data-driven method (green points), which were already shown in Fig. 3.8. The width of the grey band includes systematic and statistical uncertainties summed in quadrature. The lower panels of sub-figures a, b and c show the deviations between the data-driven approach and the projector method, expressed as a number of standard deviations  $n_\sigma$ . In the case of all three correlation functions (p–p)–p, (p–p)– $\Lambda$  and p–(p– $\Lambda$ ), an excellent agreement is observed between the two methods. To provide a statistical significance of the agreement in terms of Gaussian standard deviations  $\sigma$ , the p-value probability  $p_{val}$  is required as

$$n\sigma = \sqrt{2} \operatorname{erfc}^{-1}(p_{val}). \quad (3.7)$$

Here, the p-value probability corresponds to the integral of the Gaussian distribution's right and left side tails. The p-value for a specific  $\chi_N^2$  is calculated from the  $\chi^2$  distribution with  $N$  degrees of freedom, where  $\chi_N^2$  is obtained using the standard  $\chi^2$  method

$$\chi_N^2 = \sum_{i=1}^N \frac{(C_i^{\text{data-driven}} - C_i^{\text{projector}})^2}{\sigma_i^2}. \quad (3.8)$$

Here,  $C_i^{\text{data-driven}}$  and  $C_i^{\text{projector}}$  are the correlation function values in the  $i$ -th bin obtained using the data-driven and the projector methods, respectively. The total combined uncertainty is denoted as  $\sigma_i^2$ .

We evaluated the agreement of the data-driven and the projector methods in the region  $Q_3 < 0.8 \text{ GeV}/c$  and expressed it as the number  $n$  of standard deviations  $\sigma$ . It results in 0.167, 0.0006 and 2.75 for (p–p)–p, (p–p)– $\Lambda$  and p–(p– $\Lambda$ ), respectively. For the first time, the projector method was validated with data. While both methods are valid, the projector method provides smaller statistical uncertainties. The data-driven method requires the usage of the third particle in the triplet from the mixed-event data sample. Thus, the obtained statistical uncertainty depends on the number of events used for mixing, which is limited due to the needed computational resources. The projector method does not have this limitation as the projection to a three-body system is performed by evaluating the density of states in phase space

---

<sup>2</sup>Cut-off value in  $\chi$ EFT [25] is a parameter in an exponential regulator function used to remove high-momentum components in the calculation of the potential.

within the volume  $(k_{ij}, k_{ij} + dk_{ij})$  for a fixed value of  $Q_3$  (for more details see Eq. 1.44).

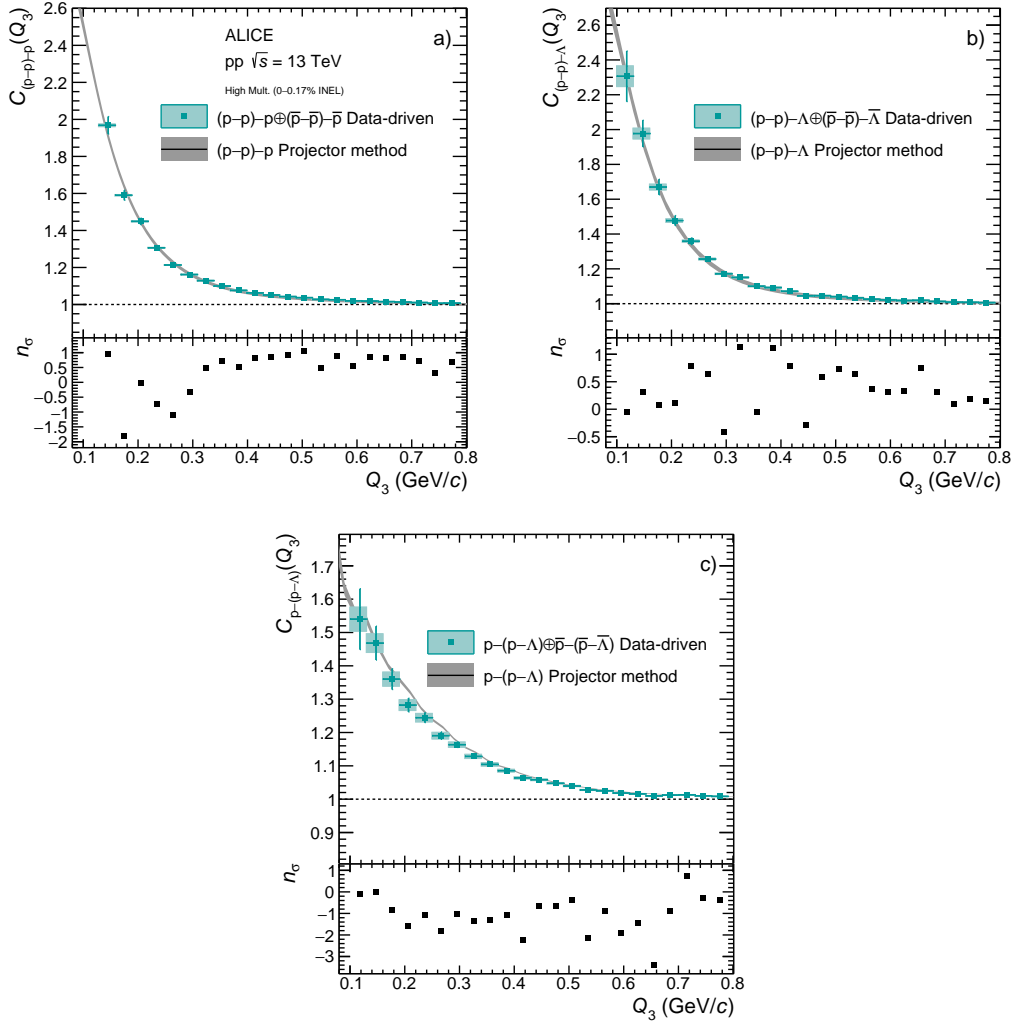


FIGURE 3.10: Comparison of lower-order correlation functions obtained using the data-driven method (green markers) and the projector method (grey band). For details, refer to the text.

Finally, Eq. 3.3 can be used to obtain the total lower-order contributions to the  $p-p-p$  and  $p-p-\Lambda$  correlations functions. The obtained results are shown in Fig. 3.11. The projector prediction agrees with the data-driven method within  $n_\sigma = 0.167$  and  $n_\sigma = 0.0014$  for the  $p-p-p$  and  $p-p-\Lambda$  lower-order contributions, respectively.

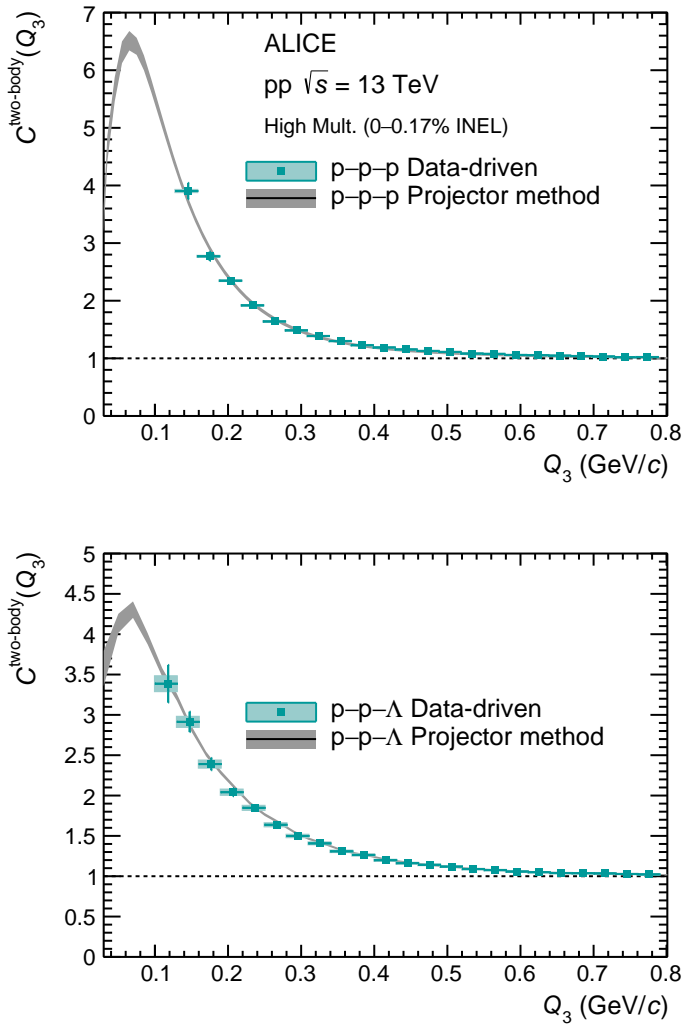


FIGURE 3.11: Comparison of total lower-order correlation functions obtained using the data-driven method (green markers) and the projector method (grey band). For details, refer to the text.

### Lower-order contributions for $p-p-\bar{p}$ system

As a cross-check to the  $p-p-p$  system, the  $p-p-\bar{p}$  triplets were studied by performing identical analysis steps as in the case of  $p-p-p$ . However, to interpret the data, the lower-order contributions ( $p-p-\bar{p}$  and  $p-(p-\bar{p})$ ) must also be estimated. This was done with both the data-driven and the projector methods. In the case of the projector method for  $(p-p-\bar{p})$  triplets, the same two-body correlation function is used as for  $(p-p)-p$  and  $(p-p)-\Lambda$  [37]. To evaluate the  $p-(p-\bar{p})$  contribution, the two-body  $p-\bar{p}$  correlation function measured by ALICE [41] and shown in Fig. 3.12 was used. The measured baryon-antibaryon correlation function is different with respect to the before-presented baryon-baryon correlation functions, as the minijet effect dominates the background component. As mentioned in Chapter 2.4, such minijet effects can be accounted for using event generators as they model the underlying event. In the case of the  $p-\bar{p}$  correlation function, an improved data-driven approach to describe this background has been developed in Ref. [41] employing event generator predictions as templates for the mini-jets background.

The resulting background is shown as a grey band in Fig. 3.12. The correlation function was evaluated by employing CATS with  $\chi$ EFT N<sup>3</sup>LO potential accounting for Coulomb interaction and including explicitly the coupled-channel process  $n - \bar{n} \rightarrow p - \bar{p}$  [146]. The obtained correlation function is shown as a blue band in Fig. 3.12. The disagreement with data at low  $k^*$  suggests that part of the annihilation dynamics is not properly accounted for in the model. This is not unexpected as there was no data at the low relative momentum before the femtoscopic measurement to constrain these interactions. Indeed, by considering in an effective way also the multi-meson annihilation channels produced as an initial state and forming  $p - \bar{p}$  pairs (red band) significantly reduces the disagreement.

The  $p - (p - \bar{p})$  correlation function was evaluated using the projector method, and the abovementioned  $p - \bar{p}$  correlation function, however, an apparent disagreement with the data-driven method was observed. This leads us to believe that the minijets are causing some deformations of the phase space that are not correctly accounted for in the projector method. To solve this problem, we re-evaluated the  $p - \bar{p}$  correlation function and required that only particle pairs emitted in  $p - p - \bar{p}$  triplets with  $Q_3 < 1 \text{ GeV}/c$  are used, which is shown in Fig. 3.13 as black markers. The shape is slightly different compared to the correlation function obtained without the special requirement (red markers). The systematic uncertainties were evaluated following the procedure described in Chapter 3.3 and additionally including the variation of the  $Q_3$  cut-off value by  $\pm 10\%$ .

Coming back to the three-body femtoscopy, the lower-order contributions in  $p - p - \bar{p}$  system estimate with the data-driven method are shown in Fig. 3.14 as green markers. The grey band represents the correlation function evaluated employing the projector method. The left panel shows results for the  $(p - p) - \bar{p}$  triplets. As the projector function depends only on the mass of the third particle, it produces the same result for  $(p - p) - \bar{p}$  and  $(p - p) - p$  correlation functions which are as well

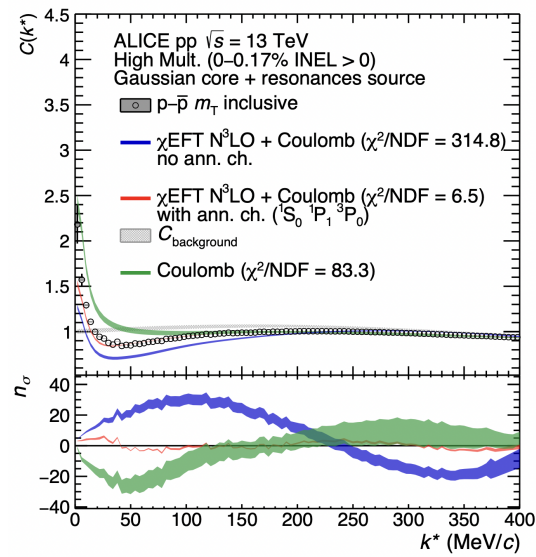


FIGURE 3.12: Two-body correlation function for  $p - \bar{p}$  [41] system.

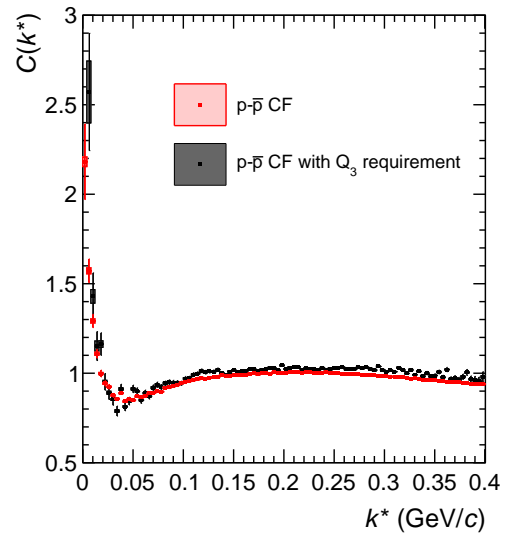


FIGURE 3.13:  $p - \bar{p}$  correlation function using only pairs which were produced in  $p - p - \bar{p}$  triplets at  $Q_3 < 1 \text{ GeV}/c$  (black markers) and all pairs (red markers).

in agreement with observations from the data. This is the case because the third particle is only a spectator. On the right panel, the correlation functions for  $p-(p-\bar{p})$  triplet are shown. The interesting shape of the  $p-(p-\bar{p})$  correlation function is caused by the interplay of the FSIs and the minijet effects.

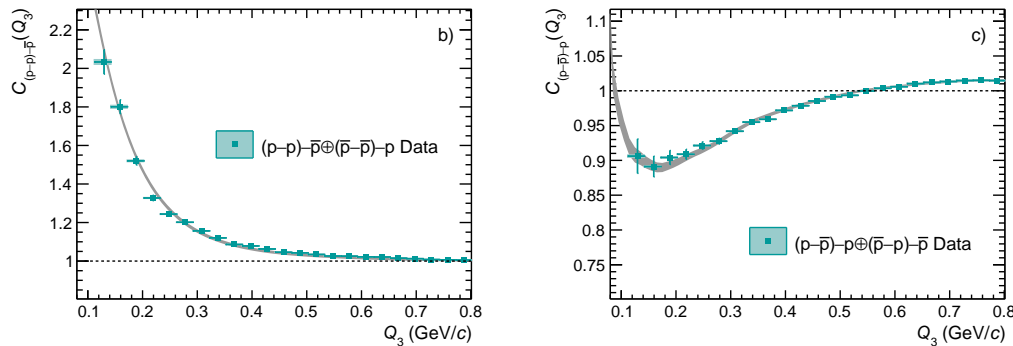


FIGURE 3.14: Comparison of lower-order  $(p-p)\bar{p}$  (left) and  $p-(p\bar{p})$  (right) correlation functions obtained using the data-driven method (green markers) and the projector method (grey band). For details, refer to the text.

### 3.6 Three-particle correlation functions and the total lower order contributions

The measured three-particle correlation functions (green markers) are compared to the lower order contributions (grey band) in Fig. 3.15. The grey band corresponds to the statistical and systematic uncertainties added in the quadrature. The green boxes correspond to the systematic uncertainty of measured correlation functions, while the green vertical lines correspond to the statistical uncertainty. The  $p-p-p$  correlation function, shown in the upper panel, can be well explained by the lower order contributions down to  $Q_3 \approx 0.25$  GeV/c. The lower-order contributions keep increasing at the lower kinematic region while the measured three-particle correlation function drops. In the case of the  $p-p-\Lambda$  system (middle panel), only the first two bins deviate from the lower-order contributions. However, the statistical uncertainties are too significant to draw any conclusion on the genuine three-body effects. Even though the  $p-p-\bar{p}$  correlation function depicted in the lower panel of Fig. 3.15 has systematically smaller values than the estimated lower-order contributions, they agree within uncertainties. The difference between the measured correlation function and the lower-order contributions results in the cumulant. Thus the deviation between the three-body correlations and the lower-order contributions for all three measured systems are discussed more quantitatively in Chapter 3.8.1, where the cumulants are presented.

The results shown here for both the projector and the data are not corrected for the misidentified particles and feed-down. It is shown in the next Chapter that this correction can be done on the level of cumulants. However, if the three-particle correlation function has to be compared to models, then either the theoretical calculations or the data must be corrected.

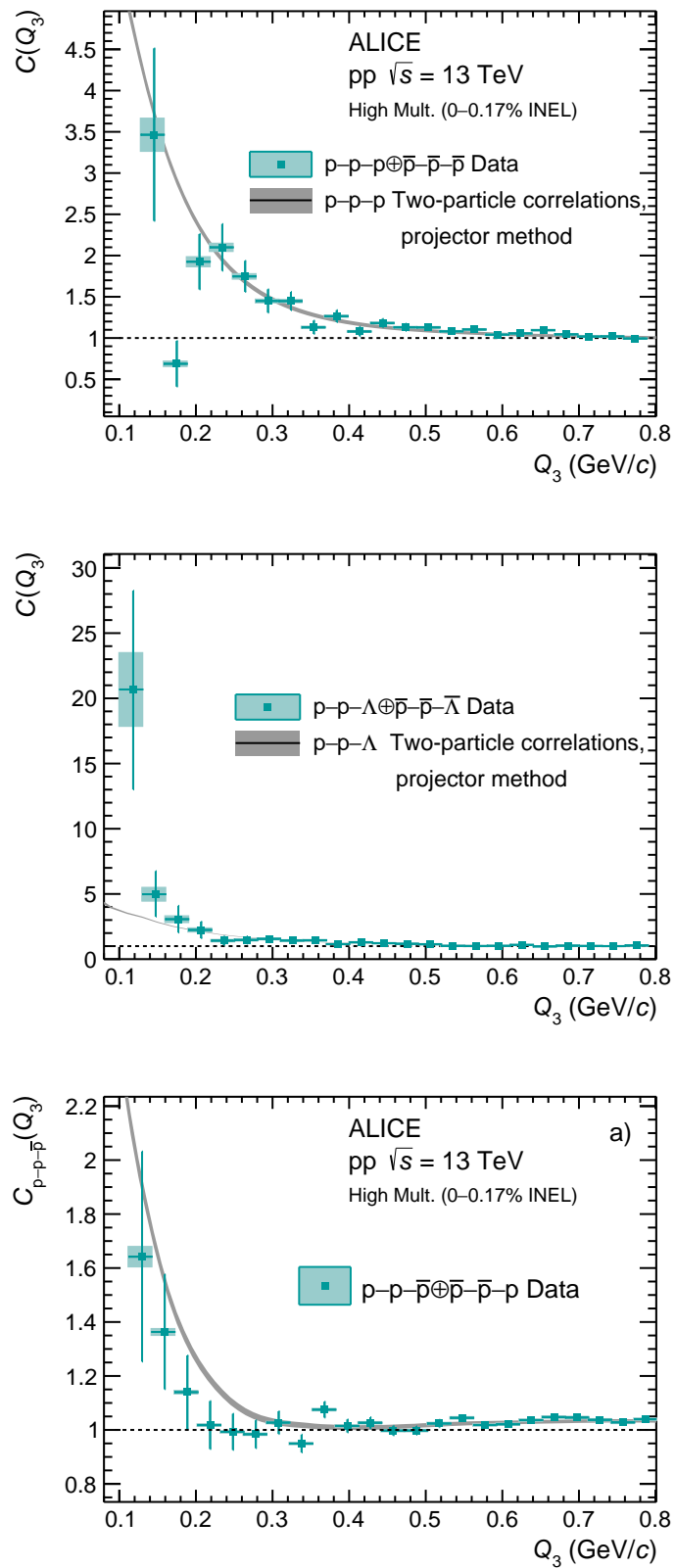


FIGURE 3.15: Measured p-p-p (upper panel), p-p- $\Lambda$  (middle panel) and p-p- $\bar{p}$  (lower panel) three-particle correlation functions.

### 3.7 Correction for misidentified particles and feed-down

The misidentified and non-primary particles are present in the sample and affect the correlation shape. Thus before comparing the measured correlation functions to theory, the corrections for such effects must be performed. The tagging of misidentified particles and feed-down correction are well-understood procedures in femtoscopy. The employed methods were suggested for the first time in Ref. [34]. Inspired by this work, we derived the corresponding procedure for three-particle correlation functions and cumulants [144].

The particle sample  $X$  used to form triplets consists of correctly identified primary particles  $X_0$ , misidentified particles  $X_M$  and feed-down particles  $X_F$  originating from weakly decaying hadrons. The latter two can originate from different channels as

$$X_F = \sum_{i=1}^{N_F} X_i, \quad (3.9)$$

$$X_M = \sum_{i=N_F+1}^{N_F+N_M} X_i, \quad (3.10)$$

where  $N_F$  and  $N_M$  are the numbers of feed-down and misidentification contributions. The fraction of correctly identified particles in the total sample of reconstructed particles is called purity and is defined as

$$\mathcal{P}(X) = (X_0 + X_F) / X. \quad (3.11)$$

The correctly identified particles can be either primary or secondary particles produced in weak decays of different hyperons. For this purpose we define the channel fraction  $f(X_i)$  as

$$f(X_i) = X_i / (X_0 + X_F). \quad (3.12)$$

The fraction of particles from origin  $i$  in the whole data sample can then be written as

$$P(X_i) = \mathcal{P}(X_i) f(X_i) = \frac{X_i}{X}. \quad (3.13)$$

The correlation function for three particles can then be expressed as

$$C(XYZ) = \frac{N(XYZ)}{M(XYZ)}, \quad (3.14)$$

where  $N$  and  $M$  denotes the yields of  $XYZ$  triplets in same and mixed events, respectively. These yields can be written as

$$N(XYZ) = N \left( \sum_{i,j,k} X_i Y_j Z_k \right) = \sum_{i,j,k} N(X_i Y_j Z_k), \quad (3.15)$$

$$M(XYZ) = M \left( \sum_{i,j,k} X_i Y_j Y_k \right) = \sum_{i,j,k} M(X_i Y_j Z_k), \quad (3.16)$$

where  $i, j, k$  denotes the channel of origin of the particles. The correlation function thus becomes

$$\begin{aligned} C(XYZ) &= \frac{\sum_{i,j,k} N(X_i Y_j Z_k)}{M(XYZ)} = \sum_{i,j,k} \frac{N(X_i Y_j Z_k)}{M(XYZ)} \frac{M(X_i Y_j Z_k)}{M(X_i Y_j Z_k)} = \\ &= \sum_{i,j,k} \underbrace{\frac{N(X_i Y_j Z_k)}{M(X_i Y_j Z_k)}}_{C_{i,j,k}(XYZ)} \underbrace{\frac{M(X_i Y_j Z_k)}{M(XYZ)}}_{\lambda_{i,j,k}(XYZ)} = \sum_{i,j,k} \lambda_{i,j,k}(XYZ) C_{i,j,k}(XYZ), \end{aligned} \quad (3.17)$$

where  $C_{i,j,k}(XYZ)$  is the correlation function of particles  $X, Y, Z$  stemming from  $i, j, k$  channels, accordingly, and the  $\lambda_{i,j,k}(XYZ)$  is the weight for such contribution. Because this parameter depends only on the mixed event sample, it can be related to previously introduced single-particle quantities, channel fraction and purity, as follows

$$\begin{aligned} \lambda_{i,j,k}(XYZ) &= \frac{M(X_i Y_j Z_k)}{M(XYZ)} \\ &= \frac{M(X_i)}{M(X)} \frac{M(Y_j)}{M(Y)} \frac{M(Z_k)}{M(Z)} = P(X_i) P(Y_j) P(Z_k) \\ &= \mathcal{P}(X_i) f(X_i) \mathcal{P}(Y_j) f(Y_j) \mathcal{P}(Z_k) f(Z_k). \end{aligned} \quad (3.18)$$

The  $\Lambda$  parameters have been estimated for the triplets of interest from the single particle quantities provided in Chapter 2.5 and are shown in Table 3.3. In the case of the correlation function  $C(XY, Z)$ , where only particles  $X$  and  $Y$  interact and particle  $Z$  is just a spectator, the latter's origin is irrelevant. Thus, similarly to Eq. 3.17, such correlation function can be expressed as

$$\begin{aligned} C(XY, Z) &= \frac{\sum_{i,j} N(X_i Y_j, Z)}{M(XY, Z)} = \sum_{i,j} \frac{N(X_i Y_j, Z)}{M(XY, Z)} \frac{M(X_i Y_j, Z)}{M(X_i Y_j, Z)} = \\ &= \sum_{i,j} \underbrace{\frac{N(X_i Y_j, Z)}{M(X_i Y_j, Z)}}_{C_{i,j}(XY, Z)} \underbrace{\frac{M(X_i Y_j, Z)}{M(XY, Z)}}_{\lambda_{i,j}(XY, Z)} = \sum_{i,j} \lambda_{i,j}(XY, Z) C_{i,j}(XY, Z), \end{aligned} \quad (3.19)$$

where  $C_{i,j}(XY, Z)$  is the correlation function of two correlated particles  $X$  and  $Y$  from origins  $i$  and  $j$ , respectively, and an uncorrelated particle  $Z$  from any origin. Here  $\lambda_{i,j}(XY, Z)$  is

$$\begin{aligned} \lambda_{i,j}(XY, Z) &= \frac{M(X_i Y_j, Z)}{M(XY, Z)} \\ &= \frac{M(X_i)}{M(X)} \frac{M(Y_j)}{M(Y)} \frac{M(Z)}{M(Z)} = P(X_i) P(Y_j) \cdot 1 \\ &= \mathcal{P}(X_i) f(X_i) \mathcal{P}(Y_j) f(Y_j). \end{aligned} \quad (3.20)$$

The cumulant is obtained by subtracting the lower-order correlations, such as  $C(XY, Z)$ , from the three-particle correlation  $C(XYZ)$ . For this purpose, the Eq. 3.19 must be rewritten to account for the origin of particle  $Z$ , even though  $C(XY, Z_l) = C(XY, Z_m)$ , where  $Z_l$  and  $Z_m$  are from a different origin. Using the property  $1 = \sum_k \lambda_k(Z)$  of the  $\lambda$  parameters, one can write

Triplet	$\lambda$ parameter	Triplet	$\lambda$ parameter
p-p-p	61.8%	p-p- $\Lambda$	40.5%
3·p-p-p $_{\Lambda}$	19.6%	p-p- $\Lambda_{\Sigma^0}$	13.5%
3·p-p-p $_{\Sigma^+}$	8.5%	p-p- $\Lambda_{\Xi^0}$	7.56%
3·p-p $_{\Lambda}$ -p $_{\Lambda}$	0.69%	p-p- $\Lambda_{\Xi^-}$	7.56%
3·p-p $_{\Lambda}$ -p $_{\Sigma^+}$	0.3%	2·p-p $_{\Lambda}$ - $\Lambda$	8.56%
3·p-p $_{\Sigma^+}$ -p $_{\Sigma^+}$	0.13%	2·p-p $_{\Sigma^+}$ - $\Lambda$	3.7%

TABLE 3.3:  $\lambda$  parameter values for the triplets which contribute the most to the correlation function.

$$\lambda_{i,j}(XY, Z) = \lambda_{i,j}(XY, Z) \sum_k \lambda_k(Z) = \sum_k \lambda_{i,j}(XY, Z) \lambda_k(Z) = \sum_k \lambda_{i,j,k}(XYZ), \quad (3.21)$$

and Eq. 3.19 can be rewritten as

$$\begin{aligned} C(XY, Z) &= \sum_{i,j} \lambda_{i,j}(XY, Z) C_{i,j}(XY, Z) \\ &= \sum_{i,j} \lambda_{i,j}(XY, Z) \sum_k \lambda_k(Z) C_{i,j}(XY, Z) \\ &= \sum_{i,j} \sum_k \lambda_{i,j}(XY, Z) \lambda_k(Z) C_{i,j}(XY, Z) \\ &= \sum_{i,j,k} \lambda_{i,j,k}(XYZ) C_{i,j}(XY, Z). \end{aligned} \quad (3.22)$$

Employing the above-defined formalism, one can express cumulant as

$$\begin{aligned} c(XYZ) &= C(XYZ) - C(XY, Z) - C(XZ, Y) - C(ZY, X) + 2 \\ &= \sum_{i,j,k} \lambda_{i,j,k}(XYZ) C_{i,j,k}(XYZ) - \sum_{i,j,k} \lambda_{i,j,k}(XYZ) C_{i,j}(XY, Z) \\ &\quad - \sum_{i,j,k} \lambda_{i,j,k}(XYZ) C_{i,k}(XZ, Y) - \sum_{i,j,k} \lambda_{i,j,k}(XYZ) C_{k,j}(ZY, X) + 2, \end{aligned} \quad (3.23)$$

the correctly identified primary particle correlations can be isolated from the rest as follows

$$\begin{aligned} c(XYZ) &= \left( \lambda_{X_0 Y_0 Z_0}(XYZ) C_{X_0 Y_0 Z_0}(XYZ) + \sum_{i,j,k \neq (X_0 Y_0 Z_0)} \lambda_{i,j,k}(XYZ) C_{i,j,k}(XYZ) \right) \\ &\quad - \left( \lambda_{X_0 Y_0 Z_0}(XY, Z) C_{X_0 Y_0}(XY, Z) + \sum_{i,j,k \neq (X_0 Y_0 Z_0)} \lambda_{i,j,k}(XYZ) C_{i,j}(XY, Z) \right) \\ &\quad - \left( \lambda_{X_0 Y_0 Z_0}(XZ, Y) C_{X_0 Z_0}(XZ, Y) + \sum_{i,j,k \neq (X_0 Y_0 Z_0)} \lambda_{i,j,k}(XYZ) C_{i,k}(XZ, Y) \right) \\ &\quad - \left( \lambda_{X_0 Y_0 Z_0}(ZY, X) C_{Z_0 Y_0}(ZY, X) + \sum_{i,j,k \neq (X_0 Y_0 Z_0)} \lambda_{i,j,k}(XYZ) C_{k,j}(ZY, X) \right) + 2. \end{aligned} \quad (3.24)$$

One can rewrite the Eq. 3.24 to group the correlation functions of the correctly identified primary particles and the rest as

$$\begin{aligned}
c(XYZ) &= \lambda_{X_0Y_0Z_0}(XYZ)C_{X_0Y_0Z_0}(XYZ) - \lambda_{X_0Y_0Z_0}(XY, Z)C_{X_0Y_0}(XY, Z) \\
&\quad - \lambda_{X_0Y_0Z_0}(XZ, Y)C_{X_0Z_0}(XZ, Y) - \lambda_{X_0Y_0Z_0}(ZY, X)C_{Z_0Y_0}(ZY, X) \\
&\quad + \sum_{i,j,k \neq (X_0Y_0Z_0)} \lambda_{i,j,k}(XYZ)C_{i,j,k}(XYZ) - \sum_{i,j,k \neq (X_0Y_0Z_0)} \lambda_{i,j,k}(XYZ)C_{i,j}(XY, Z) \\
&\quad - \sum_{i,j,k \neq (X_0Y_0Z_0)} \lambda_{i,j,k}(XYZ)C_{i,k}(XZ, Y) - \sum_{i,j,k \neq (X_0Y_0Z_0)} \lambda_{i,j,k}(XYZ)C_{k,j}(ZY, X) + 2 \\
&= \lambda_{X_0Y_0Z_0}(XYZ)(C_{X_0Y_0Z_0}(XYZ) - C_{X_0Y_0}(XY, Z) - C_{X_0Z_0}(XZ, Y) - C_{Z_0Y_0}(ZY, X)) \\
&\quad + \sum_{i,j,k \neq (X_0Y_0Z_0)} \lambda_{i,j,k}(XYZ)(C_{i,j,k}(XYZ) - C_{i,j}(XY, Z) - C_{i,k}(XZ, Y) - C_{k,j}(ZY, X)) + 2.
\end{aligned} \tag{3.25}$$

The terms inside the brackets resemble a cumulant and the expression becomes

$$\begin{aligned}
c(XYZ) &= \lambda_{X_0Y_0Z_0}(XYZ)c(X_0Y_0Z_0) + \sum_{i,j,k \neq (X_0Y_0Z_0)} \lambda_{i,j,k}(XYZ)c(X_iY_jZ_k) \\
&\quad - 2\lambda_{X_0Y_0Z_0}(XYZ) - 2 \sum_{i,j,k \neq (X_0Y_0Z_0)} \lambda_{i,j,k}(XYZ) + 2 \\
&= \lambda_{X_0Y_0Z_0}(XYZ)c(X_0Y_0Z_0) + \sum_{i,j,k \neq (X_0Y_0Z_0)} \lambda_{i,j,k}(XYZ)c(X_iY_jZ_k) \\
&\quad - 2 \sum_{i,j,k} \lambda_{i,j,k}(XYZ) + 2 \\
&= \lambda_{X_0Y_0Z_0}(XYZ)c(X_0Y_0Z_0) + \sum_{i,j,k \neq (X_0Y_0Z_0)} \lambda_{i,j,k}(XYZ)c(X_iY_jZ_k).
\end{aligned} \tag{3.26}$$

The experimentally obtained cumulant consists of the correctly identified primary particle cumulant and the cumulant, which consists of the rest of the possible contributions. Finally, the correctly identified primary particle cumulant can be obtained as

$$c(X_0Y_0Z_0) = \frac{1}{\lambda_{X_0Y_0Z_0}(XYZ)} \left( c(XYZ) - \sum_{i,j,k \neq (X_0Y_0Z_0)} \lambda_{i,j,k}(XYZ)c(X_iY_jZ_k) \right). \tag{3.27}$$

## 3.8 Three-baryon Correlation Results

### 3.8.1 Results: Cumulants

The cumulants are estimated by subtracting the lower order contributions from the measured three-particle correlation functions as explained in Chapter 1.6.3. The results are shown in Figs. 3.16 and 3.17. The p-p-p cumulant shown in Fig. 3.16 is represented by the blue square symbols, while the red open circles correspond to the p-p- $\bar{p}$  triplets. Both cumulants are corrected for misidentification and feed-down effects following the procedure explained in the previous Chapter. In the case of p-p-p triplets, the most significant feed-down contribution of 19.6% comes from the p-p-p $_\Lambda$  triplets. The procedure of estimating the p-p-p $_\Lambda$  cumulant required in Eq. 3.27 consists of the following steps

1. measuring the p-p- $\Lambda$  cumulant, or estimating it from theory,
2. obtaining a decay matrix from MC, which relates the  $Q_3$  of p-p- $\Lambda$  triplet and the  $Q_3$  of a triplet consisting of the same two primary protons, but the third particle is the  $\Lambda$  daughter p-p-p $_{\Lambda}$ ,
3. performing the convolution of p-p- $\Lambda$  cumulant and the decay matrix to obtain the p-p- $\Lambda$  cumulant projection onto p-p-p $_{\Lambda}$  phase space.

Once this is done, the obtained p-p-p $_{\Lambda}$  cumulant is used in Eq. 3.27, where it is scaled by the corresponding  $\lambda$  parameters, which in this case is 0.196. The same procedure is also required for the other feed-down contributions. The convolution with the decay matrix and the scaling by  $\lambda$  parameter results in a smearing of the original p-p- $\Lambda$  cumulant (such a procedure is described in detail in the next Chapter and the effect of the decay kinematics and  $\lambda$  parameters to the correlation functions are shown in the right panel of Fig. 3.20). While the p-p- $\Lambda$  cumulant was measured in this thesis, other cumulants required for p-p-p background are unknown. The only other cumulant contributing more than 1% is the p-p-p $_{\Sigma^+}$ ; thus, the rest of the contributions can be safely assumed to be flat. In the case of the p-p-p $_{\Sigma^+}$  cumulant, the flat shape assumption is the only reasonable choice in the current status of the field. It is also well justified because, as mentioned before, after the correction for the decay kinematics and the  $\lambda$  parameter, which in this case is 0.085, the cumulant would be strongly smeared. Such effect would be even larger than in p-p-p $_{\Lambda}$  case as the smearing depends on the accessible momentum phase space of the decay products and  $\Sigma^+$  particle is heavier. Regarding the p-p- $\Lambda$  cumulant, our measurement is compatible with zero. Thus in the results shown in Fig. 3.16, the p-p-p $_{\Lambda}$  cumulant is also assumed to be flat and equal to zero. The cumulant is negative in the range

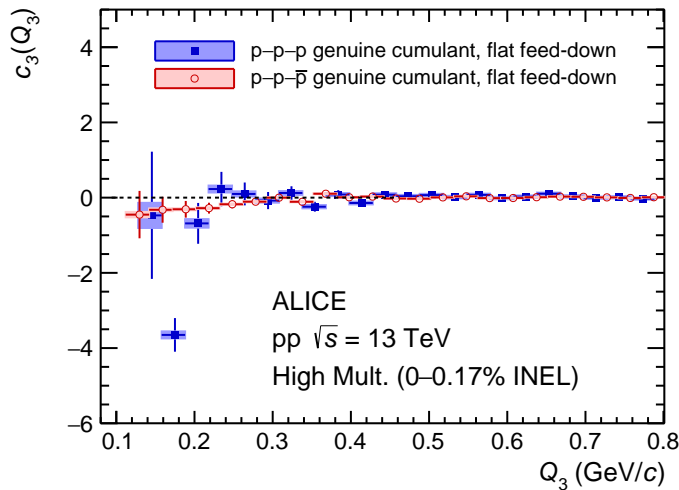


FIGURE 3.16: p-p-p cumulant (blue square symbols), corrected for particle misidentifications and feed-down contributions. The red open circles represent the cumulant for p-p-p $_{\bar{p}}$  triplets.

$0.16 < Q_3 < 0.22$  GeV/c. Due to the large statistical uncertainty in the first bin, the sign for  $Q_3 < 0.16$  GeV/c cannot be determined. The agreement between the measured cumulant and the assumption of no genuine three-body effects is evaluated following the same procedure as in Chapter 3.4, but the numerator of Eq. 3.8 is the difference of the measured cumulant with respect to zero. It is not known,

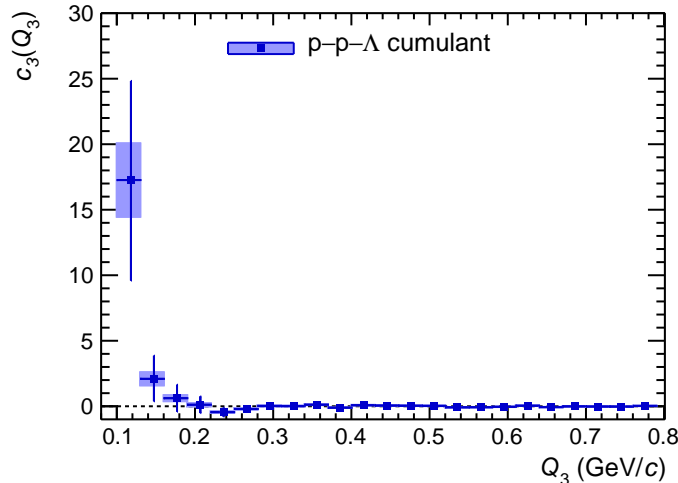


FIGURE 3.17: Measured p-p- $\Lambda$  cumulant, not corrected for particle misidentifications and feed-down contributions.

theoretically or experimentally, in which  $Q_3$  range the three-body effects are relevant; however, they are expected to contribute at lower or equal  $Q_3$  values as the two-body interactions. Thus, the statistical significance is estimated in the region  $Q_3 < 0.4$  GeV/ $c$  (where the two-body interactions are prominent) and is equal to 6.7 standard deviations. We also performed a test assuming that p-p- $\Lambda$  cumulant is not flat and employed a fit function to describe our measured cumulant shown in Fig. 3.17. The genuine p-p-p cumulant was estimated using a bootstrap procedure and the obtained statistical significance is not reduced compared to the flat p-p- $\Lambda$  feed-down assumption. The results do not change if the lower order contributions were estimated with the data-driven method instead of the projector method. The comparison of cumulants obtained with the two different methods is shown in Fig. 3.18, where the results are depicted before the misidentification and feed-down corrections. If the cumulant is obtained using the data-driven method, the statistical significance equals 6.0 standard deviations. The significant deviation hints at the presence of effects beyond the two-body interactions that could be related to Pauli blocking (theoretically accounted for as antisymmetrisation of the wave function explained in Chapter 1.6.2 and the effect for p-p-p system is shown in the upper panel of Fig. 1.19) or to the contribution of the three-body strong repulsive interaction. Long-range Coulomb interactions may also lead to significant contributions [147]. A more quantitative interpretation of the data requires sophisticated calculations for the three-body system. The comparison of the measured correlation function to the preliminary theoretical prediction by Alejandro Kievsky is shown in the next Chapter.

The p-p-p cumulant is also compared to the p-p- $\bar{p}$  cumulant in Fig. 3.16, which is represented by red open circles. For p-p- $\bar{p}$  system, all feed-down cumulants are also assumed to be flat and equal to zero. As shown in Chapter 3.5, two-body p-p and p- $\bar{p}$  interactions are known, and their correlation functions are measured. The p- $\bar{p}$  interaction contains both elastic and inelastic components. The three-body effects in the p-p- $\bar{p}$  triplet are expected to be small. For example, the system does not consist of three identical particles; thus, Pauli blocking is not acting on the three-particle level. The measurement is extended to lower  $Q_3$  values compared to the p-p-p case since the number of the mixed-charge triplets is a factor four higher than

that of the same-charge triplets. The  $p-p-\bar{p}$  cumulant evaluated using the projector method agrees with the assumption of only two-body correlations present in the system within 2.1 standard deviations in the range  $Q_3 < 0.4 \text{ GeV}/c$ . The agreement changes to 2.2 standard deviations if the data-driven approach is employed. If the agreement is tested at  $Q_3 < 0.2 \text{ GeV}/c$ , 0.9 standard deviations are obtained for both data-driven and projector methods, suggesting that genuine three-body effects are not statistically significant.

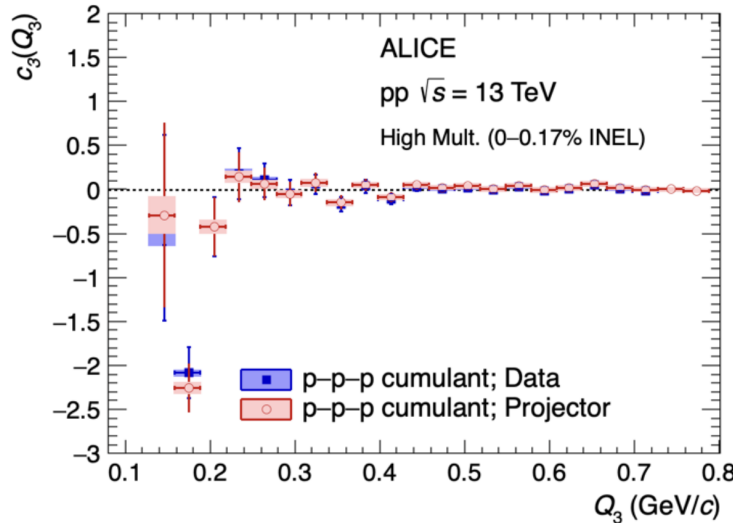


FIGURE 3.18: Comparison of  $p-p-p$  cumulants estimated subtracting lower order contributions obtained employing data-driven (blue) and projector (red) methods.

Finally, Fig. 3.17 shows the  $p-p-\Lambda$  cumulant obtained employing the projector method. The misidentification and feed-down correction is not applied because the feed-down cumulants are unknown and the statistical uncertainties are too large to provide any sensitivity to the three particle correlations. A positive cumulant is measured at  $Q_3 < 0.16 \text{ GeV}/c$ . The comparison to the cumulant obtained using the data-driven approach is shown in Fig. 3.19. For both approaches, the  $p$ -value obtained from the  $\chi^2$  test in the region  $Q_3 < 0.4 \text{ GeV}/c$  corresponds to a deviation of  $0.8 \sigma$  from the assumption of no genuine three-body correlations. The current measurement does not provide any firm conclusion yet on the three-body interaction in the  $p-p-\Lambda$  system. However, this system is of extreme interest. A non-zero cumulant can be directly linked to a strong three-body interaction, as only two particles in the triplet are identical and charged.

Further developments in this field require a larger statistical sample as the events containing three collimated baryons are extremely rare. For this purpose, we developed a dedicated software trigger for the Run 3 data-taking period to ensure that all events containing triplets of interest are triggered and stored for analysis. Chapter 4 introduces the trigger software and shows the performance on Run 3 data acquired in 2022.

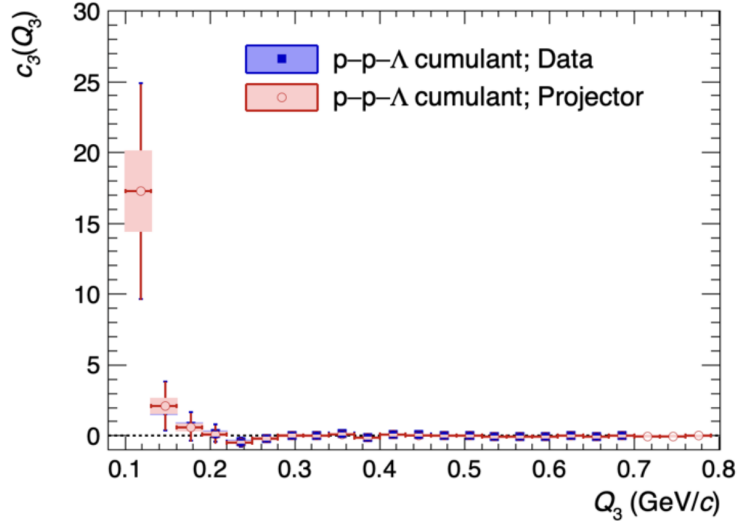


FIGURE 3.19: Comparison of p-p- $\Lambda$  cumulants estimated subtracting lower order contributions obtained employing data-driven (blue) and projector (red) methods.

### 3.8.2 Results: p-p-p correlation function and first theoretical predictions

The negative p-p-p cumulant shows a significant deviation from the assumption of no genuine three-body effect. Comparing our measured correlation function to the theoretical predictions is exciting to see if such an effect could be expected. The preliminary calculations by Alejandro Kievsky were introduced in Chapter 1.6.2. However, before comparing the theoretical correlation function to the experimental one, we must account for the misidentification and feed-down effects in the correlation function. This can be done by employing Eq. 3.17. As the only known three-body correlation function contributing to the feed-down is the p-p- $\Lambda$ , we assume the rest of the contributions to be flat and compatible with one. Similarly to the cumulants, one also needs to estimate a decay matrix which provides information on how to map the  $Q_3$  of the initial p-p- $\Lambda$  to the  $Q_3$  of p-p-p $_{\Lambda}$  where p $_{\Lambda}$  is the daughter from  $\Lambda$  decay. The *TGenPhaseSpace* is used in the ROOT package to estimate the decay phase space. In a Toy Monte Carlo, particles are simulated with the correct mass and momentum sampled from a Gaussian distribution (any distribution can be used here, as it changes only how many particles are generated for specific  $Q_3$  value of p-p- $\Lambda$  triplet, not how the  $Q_3$  transforms after the decay). The  $Q_3$  of p-p- $\Lambda$  triplet is calculated and then the  $\Lambda$  particle is used in *TGenPhaseSpace* to obtain the momentum of a proton from the decay and, finally, the  $Q_3$  is recalculated using the two initial primary protons and the proton from decay as a third particle. The resulting decay matrix is shown in the left panel of Fig. 3.20. The x-axis shows  $Q_3$  for the p-p- $\Lambda$  triplet and the y-axis -  $Q_3$  of the p-p-p $_{\Lambda}$ . The final p-p-p $_{\Lambda}$  correlation function is obtained by performing a convolution of the p-p- $\Lambda$  correlation function and the shown decay matrix. Due to the significant uncertainties of the measured p-p- $\Lambda$  correlation function and the fact that the cumulant is compatible with zero, for this study, we take advantage of the projector method and use the lower-order contributions instead of the measured p-p- $\Lambda$  correlation function. The right panel of Fig. 3.20 shows the assumed p-p- $\Lambda$  correlation function as a grey band. The red line shows the resulting p-p-p $_{\Lambda}$  correlation function once the p-p- $\Lambda$  correlation function is convoluted with the decay matrix. The uncertainties

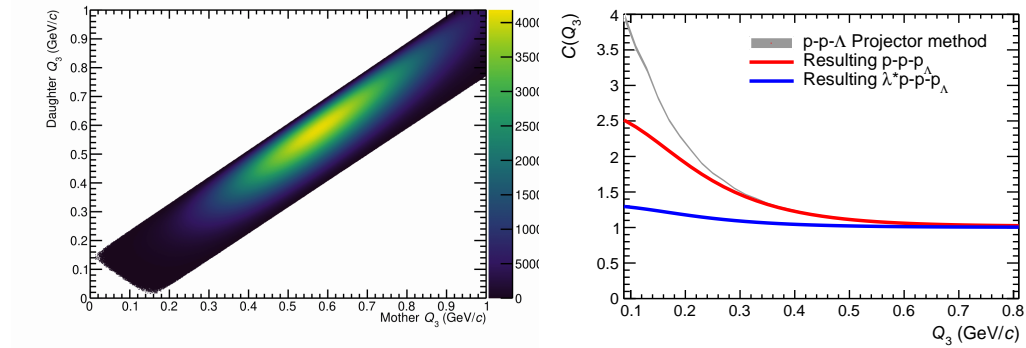


FIGURE 3.20: Left: Decay matrix for  $\Lambda$  particle decaying into  $p\pi^-$ . Right: *preliminary*  $p-p-p_\Lambda$  correlation function (red) obtained by performing a convolution of  $p-p-\Lambda$  correlation function (grey) and the decay matrix. The blue line depicts the  $p-p-p_\Lambda$  correlation function scaled by the corresponding  $\lambda$  parameter.

from the  $p-p-\Lambda$  correlation function are not propagated here, as they are negligible compared to the  $p-p-p$  correlation function uncertainties. Finally, the blue line corresponds to the  $p-p-p_\Lambda$  correlation function scaled by the corresponding  $\lambda$  parameter. As mentioned, the correlation function becomes strongly smeared as we account for the decay kinematics and scale it by the corresponding  $\lambda$  parameter. The obtained  $p-p-p_\Lambda$  correlation function is then used to correct the theoretical  $p-p-p$  correlation function shown in Chapter 1.6.2 to include the feed-down contributions following Eq. 3.17. This is necessary, as the measured correlation function always includes such feed-down effects. The corrected theoretical correlation functions are shown in Fig. 3.21 as a black line for a source size of 1.5 fm (left panel) and 2.0 fm (right panel) together with measurement results (green squares) and lower-order contributions estimated employing projector method (grey band).

The most crucial difference between the lower-order contributions and the theoretical prediction is that the latter accounts for the antisymmetrisation required to describe a wave function of a three-fermion system correctly.

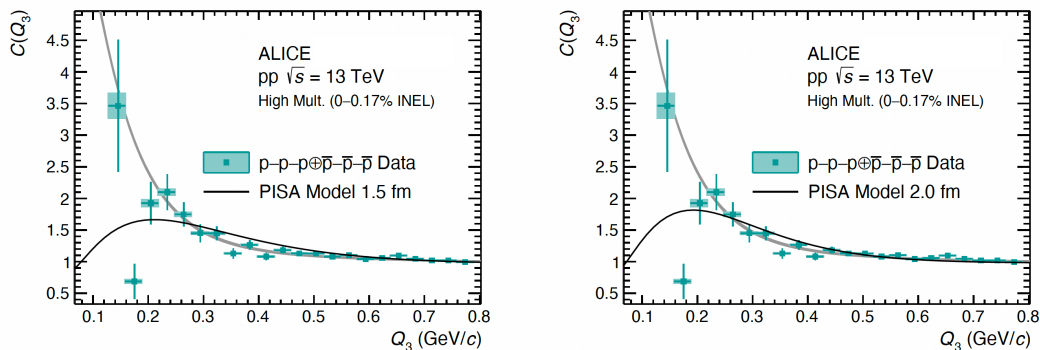


FIGURE 3.21: Measured  $p-p-p$  correlation function (green squares) compared to theoretical predictions (black line) assuming a source size of 1.5 fm (left panel) and 2.0 fm (right panel). The grey band shows lower-order contributions estimated with the projector method.

This results in the correlation function values decreasing at a low  $Q_3$  region compared to the steep increase suggested by the projector method. However, there is still a non-negligible difference between data and the theoretical prediction at the low  $Q_3 < 0.2 \text{ GeV}/c$  region (also at larger  $Q_3$ ). As mentioned in Chapter 1.6.2, these theoretical correlation functions are preliminary and have the following short-comings: approximate three-body Coulomb interaction, the strong two-body interaction is included only in the lowest channels and the assumed potential is not realistic (but it is fitted to reproduce the known p-p scattering length and effective range), the three-body potential is not included. However, these are the state-of-the-art predictions currently available in the field. Although they cannot yet be compared quantitatively, it provides a qualitative description of the three-proton correlation function. The statistical significance of the deviation between the theoretical and measured correlation functions at  $Q_3 < 0.4 \text{ GeV}/c$  is larger than for the projector method as the theoretical curve cannot precisely describe the correlation function at  $Q_3$  larger than  $0.3 \text{ GeV}/c$ . The statistical significance for source size 1.5 fm is 16 standard deviations and for 2 fm - 14 standard deviations. The sizeable statistical significance of the deviation comes from the higher  $Q_3$  bins, where the measured correlation function has small uncertainties, but the PISA model cannot reproduce the shape well. Further improvements in the theoretical calculations are required for a quantitative interpretation of the data.

## Chapter 4

# Offline three-body triggers for Run 3

The successful upgrades of the LHC and the ALICE detector resulted in the maximum 1 MHz interaction rate and 500 kHz readout rate for the pp collisions at  $\sqrt{s} = 13.6$  TeV. As the total recorded data sample of Pb-Pb and pp collisions will exceed the available storage size, the number of pp collisions to be stored must be reduced by a factor of 1000 [148]. The pp events will be selected based on fully reconstructed data by so-called offline software triggers, which will look for events containing specific physics case - high- $p_T$  jets, multi-strangeness hyperons, high-multiplicity events and others. The triggers for different physics observables must lead to a reduction factor of 10000. As shown in the previous Chapter, finding three collimated baryons in a collision is extremely rare. Thus the measurements of three-baryon correlation functions require a very large statistical sample which can be achieved in Run 3 by such custom triggers. The three-baryon interactions can also be studied in baryon-deuteron systems as a deuteron is a composite object made of proton and neutron. Indeed, it has been shown recently that a proton-deuteron correlation function can be described theoretically only if a three-nucleon wave function is used. Thus, to study the three-baryon interactions with Run 3 data, we developed four three-body triggers (ppp, pp $\Lambda$ , p $\Lambda\Lambda$ ,  $\Lambda\Lambda\Lambda$ ) and two two-body triggers, including deuteron in the pair (pd and  $\Lambda$ d). Only the three-body triggers are shown in this thesis, as they were developed by me and are directly related to the analysis presented in this thesis. Moreover, the results are concentrated on the ppp trigger, which serves as a benchmark, and the pp $\Lambda$  trigger, as the three-body pp $\Lambda$  interactions are highly relevant for the hyperon puzzle in neutron stars.

### 4.1 Number of triplets expected in Run 3

All triggers will run on the events recorded during the continuous data-taking, corresponding to a minimum bias sample. Around  $1.25 \cdot 10^{13}$  events are expected to be stored for the asynchronous reconstruction and triggering. The initial plan is to run several asynchronous reconstruction passes and once good quality is reached, the triggering takes place. Events which are not triggered as interesting are then deleted. Thus the full  $1.25 \cdot 10^{13}$  event data sample will never be accessible at once.

The HM trigger in Run 3 will reduce the number of events by a factor of 10000 which corresponds to a  $200 \text{ pb}^{-1}$  data sample ( $\approx 2 \cdot 10^9$  events). This trigger is a good candidate for the three-body analysis, as in Run 2, there was an enhancement of around a factor 20 observed in the number of triplets per event in HM

events compared to MB events (at  $Q_3 < 0.6 \text{ GeV}/c$ ). However, developing a custom three-body trigger that would analyse the entire  $1.25 \cdot 10^{13}$  event data sample and select all events with triplets at low  $Q_3$  region might be more efficient. Thus we estimate the number of expected triplets in Run 3 for both triggers. The estimations are approximate and assume that acceptance and efficiency of the detector remain the same in Run 3 as they were in Run 2.

The number of triplets in the HM sample expected in Run 3 can be estimated based on Run 2 data. Figure 4.1 shows an extrapolated charged particle multiplicity distribution for Run 3 based on Run 2 data. As noted in Ref. [148], this is an extrapolation and thus should be seen only as an educated guess. The HM trigger in Run 3 is going to accept only events with multiplicity higher than  $7 < N_{ch} >$ , where  $< N_{ch} >$  is the average charged-particle multiplicity of a pp event. The estimated number of events for different multiplicity classes for pp collisions at  $\sqrt{s} = 14 \text{ TeV}$  are shown in Table 4.1. To estimate how many triplets can be expected in these events, the number of p-p- $\Lambda$  triplets per event was estimated in Run 2 data as a function of multiplicity. This is shown by the black circles in Fig. 4.2. Only triplets fulfilling  $Q_3 < 0.6 \text{ GeV}/c$  requirement are included. The vertical line cor-

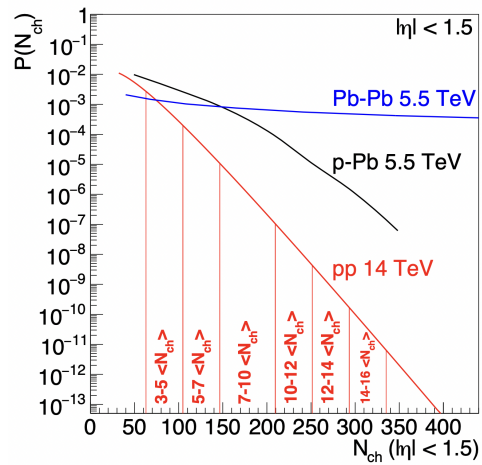


FIGURE 4.1: Extrapolated multiplicity distribution in Run 3 for  $|\eta| < 1.5$  [148].

Range	Events in $200 \text{ pb}^{-1}$
$7 - 10 \langle N_{ch} \rangle$	$2.0 \times 10^9$
$10 - 12 \langle N_{ch} \rangle$	$1.8 \times 10^7$
$12 - 14 \langle N_{ch} \rangle$	$7.3 \times 10^5$
$14 - 16 \langle N_{ch} \rangle$	$2.8 \times 10^4$

TABLE 4.1: High-multiplicity event bins with the expected number of events in Run 3. Taken from Ref. [149]

responds to statistical uncertainty. The red line corresponds to a second-order polynomial function fitted to the data, which allows us to estimate the expected number of triplets per event at multiplicities which will be reached at Run 3. Here, the  $N_{ch}$  is set to 11.5. The number of triplets is obtained by taking the expected number from the polynomial fit and multiplying it by the expected number of events. This results in 24261 triplets at region  $Q_3 < 0.6 \text{ GeV}/c$ . In the Run 2 HM data sample, only 3558 triplets were found at the same  $Q_3$  region. Thus an increase by a factor of 6.8 is expected in the number of p-p- $\Lambda$  triplets at this low  $Q_3$  region. An improvement of around a factor of 7 is also expected in the case of p-p-p and p- $\Lambda$ - $\Lambda$  triplets. These estimates are obtained assuming the ALICE detector in Run 3 will have the same acceptance and efficiency. Estimating the number of triplets for the case of the three-body trigger is simpler. The idea of the trigger is to select all events with triplets at low  $Q_3$  region, which for this estimate is selected to be  $Q_3 < 0.6 \text{ GeV}/c$ . The trigger will run on data which would correspond to the MB sample. Thus we take the number of triplets we have in the Run 2 MB sample and scale it by the total number of

events expected in Run 3. There were 263 triplets measured at  $Q_3 < 0.6 \text{ GeV}/c$  in the Run 2 MB sample, which consists of  $1.5 \cdot 10^9$  events. As mentioned, the expected total number of events the triggers will analyse is  $1.25 \cdot 10^{13}$ . Thus the expected number of triplets is  $2.19 \cdot 10^6$ , corresponding to a factor 615 larger triplet count than in Run 2 HM. A similar factor is obtained for p-p-p and p- $\Lambda$ - $\Lambda$  triplets.

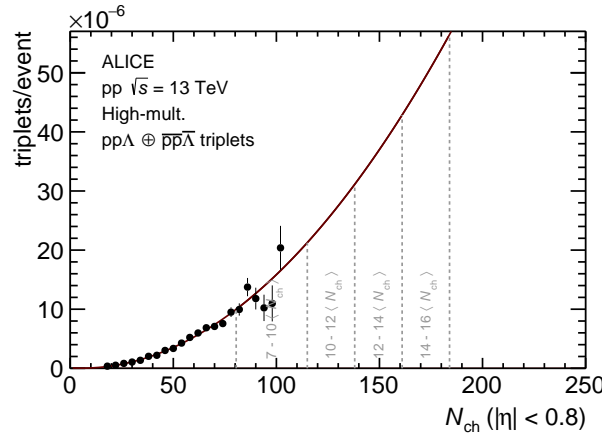


FIGURE 4.2: Triplets per event as a function of multiplicity in Run 2 (black circles) obtained using the same data which was analysed in the three-baryon femtoscopic analysis presented in this thesis.

As shown above, the expected increase in the number of p-p- $\Lambda$  triplets at region  $Q_3 < 0.6 \text{ GeV}/c$  is 6.8 times for the HM trigger, while for the specific three-body trigger, it is a factor 615. In both cases, the ALICE detector is assumed to have the same efficiency and acceptance in Run 3 as in Run 2. This shows that the development of the three-body trigger is of extreme relevance.

## 4.2 Trigger results

The triggering scheme for Run 3 is shown in Fig. 4.3. As explained in Chapter 2.3, the synchronous reconstruction occurs during the data taking. Once the data is

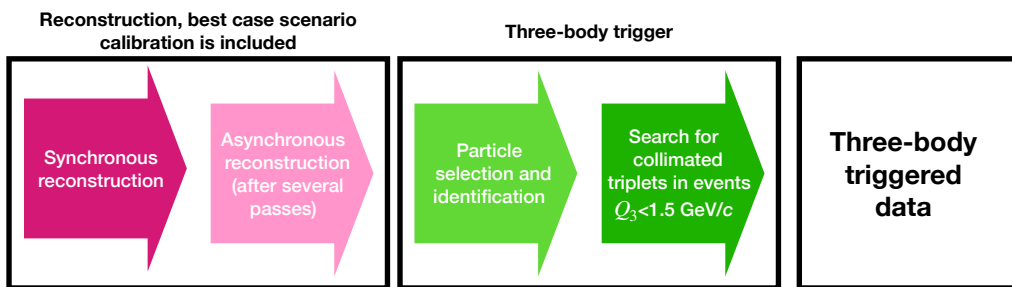


FIGURE 4.3: Scheme for the three-body triggers in Run 3.

recorded, the calibrations are performed, followed by several asynchronous reconstruction passes. Once the required quality of reconstructed data is achieved, the triggering takes place.

It consists of two steps - track selection to have proper particle candidates and the search for triplets at low  $Q_3$  in the region  $Q_3 < 1.5 \text{ GeV}/c$ . As shown later, such a range results in the required reduction factor. In Run 2, the normalisation region of the measured correlation function was at  $1.0\text{-}1.2 \text{ GeV}/c$  which sets the lower bound

for the trigger, while the interactions were observed at  $Q_3 < 0.4 \text{ GeV}/c$ . The complete calibration of the data might not be available before the triggering is carried out, depending on the time frame between the data taking and the requirement to delete the non-triggered events. There were 600 billion events recorded during the 2022 pp collision campaign. The triggering should have been performed before Pb-Pb data-taking at the end of 2022; however, due to the electricity price crises, the Pb-Pb campaign was postponed to April 2023. This allowed a more in-depth analysis of the asynchronous reconstruction, resulting in three asynchronous reconstruction passes. This thesis presents only the results obtained with pass3 data, as this pass will be used for the final triggering. The trigger had to be developed in the O2Physics analysis framework, completely newly developed software for Run 3 analysis. The data format also changed in Run 3 and is now based on tables. There are separate tables for collisions, tracks, V0s and other information. These tables are related by collision ID so that, for example, the tracks of specific collision can be easily retrieved from the tables. As the analysis framework is new, the trigger code had to be validated using converted data. Converted data is Run 2 MB data which was converted from AOD format (introduced in Chapter 2.4) used by AliPhysics (Run 2 software) to AO2D format used in O2Physics. Before the first Run 3 data was obtained, general-purpose MC data was released, which was also investigated in detail to inspect which selection criteria provided the best acceptance without significantly reducing the purity. While the final selections we apply are tested with MC, we do not show any specific results as it was not anchored to actual data. It was just a playground to test triggers before the first real Run 3 data became available.

#### 4.2.1 Benchmark: converted data

The benchmark results were obtained with converted Run 2 data and are shown in this Chapter for p-p-p triplet. The results employing O2Physics were obtained on February 2022 with a specific configuration of the framework and calibration objects uploaded to CCDB (Calibration and Constants Data Base) available on that day. After this date, the results for proton  $p_T$  spectra changed, which was most probably caused by the updated TPC and TOF calibrations. The results obtained with the O2Physics framework analysing the converted data will be compared to those obtained with AliPhysics and the original Run 2 data for runs LHC18b and LHC18m. For this, we had to develop the trigger code in both frameworks. The resulting distributions are not normalised as the converted data corresponds to the same runs in both cases.

Table 4.2 shows the track selection criteria used for the benchmark results. They were selected such that it fully covers the systematic variation ranges applied in the Run 2 analysis shown in Chapter 3.3. The event selection is the same as in the Run 2 analysis except for the primary vertex position along the z-axis, which is required to be  $|vtx_z| < 12 \text{ cm}$  instead of  $|vtx_z| < 10 \text{ cm}$ . The multiplicity distributions are shown in the left panel of Fig. 4.4, where the red line corresponds to the O2Physics result and the black line to the AliPhysics results. The statistical uncertainties are not shown here; however, they are negligible and would not be visible in this figure. The ratio of the two distributions is shown on the right panel of Fig. 4.4. The ratio is flat except for a sharp dip when multiplicity approaches 0. The ratio decreases from 1.22 to 1.15 with the increasing multiplicity, which can also be an artefact of a different number of failed train jobs.

Selection criteria O2	Value
Pseudorapidity	$ n  < 0.85$
Transverse momentum	$p_T < 0.35 \text{ GeV}/c$
TPC cluster	$n_{\text{TPC}} > 65$
Crossed TPC pad rows	$n_{\text{crossed}} > 70$ (out of 159)
Findable TPC clusters	$n_{\text{crossed}} / n_{\text{findable}} > 0.83$
Tracks with shared TPC clusters	rejected
Distance of closest approach $xy$	$ \text{DCA}_{xy}  < 0.15 \text{ cm}$
Distance of closest approach z	$ \text{DCA}_z  < 0.3 \text{ cm}$
Particle identification	$ n_{\sigma, \text{TPC}}  < 4$ for $p < 0.75 \text{ GeV}/c$ $n_{\sigma, \text{combined}} < 4$ for $p > 0.75 \text{ GeV}/c$

TABLE 4.2: The trigger selection criteria applied in the benchmark.

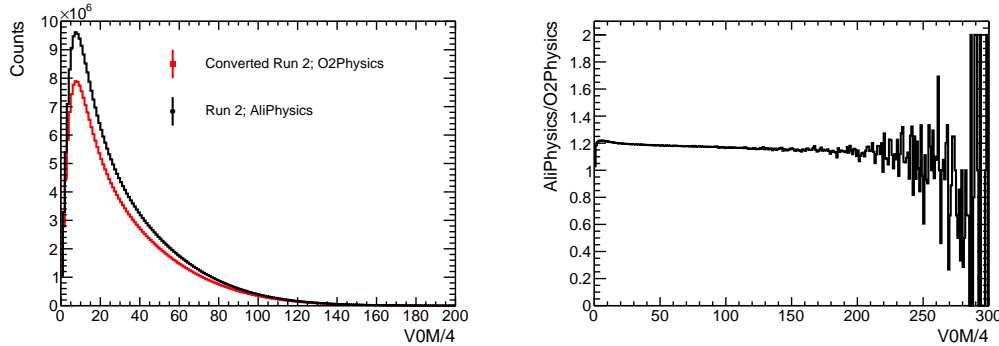


FIGURE 4.4: Multiplicity distribution obtained with O2Physics (red line) and with AliPhysics (black line), employing trigger selection criteria shown in Table 4.2.

The transverse momentum distributions for particles identified as protons are shown in the left panel of Fig. 4.5, where the red line corresponds to the O2Physics result and the black line to the AliPhysics results. The right panel shows the ratio of the two distributions. The ratio at low  $p_T$  is around 1.15, which is expected since we also have fewer collisions, as shown in Fig. 4.4. However, the ratio, in this case,

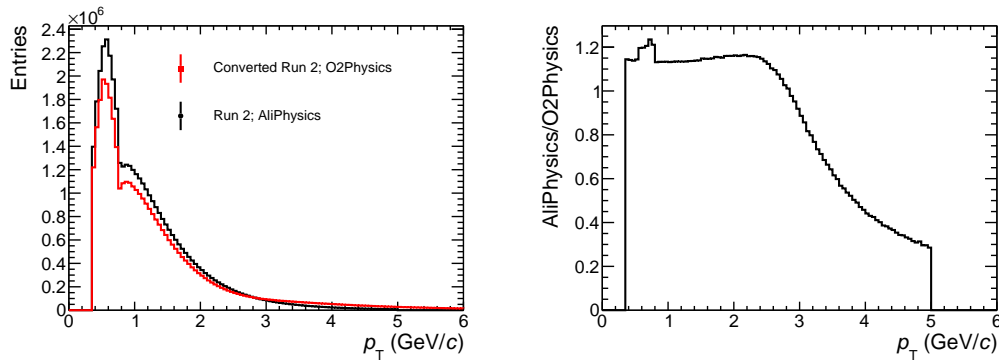


FIGURE 4.5: Proton transverse momentum distribution obtained with O2Physics (red line) and with AliPhysics (black line), employing trigger selection criteria shown in Table 4.2.

is not uniform in the shown  $p_T$  range as it has a peak structure at low momentum, and also, the ratio quickly decreases at  $p_T > 2.5 \text{ GeV}/c$ . The shapes are similar at the transverse momentum, where most of the protons are distributed.

The ultimate benchmark is the comparison of the same event distributions. In this case, we compare the distributions obtained with standard analysis cuts presented in Chapter 2.5. It is important here to compare the shape of the distribution, and thus the two distributions are normalised at the region  $Q_3 < 3 \text{ GeV}/c$ , where they are in good agreement. At larger  $Q_3$  values, a disagreement is observed. However, it was shown that there are more large  $p_T$  particles in the results obtained using O2Physics than AliPhysics. Thus also, the larger tail at the higher  $Q_3$  is expected.

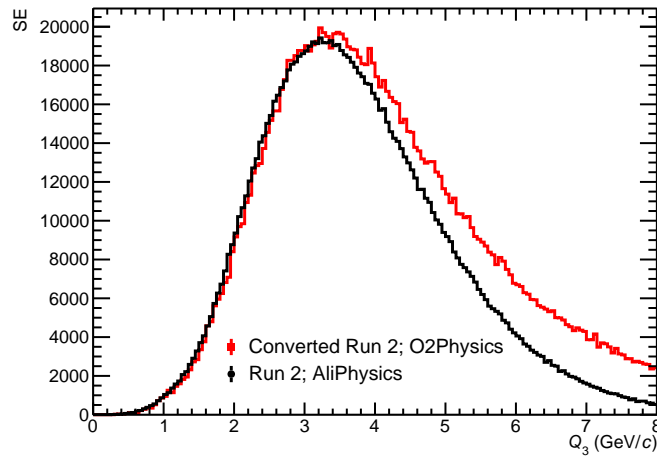


FIGURE 4.6: Same event distribution for p–p–p triplets obtained with O2Physics (red line) and with AliPhysics (black line), employing standard analysis selection criteria.

Table 4.3 compares analysed events, selected protons and antiprotons and the final rejection factor obtained with the O2Physics and the AliPhysics. Only events with at least one p–p–p triplet with  $Q_3 < 1.5 \text{ GeV}/c$  are accepted. The rejection factors are almost identical for the two cases. This check is a benchmark for the three-body trigger code in O2Physics.

	Events Selected	Protons	Anti-protons	Accepted events	Rejection factor
AliPhysics	$3.348 \times 10^8$	$4.8 \times 10^7$	$4.1 \times 10^7$	24398	13722
O2Physics	$2.848 \times 10^8$	$4.37 \times 10^7$	$3.8 \times 10^7$	20994	13566
Ratio	1.18	1.1	1.08	1.16	1.012

TABLE 4.3: Comparison of the trigger results obtained with AliPhysics and O2Physics.

### 4.2.2 Results: Run 3 data

There were 600 billion events collected during the pp campaign in 2022. Most of the events were collected during the high interaction (HI) rate (500 kHz) periods (>99%).

Table 4.4 shows the available data-taking periods with relevant information such as the interaction rate (IR), the number of runs in the period and the dataset size. As the pass3 reconstruction is ongoing, the storage size is given for pass2 files. However, all results will be shown for the available pass3 data. All collisions are taken at  $\sqrt{s} = 13.6$  TeV and a magnetic field of 0.5 T. The two smallest periods correspond to the low interaction rate data sets. The low interaction rate results in reduced space charge distortions in the TPC, and also such conditions are easier for other detectors. Thus after the second asynchronous reconstruction pass, a good quality of the data was reached. However, the calibration is much more complicated for the high interaction rate runs for which three asynchronous reconstruction passes were required. The triggering will be performed on the pass3 data when available.

Period	IR	Number of runs	AO2D Storage
LHC22f	5-20 kHz	5	0.56 TB
LHC22m	500 kHz	29	340.5 TB
LHC22o	500 kHz	117	2.19 PB
LHC22p	500 kHz	9	94.5 TB
LHC22q	6-15 kHz	12	9.5 TB
LHC22r	500 kHz (100 kHz)	29	299.7 TB
LHC22t	500 kHz	14	169.4 TB

TABLE 4.4: Available Run 3 data. The LHC22r period has two runs out of 28, collected at a 100 kHz interaction rate.

In this thesis, we will show results only for the LHC22m period (Run 523308), which provides the best reconstruction quality so far. For example, the standard particle identification based on the TPC measurement is best compared to other HI periods. The total number of analysed collisions is  $1.73 \times 10^9$ .

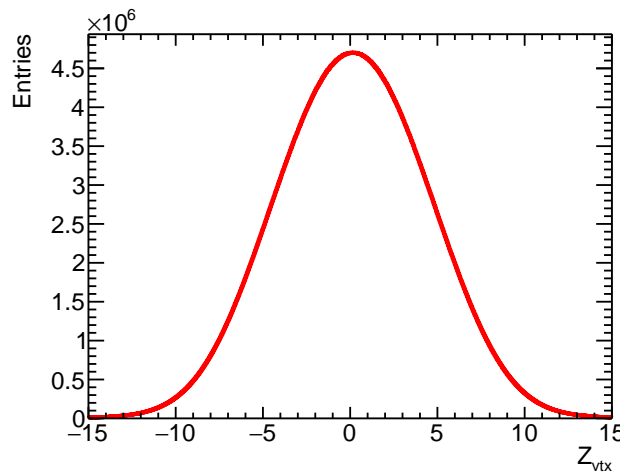


FIGURE 4.7: Primary vertex position in the z-axis in Run 3 data.

Figure 4.7 shows the primary vertex position along the z-axis. No collision selection criteria are performed at the trigger level, as the collision reconstruction

could still improve in the future asynchronous passes performed after the triggering. However, this does not change the final selected event sample much once the track and V0 selection and triplet requirements are applied.

This Chapter will show the results for both  $\text{ppp}$  and  $\text{pp}\Lambda$  triggers. The track selection criteria used for triggers are shown in Table 4.5. The  $n_\sigma$  distributions for

Selection criterion	Value
Pseudorapidity	$ \eta  < 0.85$
Transverse momentum	$0.35 \leq p_T \leq 6 \text{ GeV}/c$
TPC cluster	$n_{\text{TPC}} > 60$
Crossed TPC pad rows	$n_{\text{crossed}} > 50$ (out of 159)
Findable TPC clusters	$n_{\text{crossed}}/n_{\text{findable}} > 0.83$
Distance of closest approach $xy$	$ \text{DCA}_{xy}  < 0.15 \text{ cm}$
Distance of closest approach $z$	$ \text{DCA}_z  < 0.3 \text{ cm}$
Particle identification	$ n_{\sigma,\text{TPC}}  < 5$ for $p < 0.75 \text{ GeV}/c$ $n_{\sigma,\text{combined}} < 5$ for $p \geq 0.75 \text{ GeV}/c$

TABLE 4.5: Proton selection criteria.

selected proton (left) and antiproton (right) candidates are shown in Figs. 4.8 and 4.9. The first figure shows  $n_\sigma$  distributions for the TPC detector evaluated using the Bethe Bloch parametrisations provided by the TPC group. The distributions are shown as a function of the momentum reconstructed at the inner wall of the TPC. The distribution is slightly shifted towards negative values for protons and positive values for antiprotons. This is an artefact of space charge distortions which are not yet completely corrected. The corrections will appear available after the triggering. At higher momentum, the requirement is set for the combined value  $\sqrt{n_{\sigma,\text{TPC}}^2 + n_{\sigma,\text{TOF}}^2} < 6$ .

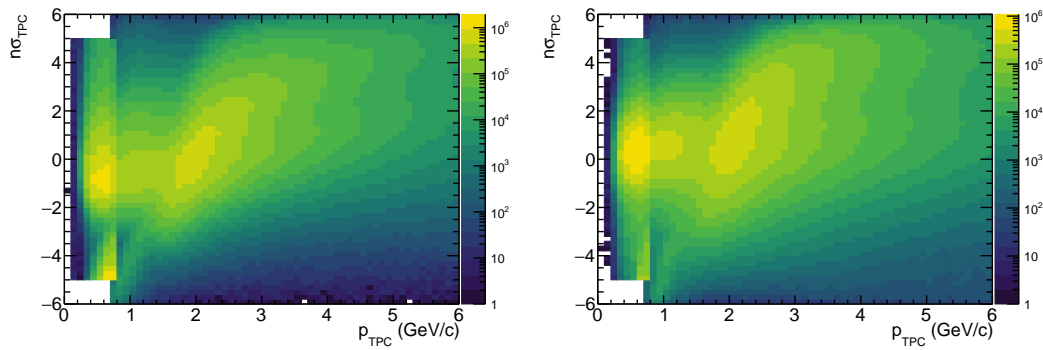


FIGURE 4.8:  $n_\sigma$  distributions for protons (left) and antiprotons (right) for the TPC detector.

The upper panels in Fig 4.9 show the  $n_\sigma$  distribution for the TOF detector. The distributions for protons and antiprotons are not centred around zero and are a mirror image around zero. The second shape, which peaks at around  $2 \text{ GeV}/c$ , stems from contamination. The lower panels show the combined  $n_{\sigma,\text{combined}}$  results. The shape centred at  $1\text{-}2 \text{ GeV}/c$  corresponds to the (anti)proton signal. The second shape at around  $2.5 \text{ GeV}/c$  corresponds to contamination.

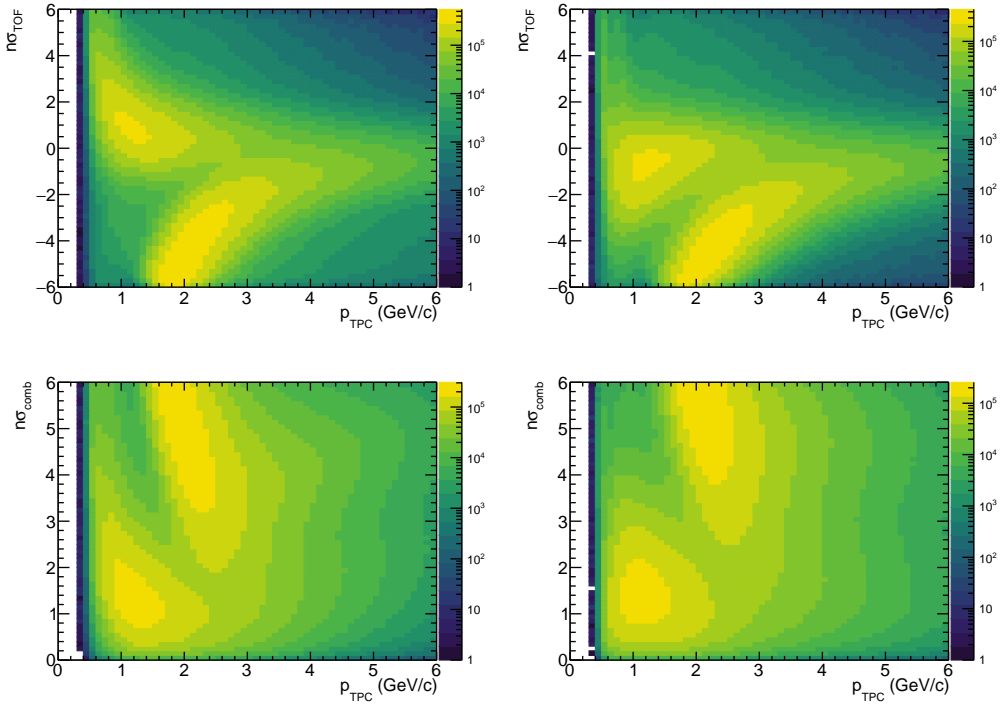


FIGURE 4.9:  $n_\sigma$  distributions for protons (left) and antiprotons (right) for TOF (upper panels) and combined TPC and TOF (lower panels).

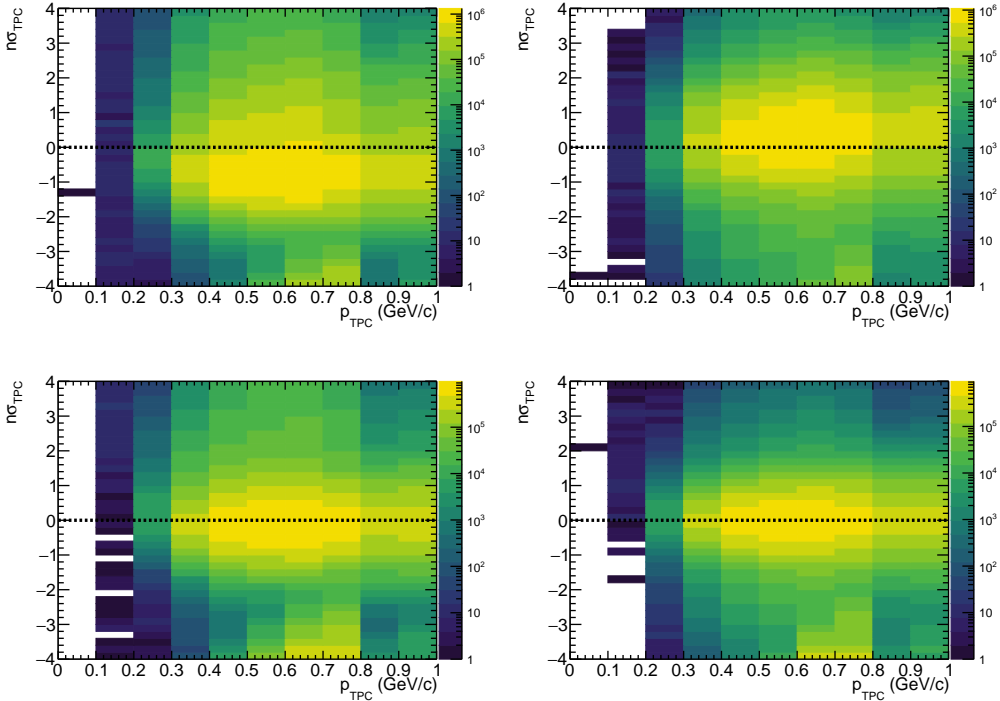


FIGURE 4.10:  $n_\sigma$  distributions for protons (left) and antiprotons (right) employing the TPC detector and default Bethe-Bloch parametrisation values (upper panels) and customised parametrisation values as explained in the text (lower panels).

The acceptance threshold is set to relatively high  $n_{\sigma,\text{combined}}$  values; however, in such a way, we ensure that the lower momentum particles which correspond to the (anti)proton signal but have higher  $n_{\sigma,\text{combined}}$  are not lost. After the triggering, there will be new asynchronous reconstruction passes and the PID for both TPC and TOF detectors is expected to improve.

The particle identification can also be performed by fitting the TPC signal manually and using obtained parameters of the fit function (Eq. 2.2) in the trigger. Such an option was implemented and results in more centred  $n_{\sigma,\text{TPC}}$  distributions as the fits are performed on a run-by-run basis as shown in Fig. 4.10. The upper panels show the same results as in Fig. 4.8 but for smaller momentum and  $n_{\sigma,\text{TPC}}$  range. The lower panels show the  $n_{\sigma,\text{TPC}}$  distribution obtained by employing the manually obtained parameterisation of the function describing the TPC signal for the different particle species. While the  $n_{\sigma,\text{TPC}}$  distribution is not very well centred for the default approach, the manual fit provides much better results. However, as the default parametrisation provides rather good results, there is no large difference in the final selection. The manual PID becomes relevant when the shift in the mean  $n_{\sigma,\text{TPC}}$  is large for a specific run as the central PID is such that it simultaneously fits all runs and thus is not run-dependent. The manually obtained PID will be employed in the final trigger selections, performed on multiple good runs from all available periods. The kinematic variable distributions for the selected protons (red line) and antiprotons (black line) are shown in Fig. 4.11.

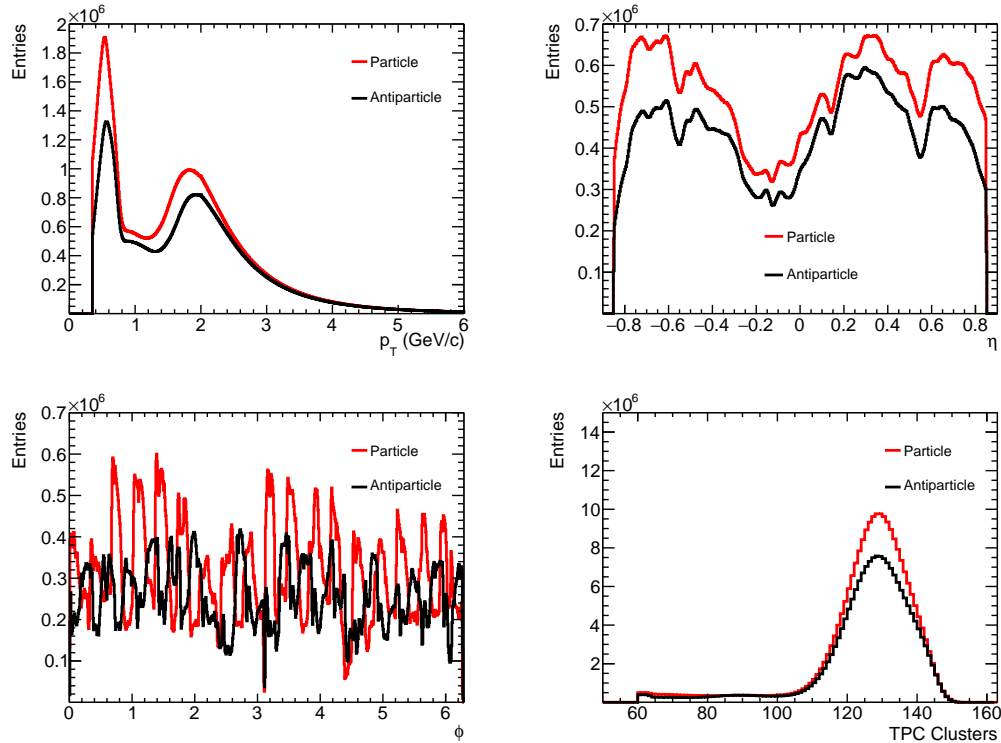


FIGURE 4.11:  $p_T$ , pseudorapidity,  $\phi$  angle and number of TPC clusters associated to the track distributions for the selected (anti)proton sample in Run 3.

The upper left panel shows the  $p_T$  distributions. The first peak at  $p_T$  around 0.6 GeV/c is expected as  $p_{TPC}=0.75$  GeV/c is the threshold for the switch between

$n_{\sigma,\text{TPC}}$  and  $n_{\sigma,\text{combined}}$ . However, the second peak at  $p_T=2 \text{ GeV}/c$  is a signature of the contamination. The upper right panel shows the pseudorapidity distribution and the lower left panel represents the  $\phi$  distribution. The number of TPC clusters associated with the track is shown in the lower right panel. The distance of closest approach distributions for  $x - y$  plane and  $z$  axis are shown in the left and right panels of Fig. 4.12, respectively.

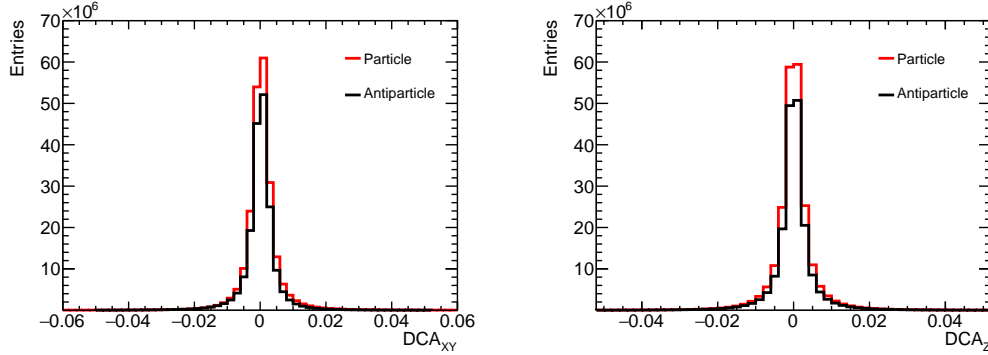


FIGURE 4.12: Distance of closest approach distributions for the selected (anti)proton sample in Run 3.

The selection criteria applied to  $\Lambda$  candidates are shown in Table 4.6. An extensive invariant mass window is allowed so that the selected sample also includes background contributions which can be employed in future analysis to correct the measured correlation function for misidentified particles. Figure 4.13 shows the

Selection criterion	Value
<i>Daughter track selection criteria</i>	
Pseudorapidity	$ \eta  < 0.85$
TPC cluster	$n_{\text{TPC}} > 50$
Distance of closest approach	$\text{DCA} > 0.04 \text{ cm}$
Particle identification	$ n_{\sigma,\text{TPC}}  < 6$
<i>V<sup>0</sup> selection criteria</i>	
Transverse momentum	$p_T > 0.3 \text{ GeV}/c$
decay vertex	$ i_{\text{vertex}_\Lambda}  < 100 \text{ cm}, i=x,y,z$
Transverse radius of the decay vertex $r_{xy}$	$0.2 < r_{xy} < 100 \text{ cm}$
DCA of the daughter tracks at the decay vertex	$\text{DCA}( p, \pi ) < 1.8 \text{ cm}$
Pointing angle $\alpha$	$\cos \alpha > 0.96$
K <sup>0</sup> rejection	$0.49 < M_{\pi^+\pi^-} < 0.504 \text{ GeV}/c^2$
selection	$1.05 < M_{p\pi} < 1.2 \text{ GeV}/c^2$

TABLE 4.6:  $\Lambda$  selection criteria.

kinematic and topological distributions for selected  $\Lambda$  candidates. The upper left panel shows the invariant mass distribution with a distinctive peak of the  $\Lambda$  candidates for particles (red line) and antiparticles (black line). The upper right panel shows the  $p_T$  distributions, the middle left - the cosine pointing angle, the middle right - a distance of closest approach between the daughter tracks and the lower panel - the transverse radius distributions.

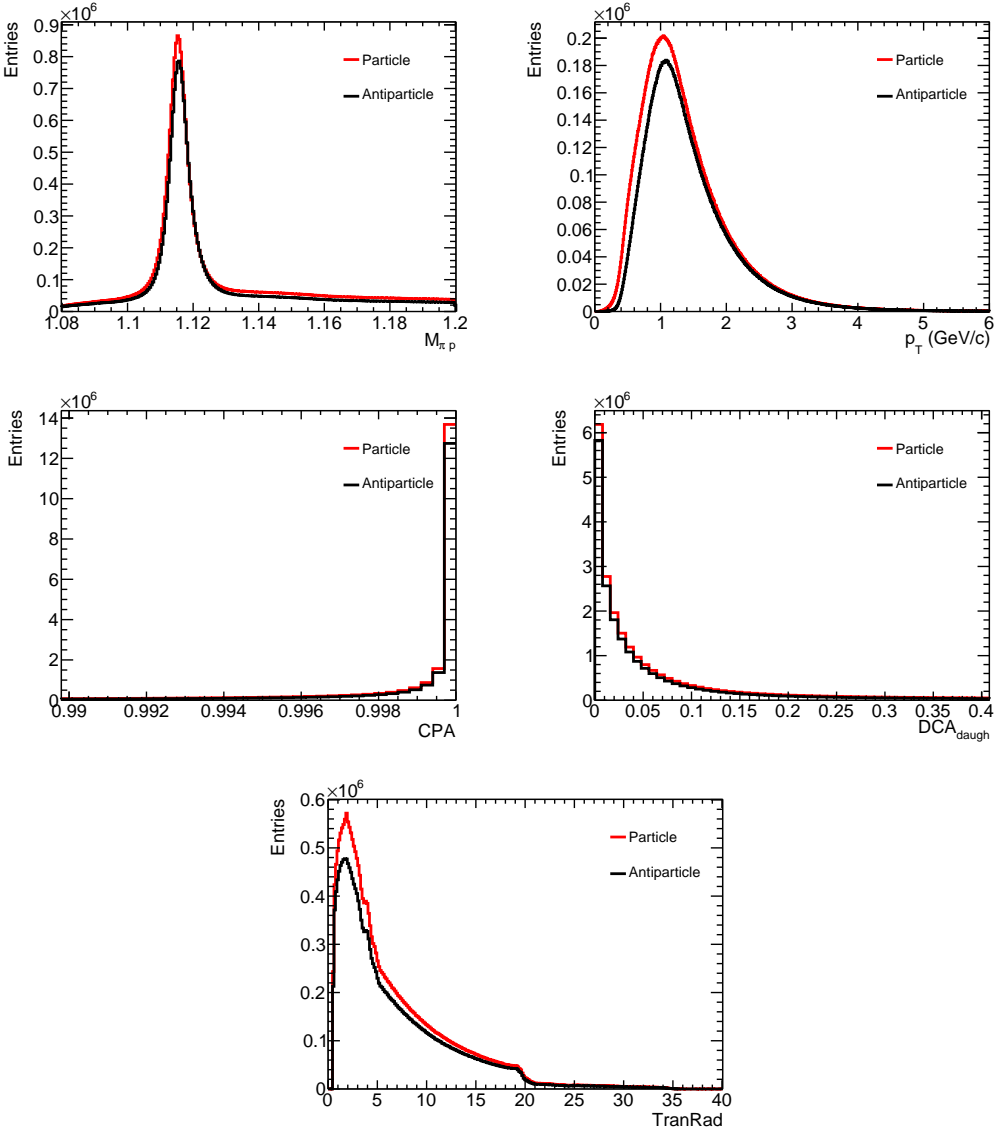


FIGURE 4.13: Invariant mass,  $p_T$ , CPA, DCA between the daughter tracks and transverse radius of the V0 distributions for the selected (anti) $\Lambda$  candidates in Run 3.

After the track and V0 selections, the trigger rejects events that do not contain particle candidates of interest. The last step of the trigger is checking if the surviving events have at least one triplet at the  $Q_3 < 1.5 \text{ GeV}/c$ . The resulting particle (red line) and antiparticle (black line) same event triplet distributions are shown in Fig. 4.14 as a function of  $Q_3$ . The left panel shows results for the ppp trigger and the right panel - for the pp $\Lambda$  trigger. In both cases, much more particle triplets are found than antiparticles. Figure 4.15 shows the same result, but at a low  $Q_3$  region, the  $y$  axis is shown in logarithmic scale. In the case of both triggers, the number of triplets at the first bins is very small - few entries per bin.

The rejection factors can be calculated by taking the ratio of accepted events and the total number of events. As introduced earlier, the complete set of triggers, for which the total rejection factor must be  $1 \times 10^{-4}$ , includes the ppp, pp $\Lambda$ , p $\Lambda\Lambda$ ,  $\Lambda\Lambda\Lambda$ , pd and  $\Lambda d$  triggers. Thus the results for the rejection factor will be shown for all these triggers, even though some of them are not introduced explicitly. The important part

is to reach the total rejection factor of  $1 \times 10^{-4}$ . The results for all triggers and the total rejection factor are shown in Fig. 4.16. All single triggers are below the  $1 \times 10^{-4}$  limit. The total rejection factor corresponds to the bin named *accepted*, precisely at the  $1 \times 10^{-4}$  limit. Thus the trigger is validated and achieves the required rejection factor.

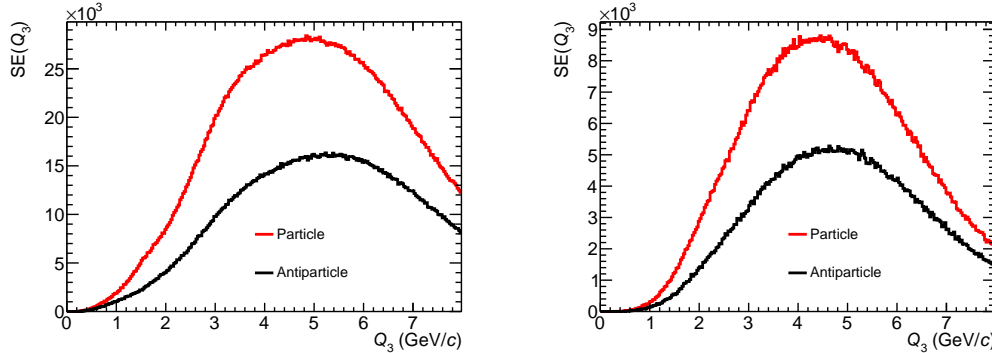


FIGURE 4.14: Same event triplet distributions as a function of  $Q_3$  for (anti)p-p-p and (anti)p-p- $\Lambda$  triplets in Run 3.

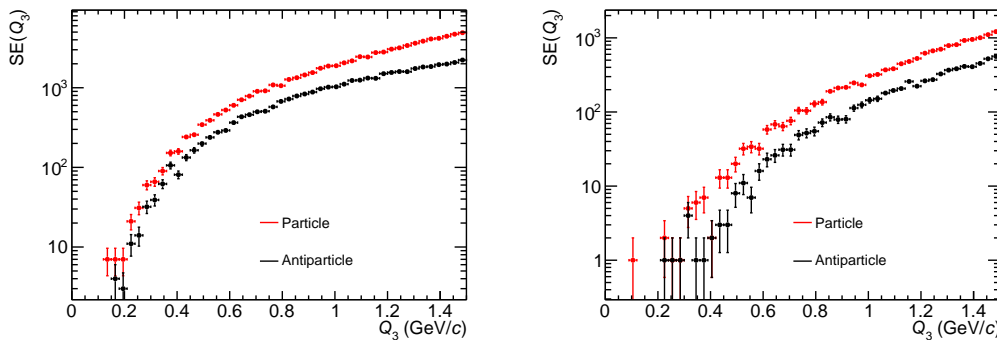


FIGURE 4.15: Same event triplet distributions at low  $Q_3$  region for (anti)p-p-p and (anti)p-p- $\Lambda$  triplets in Run 3.

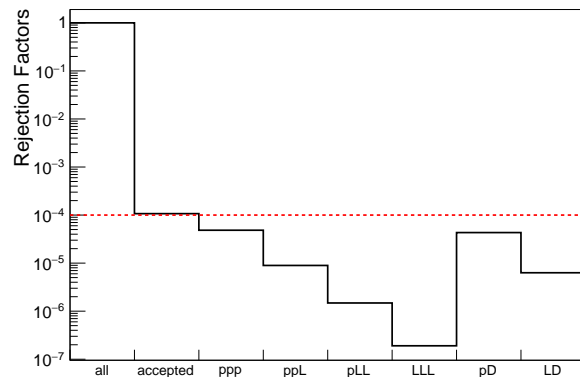


FIGURE 4.16: Trigger rejection factors. The bin *accepted* corresponds to the total rejection factor of all shown triggers.

All events selected by the triggers will be kept, while the rest will be deleted. It is interesting to estimate how many triplets we expect from the entire 2022 Run 3 data set. To compare the result to the previous estimations, we include only triplet at  $Q_3 < 0.6 \text{ GeV}/c$ . There are 4474 p–p–p and 228 p–p– $\Lambda$  triplets, including particles and antiparticles. As mentioned, the total number of analysed events is  $1.73 \times 10^7$ . This results in 32324650 p–p–p and 1647300 p–p– $\Lambda$  triplets in total Run 3 dataset consisting of  $1.25 \times 10^{13}$  events. The number of p–p– $\Lambda$  triplets can be compared to our estimate from Run 3 data presented at the beginning of this Chapter and it is 75% of the predicted value. However, the estimate provided from Run 3 data is based on results obtained with trigger selections. As the reconstruction and calibration are not finalised for the data, the strict analysis cuts cannot yet be applied reasonably, and the trigger selections are the only viable option. Finally, we can expect around 136800 p–p– $\Lambda$  triplets in the already collected 600 billion collisions, which is 38 times more than in Run 2 HM.

The triggers allow us to take advantage of all  $1.25 \times 10^{13}$  events and specify which events should be kept once the deletion process to release storage space starts. It should result in an almost 100 times larger data sample of triplets at low  $Q_3$  compared to a simple HM trigger which will be applied in Run 3. The development of this trigger ensures that the three-baryon interactions will be measured with Run 3 data for the p–p–p and p–p– $\Lambda$  triplets. The p– $\Lambda$ – $\Lambda$  and  $\Lambda$ – $\Lambda$ – $\Lambda$  triplets will also be measured, but it is clear from the rejection factor values that it is yet to see if Run 3 will have enough statistics to constrain the interactions.

## Chapter 5

# Introduction to dark matter and cosmic ray antinuclei

Many particles and hadrons were discovered by measuring cosmic rays. Paul Dirac predicted the existence of a positively charged electron; however, this was not widely accepted in the field as no such particle has been observed at the time. Five years later, a particle of the right mass and charge was found by Carl D. Anderson in measured cosmic rays, confirming Dirac's prediction [150]. Similarly, pions were proposed first by Yukawa and discovered ten years later in cosmic ray studies performed by C. F. Powell [151]. Nowadays, new particles and hadrons are mainly discovered at accelerator facilities such as the LHC. However, some of the most searched particles currently are the dark matter candidates which remain undetected. Once again, cosmic rays might play a significant role and serve as an indirect probe in dark matter searches.

The amount of visible matter cannot explain the velocity dispersion measurements of the galaxies in the galaxy clusters. Fritz Zwicky made such an observation for the first time in 1933 [152]. He called the missing mass required to explain the measurement *dunkle Materie* - the dark matter. Since then, a lot more evidence for the dark matter existence in our Universe has been found - galactic rotational curves [153], gravitational lensing [154], the distribution of the anisotropy in the cosmic microwave background [155] and mass distribution during galaxy collisions [156]. Despite the immense observations of its gravitational effects, dark matter remains one of the least understood constituents of our Universe, as no dark matter particles have been detected yet. Many theories suggest the competing different nature of the dark matter particles [157], out of which some propose that such particles could be weakly coupled to the ordinary matter. This would result in dark matter annihilating in ordinary matter, such as neutrinos, photons, hadrons or even antinuclei. Such an annihilation process also would take place in our Galaxy. Its products would contribute to the cosmic ray, neutrino and gamma-ray fluxes measured at Earth, providing an indirect probe for dark matter annihilation. Cosmic ray antinuclei constitute the most promising channel for indirect dark matter searches in the scope of cosmic ray measurements. Protons and light nuclei are abundant in our Galaxy because of their production mechanism related to the supernova explosions and thus are not optimal probes for indirect dark matter searches [158]. The situation for antinuclei is entirely different. The main confirmed production mechanism for antinuclei in the Galaxy is ordinary cosmic ray collisions with interstellar gas (such as p+p collisions) as shown in the upper part of Fig. 5.1. This results in relatively small cosmic ray antinuclei fluxes with a kinetic energy per nucleon distribution that peaks at around 10 GeV/A and constitute the background for indirect dark matter searches. The cosmic ray antinuclei flux stemming from

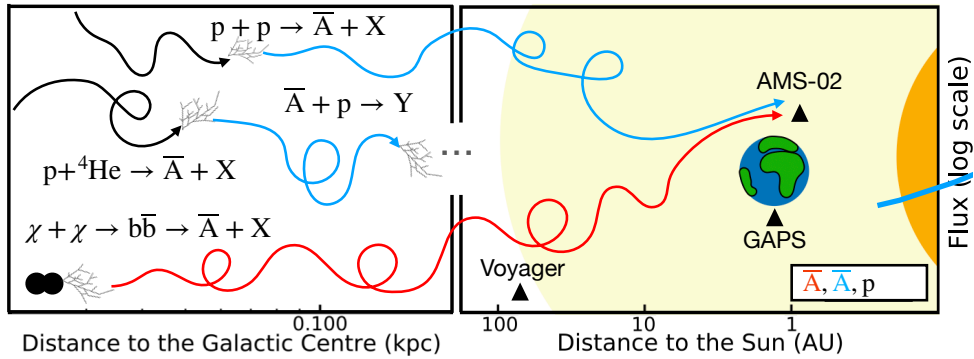


FIGURE 5.1: Sketch of cosmic rays in the Galaxy. Antinuclei ( $\bar{A}$ ) production, propagation and inelastic interaction are shown.

dark matter annihilation (shown in the lower part of Fig. 5.1) is expected to be of a similar order of magnitude and peak at around 1 GeV / A [159], providing a signal to background ratio at low energies reaching up to several orders of magnitude. While no confirmed observation of cosmic ray antideuteron or antihelium-3 exists, several experiments are working towards it [160–162]. Once the antinuclei are detected, exact estimations of the expected cosmic ray fluxes will be needed for the signal and background components to provide any constraints on dark matter.

Predictions of the antideuteron and antihelium fluxes were performed in the scope of this thesis together with systematic studies of the most relevant uncertainties. Such studies require knowledge about the antinuclei production mechanism, cosmic ray propagation in the Galaxy and the antinuclei interactions with the matter in the interstellar medium (as shown in the middle part of Fig. 5.1). This Chapter will discuss the following subjects in the following order: the current status of dark matter models and experimental searches, the production and propagation mechanisms of cosmic rays, the GALPROP transport model, which was used in this work to perform the calculations of cosmic ray fluxes, and light (anti)nuclei production mechanisms.

## 5.1 Dark matter

The work presented in this thesis contains estimates of cosmic ray antideuteron and antihelium-3 fluxes stemming from the matter cosmic ray collisions with the interstellar medium. Such fluxes are relevant for indirect dark matter searches as they are the only known background contribution.

### 5.1.1 Evidence for dark matter

From the mentioned evidence of dark matter existence, only two are further discussed here. First, the cosmic microwave background radiation measurement shows evidence of dark matter and provides information on how much of such matter exists in our Universe. Second, the rotation curve measurement of the Milky Way Galaxy allows us to access information on the dark matter distribution in our own Galaxy.

### Cosmic Microwave Background radiation

The Cosmic Microwave Background (CMB) was discovered accidentally in 1965. Two astronomers, Arno Penzias and Robert Wilson, measured a persistent excess noise with their antenna and could not find a source for measured microwave radiation [163]. At the time of the measurement, there was already a theoretical prediction of low-temperature radiation from the early universe [164]. During the recombination epoch after the Big Bang, the electrons and protons became bound to form electrically neutral hydrogen atoms. Before recombination, the Universe existed in the form of hot and dense plasma which was opaque as the photons were scattered off electrons. Once neutral hydrogen atoms were formed, the Universe became transparent. The photons decoupled from the matter at that time are now observed as CMB radiation; however, they are strongly red-shifted due to the expansion of the Universe. The CMB was first observed to high precision by the Cosmic Background Explorer (COBE) satellite, which confirmed that CMB has a near-perfect black-body spectrum [165]. It also showed only slight anisotropies in the CMB sky map, suggesting that our Universe is homogeneous.

The most accurate measurement of CMB was performed during the Planck mis-

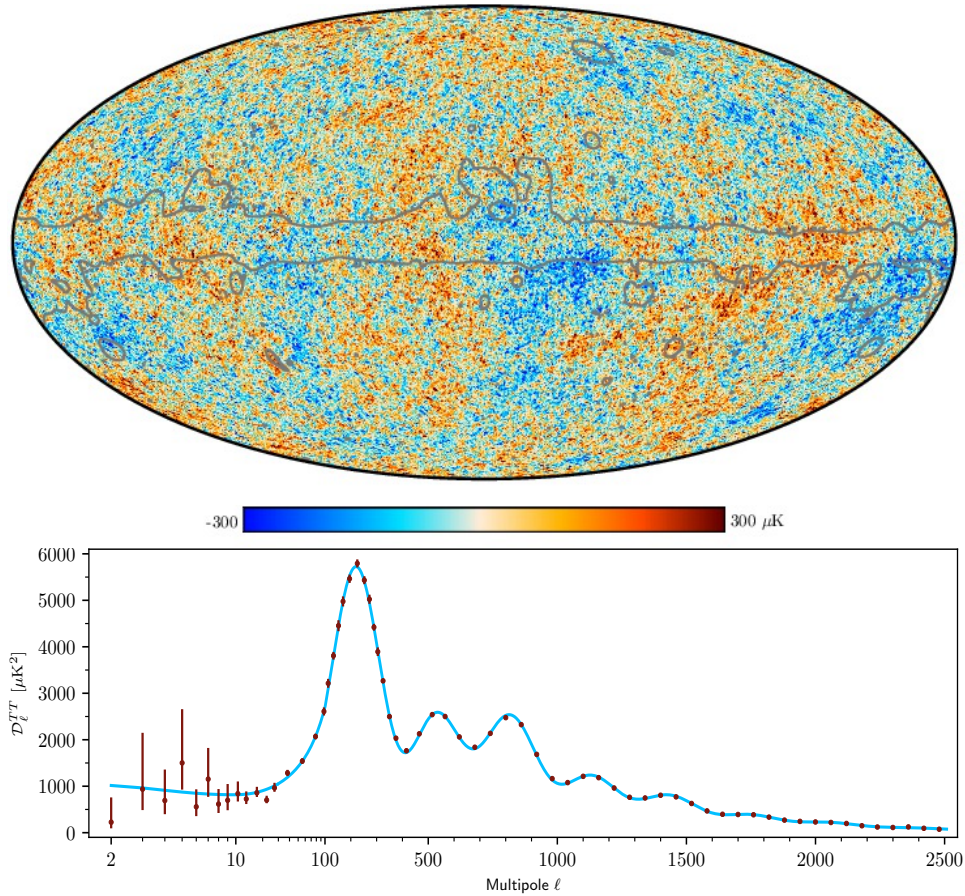


FIGURE 5.2: Upper panel: Temperature map of Planck CMB sky. Lower panel: Resulting temperature power spectrum. Figures taken from Ref. [166].

sion [166]. The temperature map of the CMB sky measured by Planck is shown in the upper panel of Fig. 5.2. The observed temperature fluctuations in the CMB can be decomposed as a two-dimensional function into a sum of spherical harmonics,

where every spherical harmonic function has its' amplitude and order (multipole). The set of such parameters can be represented as a power spectrum of temperature fluctuations, as shown in the lower panel of Fig. 5.2. Cosmological models can predict such a spectrum. The standard model of Big Bang cosmology is the  $\Lambda$  Cold Dark Matter ( $\Lambda$ CDM) model which assumes three main components of the Universe: dark energy, dark matter and baryonic matter. The best-fit prediction of such a model is shown as the blue line in the lower panel of Fig. 5.2 and, besides other cosmological parameters, provides information about the amount of the different components in the Galaxy. The position of the first peak in the power spectrum is related to the geometry of the Universe. The ratio of the second to the first peak provides information about the baryonic component. The peaks' overall value and especially the third peak's height are related to the dark matter density. The Planck collaboration reached the following conclusions: the Universe is flat, and dark matter must be dark, cold and "nearly" stable. If dark matter is thermally produced, the particles should be massive. Finally, the best-fit parameters provide the percentages of the different components in the Universe; around 69% of the Universe is dark energy, 5% of ordinary matter and 26% of dark matter [167].

### Galactic rotation curves

The rotation curve measurement is the best evidence of the dark matter's presence in our Galaxy (and other galaxies). The rotation curve shows the velocity of visible stars or gas in the galaxy as a function of distance from the galactic centre. A compilation of available observations is shown in Fig. 5.3. The velocity of stars and gas in the Galaxy depends on the gravitational potential. If it is calculated accounting for all visible matter in the Galaxy, the measured rotation curve cannot be reproduced as obtained velocities are too small. This suggests that there is additional matter in our Galaxy that we cannot observe electromagnetically, but we see its gravitational effects. In Fig. 5.3, the blue line represents a model rotation curve obtained by Sofue et al. including three main components of the galactic matter - the bulge, the disk with arms and the dark matter. The galactic bulge is the group of stars located at the spiral Galaxy's centre. As shown in Fig. 5.3, it results in the rotation curve that peaks at around 0 kpc. The galactic disk is mainly made of gas and results in the highest contribution to the rotation curve at around 10 kpc. The available measurements of interstellar gas and stars in the Galaxy can constrain the latter two components. Finally, the dark matter halo is extracted as the missing mass distribution required to fit the data at large distances. An isothermal dark matter density profile was used for the fit. There are several proposed dark matter profiles which can well explain not only the observations of the Milky Way but also other galaxies. The isothermal-density profile was proposed to explain the first observed rotation curves of distant galaxies [153]. In later studies, the shape of the dark matter profile

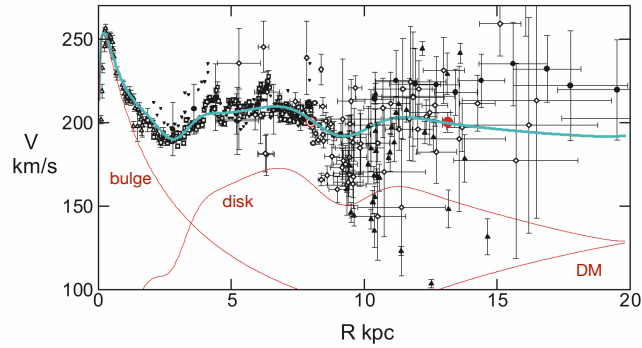


FIGURE 5.3: Modelled rotation curve (lines) of the Milky Way with a compilation of the available data shown as different shape markers [168].

that peaks at around 0 kpc. The galactic disk is mainly made of gas and results in the highest contribution to the rotation curve at around 10 kpc. The available measurements of interstellar gas and stars in the Galaxy can constrain the latter two components. Finally, the dark matter halo is extracted as the missing mass distribution required to fit the data at large distances. An isothermal dark matter density profile was used for the fit. There are several proposed dark matter profiles which can well explain not only the observations of the Milky Way but also other galaxies. The isothermal-density profile was proposed to explain the first observed rotation curves of distant galaxies [153]. In later studies, the shape of the dark matter profile

was determined by performing cosmological N-body simulations of structure formation which resulted in numerical data for the dark matter halo shape [169]. The obtained dark matter density could be well described with the following formula:

$$\rho(r) = \frac{\rho_0}{\frac{r}{R_s} \left(1 + \frac{r}{R_s}\right)^2}, \quad (5.1)$$

called the Navarro-Frenk-White (NFW) profile. Here,  $\rho_0$  is an overall normalisation and  $R_s$  is a scale radius that must be obtained from the fits to rotation curves.

There are also several more empirical and simulation-based dark matter profiles [170]. The overview of available density profiles is shown in Fig. 5.4. The dark matter density is constrained the least at low distances from the galactic centre, where all dark matter profiles have a different shape. They converge at the solar system's location, denoted by the dashed vertical line in Fig. 5.4, where they are set to reproduce the local dark matter density of  $0.3 \text{ GeV/cm}^3$  [171]. The limited knowledge about the dark matter density profile in our Galaxy affects both the direct and indirect dark matter searches, and thus several different dark matter profiles are usually tested [172].

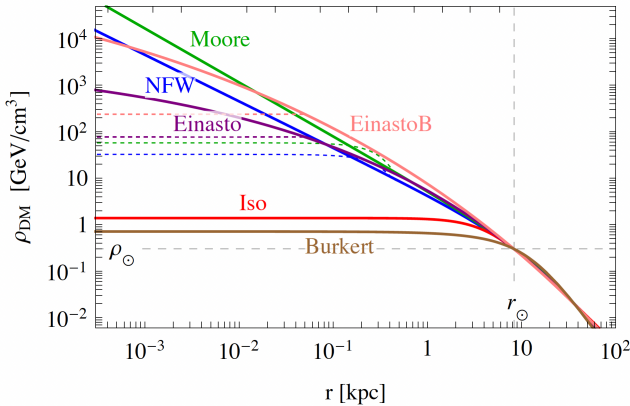


FIGURE 5.4: Compilation of available dark matter profiles for Milky Way galaxy [170].

### 5.1.2 Dark matter candidates

The non-observation of dark matter particles leads to a large variety of proposed dark matter candidates. Most of the theories are motivated by open questions in modern physics: some of the Weakly Interacting Massive Particles are developed following the hierarchy problem and are related to the supersymmetry; axions are described in a framework which would help to solve the strong CP problem, and sterile neutrinos are related to the problem of neutrino masses and mixing [10]. Such theories suggest a wildly different nature of the dark matter, resulting in different predictions of dark matter masses, interaction cross sections with ordinary matter, annihilation cross sections and decay probabilities. Several of the well-motivated dark matter candidates are shown in Fig. 5.5. We will not describe all models in detail; however, it is essential to note that the predicted dark matter particle mass ranges over 30 orders of magnitude. A similar range is also observed for the case of the interaction cross section with ordinary matter. The indirect dark matter searches via cosmic ray antinuclei fluxes can be employed if the dark matter particles couple to Standard Model particles and thus can produce ordinary matter when annihilating. One such candidate is the mentioned Weakly Interacting Massive Particles (WIMPs). WIMPs are a broad class of dark matter candidates with two characteristics - they are relatively heavy and

interact only weakly (any interaction with cross sections not higher than the electroweak scale). Many such models assume that the WIMPs were produced thermally in the early Universe, just as the Standard Model particles. To obtain the observed dark matter abundance in the Universe today, any thermally produced dark matter candidate must have annihilation cross section  $\langle \sigma v \rangle \simeq 3 \times 10^{-26} \text{ cm}^3 \text{ s}^{-1}$ . Such interaction cross section is expected for particles that interact at electroweak scale and have a mass of the order of 100 GeV.<sup>1</sup> This is exactly the expectation for the WIMP candidates. Thus such a coincidence is called the "WIMP miracle". Constraints provided by direct and indirect dark matter searches already reduced the available parameter space of interaction cross section and mass compatible with WIMPs predictions; however, more experimental limits are needed to rule out WIMP candidates completely [174].

WIMPs are expected to constitute Cold Dark Matter, which, as already mentioned, is also the preferred scenario by the CMB observations. There are many WIMP candidates, but here we introduce only two

with very different underlying theories. One of the popular WIMP candidates are the neutralinos. In supersymmetry, all standard model particles have partners which have the same gauge interactions and quantum numbers except for the spin, which differs by  $1/2$  [175]. This results in a zoo of new, yet undiscovered, supersymmetric particles, including four neutralinos. The lightest neutralino constitutes a dark matter candidate. Another very different WIMP candidate is the Kaluza-Klein dark matter. The Universal Extra Dimensions theory includes new dimensions with which an infinite number of partner particles of the Standard Model particles are introduced [175]. Differently from the supersymmetry, the partners also have the same spin as the Standard Model particles.

WIMP particles are usually believed to annihilate or decay to ordinary matter particles. We will take here the example of neutralino. The neutralino annihilation can be studied employing perturbation theory, accordingly to which the most relevant final states contributing to the total annihilation cross section are two-body states, such as fermion-antifermion (Standard Model neutrinos, leptons and quarks),  $W^+W^-$  or  $Z^0Z^0$  [176]. The Feynman diagrams contributing to neutralino annihilation to  $W^+W^-$  state are shown in the left panel of Fig. 5.6. The possible mediators of the interaction are the  $Z^0$  boson, light scalar and heavy scalar Higgs ( $h, H$ ) or supersymmetric partner of  $W$  boson - chargino  $\chi_n^+$ . The production of  $W$  boson pairs is

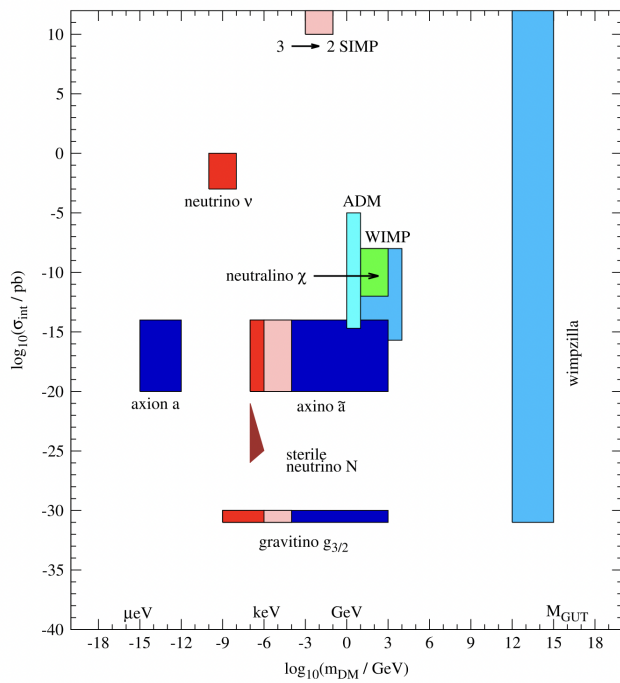


FIGURE 5.5: Several dark matter candidates are shown in the log-log plane of the DM mass and cross section of interaction with ordinary matter [173].

<sup>1</sup>Natural units are usually used in the community to describe the dark matter particles masses

followed by the hadronization which can result in fermions, hadrons or even nuclei, as shown in the right panel of Fig. 5.6. The momentum distribution of annihilation products depends on the dark matter mass. Cosmic ray antinuclei studies usually consider the dark matter mass from a few GeV to a TeV scale. As it will be shown later, the expected cosmic ray antinuclei fluxes decrease with the increasing dark matter mass assumption. On the other hand, if dark matter mass is too low, the annihilation would not result in the production of antinuclei.

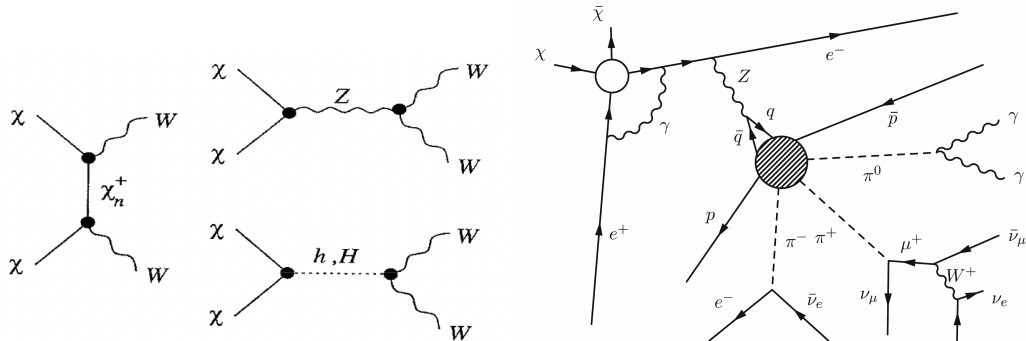


FIGURE 5.6: Left: Feynman diagrams contributing to the neutralino annihilation to  $W^+W^-$  state [176]. Right: Example of possible hadronisation process after the dark matter annihilation [177].

### 5.1.3 Searches for dark matter

There are three experimental approaches to look for dark matter candidates, as shown in Fig 5.7. DM stands for the dark matter candidate, and SM for the Standard Model particle. The colliders search for the DM production in ordinary matter collisions. Direct detection experiments try to observe dark matter and ordinary matter scattering events. Finally, the indirect searches look for the Standard Model particles produced in dark matter decays and annihilations.

The collider searches have been performed at such high-energy colliders as the Tevatron at Fermilab [178] and LEP and LHC at CERN [179]. The latter provided the most stringent limits for dark matter [180]. The dark matter particles do not leave a track in the detector and thus cannot be reconstructed directly. Instead, the observables of missing transverse momentum and energy are introduced. The distribution of the number of events as a function of the missing transverse energy can be modelled for the Standard Model employing event generators and perturbative QCD calculations. The difference between expected and observed distributions provides limits for the number of events which could be related to dark matter and constitute a model-independent measurement [181]. However, further constraints on specific dark matter candidates and comparisons to the results from direct detection experiments also require calculating the dark matter interactions, which is strongly model dependent. More

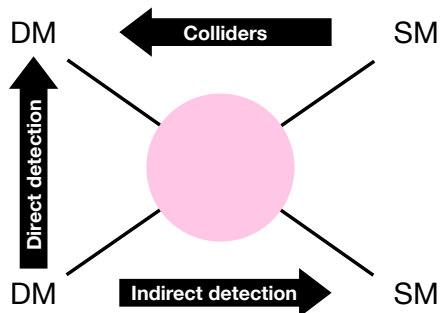


FIGURE 5.7: Different approaches to look for dark matter.

details about the search for dark matter by the ATLAS Collaboration can be found in Ref. [181] and by the CMS Collaboration in Ref. [182].

Both direct and indirect dark matter searches take advantage of the expected dark matter halo of the Milky Way. The direct detection experiments try to detect dark matter particles via the nuclear recoils caused by elastic dark matter scattering [183]. Such experiments quantify the effect by measuring the rate and the energies of the nuclear recoils. The recoil energies for an assumed dark matter particle with a mass of 10-1000 GeV are expected to be around 1 - 100 keV [184]. Thus detectors sensitive to keV signals are required. The event rate depends on the local dark matter density, dark matter mass, dark matter - nucleus elastic scattering cross section and dark matter speed distribution in the detector frame. The direct detection experiments usually provide the exclusion limits in the interaction cross section - dark matter mass plane, while the rest of the components are constrained by astrophysical observations (which introduce large uncertainties) [184]. Such studies are susceptible to background events related to cosmic rays, environmental gamma-ray radiation, cosmogenic neutrons, neutrinos, and traces of radioactive materials in the detectors themselves. Current state-of-the-art detectors manage to measure these keV scale signals and reduce the background effects enough to provide very stringent limits on the dark matter mass and interaction cross section with nucleons, as shown in Fig. 5.8. In this example, the exclusion limits are provided for WIMP particles. The most recent measurement, published by XENONnT, improved the sensitivity with respect to XENON1T (red line in Fig. 5.8) by a factor of 1.7 at a WIMP mass of 100 GeV and brought the limit on WIMP-nucleon cross section even lower [185].

The indirect dark matter searches look for the Standard Model particles produced in dark matter decays and annihilations in our Galaxy, especially gamma-rays, neutrinos and antimatter. Such experiments provide the constraints in dark matter annihilation cross section - dark matter mass plane. The gamma-rays and neutrinos traverse the Galaxy unaffected by the galactic magnetic field and thus can be traced back to the origin. The gamma-ray searches are usually directed to the nearby dwarf spheroidal

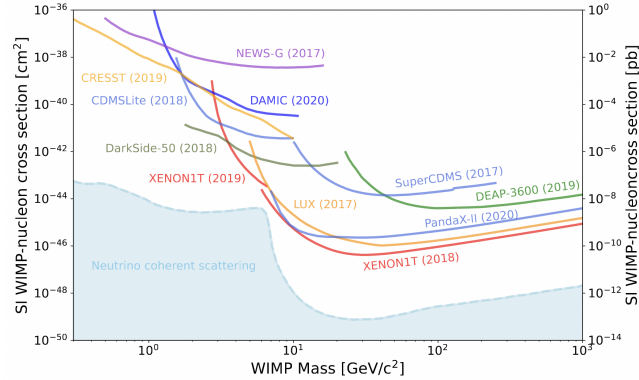


FIGURE 5.8: Dark matter exclusion plot based on direct detections experiments [10].

density, dark matter mass, dark matter - nucleus elastic scattering cross section and dark matter speed distribution in the detector frame. The direct detection experiments usually provide the exclusion limits in the interaction cross section - dark matter mass plane, while the rest of the components are constrained by astrophysical observations (which introduce large uncertainties) [184]. Such studies are susceptible to background events related to cosmic rays, environmental gamma-ray radiation, cosmogenic neutrons, neutrinos, and traces of radioactive materials in the detectors themselves. Current state-of-the-art detectors manage to measure these keV scale signals and reduce the background effects enough to provide very stringent limits on the dark matter mass and interaction cross section with nucleons, as shown in Fig. 5.8. In this example, the exclusion limits are provided for WIMP particles. The most recent measurement, published by XENONnT, improved the sensitivity with respect to XENON1T (red line in Fig. 5.8) by a factor of 1.7 at a WIMP mass of 100 GeV and brought the limit on WIMP-nucleon cross section even lower [185].

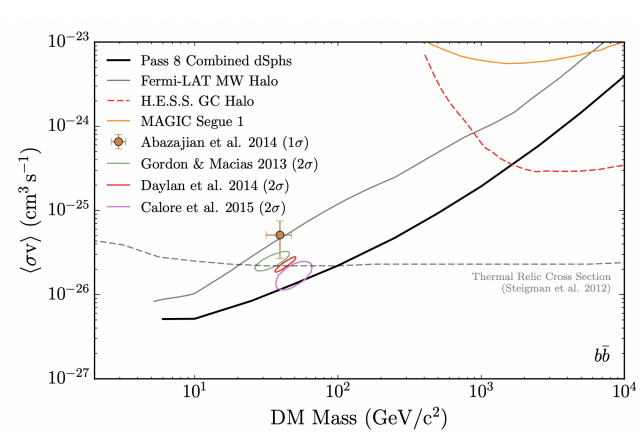


FIGURE 5.9: Compilation of constraints on the dark matter particles from some gamma-ray experiments [186].

galaxies, which contain a tiny amount of gas and generally do not have any significant astrophysical background in the relevant frequencies [186]. Another good observation point is the inner region of the Milky Way, as it should host a large amount of dark matter and is nearby; however, the galactic centre is very bright and limits precise signal extraction [187]. Also, other targets for the gamma-ray observations are used for indirect dark matter searches [10]. A compilation of the provided constraints on the dark matter annihilation via some of the gamma-ray data is shown in Fig. 5.9; however, such measurements can be used to constrain both annihilation [188] and decay [189] processes.

The neutrino signals are interesting as they are the only messenger to look for dark matter accumulated in dense objects such as the Sun or the Earth. However, neutrino detection poses a significant technological challenge as they interact very weakly with matter and thus are hard to detect. Also, the neutrinos from other galaxies constitute a possible channel for dark matter searches. More about neutrinos as a probe for dark matter searches can be found in Ref. [170].

The antimatter cosmic rays are strongly affected by the magnetic fields in the Galaxy and interactions with the interstellar gas. Thus they cannot be traced to their origin. The possible probes, in this case, are the positrons, antiprotons and antinuclei. So far, only positron and antiproton fluxes have been measured. In the case of the positrons, an excess was observed by PAMELA [191], which was later confirmed by Fermi-LAT [192] and AMS-02

experiments [193]. The positron flux observed by AMS-02 is shown in Fig. 5.10 as red points. The positron flux expected from cosmic ray collisions with the interstellar medium is shown as the grey region. The purple area corresponds to an additional source required to explain the data. Such an additional source has been initially interpreted as a dark matter signal; however, astrophysical sources, such as nearby and young pulsars or supernova remnants, have also been shown to reproduce the measured positron spectra [194]. The interpretation of the source at high positron energies as a dark matter component is also challenged by the missing signal in the measured antiproton spectrum. Indeed, if the positrons stem from dark matter, a similar signal would also be expected for other antimatter cosmic rays. Thus the interpretation of positron data requires the dark matter to be leptophilic and decay or annihilate predominantly into leptons. However, the list of proposed solutions to explain the measured flux is long [195–198] and thus the excess does not provide conclusive evidence for dark matter searches. While the measured antiproton flux did not include the significant signal expected from the positron observation, it also invoked extensive discussions in the field. State-of-the-art modelling suggests that a slight excess in the antiproton-to-proton flux ratio at around 10 GV rigidity is observed, as shown on the left panel of Fig. 5.11 [199]. The purple points represent the antiproton-to-proton flux ratio measured by AMS-02 [200], the

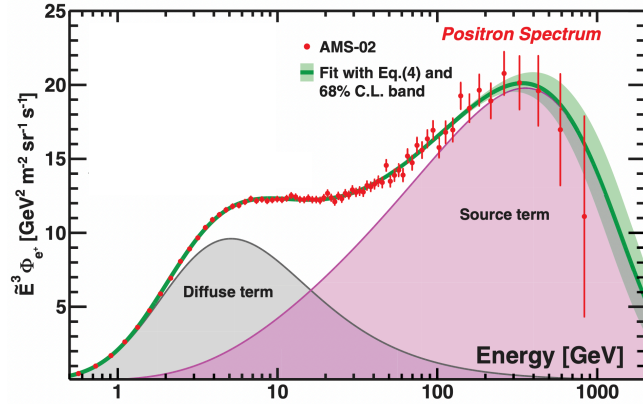


FIGURE 5.10: Positron flux measured by AMS-02. Figure adapted from Ref. [190].

solid line corresponds to the state-of-the-art modelling of the expected ratio from ordinary processes in the Galaxy and the dark and light grey bands show the 1 and  $2\sigma$  uncertainty bands. The lower panel shows the ratio of data versus the model. The excess observed at around 10 GV is small compared to the model uncertainties. The authors of Ref. [199] also evaluated the limits for the thermally averaged dark matter annihilation cross section and the dark matter mass, as shown on the right panel of Fig. 5.11. The upper limit is shown as the solid black line, while the most preferred parameter space if the excess is interpreted as dark matter, is shown by the red regions. The dashed blue and green lines correspond to the limits obtained from

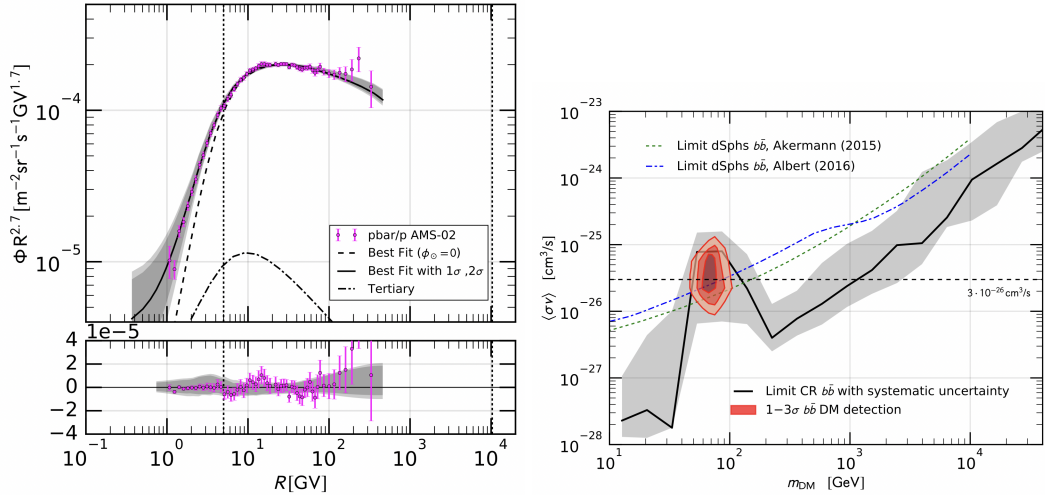


FIGURE 5.11: Left: Antiproton-to-proton cosmic ray flux ratio measured by AMS-02 (pink points), ratio expected from antiproton production in cosmic ray collisions with the interstellar medium (dashed line), the tertiary component of the ratio (dotted-dashed line) and the total expected ratio from ordinary processes in the Galaxy (solid line). Right: Extracted limits on the dark matter masses and annihilation cross sections. Both figures are taken from Ref. [199].

gamma-ray measurements of dwarf galaxies, and the black dashed lines correspond to the mentioned thermal value of the annihilation cross section expected from the current abundances of dark matter in the Universe. While such a study is relevant to constrain dark matter parameters, the observed excess in antiproton-to-proton ratio cannot be seen as a ultimate dark matter signal. It becomes apparent that a cosmic ray probe with a much higher signal-to-background ratio is required to provide a "smoking-gun" signal.

The cosmic ray antinuclei have yet to be measured; however, there are a lot of ongoing studies to estimate the expected fluxes. The state-of-the-art predictions for cosmic ray antideuteron and antihelium fluxes suggest that such measurements would have a very high signal-to-background ratio at low energies. The following Chapters will explain how the antinuclei flux from dark matter annihilations and the cosmic ray collisions with the interstellar medium can be estimated. In the last decades, there have been numerous efforts to predict antinuclei fluxes, for example, Refs. [201–205]. One such study is shown in Fig. 5.12. The black dashed line depicts the predicted background flux, while the three red lines represent the fluxes expected from dark matter annihilation, assuming dark matter masses of 50, 100 and 500 GeV (ordered by decreasing flux). Indeed,

the signal-to-background ratio reaches even several orders of magnitude for the lower dark matter mass assumptions. In the shown study, no uncertainties have been provided. However, such studies have significant uncertainties as they require experimental constraints on antinuclei production mechanism, antinuclei interaction with matter, propagation of cosmic rays in the Galaxy, information on dark matter distributions, annihilation cross section, and so on. The available predictions so far use different antinuclei production cross sections, propagation models, and different values for describing parameters related to dark matter. It is hard to compare the predicted fluxes and influence of the different models, as most of the time, for example, both the employed production cross section and the propagation models are different. Also, none of the existing predictions uses data-driven estimates for the antinuclei interactions with the interstellar medium, as no measurements of inelastic antinuclei-matter cross sections were available. In this thesis, we revise the predictions of antideuteron and antihelium-3 fluxes stemming from cosmic ray collisions with the interstellar medium by including, for the first time, data-driven estimates of the antinuclei inelastic cross sections. For this purpose, we implemented the antinuclei propagation in GALPROP. In the case of the antideuteron studies, we also used a unified propagation scheme to test several different production models, allowing us to provide a realistic estimate of the uncertainty on the cosmic ray fluxes. The propagation uncertainties were also estimated using different propagation parameter sets in GALPROP. We also obtained the secondary antihelium-3 flux. For both antinuclei secondary fluxes, we estimated the transparency of the Galaxy to the propagation of such cosmic rays.

### Experiments searching for cosmic ray antinuclei

As the signal-to-background ratio for antinuclei fluxes is expected to be at least a few orders of magnitude at low energies, even detecting one or a few cosmic antideuterons and antihelium would be a potential breakthrough. However, as the cosmic ray antinuclei fluxes are tiny, such experiments require detectors with large acceptance, long measurement time, and high particle identification power. The BESS experiment collaboration [206] provided so far the best exclusion limits for cosmic ray antideuterons.

The AMS-02 experiment on the International Space Station is also trying to measure antinuclei; however, already recorded data analysis is ongoing. Interestingly, several antihelium candidate events were reported by AMS-02 Collaboration with an approximate rate of around one antihelium event per year.<sup>2</sup> Such a rate is higher than expected, especially due to the relatively high energies of detected candidates.

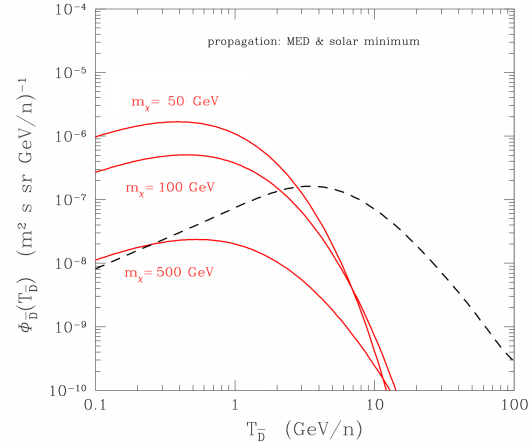


FIGURE 5.12: Cosmic ray antideuteron flux predicted for dark matter annihilation (red lines) and from the cosmic ray collisions with the interstellar medium (black dashed line) [201].

<sup>2</sup>Presented preliminary results by AMS-02 in MIAPP workshop 2022.

While these results are not yet published and undergoing analysis checks, the mentioned candidates spiked theoretical interests in the possible origin of such antinuclei, ranging from dark matter to anti-clouds [207, 208].

Another candidate to measure the antinuclei fluxes is the upcoming balloon-borne experiment GAPS dedicated to low-energy cosmic antinuclei search and is expected to have its first flight by the end of 2023 [162, 209, 210]. GAPS has a specific approach to identifying the low-energy antinuclei by employing an exotic atom technique which should result in high-precision particle identification capabilities. Finally, there is a new generation magnetic spectrometer experiment proposed, called AMS-100.<sup>3</sup> If the experiment is funded and developed, it will result in a 40 t detector system which will require to be launched by a rocket and reside in Lagrange Point 2. The projected sensitivities suggest that such an experiment would be able to not only detect the few antinuclei candidates but also provide high precision measurements of antideuteron and antihelium fluxes.

As shown by the above examples, experimental indirect dark matter searches using cosmic ray antinuclei are very active. Thus the theoretical and phenomenological studies of the cosmic ray fluxes are very timely.

## 5.2 Cosmic rays

Cosmic rays are charged particles traversing the Galaxy. They mainly comprise protons (around 90%), helium (around 9%) and heavier elements. The cosmic ray energies span a range up to  $10^{11}$  GeV as shown in Fig. 5.13. Here a compilation of available data on all cosmic ray species is shown. The spectral shape of observed cosmic rays has two breaks, so-called *knee* at around  $10^6$  GeV and *ankle* at around  $10^9$  GeV. It is generally believed that cosmic rays up to the knee energy are produced in the Galaxy. In contrast, the cosmic rays above the ankle energies are expected to be extra-galactic. The most convincing origin of galactic cosmic rays are shock waves associated with supernova remnants (SNR). The hypothesis that cosmic rays originate from shock waves propagating through the interstellar medium was proposed already in 1978 [212, 213], based on the first-order Fermi acceleration mechanism. Such a mechanism for cosmic ray production would lead to several signatures, for example, the synchrotron radio emission of accelerated electrons, which has already been detected at SNR shock fronts [214]. However, the rate of supernovae in our Galaxy is around 2 per century, and, to obtain the observed spectra, the SNRs should transfer around 10-20% of their energy to cosmic rays [215]. Recently it was shown that one of the observed supernovae could be such an efficient accelerator for

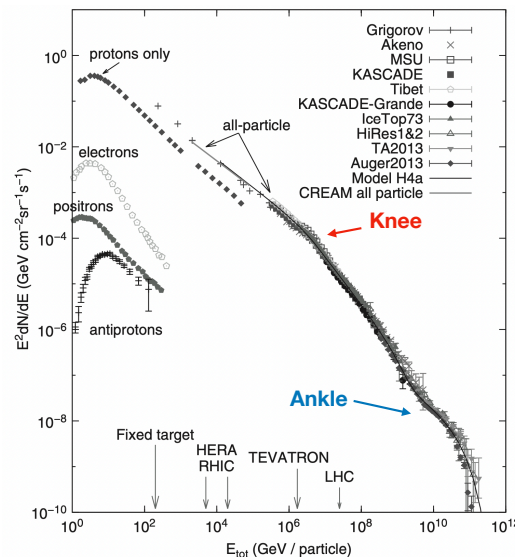


FIGURE 5.13: Overview of energy spectra of all cosmic ray particle species. Adapted from Ref. [211].

<sup>3</sup>Motivation and technical design of AMS-100 has been presented in CERN detector seminar.

cosmic rays [215]. Pulsars and pulsar wind nebulae have also been considered possible cosmic ray accelerators [216].

Cosmic rays produced in such astrophysical processes are referred to as primary. There is also a relevant secondary cosmic ray component, consisting of cosmic rays produced in heavier cosmic ray fragmentation events or collisions with the interstellar medium. The tertiary component - cosmic rays inelastically scattered in interstellar medium without annihilating but that can lose a fraction of their energy - are more relevant at low energies.

In the case of the indirect dark matter searches, kinetic energies of around 0.1-100 GeV are of interest. As mentioned, the secondary cosmic ray antinuclei constitute the background to such studies and thus must be understood well. Their production in the Galaxy depends on the number of collisions of cosmic rays with the interstellar medium and at what energies those collisions happen. Thus, understanding also primary cosmic rays and their transport in the Galaxy is necessary.

### 5.2.1 Cosmic ray transport

The galactic magnetic fields mainly drive the cosmic ray propagation in the Galaxy; however, effects from possible galactic winds are usually also considered [217]. For particular particle species, the cosmic ray flux can be described by the Fokker-Planck transport equation

$$\frac{\partial \psi}{\partial t} = Q(\mathbf{r}, p) + \text{div} (\mathbf{D}_{xx} \mathbf{grad} \psi - \mathbf{V} \psi) + \frac{\partial}{\partial p} p^2 \mathbf{D}_{pp} \frac{\partial}{\partial p} \frac{\psi}{p^2} - \frac{\partial}{\partial p} \left[ \psi \frac{dp}{dt} - \frac{p}{3} (\text{div} \cdot \mathbf{V}) \psi \right] - \frac{\psi}{\tau}, \quad (5.2)$$

where  $\psi = \psi(\mathbf{r}, p, t)$  is the time-dependent cosmic-ray density per unit of the total particle momentum at position  $\mathbf{r}$ . The source term of the cosmic rays is denoted as  $Q(\mathbf{r}, p)$  and can include primary particles injected by SNRs, secondaries coming from spallation and cosmic-ray collisions with the interstellar medium but also dark-matter annihilation and other exotic sources.  $D_{xx}$ ,  $\mathbf{V}$ , and  $D_{pp}$  are the spatial diffusion coefficient, the convection velocity, and the diffusive re-acceleration coefficient, respectively. The last term  $\psi/\tau$  accounts for processes that result in a particle loss: decay, fragmentation and inelastic interactions in the interstellar medium. The transport equation is time-dependent, and the steady-state solution is usually needed. The propagation describes changes in momentum and coordinate space and is defined by the propagation parameters shown in pink in Eq. 5.2. The processes involved in propagation are diffusion, convection, diffusive re-acceleration and energy losses in the medium. Only continuous momentum losses are treated with this equation, and thus if catastrophic momentum losses must be included, it has to be done via the  $\psi/\tau$  term [217]. The previous Chapter mentioned such a case as a tertiary component of cosmic rays. In the following, we introduce all relevant terms in the transport equation.

#### Source functions

The source function for primary particles depends on the source distribution in the Galaxy (which usually follows SNRs), the momentum injection spectrum of the specific cosmic ray species, and their abundance. Astrophysical and cosmic ray measurements can constrain the source distributions and abundances. The injection spectrum can be parametrised as power-law in momentum  $p^{-\alpha}$ , and usually, few

regions in momentum with different spectral index  $\alpha$  are assumed. The spectral indexes are also considered as a fit parameter in cosmic ray models.

The source of secondary cosmic rays, such as antinuclei, is defined as

$$Q_{\bar{N}}^{\text{sec}}(\mathbf{r}, E_{\text{kin}}^{\bar{N}}) = \sum_i \sum_j 4\pi n_j(\mathbf{r}) \times \int_{E_{\text{kin}, \text{min}}^i}^{\infty} dE_{\text{kin}}^i \left( \frac{d\sigma_{\text{prod}}}{dE_{\text{kin}}^{\bar{N}}} \right)_{ij} \psi_i(\mathbf{r}, E_{\text{kin}}^i) \quad (5.3)$$

where  $\bar{N}$  denotes the antinuclei,  $i$  stands for the cosmic ray species which collide with the interstellar medium gas  $j$ . The most relevant systems for antinuclei production in cosmic ray collisions are p–H, He–H, p–He, He–He,  $\bar{p}$ –p and  $\bar{p}$ –He collisions are also relevant to some extent [202]. The gas distributions are denoted as  $n_j(\mathbf{r})$ . The cosmic ray act as a projectile of kinetic energy  $E_{\text{kin}}^i$  with the flux  $\psi_i(\mathbf{r}, E_{\text{kin}}^i)$ . The number of gas and cosmic ray particles determine the number of collisions.  $d\sigma_{\text{prod}}/dE_{\text{kin}}^{\bar{N}}$  denotes the differential production cross section for antinuclei. In principle, all components required to estimate the secondary cosmic ray flux can be constrained using experimental data. However, light (anti)nuclei production is a poorly understood process and thus extrapolation of the available data to required collision energies for cosmic ray studies results in large uncertainties. The work presented in this thesis will evaluate realistic uncertainties depending on the chosen production model. The light (anti)nuclei production models are introduced in Chapter 5.3.

Also, more exotic sources such as dark-matter annihilation [172] or anti-stars [207, 218] can be considered. In this work, we focus on indirect dark matter searches and will consider only the dark-matter scenario. The secondary antinuclei fluxes obtained in this thesis will be compared to antinuclei fluxes stemming from dark matter annihilation presented in Ref. [159].

The source function for antinuclei produced in dark matter annihilation is

$$Q_{\bar{N}}^{\text{DM,ann}}(\mathbf{r}, E_{\text{kin}}^{\bar{N}}) = \frac{1}{2} \left( \frac{\rho(\mathbf{r})}{m_{\text{DM}}} \right)^2 \langle \sigma v \rangle_f \frac{dN_f^{\bar{N}}}{dE_{\text{kin}}^{\bar{N}}}, \quad (5.4)$$

where  $\rho(\mathbf{r})$  is the dark matter density as shown in Fig. 5.4,  $m_{\text{DM}}$  - the dark matter mass,  $\langle \sigma v \rangle_f$  - the thermally averaged dark matter annihilation cross section and  $dN_f^{\bar{N}}/dE_{\text{kin}}^{\bar{N}}$  is the antinuclei production spectra in one dark matter annihilation event.

## Diffusion

The diffusion of cosmic rays is driven by their interaction with turbulent magnetic fields in the interstellar medium, which is sufficiently ionised to behave as plasma [219]. The magnetohydrodynamic (MHD) theory can describe such a process mathematically. Most authors studying cosmic ray propagation consider the Alfvén waves, low-frequency oscillation of ions and magnetic field traversing the plasma. It was proposed in 1968 that the cosmic ray scattering by resonant Alfvén waves and discontinuities is responsible for the cosmic ray confinement in the galaxy [220]. The spacial diffusion parameter  $D_{xx}$  in the transport equations can be related to the total

magnetic field and also the properties of the formed MHD waves.  $D_{xx}$  is proportional to a power law of the cosmic ray particle rigidity  $R = p/c$  as  $D_{xx} \sim R^\delta$ . The exponent  $\delta$  depends on what turbulence of the galactic magnetic field is assumed. For example,  $\delta$  equals  $1/3$  under the Alfvén wave assumption; however, more isotropic waves could result in  $1/2$  [217]. Determining the actual diffusion coefficient for our Galaxy has to be done employing an empirical model fitted to the available cosmic ray flux measurements. The secondary-to-primary ratio is, in general, an essential probe for propagation models. As shown in the following Chapters, the primary cosmic ray spectra have been measured to high precision. Also, the gas distribution in the Galaxy is relatively well known, and the secondary particle production cross sections can be measured in accelerator facilities. All these components are required to constrain the secondary particle production in the Galaxy. Thus the resulting secondary-to-primary flux ratio is determined only by the propagation model.

### Convection

Another possible mechanism for cosmic ray propagation is the convection due to galactic winds. Galactic winds have been observed in many other galaxies; however, their existence in Milky Way is partially questioned. The total thermal pressure in the spiral galaxies, such as the Milky Way, is expected to be not high enough to form galactic winds. Nevertheless, it has been shown that cosmic rays can also contribute to the formation of galactic winds via their coupling to the thermal plasma and essentially pushing the plasma against the gravitational pull [221]. Thus, the cosmic ray propagation might be driven by diffusion in the galactic disk, but the advective component dominates in the galactic halo. The strength of the convection is determined in the transport equation by the convection velocity  $\mathbf{V}$ , which is usually considered as a fit parameter in cosmic ray models. The term  $\text{div} \cdot \mathbf{V}$  accounts for the adiabatic momentum gain or loss related to the scattering off inhomogeneities in the galactic magnetic field during the movement caused by convection.

Such a transport component has been shown to help explaining the observed energy dependence of the secondary-to-primary flux ratios and radioactive isotopes [217].

### Re-acceleration

The cosmic ray scattering off the randomly moving MHD waves can also result in stochastic acceleration. While the cosmic rays would gain energy in such a process, the MHD turbulence would lose energy. The rigidity dependence of the diffusion coefficient thus would also be affected by such a process at low rigidities. The re-acceleration effects are expected to be relevant at energies of around 1 GeV [217]. The effect of re-acceleration in the transport equation is expressed via the diffusive re-acceleration coefficient  $D_{pp}$  which is quadratically proportional to so-called Alfvén velocity, which is the characteristic velocity of disturbances traversing in the magnetic field. The Alfvén velocity is usually treated as a free fit parameter in cosmic ray propagation models. It has also been shown that the re-acceleration component of transport can help to explain the energy dependence of secondary nuclei in cosmic rays [217].

### Energy loss

Possible energy losses are included via  $dp/dt$  term to account for ionisation and Coulomb interactions in the case of nucleons [222]. Bremsstrahlung, inverse Compton, and synchrotron radiation play a crucial role for electrons.

## Particle loss

The particle losses of generic cosmic ray nuclei can occur via decay, fragmentation and inelastic interactions in the interstellar medium. The particle loss is determined by the  $1/\tau$  term in the transport equation and depends on fragmentation and decay rates, the inelastic cross section and the gas distribution in the Galaxy. In the case of the studied cosmic ray antinuclei, this component includes only the inelastic interaction term. Including the data-driven inelastic cross section for interactions of antinuclei with the interstellar medium is a core part of the work presented in this thesis. The value of  $1/\tau$  for antinuclei can be determined as

$$\frac{1}{\tau} = \beta c \left( n_{\text{H}}(\mathbf{r}) \sigma_{\text{inel}}^{\text{Np}}(p) + n_{\text{He}}(\mathbf{r}) \sigma_{\text{inel}}^{\text{N}^4\text{He}}(p) \right), \quad (5.5)$$

where  $\beta c$  is the velocity of cosmic ray particles,  $n_{\text{H}}(\mathbf{r})$  and  $n_{\text{He}}(\mathbf{r})$  are the densities of hydrogen and helium gas, and  $\sigma_{\text{inel}}^{\text{Np}}(p)$  and  $\sigma_{\text{inel}}^{\text{N}^4\text{He}}(p)$  are the inelastic cross sections for corresponding interactions. The distribution of the gas can also be determined by experimental data, as shown in the next Chapters.

The cosmic ray transport equation can be solved analytically or numerically. Usually, the numerical solvers are tested by reproducing the simple case scenarios, which are solvable with an analytical approach. There are three main codes which are available to solve the cosmic ray propagation: GALPROP[222, 223], DRAGON [224] and PISCARD [225]. In this thesis, we chose to use the GALPROP code; thus, only this model will be discussed in details.

### 5.2.2 GALPROP

GALPROP is a numerical code which solves the transport equation and provides cosmic ray fluxes for different particle species. The code is publicly available.<sup>4</sup> The GALPROP version 56 was used in this work. GALPROP uses available astrophysical and nuclear physics data to incorporate as much realistic physics as possible, for example, the distributions of the gas or cosmic ray sources in the Galaxy. In the following, we will describe how different components necessary to solve the transport equation are included in GALPROP.

#### Galaxy and cosmic ray halo

Cosmic rays propagate in the galactic disk and, eventually, they leave the Galaxy, filling a region known as the cosmic ray halo. This halo also acts as a boundary, where cosmic rays escape into intergalactic space. It has a vertical extent of a few kpc, and cosmic rays are expected to reside there for around 10-100 Myr [159]. In GALPROP, our Galaxy is approximated as a cylinder, as shown in Fig. 5.14. Where the inner cylinder depicts the galactic disk, and the pink cylinder corresponds to the cosmic ray halo. We used the 2D solver in GALPROP, which defined the Galaxy in  $z$  and  $r$  coordinate system, as shown in Fig. 5.14, and assumes the galaxy to be rotationally

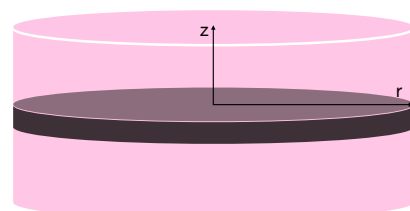


FIGURE 5.14: Sketch of the Galaxy approximation in GALPROP as a cylinder.

<sup>4</sup><https://galprop.stanford.edu/>

symmetric around the galactic centre. The halo height  $z_h$  and radius of such halo  $R$  are parameters of the model. The halo height must be fitted such that GALPROP could reproduce measured cosmic ray fluxes while  $R$  does not have a huge influence on the secondary fluxes and is assumed to be around 20 kpc. As mentioned, the propagation parameters are best constrained by the secondary-to-primary ratio. However, such observable is sensitive only to the ratio  $z_h/D_{xx}$  and thus is not sufficient to constrain the  $z_h$  and  $D_{xx}$  values separately. For antinuclei fluxes stemming from cosmic ray collisions with the interstellar medium, this parametrisation is sufficient since those are also secondary and thus sensitive only to the grammage - column of matter traversed [159]. However, the halo height  $z_h$  becomes relevant for studying radioactive species or fluxes stemming from dark matter annihilation.

### Gas distribution

Around 90% of the gas is hydrogen, 9% helium and 1% heavier elements [211]. Hydrogen contributes in three forms - neutral, molecular and ionised. Neutral hydrogen can be mapped in the Galaxy by detecting the 21 cm hyperfine line. The molecular hydrogen in the Galaxy is cold, and there are no emission lines in optical and radio bands. Thus direct detection of such gas is complicated; however, the molecular hydrogen can be traced by CO molecules. Finally, the ionised hydrogen can recapture an electron and become again neutral, emitting a photon. The gas distributions implemented in GALPROP are based on such measurements and shown in Fig. 5.15 [226]. Most gas is in molecular ( $H_2$ ) and neutral (HI) forms. Both distributions peak nearby the solar system (around 8.5 kpc), meaning that many antinuclei are produced in the local environment.

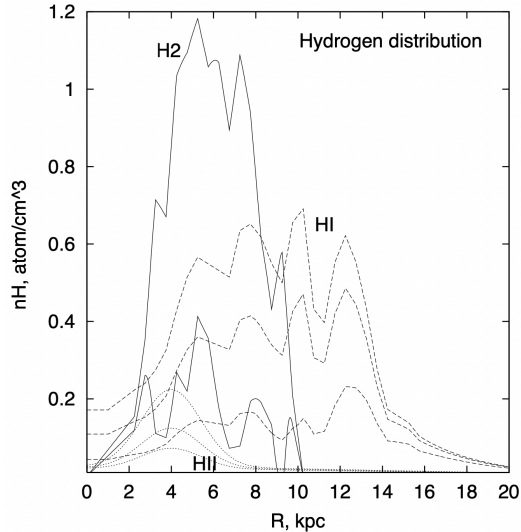


FIGURE 5.15: Ionised (HII), molecular ( $H_2$ ) and neutral (HI) hydrogen gas distributions implemented in GALPROP [226]. The three lines, shown for every form of gas, represent distributions at different  $z$  values in decreasing order: 0.0, 0.1, and 0.2 kpc.

### Primary cosmic ray source distribution

As introduced earlier, SN explosions are believed to be the leading primary cosmic ray source via the acceleration by shock waves. Thus the source distribution should follow the distribution of SNRs in the Galaxy. In GALPROP, it is implemented accordingly to the measured pulsar distribution in the Galaxy, which is used as a tracer for the SNRs [227]. It is done so because there are more available observations of pulsars, and their distances are measured more precisely.

### Solar modulation

GALPROP provides cosmic ray fluxes outside the solar system, which are called interstellar flux. However, most of the cosmic ray experiments are conducted inside

the heliosphere, where cosmic rays get affected by the solar winds and the magnetic field of Sun. These are not constant and have an 11-year cycle, with the polarity reversing every 22 years. Solar activity can be measured and followed in time in two anticorrelated ways - sunspot number and neutron monitoring. However, in a perfect case scenario, the experiments searching for antinuclei would have their missions during the solar minimum, when solar magnetic field is the weakest. Thus, for the cosmic ray antinuclei predictions, minimum solar modulation is usually applied. Solar modulation can be represented by a random walk, a Markov process that can be described employing Fokker-Planck equations. Parker first proposed such treatment in 1965, introducing the so-called Parker transport equation [228]. The most sophisticated numerical way to solve the Parker equation is the HELMOD code [229]; however, the public version does not include antinuclei. Another approach to account for solar modulation is the so-called Force-Field approximation suggested by Gleeson and Axford [230]. It works only under certain assumptions, cannot be trusted at very low energies and is charge-sign and polarity independent. While more sophisticated models are required, for example, to explain the very precise AMS-02 data, the solar modulation effect is sufficiently mimicked for the predictions of cosmic ray antinuclei studies, where many other significant modelling uncertainties are involved. The Force-Field approximation has only one parameter, the so-called Fisk potential  $\phi$ , and the modulated flux can be obtained from the interstellar flux as

$$\psi(E_{kin}, \phi) = \psi_{LIS} \left( E_{kin} + \frac{Ze}{A} \phi \right) \frac{E_{kin} (E_{kin} + 2m)}{(E_{kin} + \frac{Ze}{A} \phi) (E_{kin} + \frac{Ze}{A} \phi + 2m)}, \quad (5.6)$$

where  $\psi$  denotes the modulated flux and  $\psi_{LIS}$  corresponds to the local interstellar flux (LIS), which in our case is obtained from GALPROP;  $Ze$  is the charge of the particle. Regarding the solar minimum, the Fisk potential value is around 0.4-0.5 GV. This work will use the Force-Field approximation to compare the obtained antinuclei fluxes to the sensitivity limits of experiments that plan to measure antinuclei.

## Antinuclei

Antinuclei are not implemented in the official GALPROP version 56. Thus we had to implement them ourselves. The propagation part is the same for all cosmic ray species and thus does not require any modification. However, the source functions had to be implemented, including production cross sections and the inelastic cross section of antinuclei interaction with the interstellar medium. The experimental constraints on the cross sections are presented in the next Chapter.

## Benchmarks and GALPROP parameters

The GALPROP model has many parameters which have to be fitted. Such fits are not part of the work presented in this thesis; instead, we used and compared the state-of-the-art parameter sets available in the field. In this Chapter, we present the relevant data to constrain propagation models together with the available studies which provide the best estimates of GALPROP parameters.

Cosmic ray experiments can be separated into two main sectors: detectors outside and inside the heliosphere. The Voyager program is the only experiment to date with detectors outside the solar system - the twin spacecrafts Voyager 1 and Voyager 2, launched in 1977. Decades later, they provided the only measurements of low energy LIS fluxes of several species, including proton, helium, carbon and boron [231].

This data is extremely relevant, as it is not affected by solar modulation and thus allows to disentangle effects from the galactic and solar propagation. All other experiments are inside the solar system and thus are affected by solar modulation at low energies. The most precise data of cosmic ray fluxes at wide energy ranges were provided by the Alpha Magnetic Spectrometer Experiment (AMS-02), which resides on the International Space Station [232–237]. The AMS-02 Collaboration is also trying to measure antinuclei fluxes. Another spacecraft, relevant for low

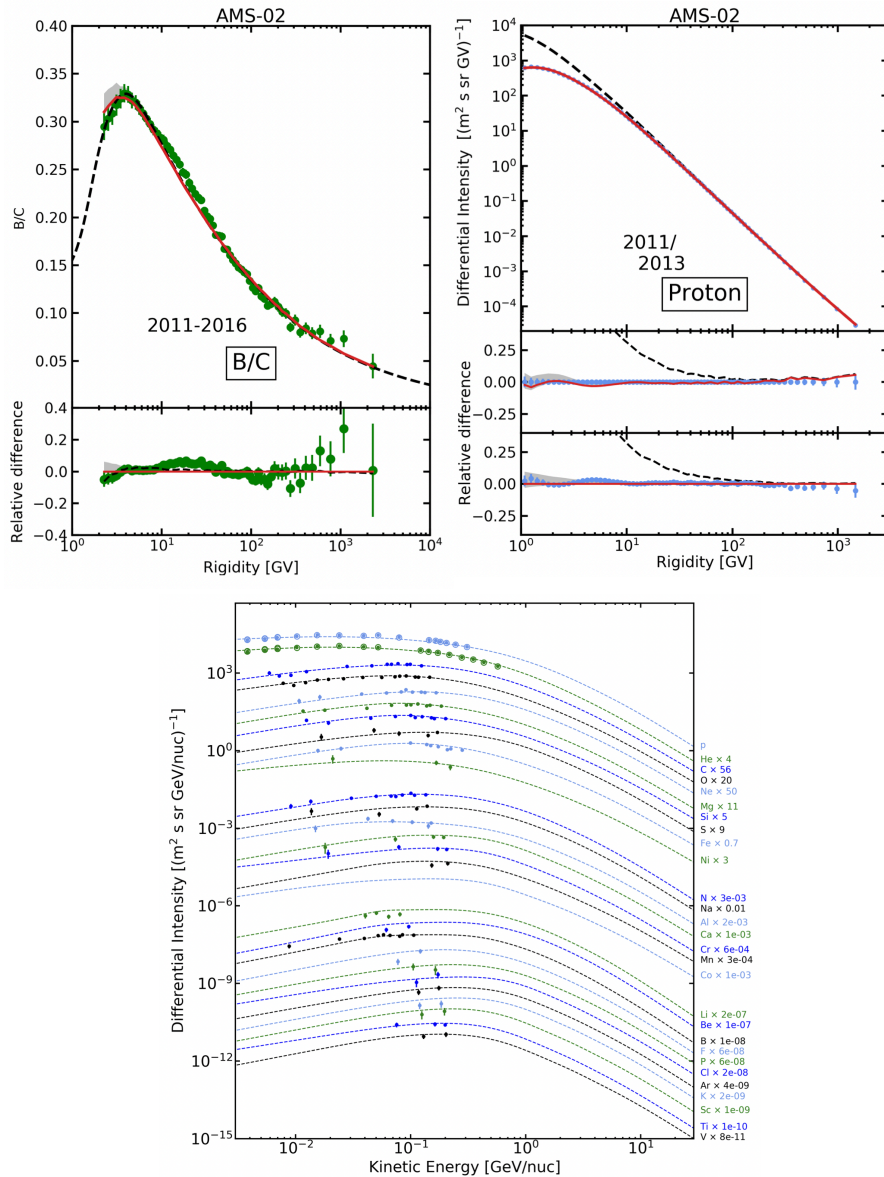


FIGURE 5.16: GALPROP fit to the available data performed by Boschini et al. [238]. Dashed curves represent LIS flux, solid red lines - solar modulated fluxes, blue and green points - data. Upper left panel: Modelled boron-to-carbon ratio compared to AMS-02 data. Upper right panel: Modelled proton flux compared to AMS-02 data. Lower panel: Modelled cosmic ray fluxes for a range of nuclei compared to Voyager 1 data.

energy cosmic rays, is called Advanced Composition Explorer (ACE) and has an

onboard Cosmic-Ray Isotope Spectrometer (CRIS).<sup>5</sup> It operates in an orbit close to the L1 Lagrange point between Sun and Earth. At high energies, the High Energy Astronomy Observatory Program (HEAO) provided precise data for different nuclei species [239]. Also, more experiments provide cosmic ray fluxes used to constrain propagation parameters: CREAM-I [240], PAMELA [241] and others.

The fits of GALPROP parameters to the available data have been performed by Boschini et al. [238] and Cuoco et al. [199]. While Boschini et al. used HELMOD for solar propagation, Cuoco et al. used the Force-Field approximation. Another difference between the two studies is the data used to perform the fit and validate the results. Boschini et al. included all nuclei up to  $Z \leq 28$  in the fit. We show their obtained results, as a benchmark of the GALPROP model, in Fig. 5.16. The upper left panel shows the boron-to-carbon ratio measured by AMS-02 (green points), the LIS flux obtained with best-fit GALRPOP parameters (dashed black line) and solar modulated flux employing HELMOD (red line). As mentioned before, the secondary-to-primary ratio is the most sensitive observable to propagation parameters and as shown in the figure, GALPROP can reproduce the shape very well. The upper right panel shows results for proton flux, where blue points represent the AMS-02 data. An excellent agreement between the measured and modelled fluxes is observed. Finally, the lower panel shows cosmic ray fluxes measured for different nuclei by Voyager 1 as blue and green points, while dashed lines represent the best-fit results using GALPROP. These fluxes are measured outside the solar system, and thus, good agreement between GALPROP and data ensures that the LIS fluxes are modelled correctly. GALPROP has been shown to also well reproduce the antiproton fluxes with such propagation parameter values [242]. In our work, we use the resulting parameter set from Boschini et al. [238] referred to as P-scenario.

Cuoco et al. had a different approach and fitted only the proton and helium fluxes measured by AMS-02, CREAM and Voyager and the antiproton-to-proton ratio measured by AMS-02. They also performed the fits, including and excluding the dark matter component; however, such studies would provide propagation parameters specific to the employed dark matter model. Thus, our study uses their best-fit values without the dark matter component. The authors published only the antiproton-to-proton ratio results, already shown in the left panel of Fig. 5.11.

Parameter	Units	Boschini et al.	Cuoco et al.
$z_h$	kpc	4	6.78
$D_0$	$\text{cm}^2 \text{s}^{-1}$	$4.3 \times 10^{28}$	$7.48 \times 10^{28}$
$\delta^a$		0.415	0.361
$V_{\text{alf}}$	$\text{km s}^{-1}$	30	23.8
$V_{\text{conv}}(z=0 \text{ kpc})$	$\text{km s}^{-1}$	0	26.9
$dV_{\text{conv}}/dz$	$\text{km s}^{-1} \text{kpc}^{-1}$	9.8	0

TABLE 5.1: Propagation parameter values from Boschini et al. [238] and Cuoco et al. [199].

The comparison of propagation parameters from the two studies is shown in Table 5.1. The differences between the two sets will be discussed in detail in the next Chapter, together with our results for cosmic ray antideuterons.

<sup>5</sup>Data is publicly accessible on <https://izw1.caltech.edu/ACE/ASC/level2/new/intro.html>.

## 5.3 Antinuclei studies at accelerators

The cosmic ray antinuclei studies require experimental constraints on the antinuclei production cross sections and the inelastic cross section with matter. The state-of-the-art models and available experimental data are presented in this Chapter.

### 5.3.1 Light (anti)nuclei production

No first-principle calculations of light (anti)nuclei production following hadron collisions exist, and the production mechanism is studied at the accelerator facilities and usually interpreted utilising statistical hadronisation or coalescence models. The thermal model assumes that particles are produced from a fireball, which is described as hadron resonance gas in global chemical equilibrium. The abundances of the final state hadrons are fixed at a sharp chemical freeze-out phase when all interactions changing the hadrons yields cease [243]. The statistical hadronisation model can successfully predict the yields of different hadrons and even light nuclei for nucleus-nucleus collision from SIS18 [244] and AGS [245] to ALICE [243] energies. The chemical freeze-out temperature is a fit parameter in such models, and it has been shown that the chemical freeze-out temperature is the same for hadrons and light nuclei [246]. This is somewhat surprising, as it would mean that such loosely bound objects as deuterons (with a binding energy of 2.2 MeV) would survive the hot fireball environment created at the high collision energies. Such a model can also successfully predict some of the observables in pp collisions [247]. However, the thermal model provides only yields, while differential production cross section as a function of the antinuclei energy or momentum is required in cosmic ray studies. The transverse momentum distribution can be obtained employing the blast-wave model, which is in agreement with Pb-Pb collision data [248]; however, it fails for the p-Pb system [249]. In cosmic ray studies, the antinuclei production cross section is also required at different collision energies, ranging from the production threshold energy to a few TeV. The statistical hadronisation models have several parameters defining the system, for example, the chemical freeze-out temperature and volume, which must be fitted to data for every collision system. So far, there is no easy way to extract these parameters as a function of the collision energy. The last two issues limit the usage of statistical hadronisation for cosmic ray studies. On the other hand, the coalescence model provides the produced antinuclei spectra "naturally". The coalescence model assumes that the nucleons are produced as degrees of freedom, which coalesce to form a bound nucleus if the nucleons are close enough in phase space. There are so-called simple coalescence models and advanced coalescence models. The latter has been shown to reproduce the antideuteron transverse momentum spectra in pp collisions at the LHC without fitting it to the spectra [250]. There are ongoing debates if one of the models - statistical hadronisation or coalescence - describes the fundamental antideuteron production mechanism. Several studies are trying to compare the two models employing different observables, and in many cases, both models perform similarly well [251]. However, new experimental observables are also being suggested, which are more sensitive to the two production mechanism assumptions [252]. In the following, only the coalescence models are discussed further as they are used in our work.

### Simple coalescence model

The simple coalescence model implies that if an antiproton and an antineutron are produced in a collision with relative momentum smaller than the so-called coalescence momentum  $p_0$ , they form an antideuteron. The same principle holds for heavier antinuclei, but the relative momentum between all nucleon pairs must be smaller than the  $p_0$  value. Due to a lack of underlying physics, this parameter must be obtained from fits to data. What accelerator experiments usually measure are the momentum spectra of the particles. Within the coalescence picture, the nucleon spectra ( $d^3N_p / dP_p^3$ ,  $d^3N_n / dP_n^3$ ) can be related to the nuclei spectrum ( $d^3N_A / dP_A^3$ ) by the following relation [202]

$$E_A \frac{d^3N_A}{dP_A^3} = B_A \left( E_p \frac{d^3N_p}{dP_p^3} \right)^Z \left( E_n \frac{d^3N_n}{dP_n^3} \right)^N \Big|_{P_p=P_n=P_A/A}, \quad (5.7)$$

where  $E_A$ ,  $E_p$ ,  $E_n$  are the energies of nuclei, proton and neutron with corresponding momentum  $P_A$ ,  $P_p$ ,  $P_n$ ;  $A$  is the mass number for nuclei of interest, while  $Z$  and  $A$  are the proton and neutron numbers, respectively. Finally,  $B_A$  is the so-called coalescence parameter, which can be related to the  $p_0$  parameter, assuming isotropic nucleon yields, as

$$B_A = A \left( \frac{4\pi}{3} \frac{p_0^3}{m_N} \right)^{A-1}. \quad (5.8)$$

The nucleon spectra in Eq. 5.7 must be known to model the nuclei spectra. As in cosmic ray studies, we are interested in antinuclei production within a wide range of collision energies; such nucleon spectra could not be possibly measured at all collision energies of interest. Thus, the event generators are employed to infer nucleon spectra at energies without available data. However, such a model is extremely simplistic, not including the momentum correlations. Thus, the event-by-event coalescence is employed instead of using the factorised coalescence model and Eq. 5.7. In such a case, an event generator simulates collisions and nucleons are produced. Then a coalescence afterburner is implemented, which checks on an event-by-event basis if the relative momentum between nucleons is smaller than  $p_0$ . However, one must ensure the particle production and momentum correlations are correctly implemented in the employed event generator. In some studies, the relative distance between nucleons is also checked in the event-by-event coalescence.

The event-by-event coalescence, checking only for the relative momentum, has been implemented by Shukla et al. [204] and employed to predict antideuteron and antihelium-3 cosmic ray fluxes stemming from cosmic ray collisions with the interstellar medium. In Shukla et al., the EPOS-LHC [253] event generator was employed, which has been proven to reproduce the available measured nucleon spectra the best [254]. The authors found that to reproduce the best available antideuteron data, the coalescence momentum  $p_0$  must be parametrised as a function of collision energy. While the  $p_0$  value should not be energy dependent, the different collision energies result in different collision system sizes, which can impact the probability for nucleons to coalesce [202]. The function used for antideuterons in Refs. [204, 254]

$$p_0 = \frac{A}{1 + \exp(B - \ln(E_{\text{kin}}/\text{GeV})/C)}, \quad (5.9)$$

where  $A, B, C$  are parameters. The best-fit result showed that the  $p_0$  value saturates at high energies and equals 179.2 MeV. Once Shukla et al. constrained their coalescence model to the available antideuteron data from lower energy collisions, they validated it employing ALICE data. Their obtained results are shown in Fig. 5.17.

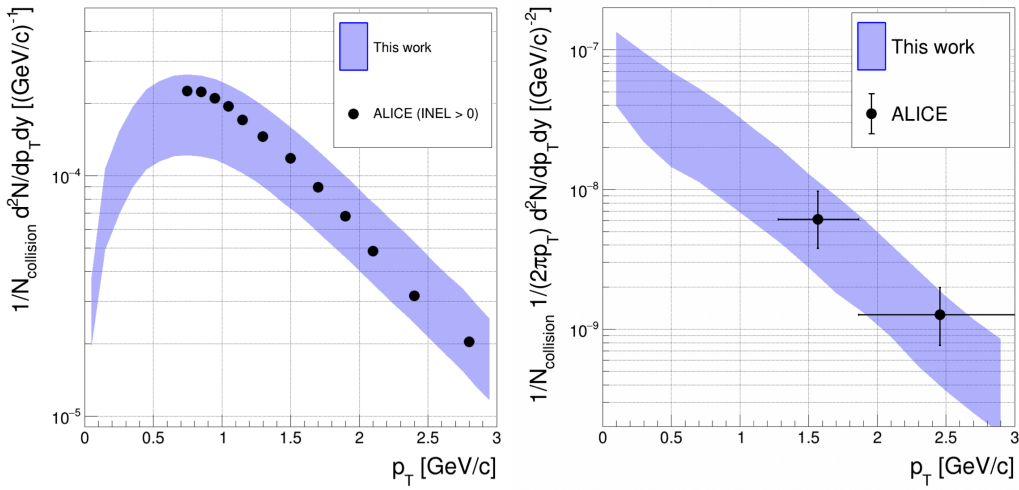


FIGURE 5.17: Left: Number density of antideuterons as a function of transverse momentum measured by ALICE in pp collisions at  $\sqrt{s} = 13$  TeV (black circles) and prediction of coalescence model (blue band). Right: Number density of antihelium-3 as a function of transverse momentum measured by ALICE in pp collisions at  $\sqrt{s} = 7$  TeV (black circles) and prediction of coalescence model (blue band). The bands are obtained by varying the coalescence parameter by plus 30%. Figures taken from Ref. [204].

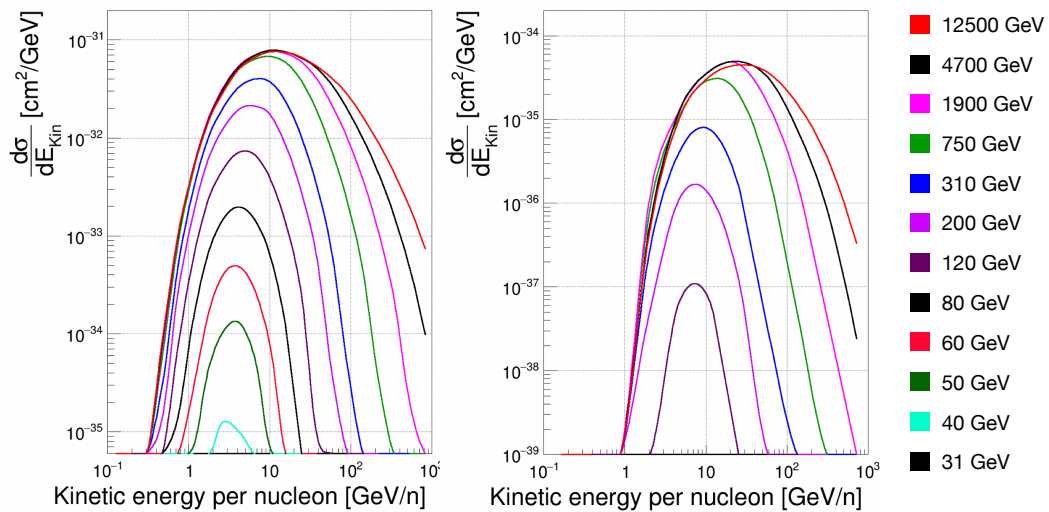


FIGURE 5.18: Differential antideuteron (left) and antihelium-3 (right) production cross sections for different pp collision energies, shown as different colour lines. Figures adapted from Ref. [204].

The left panel compares the antideuteron number density, while the right panel present the antihelium-3 case. The blue band corresponds to the Shukla et al. coalescence model predictions, with the coalescence momentum varied from the best-fit value up to plus 30%. The model reproduces the ALICE data shown as black circles; however, the chosen uncertainty is large. Once the model was validated, the authors produced what is necessary for cosmic ray studies - the differential antinuclei production cross section as a function of the kinetic energy per nucleon for different pp collision energies. The obtained results are shown in Fig. 5.18. The antideuteron results are shown in the left panel, while the antihelium-3 case is presented in the right panel. The different colour lines represent different collision energies. We implemented these differential production cross sections in GALPROP to predict the cosmic ray antinuclei fluxes, following Eq. 5.3, as shown in Chapter 6.

### Advanced coalescence model

Advanced coalescence models take into account the antinuclei wave function. The antinuclei production spectra for deuterons can be expressed as [255]

$$\frac{d^3 N_d}{d P_d^3} = \frac{S}{(2\pi)^6} \int d^3 q \int d^3 r_p d^3 r_n \mathcal{D}(\mathbf{r}, \mathbf{q}) W_{np}(\mathbf{P}_d/2 + \mathbf{q}, \mathbf{P}_d/2 - \mathbf{q}, \mathbf{r}_n, \mathbf{r}_p), \quad (5.10)$$

where  $S$  is a statistical factor to take care of spin and isospin values of the two-nucleon state and for deuteron equals to 3/8;  $\mathcal{D}(\mathbf{r}, \mathbf{q})$  is the Wigner function of the internal deuteron wave function;  $W_{np}(\mathbf{P}_d/2 + \mathbf{q}, \mathbf{P}_d/2 - \mathbf{q}, \mathbf{r}_n, \mathbf{r}_p)$  is the two-body Wigner function of proton and neutron;  $\mathbf{P}_d$  corresponds to the deuteron momentum;  $\mathbf{r}_n, \mathbf{r}_p$  are the average positions of neutron and proton and  $\mathbf{q}$  is half the relative momentum between neutron and proton. In such formalism, the Wigner function of neutron and proton depends simultaneously on relative momentum and distance between the nucleons. However, usually, the factorisation of momentum and coordinate space is assumed as

$$W_{np}(\mathbf{P}_d/2 + \mathbf{q}, \mathbf{P}_d/2 - \mathbf{q}, \mathbf{r}_n, \mathbf{r}_p) = H_{np}(\mathbf{r}_n, \mathbf{r}_p) G_{np}(\mathbf{P}_d/2 + \mathbf{q}, \mathbf{P}_d/2 - \mathbf{q}), \quad (5.11)$$

where the coordinate-space component  $H_{np}(\mathbf{r}_n, \mathbf{r}_p)$  is approximated to be a Gaussian source, which, as explained in Chapter 1.5.1, is a valid assumption following the femtoscopic studies. The momentum-space component  $G_{np}(\mathbf{P}_d/2 + \mathbf{q}, \mathbf{P}_d/2 - \mathbf{q})$  in such models is obtained from Monte Carlo generators which also account for possible momentum correlations between neutrons and protons.

Kachelriess et al. described such a formalism in their recent publication [255]. The coordinate-space component can be rewritten as  $H_{np}(\mathbf{r}_n, \mathbf{r}_p) = h(\mathbf{r}_n) h(\mathbf{r}_p)$ , where

$$h(\mathbf{r}) = (2\pi\sigma^2)^{-3/2} \exp\left\{-\frac{r^2}{2\sigma^2}\right\}, \quad (5.12)$$

with  $\sigma$  being the only free parameter in the entire model. This parameter was estimated to be around 1 fm [255] but is used as a fit parameter. Kachelriess et al. also used this model to study cosmic ray antinuclei fluxes [202]. They employed two event generators, Pythia and QGSJET II, and fitted their model to available antideuteron data, including ALICE measurements. The obtained best-fit results compared to ALICE data are shown in Fig. 5.19. The blue circles correspond to the differential antideuteron spectra measured by ALICE; the solid orange line - coalescence prediction employing QGSJET II event generator; the red dotted-dashed

line - results obtained with QGSJET II but including a weight applied on the antiproton spectrum to improve agreement with the antiproton measurements; green dashed line, shown only for  $\sqrt{s}=7$  TeV energy collisions, shows prediction employing Pythia 8.23 event generator. QGSJET II results in a good agreement with data for the lowest collision energy. As the collision energy increases, the QGSJET II can no longer reproduce the antideuteron spectra at a high transverse momentum region. However, as the authors show, the discrepancy disappears if the antiproton momentum obtained from QGSJET II is weighted to be in better agreement with the antiproton data. This shows that the coalescence model itself is not the issue. The main improvement of such an advanced model, compared to the simplistic one, is that only one  $\sigma$  parameter value can explain data at different collision energies, the model takes into account the deuteron wave function and the coordinate-space distribution of the produced nucleons.

Kachelriess et al. also calculated the differential antideuteron production cross section for different collision energies. We employ their obtained results to estimate the cosmic ray antideuteron fluxes, as shown in Chapter 6. A more detailed comparison of the simplistic and advanced coalescence models will be provided there.

### 5.3.2 Inelastic interactions of antinuclei with matter

The antinuclei produced in the galaxy might collide with the interstellar gas and disappear. Such disappearance probability can be quantified by measuring the inelastic cross section. Such measurements are usually performed in a fixed target experiment with a beam of particles of interest. However, producing and manipulating a beam of antinuclei is extremely complicated. There was a successful attempt in 1970, where a 70 GeV accelerator was used to collide protons with an aluminium target to produce antideuterons which were then directed to a target of interest [256]. However, the experiment measured only antideuterons with a momentum of 13.3  $\text{GeV}/c$ . The newest antideuteron inelastic cross section measurement was performed by the ALICE Collaboration, using the detector itself as a target material [109]. ALICE also measured the antihelium-3 inelastic cross sections, which have never been measured before [110]. ALICE uses the antimatter-to-matter ratio method and the TOF-to-TPC matching method. The former takes advantage of the primordial antimatter-to-matter ratio reaching unity at the LHC energies [257], while the reconstructed raw ratio is below unity, as the antinuclei and nuclei interact differently with the material. The measured ratio can be used with Monte Carlo simulating the nuclei and antinuclei interactions with the detector to extract the antinuclei inelastic cross section. The second method, TOF-to-TPC matching, is similar to a fixed target experiment. The number of antinuclei is counted by the TPC detector, which is closer to the antinuclei

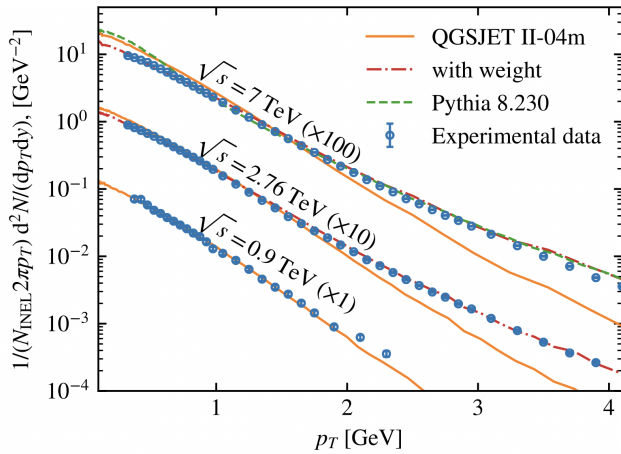


FIGURE 5.19: Best-fit coalescence model results compared to ALICE data. [202]. The details are provided in the text.

production point. Then the antinuclei are counted by the TOF detector and some of the antinuclei are lost in the TRD detector material, which is installed between the TPC and TOF. The ratio of reconstructed antinuclei in both detectors can be again used with the Monte Carlo simulations to extract the relevant inelastic cross section. The antideuteron and antihelium-3 measured inelastic cross sections are shown in Figs. 5.20 and 5.21, respectively.

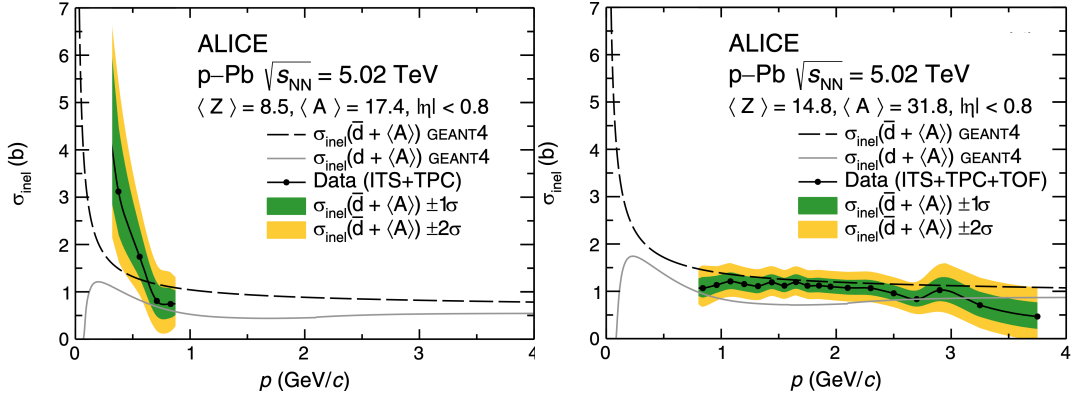


FIGURE 5.20: Antideuteron inelastic cross sections measured by the ALICE Collaboration [109]. The dashed and grey lines correspond to the GEANT4 prediction. The black circles show the data while the green and yellow bands represent  $1\sigma$  and  $2\sigma$  total uncertainty. Left panel shows low momentum antideuteron measurements obtained employing the ITS and TPC detectors, while the right panel shows results for higher momentum range obtained employing ITS, TPC and TOF detectors.

Antideuterons can be identified employing the TPC only at low momentum (below  $\sim 2$  GeV) while the TOF detector has high enough efficiency only at larger momentum range, see Figs. 2.6 and 2.7. The missing overlap between the momentum range at which antideuterons can be identified with either of the two detectors prevents one from using the TOF-to-TPC method. Thus, the antideuteron inelastic cross section was measured only employing the antimatter-to-matter ratio method in pp collisions. At large momentum, the antideuterons are reconstructed by requiring a hit in the TOF detector, ensuring that all measured particles traversed the entire detector up to TOF. The more material particles traverse, the more sensitive the measurement to the inelastic interactions is. The result is shown in the right panel of Fig. 5.20. The average traversed material was estimated to have charge and mass numbers  $\langle Z \rangle = 14.8, \langle A \rangle = 31.8$ , respectively. However, the low-momentum particles usually do not reach TOF because of their curvature in the magnetic field and the more significant probability of interacting inelastically. For the low momentum particles, the antideuteron inelastic cross section was measured without the specific requirement in the TOF, resulting in average material with  $\langle Z \rangle = 8.5, \langle A \rangle = 17.4$ , as shown in the left panel of Fig. 5.20. In both cases, the solid and dashed lines show the ratio expected from the Monte Carlo simulation, obtained employing the GEANT4 simulations with full implementation of the ALICE detector (except the line connecting the data points).

The antihelium-3 inelastic cross section was measured with both methods, as such antinuclei can be very well identified employing the TPC at full momentum range because of their double charge. The result published by ALICE for the inelastic antihelium-3 cross section employing the antimatter-to-matter method is shown in the left panel of Fig. 5.21. The low momentum region was measured without the

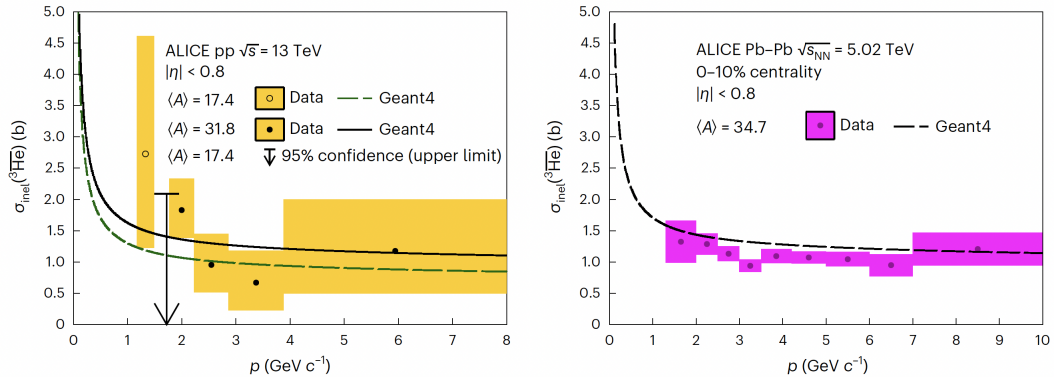


FIGURE 5.21: Antihelium-3 inelastic cross sections measured by the ALICE Collaboration [110]. The lines represent GEANT4 predictions, black circles show the data, while yellow and pink bands correspond to  $1\sigma$  total uncertainty. Left: Results obtained employing the antimatter-to-matter ratio method in pp collisions. Right: Results obtained employing the TOF-to-TPC matching method in Pb-Pb collisions.

TOF hit requirement (empty circle and arrow, averaged target material  $\langle A \rangle = 17.4$ ). In contrast, results for the high momentum region were obtained with the TOF hit requirement (average material  $\langle A \rangle = 31.8$ ). The right panel of the Fig. 5.21 represents the inelastic antihelium-3 cross section obtained with the TOF-to-TPC matching method (average material  $\langle A \rangle = 34.7$ ).

The presented ALICE measurements employ the detector as a target material, resulting in a relatively heavy average target material. However, hydrogen and helium-4 are the primary targets in the interstellar medium. Thus the results obtained by ALICE will have to be extrapolated to the lighter targets before implementing them in GALPROP. Such procedure is described in Chapter 6.



## Chapter 6

# Secondary cosmic ray antideuteron and antihelium fluxes

A precise and data-driven estimation of expected secondary cosmic ray antinuclei fluxes is necessary for indirect dark matter searches. While some ingredients can be constrained by astrophysicists, such as the interstellar gas or supernova distributions in our Galaxy, others must be measured in accelerator facilities on Earth. The crucial ingredients for the secondary antinuclei fluxes are the propagation model, the production cross section and the inelastic interaction cross section. The propagation of cosmic rays in the Galaxy is a long-studied problem, and many available models exist to solve the necessary transport equation. However, even for the same codes, several different parameter sets can be obtained by fitting the model to different selections of measured cosmic ray fluxes [199, 238, 258]. The propagation parameters are related to the underlying processes thus the obtained parameter values are related to different physics assumptions - is re-acceleration or convection relevant for our Galaxy? Another relevant question is the production cross section of light (anti)nuclei - there is no agreed-upon process for how the light nuclei are formed. This results in many different models, ranging from statistical hadronization to coalescence, which try to interpret the data from accelerator experiments. While the models might explain the data equally well, they are used in cosmic ray studies to extrapolate and interpolate the available data. Thus it is essential to compare the uncertainties on the fluxes not only related to the uncertainty of a specific model but also between the different models. Finally, the inelastic cross section is required to know how many of the produced antinuclei can reach the detectors at Earth without disappearing in the interstellar medium. Up to recently, there were only very limited measurements for antideuterons and no data at all for antihelium-3. Usually, a proton-antiproton inelastic cross section scaling was used for the cosmic ray antinuclei predictions. However, evaluating the uncertainty of the flux stemming from the inelastic cross section measurement is essential, which is possible only if data is available. While the expected uncertainty for the inelastic component is much smaller than the uncertainty stemming from the production mechanism, it is a pivotal part of future cosmic ray studies once precise measurements of antinuclei fluxes become available. In this work, we study how the antideuteron fluxes are affected by the points mentioned above - how does the flux change if we use different propagation parameters in GALPROP? How different are the predicted fluxes if two different coalescence models are used for the antinuclei production? Moreover, finally - what are the effect and the uncertainty on the flux from the recently measured antinuclei inelastic cross sections by ALICE? For the first time, we performed these studies in a unified framework, which allowed us to pinpoint the realistic uncertainties in the field. Finally, we estimated the secondary cosmic ray antihelium-3 flux. We quantified the

effect of inelastic interactions in the Galaxy by defining the so-called transparency observable for both antideuteron and antihelium-3 nuclei. Such observable allows us to estimate how many produced particles that could reach dedicated detectors would survive the trip. In the following, we discuss the source functions obtained with different coalescence models, show how we estimated the inelastic cross section for light targets employing ALICE data, and finally show the resulting fluxes and uncertainties.

The secondary flux results will be compared to a specific prediction of cosmic ray antinuclei fluxes stemming from dark matter annihilations obtained by my colleague Stephan Königstorfer, employing the same GALPROP setup [259].

The results obtained in this thesis on cosmic ray antideuterons were published in PRD [159] and antihelium-3 in Nature Physics [110]. The Nature Physics publication also has a related public ALICE note [260].

## 6.1 Source functions

The source function (Eq. 5.3) for secondary antinuclei was shown and explained in Chapter 5.2.1. This equation can also be used to estimate the local source function at the Solar System location. In such a case, the gas distribution is assumed to be uniform, and the gas number densities are set to  $n_p = 0.9 \text{ cm}^{-3}$  and  $n_{\text{He}} = 0.1 \text{ cm}^{-3}$ . The AMS-02 data serves as an input cosmic ray flux in Eq. 5.3. The authors of Ref. [159] estimated such source functions for antideuterons employing the two coalescence models introduced in Chapter 5.3. The left panel of Fig. 6.1 shows the total antideuteron production cross sections as a function of the projectile energy. The

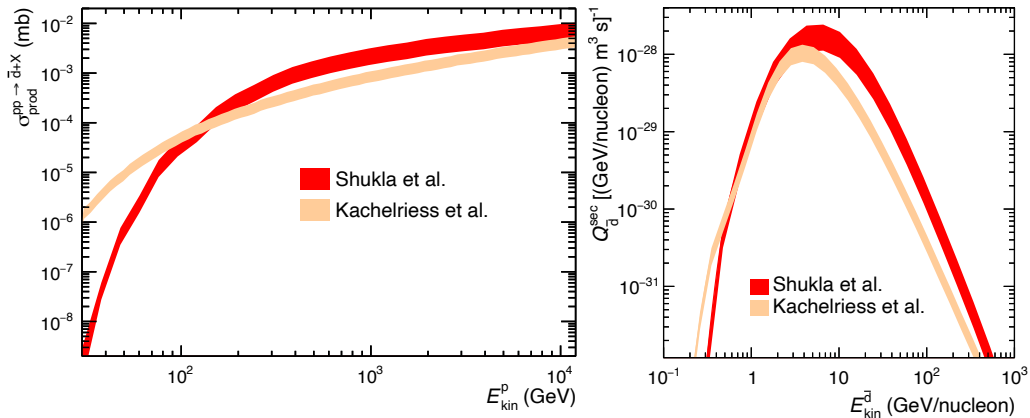


FIGURE 6.1: Left: Antideuteron production cross section in pp collisions as a function of the projectile kinetic energy. Right: Local source function (see Eq. 5.3) as a function of the antideuteron kinetic energy. The included collision systems are  $p - H$ ,  $p - \text{He}$ ,  $\text{He} - p$ ,  $\bar{p} - p$ , and  $\bar{p} - \text{He}$ . Figures taken from Ref. [159].

red band corresponds to the Shukla et al. coalescence model [204], while the peach colour band corresponds to the Kachelriess et al. model [202]. In the case of the latter, we used their production cross sections obtained with the QGSJET II model. The cross section is shown for the pp collision system. The two approaches consider slightly different data sets and employ different event generators. The cross sections predicted by Kachelriess et al. have up to several orders of magnitude higher

values at lowest projectile energies  $E_{\text{kin}}^{\text{P}} < 100 \text{ GeV}$ . At this energy range, Shukla et al. included deuteron and antideuteron production cross section at p-p and p-Be collisions with projectile proton momentum of  $70 \text{ GeV}/c$  measured at Serpukhov [261] in their fits, while Kachelriess et al. did not. It has already been observed that this dataset suggests lower antideuteron yields than was expected from observations at higher energies [254]. At  $E_{\text{kin}}^{\text{P}} > 200 \text{ GeV}$ , the antideuteron production cross section from Kachelriess et al. becomes lower than the Shukla et al. The effect can be related to the underproduction of antinucleons in QGSJET-II at such high energies, with associated uncertainties that are not quantified yet [202]. The observed differences between the predictions by the two coalescence models suggest that more high precision data of antideuteron and antiproton production in p – p collisions is necessary to both fine-tune the employed event generators and better fit the free parameters of the coalescence model. Additionally, the antinuclei production measurements in other relevant collision systems, such as p – He, He – He, are required.

The local source functions obtained employing these production cross sections are shown on the right panel of Fig. 6.1 as a function of the antideuteron kinetic energy per nucleon. The p – H, p – He, He – p,  $\bar{p}$  – p, and  $\bar{p}$  – He collision systems are included in these results. Kachelriess et al. estimated the production cross sections for all collision systems employing their coalescence model, while Shukla et al. studied only the pp system explicitly and obtained the rest of the collision systems by applying scaling factor  $(A_{\text{T}} A_{\text{P}})^{2.2/3}$  [204]. The source function, in simple words, corresponds to the convolution of the projectile cosmic ray flux and the production cross section. At low antideuteron energies, the local source function for Kachelriess et al. production cross section is higher than that for Shukla et al. At high energies, the opposite is observed. The shown uncertainty corresponds to the uncertainty from coalescence models.

While such studies are interesting to compare the two models, the main goal of this work is to obtain the secondary cosmic ray fluxes within the GALPROP framework. Thus, we implemented the Eq. 5.3 in GALPROP. The default gas distribution, presented in Chapter 5.2.2, was used. GALPROP solves the transport equation simultaneously for all particle species, following the nuclear reaction network [262]. The cosmic ray distributions are first calculated for the ordinary cosmic rays, and the obtained results are used to estimate the secondary fluxes. The antideuteron and antihelium-3 production cross sections were implemented in GALPROP as read-only tables. In the case of the production cross sections from Shukla et al., an interpolation had to be used to obtain the logarithmic energy grid in both the projectile kinetic energy and produced antideuteron kinetic energy per nucleon as required in GALPROP. An interpolation as a function of collision energy had to be performed. Figure 6.2 shows the result of such an interpolation for antihelium-3 nuclei. The black circles depict the Shukla et al. results, while the red crosses correspond to the values obtained employing the cubic interpolation function in Python. The left panel shows results for the antihelium-3 production cross section with  $E_{\text{kin}} = 4.71 \text{ GeV}/A$ , while the right panel represents the case of  $E_{\text{kin}} = 134.25 \text{ GeV}/A$ . More details can also be found in the ALICE public note [260]. The source function was implemented for antideuterons employing both Kachelriess et al. and Shukla et al. cross sections, while only the latter was implemented for the antihelium-3 case.

We investigated the 2D source for antideuterons in p-H collisions as a function of the kinetic projectile energy and the produced antideuteron kinetic energy per nucleon. The source function was extracted from GALPROP and estimated at the

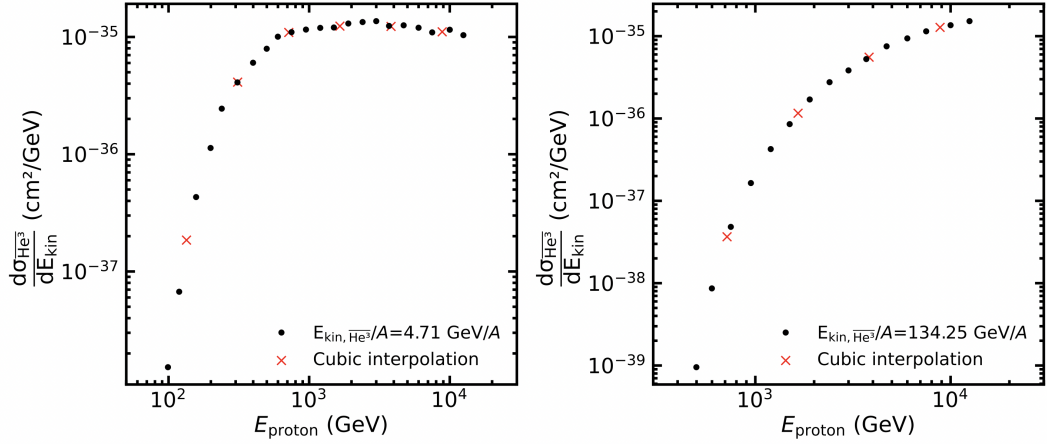


FIGURE 6.2: Production cross section as a function of projectile kinetic energy for antihelium-3 with kinetic energy per nucleon of  $4.71 \text{ GeV}/A$  (left) and  $134.25 \text{ GeV}/A$  (right). The black circles correspond to the Shukla et al. cross sections, and the red crosses show the interpolated values.

Solar System location. Fig. 6.3 shows that the most significant contribution to the antideuteron yield comes from cosmic-ray energies around  $300 \text{ GeV}$ , suggesting that centre-of-mass energies around  $\sqrt{s} = 20 \text{ GeV}$  are the most relevant for the antideuteron production in our Galaxy and that the coalescence models should be precisely tuned in this energy regime. Most importantly, both panels of Figure 6.1 show that the uncertainties of specific coalescence models are smaller than the difference between them.

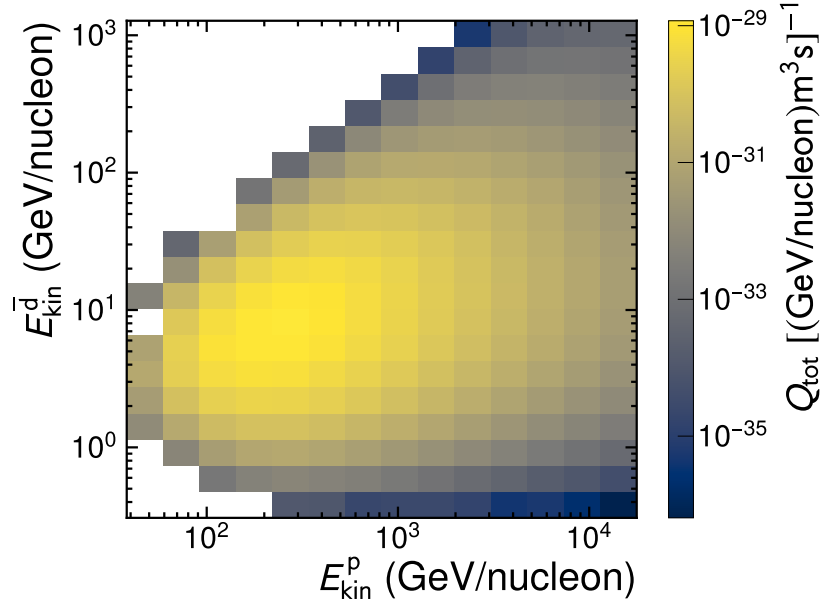


FIGURE 6.3: Antideuteron source as a function of the kinetic projectile energy and the produced antideuteron kinetic energy per nucleon. Only the p-H collision system is included.

## 6.2 Inelastic cross sections

Inelastic cross sections shown in Chapter 5.3 are measured employing the ALICE detector as a target material, which corresponds to target nuclei with relatively high mass number  $\langle A \rangle = 17.4 - 34.7$ . In the Galaxy, hydrogen and helium gases constitute the main targets. Thus the results published by ALICE must be extrapolated to lighter targets. There are no first-principle calculations that can predict the inelastic interactions and could thus be constrained by the ALICE data. However, nuclear models allow scaling the measured inelastic cross sections to different targets. The GEANT4 toolkit includes predictions for antinucleus–nucleus inelastic cross sections based on Glauber modelling [263–265]. The Glauber model describes antinucleus–nucleus interactions by scaling antinucleon–nucleon cross sections accordingly to the overlap of the antinucleus and nucleus wave functions [264].

The cross sections in GEANT4 are described by a parametrization which depends on the projectile and target nuclei radii and nucleon number because performing Glauber calculations during the GEANT4 run is too computationally expensive. Such parametrization is then fitted to available experimental data and Glauber calculation results and shown to agree within 8% for the different nuclei targets [264]. Thus, the authors of Ref. [159] used GEANT4 to extrapolate the ALICE results to lighter nuclei. A correction factor for the GEANT4 was obtained as a ratio of the ALICE data and the GEANT4 prediction for the corresponding target nuclei with mass number  $\langle A \rangle = 17.4$  at low momentum and  $\langle A \rangle = 31.8$  at large momentum [110, 259]. The inelastic cross sections on relevant targets were then estimated by taking the default GEANT4 values of antideuteron inelastic cross sections on proton and helium-4 nuclei and scaling it by the corresponding correction factors.

In addition to the experimental uncertainty from the ALICE collaboration, such an estimate includes 8% uncertainty on the target nuclei scaling. The same procedure was followed by ALICE Collaboration to extrapolate the measured antihelium-3 inelastic cross section for targets with mass numbers  $\langle A \rangle = 17.4, 31.8, 34.7$  to lighter targets [110]. The inelastic cross sections obtained for antideuteron (left) and antihelium (right) nuclei on proton targets are shown in Fig. 6.4.

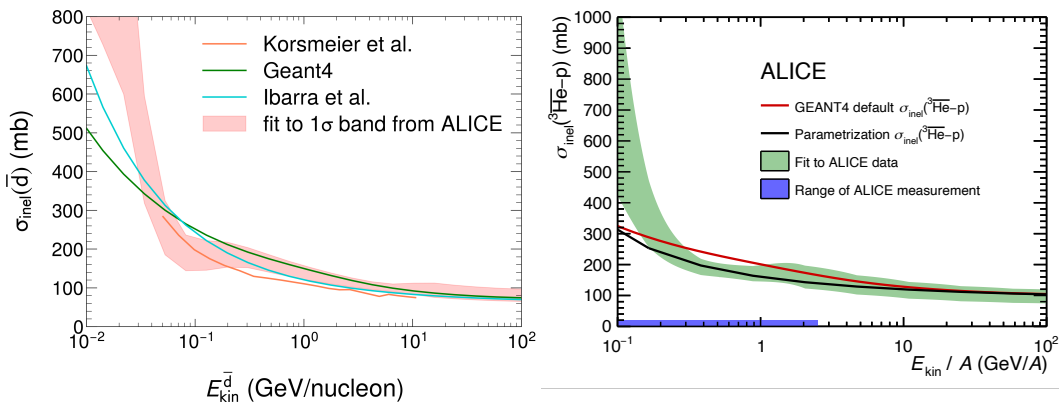


FIGURE 6.4: Antideuteron [159] (left) and antihelium-3 [110] inelastic cross section on a proton target. The red (left panel) and green (right panel) bands correspond to the inelastic cross section estimated based on ALICE data. The green (left) and red (right) lines correspond to the default GEANT4 values. The rest of the lines represent different parametrizations employed so far in the cosmic ray field.

The green line in the left panel represents the default antideuteron inelastic

cross section values in GEANT4. These values are scaled by a correction factor from ALICE data, and the result is shown as the red band. The band includes the experimental  $1\sigma$  uncertainty and the 8% uncertainty from the target  $A$  scaling in GEANT4. The red and blue lines show inelastic cross sections used in cosmic ray studies by Korsmeier et al. [205] and Ibarra et al. [172]. The results for antihelium-3 are shown in the right panel. The red line corresponds to the GEANT4 prediction; the green band shows the obtained inelastic cross section corrected by ALICE measurement, and the black line shows a parametrization used by Korsmeier et al. [205].

We implemented antideuteron and antihelium-3 inelastic cross sections from GEANT4 and the new estimates based on ALICE data in GALPROP for proton and helium-4 targets.

### 6.3 Resulting antideuteron fluxes and transparency

The main results for cosmic ray antideuterons were obtained employing the Boschini et al. propagation parameters discussed in Chapter 5.2.2. The resulting LIS flux is shown on the upper panel of Fig. 6.5. The secondary fluxes (red bands and lines) were obtained in this thesis. They are compared to a prediction of cosmic ray antideuteron flux stemming from dark matter particle annihilation. The latter is obtained using the same propagation scheme with the same implementation of inelastic cross sections [159, 259]. The dark matter particle is assumed to annihilate via the  $W^+W^-$  channel and the mass hypothesis of  $m_{DM,WW} = 94, 100, 1000$  GeV were tested based on the production spectra published in Refs. [172, 203]. Indeed, the obtained results show that cosmic ray antideuterons provide an almost background-free probe for dark matter annihilations at low kinetic energies for low mass assumption of  $m_{DM,WW} = 100$  GeV. However, for the higher  $m_{DM,WW} = 1000$  GeV mass case, the background flux is much higher than the signal. Same conclusion was reached for other dark matter annihilation channels, such as  $\chi + \chi \rightarrow b\bar{b} \rightarrow \bar{d} + X$  or the production of antideuterons via the dark matter annihilation to  $\Lambda_b$  and its subsequent decay [159].

The bands in Fig. 6.5 correspond to the result obtained using the inelastic cross section constrained by ALICE data. The line shows results obtained with the default GEANT4 values. The band width represents uncertainty stemming only from the inelastic cross section evaluation. The red band shows results obtained employing Shukla et al. production cross sections, while the peach colour band represents results obtained with the Kachelriess et al. production cross sections. Even though the shapes of the total production cross section and the source function were relatively different (Fig. 6.1), the shapes of resulting fluxes are somewhat similar. However, the flux obtained with Shukla et al. cross section is higher.

The lower panel of Fig. 6.5 shows results after solar modulation. The solar modulation was performed employing the Force-Field approximation, and the Fisk potential value is 0.5 GV. Such a value corresponds to a solar minimum, providing the best conditions for cosmic antinuclei detection. The solar-modulated flux can also be called top-of-the-atmosphere (TOA) flux. There are only slight changes in contrast to the LIS flux. The TOA fluxes can be compared to the existing experimental upper limits, corresponding to the BESS measurement depicted as a black horizontal line [206].

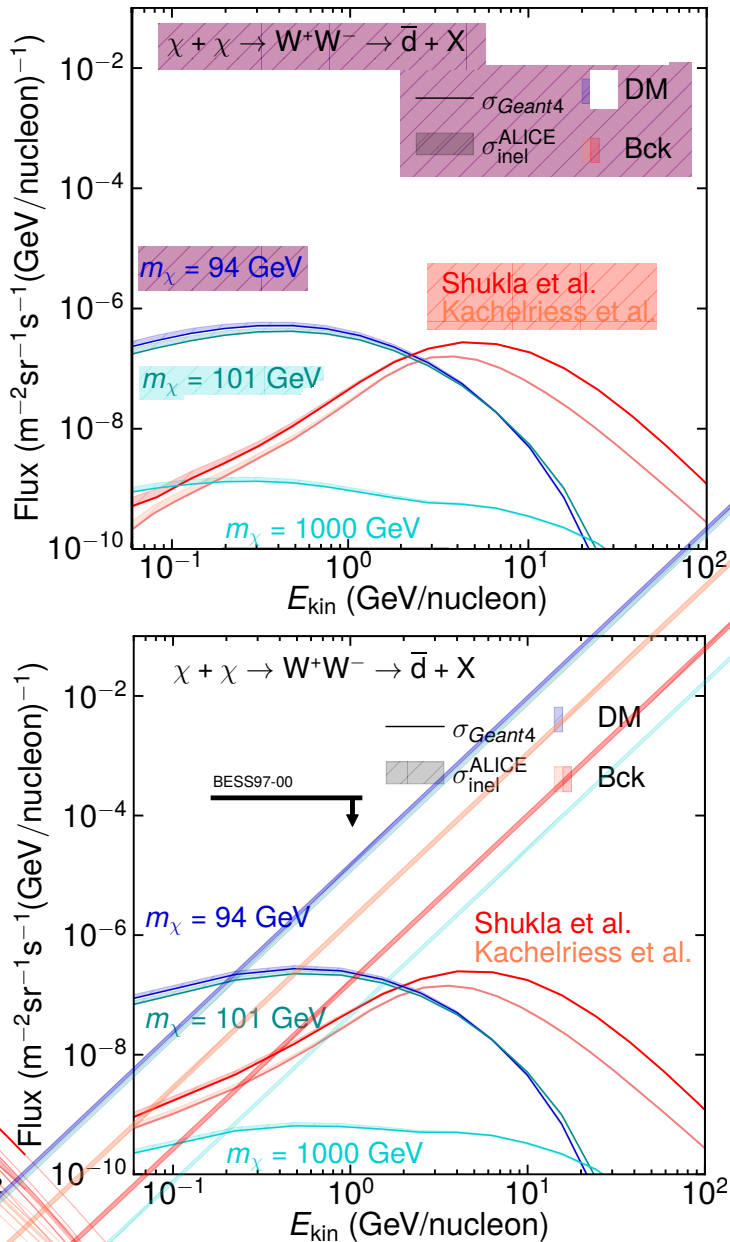


FIGURE 6.5: Upper panel: Antideuteron local interstellar flux from the secondary origin (red bands and lines) obtained in this thesis. The result is compared to prediction of cosmic ray antideuteron fluxes stemming from dark matter annihilation (blue bands and lines) for different dark matter mass assumptions from Ref. [159]. Lower panel: Same results but after the solar propagation. The BESS97-00 line shows exclusion limits obtained by the BESS experiment [206].

The top panel of Fig. 6.6 shows the comparison of the LIS fluxes obtained employing different inelastic cross section parametrizations used in the field (shown in Fig. 6.4). The obtained cosmic ray fluxes are in good agreement. The relative uncertainty on the flux, stemming from inelastic cross section estimation with ALICE data, is shown in the lower panel of Fig. 6.6. The relative uncertainty reaches a maximum of 25%, which is small compared to the uncertainties observed from the different production models.

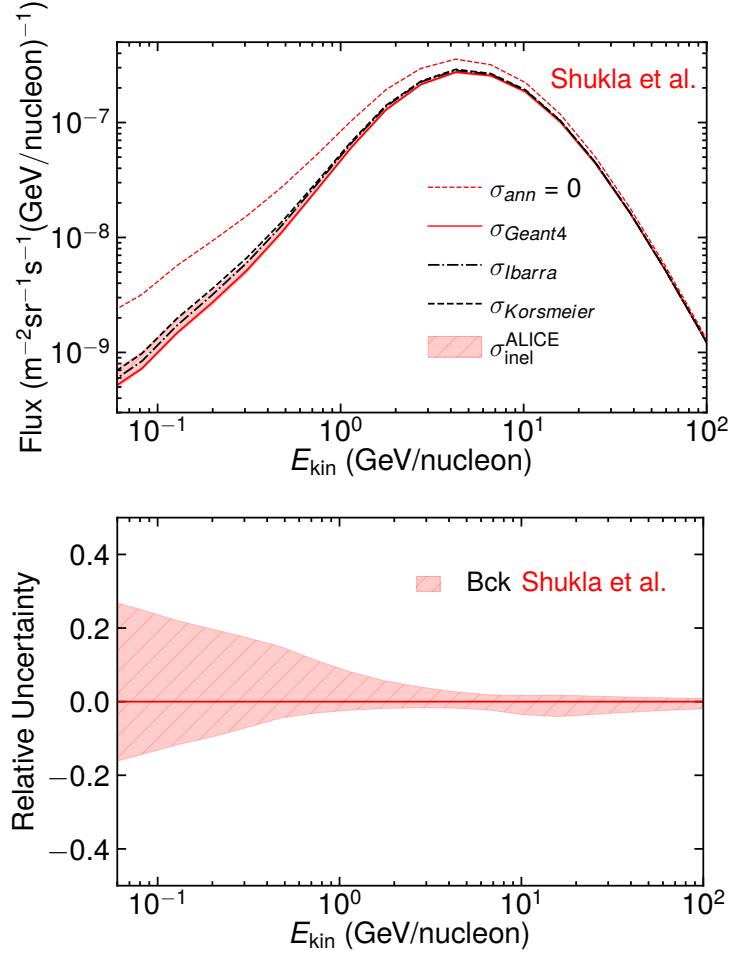


FIGURE 6.6: Upper panel: Secondary antideuteron LIS fluxes obtained employing different inelastic cross section parametrizations, as explained in the text. Lower panel: The relative uncertainty on the flux stemming from inelastic cross section estimation.

The obtained fluxes were used to estimate the transparency of the Galaxy to the cosmic ray antideuteron flux propagation. The transparency is defined as the ratio of the flux obtained with inelastic interactions and the flux obtained without inelastic interactions in the Galaxy. The results are shown in Fig. 6.7 for the LIS fluxes (left) and for TOA fluxes (right). The transparencies for secondary fluxes obtained in this thesis (red and peach colours) are compared to the transparency expected for cosmic ray antideuterons from dark matter annihilation (blue colour) from Ref. [159]. The transparency expected for the dark matter component is around 50%. For the secondary LIS fluxes, it increases from 20% to 90% with increasing energy; while for the TOA fluxes, it increases from 40% to 90%.

The transparency is different for the antideuteron cosmic rays stemming from dark matter annihilation and from cosmic ray collisions with the interstellar medium even though the inelastic cross section is not sensitive to the origin of the antideuteron. However, transparency depends not only on the inelastic cross section but also on the initially produced antideuteron spectra, the location of the production which determines the amount of traversed gas in the interstellar medium and also the propagation as it changes the momentum of the antinuclei. The transparency for secondary flux was estimated employing both introduced antideuteron production

cross sections. The results are almost identical; thus, the lines and the band corresponding to different production cross sections are on top of each other in Fig. 6.7. Such an agreement shows that transparency is indeed the same if the antinuclei source functions have a similar shape (see right panel of Fig. 6.1) and the production location and propagation are the same.

Our results show that the Galaxy is transparent to the cosmic ray antideuterons and that future experiments have a chance at measuring such antideuteron fluxes stemming from both dark matter annihilation and from cosmic ray collisions with the interstellar medium.

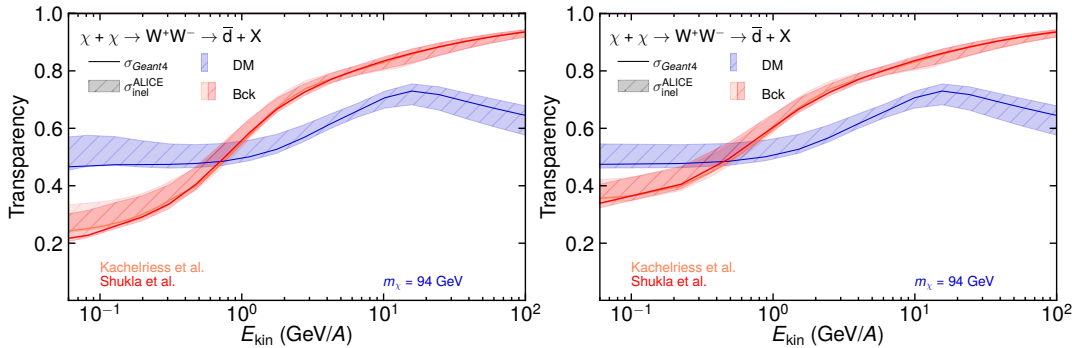


FIGURE 6.7: Transparency of the Galaxy to the cosmic ray antideuteron propagation. Red bands and lines show results for the secondary fluxes obtained in this thesis. The results are compared to transparencies expected for cosmic ray antideuteron fluxes stemming from dark matter annihilation from Ref. [159]. The transparencies are shown for LIS (left) and TOA (right) fluxes.

Finally, we also tested how the secondary cosmic ray antideuteron flux depends on the propagation parameters used in GALPROP. The two parameter sets presented in Chapter 5.2.2 were employed. The comparison of the LIS fluxes obtained with the two different propagation parameter sets is shown in Fig. 6.8. The dotted-dashed line corresponds to the flux obtained with Boschini et al. parameters, and the dashed line with Cuoco et al. While propagation parameters are rather different, the obtained fluxes are in good agreement at kinetic energies above 1 GeV/ $A$ . This is expected since both sets were obtained by fitting GALPROP to the available AMS-02 data, which constrains this energy regime very well. At lower energies, the Boschini et al. parameters result in flux up to one order of magnitude larger than predicted employing Cuoco et al. parameters. The difference at low energies can be attributed to the stronger convection effects assumed by Cuoco et al., as the galactic wind forces the particles to move away from the galactic disk and halo. This hypothesis was tested by running GALPROP with Cuoco propagation parameters except the convection parameters  $V_{\text{conv}}$  and  $dV_{\text{conv}}/dz$  set to Boschini et al. values. Indeed, the discrepancy at low energies disappeared. A good agreement at large energies is also observed because the secondary fluxes are most sensitive to the ratio of the spatial diffusion parameter and the halo height (which for both parametrizations is similar), not the single values.

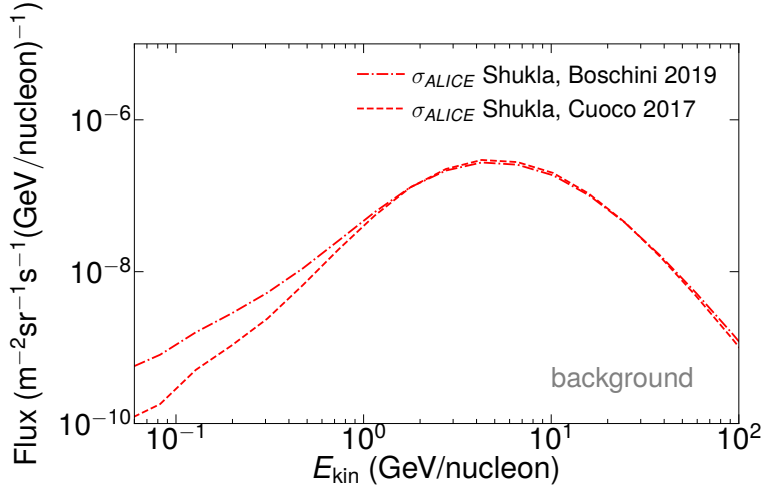


FIGURE 6.8: Comparison of antideuteron LIS fluxes obtained employing different propagation parameters. The dotted-dashed line corresponds to the flux obtained with Boschini et al. parameters and the dashed line with Cuoco et al.

### 6.3.1 Discussion on the uncertainties

There are some uncertainties on the cosmic ray antinuclei which are generic and influence both signal and background fluxes, and there are some which are antideuteron origin-specific. The uncertainties specific to dark matter have been discussed in Ref. [159] and include the unknown dark matter properties such as mass, self-annihilation cross section, and dominant annihilation channel. Also, the dark matter density distribution in the Galaxy is not very well known as different profiles can be used to describe the available data. In the case of the antideuterons produced in cosmic ray collisions with interstellar gas, the gas distributions can be mapped as explained in Chapter 5.2.2.

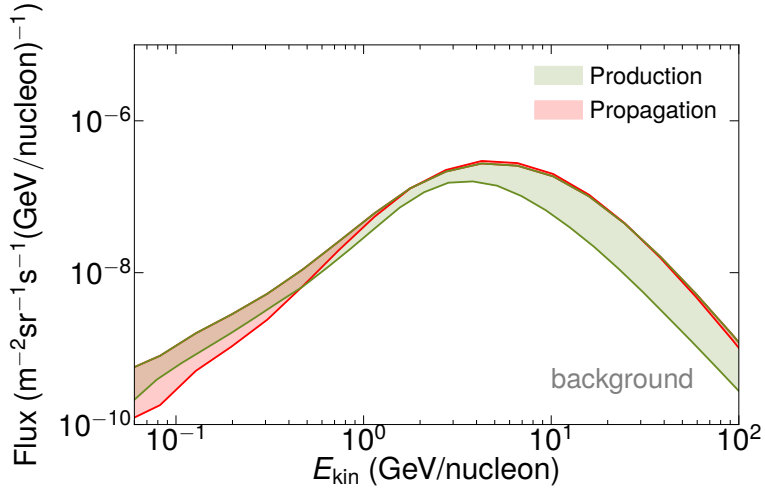


FIGURE 6.9: Comparison of systematic uncertainties stemming from the choice of the production and propagation models of antideuterons. The red band shows the uncertainty related to the propagation while the green band corresponds to the uncertainty coming from the choice of the production model (the model-specific uncertainty is not included).

The main uncertainties for the secondary cosmic ray antideuteron fluxes thus are, as mentioned, the production, propagation, and inelastic cross section with matter. The latter constitutes maximally a 25% uncertainty, as shown in Fig. 6.6. The dominating uncertainties coming from the choice of propagation parameters and production mechanism are compared in Fig. 6.9. The red band shows the difference between LIS obtained with Boschini et al. and Cuoco et al. propagation parameters, while the green band represents the difference between fluxes obtained employing two different production descriptions by Shukla et al. and Kachelriess et al. Here, the band does not include the model-specific uncertainties. The systematic uncertainty coming from the choice of production mechanism dominates the higher kinetic energy regime above 1 GeV/A. At lower energies, both systematic uncertainties are significant but the propagation uncertainty dominates.

## 6.4 Resulting antihelium fluxes and transparencies

The same procedure was performed to estimate the secondary cosmic ray antihelium-3 fluxes and the transparency of the Galaxy to the antihelium-3 propagation. The antihelium-3 production cross section was taken from Shukla et al. The secondary fluxes obtained in this thesis are again compared to the prediction of cosmic ray antihelium-3 flux stemming from dark matter annihilations from Ref. [159]. The assumed dark matter mass is 100 GeV. The obtained LIS (upper figure) and TOA (lower figure) fluxes are shown in the upper panels of Fig. 6.10. The dashed lines represent antihelium-3 fluxes if it is assumed that antihelium-3 does not interact with the interstellar gas at all. The solid lines and the bands correspond to the fluxes obtained with the default inelastic cross section values in GEANT4 and corrected by ALICE data, respectively. The signal-to-background ratio at low energies reaches up to four orders of magnitude, providing essentially background-free probe for dark matter annihilation. The band represent the uncertainty stemming from inelastic cross section estimation. The right panel also includes the sensitivity limits from the GAPS [210] and AMS-02 [205] experiments. Neither signal nor background fluxes reach either of the experimental sensitivities. This is expected for the background flux. It is important to remember that only one specific prediction for the antihelium-3 flux stemming from dark matter annihilation is shown here. One promising antihelium-3 production channel is the dark matter annihilation to  $\bar{\Lambda}_b$  hadron and its subsequent decay to antinuclei. Such production was proposed in Ref. [208] and it was shown employing event generators that the resulting antihelium-3 cosmic rays would have an enhancement in flux at around 10 GeV/A kinetic energy. However, such a hypothesis must be validated by accelerator experiments measuring the antihelium-3 production from  $\bar{\Lambda}_b$  decays.

The transparencies are depicted in the lower panels of Fig. 6.10. In the case of the dark matter component, the transparency is around 40-50%. For the background flux, the transparency ranges from around 20% to 90%. The transparencies are similar for both LIS (upper figure) and TOA (lower figure) fluxes. Such high transparencies for antihelium-3 propagation show that such fluxes can be potentially measured in the future.

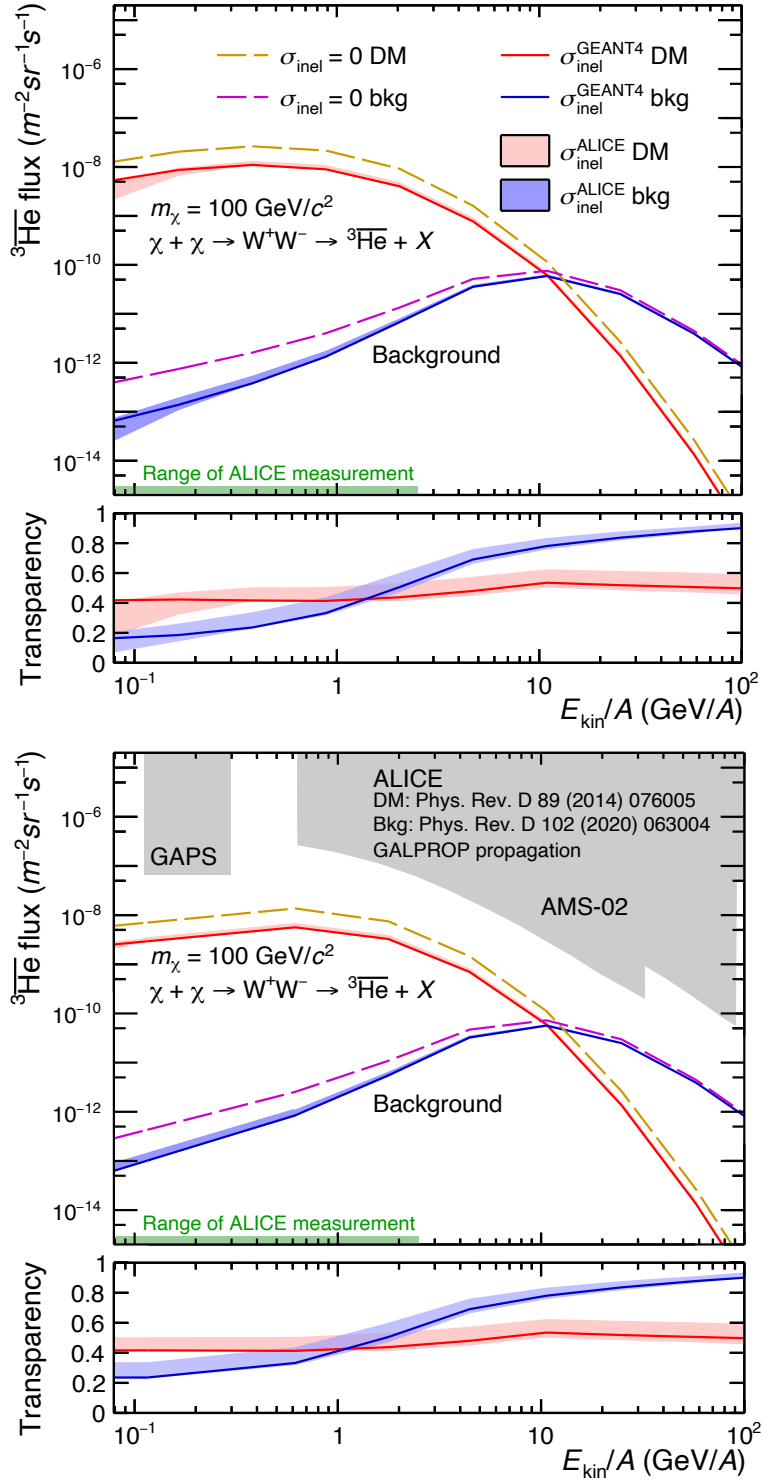


FIGURE 6.10: Top panels: Antihelium-3 LIS (upper figure) and TOA (lower figure) fluxes. Lower panels: The corresponding transparencies. The blue band and lines represent the secondary cosmic ray antihelium-3 fluxes obtained in this work. They are compared to the predictions of a flux stemming from dark matter annihilation (red band and lines). The dashed lines correspond to the fluxes if no inelastic interactions are included in GALPROP for antihelium-3. The solid line and the band represents fluxes obtained with inelastic cross section values default in GEANT4 and corrected by ALICE data, respectively.

## Chapter 7

# Summary and outlook

This work investigated two topics - the strong interaction measurement in three-body systems and the cosmic ray antinuclei flux predictions for indirect dark matter searches.

The first measurements of the three-body interaction in non-bound systems were presented in the first part of this thesis. The strong interaction can be accessed via femtoscopic correlations. The measured correlation functions are affected by two- and three-body effects, as well as quantum statistics, Coulomb and strong interactions. The genuine three-body effects were studied employing Kubo's cumulant method, which allows us to subtract the correlations induced only by two particles interacting in the triplet. The correlation functions and corresponding cumulants were measured for p-p-p and p-p- $\Lambda$  triplets in pp collisions at  $\sqrt{s}=13$  TeV. The high-multiplicity data sample recorded by ALICE was analysed in which hadrons are emitted at average relative distances of about 1 fm. This provides a unique environment to test three-body interactions at scales shorter than inter-particle ones in nuclei, mimicking a high-density environment. The lower-order contributions in Kubo's cumulant method were estimated using a data-driven approach and a newly developed projector method. Both methods are in good agreement, which constitutes the first experimental validation of the projector method. A deviation from zero in the low  $Q_3$  region was observed in both p-p-p and p-p- $\Lambda$  cumulants, suggesting genuine three-body effects.

A negative three-particle cumulant was measured for p-p-p triplets. The p-value extracted from the  $\chi^2$  test corresponds to a deviation of  $6.7\sigma$  from the assumption of only two-body correlations present in the system for  $Q_3 < 0.4$  GeV/c, suggesting genuine three-body effects present in the system. The measured p-p-p correlation function was also compared to the first preliminary calculations performed employing the hyperspherical harmonic technique, which provides a hint that the decrease of correlation function at low  $Q_3$  is partially related to the antisymmetrisation of the three-particle wave function. More qualitative conclusions require a larger data sample which is expected from the Run 3 data taking. For this purpose, a three-body software trigger was also developed in this thesis, ensuring that all events, which include a collimated triplet, are stored.

While the p-p-p triplet is affected by the Pauli blocking at three particle level and the long-range Coulomb interaction, the p-p- $\Lambda$  system is free of such effects and thus provides a unique opportunity to test genuine strong three-body interaction. The three-body effects have been studied only employing the Kubo's cumulant method, as no calculations are currently available. A positive cumulant was observed at low  $Q_3$ . However, the deviation from zero at  $Q_3 < 0.4$  GeV/c is  $0.8\sigma$ , which suggests that data can be sufficiently well explained by the assumption of only two-body correlations present in the system within the current uncertainties.

While a larger statistical sample is required to constrain the quantitative three-body effects in the p-p- $\Lambda$  system, such a result is already very intriguing. The currently accepted hypothesis on solving the hyperon puzzle for neutron stars is a repulsive genuine strong three-body interaction in the p-p- $\Lambda$  system. However, the result obtained in this thesis does not show any evidence for this, in fact the measured cumulant suggests the absence of three-body repulsion. However, further studies are required, and for this purpose, a three-body software trigger for p-p- $\Lambda$  triplets was also developed.

The development of the three-body trigger and studies of the expected number of triplets in the total Run 3 data sample suggests that we can expect up to two orders of magnitude increase in statistics. Such a number of triplets would be sufficient to measure high-precision three-body correlation functions. However, once the problem of recorded statistics is resolved with the Run 3 data, the challenge of constraining a three-body source will remain. The good news is that the preliminary calculations of the correlation function for p-p-p system suggests that the three nucleons never get close enough to have relevant effects from the genuine three-body strong interaction because of the Pauli blocking. Thus, once the preliminary p-p-p calculation employing the hyperspherical harmonics is improved, the p-p-p correlation function can be used as a benchmark to constrain the three-body source as the relevant two-body strong interaction is very well known. Once this is done, the measurement of p-p- $\Lambda$  correlation function with Run 3 data will provide the ultimate result towards which the work of this thesis was performed.

Another exciting way to study the three-body system employing femtoscopy are the measurements of hadron-nucleus correlations. My colleague Bhawani Singh performed such a study with Run 2 data. It was shown that the p-d correlation function could only be described satisfactorily if the calculations use the individual nucleons as degrees of freedom. While the Run 2 data was not sensitive enough to study the genuine three-body strong interaction in the p-d system, there is hope for Run 3. To summarise, there is a bright future coming for the studies of three-body systems employing the femtoscopic technique which will provide relevant input for theoretical nuclear physicists and related interdisciplinary fields, such as astrophysics.

The secondary cosmic ray antinuclei flux calculations were performed for antideuterons and antihelium-3 in the second part of the thesis. The antinuclei source functions and inelastic cross sections based on data-driven methods were implemented in GALPROP. In the case of the antideuteron studies, different propagation and production models were employed. It was shown that the systematic uncertainty coming from the choice of the production model is the main contributor to the total uncertainty at larger kinetic energies above 1 GeV/A. The lower energy is also characterized by a significant systematic uncertainty stemming from the choice of the propagation parameters in GALPROP. The uncertainty stemming from the inelastic cross section evaluation based on ALICE measurements is 25% at low energies, constituting the smallest contribution to the total uncertainty budget for the secondary antideuteron flux. However, this study was the first to implement the data-driven estimation of the inelastic cross sections. Thus, it was used to estimate how transparent our Galaxy is to the propagation of antideuteron cosmic rays. The transparency for secondary cosmic ray antideuteron propagation was found to increase from around 35% to 90%, depending on the kinetic energy per nucleon. The transparency for the propagation of antideuterons stemming from dark matter annihilation, obtained in Ref. [259], is around 50% with an increase up to almost

80% at 10 GeV/ $A$  kinetic energy per nucleon. Our Galaxy is very transparent to the antideuteron propagation, which suggests that the measurements of such fluxes will be feasible in the future. Finally, a similar study was performed for cosmic ray antihelium-3. The transparency of the Galaxy to the propagation of secondary antihelium-3 increases from around 20% to 90% with increasing energy. It is around 50% for the dark matter component, as shown in Ref. [110].

It was shown that the inelastic cross section measurements provided by the ALICE Collaboration are sufficiently precise for the cosmic ray antinuclei studies. The next challenge for the accelerator experiments and theorists is to find out the production mechanism of antinuclei and provide measurements at the relevant collision energies to constrain the models. The production mechanisms should be studied not only in pp collisions, which are relevant for the secondary cosmic ray antinuclei flux, but also in elementary (point-like) particle collisions, such as  $e^+e^-$  at Belle. As the dark matter particles are assumed to be elementary, studies of  $e^+e^-$  collisions would better constrain antinuclei production in dark matter annihilations. Measuring femtoscopic correlation functions of well-known pairs, such as p–p, is important to constrain the source size in  $e^+e^-$  collisions. This would provide relevant input for the advanced coalescence models, which require information on the distances between the produced nucleons.

The work presented in this thesis is only the first footstep in much larger efforts required to solve some of the mysteries of our universe. However, it provides one more piece of the puzzle related to the underlying physics.



## Appendix A

# Relevant Publications

The author has contributed to the following publications, with the highlighted ones being subject of this work.

- Šerkšnytė, L., Königstorfer, S. et al. (2022). Reevaluation of the cosmic antideuteron flux from cosmic-ray interactions and from exotic sources. *Physical Review D*, 105(8), 083021
- Del Grande, R., Šerkšnytė, L., Fabbietti, L., Mantovani Sarti, V., Mihaylov, D. (2022). A method to remove lower order contributions in multi-particle femtoscopic correlation functions. *The European Physical Journal C*, 82(3)
- ALICE Collaboration. (2022). Towards the understanding of the genuine three-body interaction for  $p - p - p$  and  $p - p - \Lambda$ . *arXiv preprint arXiv:2206.03344* (Accepted by EPJA)
- ALICE Collaboration. (2023). Measurement of anti- ${}^3\text{He}$  nuclei absorption in matter and impact on their propagation in the Galaxy. *Nature Physics* 19 (1)
- ALICE Collaboration. (2023). Study of the  $p - p - K^+$  and  $p - p - K^-$  dynamics using the femtoscopy technique. *arXiv preprint arXiv:2303.13448* (Submitted to EPJA)



# Bibliography

- [1] A. Nogga, P. Navrátil, B. R. Barrett, and J. P. Vary. Spectra and binding energy predictions of chiral interactions for  $^7\text{Li}$ . *Phys. Rev. C*, 73:064002, Jun 2006. doi: 10.1103/PhysRevC.73.064002. URL <https://link.aps.org/doi/10.1103/PhysRevC.73.064002>.  
Cited on pages 3, 12, 14, and 15.
- [2] D. Lonardoni, S. Gandolfi, and F. Pederiva. Effects of the two-body and three-body hyperon-nucleon interactions in  $\Lambda$ -hypernuclei. *Phys. Rev. C*, 87:041303, 2013. doi: 10.1103/PhysRevC.87.041303.  
Cited on pages 3, 12, 15, 16, and 18.
- [3] J. Fujita and H. Miyazawa. Pion Theory of Three-Body Forces. *Prog. Theor. Phys.*, 17:360–365, 1957. doi: 10.1143/PTP.17.360.  
Cited on pages 3 and 12.
- [4] Feryal Özal and Paulo Freire. Masses, Radii, and the Equation of State of Neutron Stars. *Ann. Rev. Astron. Astrophys.*, 54:401–440, 2016. doi: 10.1146/annurev-astro-081915-023322.  
Cited on pages 3 and 16.
- [5] Wikipedia.  
Standard Model  
[https://en.wikipedia.org/wiki/Standard\\_Model](https://en.wikipedia.org/wiki/Standard_Model)  
Accessed: 7th Nov 2022, .  
Cited on page 5.
- [6] Georges Aad et al. Observation of a new particle in the search for the Standard Model Higgs boson with the ATLAS detector at the LHC. *Phys. Lett. B*, 716: 1–29, 2012. doi: 10.1016/j.physletb.2012.08.020.  
Cited on pages 5 and 35.
- [7] Serguei Chatrchyan et al. Observation of a New Boson at a Mass of 125 GeV with the CMS Experiment at the LHC. *Phys. Lett. B*, 716:30–61, 2012. doi: 10.1016/j.physletb.2012.08.021.  
Cited on pages 5 and 35.
- [8] Wikipedia.  
Strong Interaction  
[https://en.wikipedia.org/wiki/Strong\\_interaction](https://en.wikipedia.org/wiki/Strong_interaction)  
Accessed: 3rd Jan 2023, .  
Cited on page 6.
- [9] David Griffiths. *Introduction to elementary particles*. 2008. ISBN 978-3-527-40601-2.  
Cited on page 6.

- [10] R. L. Workman and Others. Review of Particle Physics. *PTEP*, 2022:083C01, 2022. doi: 10.1093/ptep/ptac097.  
Cited on pages 6, 7, 101, 104, and 105.
- [11] K Aamodt et al. Elliptic flow of charged particles in Pb-Pb collisions at 2.76 TeV. *Phys. Rev. Lett.*, 105:252302, 2010. doi: 10.1103/PhysRevLett.105.252302.  
Cited on pages 7 and 35.
- [12] K. Aamodt et al. Higher harmonic anisotropic flow measurements of charged particles in Pb-Pb collisions at  $\sqrt{s_{NN}}=2.76$  TeV. *Phys. Rev. Lett.*, 107:032301, 2011. doi: 10.1103/PhysRevLett.107.032301.  
Cited on pages 7 and 35.
- [13] John Adams et al. Experimental and theoretical challenges in the search for the quark gluon plasma: The STAR Collaboration's critical assessment of the evidence from RHIC collisions. *Nucl. Phys. A*, 757:102–183, 2005. doi: 10.1016/j.nuclphysa.2005.03.085.  
Cited on page 7.
- [14] L. Adamczyk et al. Bulk Properties of the Medium Produced in Relativistic Heavy-Ion Collisions from the Beam Energy Scan Program. *Phys. Rev. C*, 96 (4):044904, 2017. doi: 10.1103/PhysRevC.96.044904.  
Cited on page 7.
- [15] S. Durr et al. Ab-Initio Determination of Light Hadron Masses. *Science*, 322: 1224–1227, 2008. doi: 10.1126/science.1163233.  
Cited on pages 8 and 10.
- [16] Hideki Yukawa. On the Interaction of Elementary Particles I. *Proc. Phys. Math. Soc. Jap.*, 17:48–57, 1935. doi: 10.1143/PTPS.1.1.  
Cited on page 8.
- [17] Evgeny Epelbaum, Hans-Werner Hammer, and Ulf-G. Meissner. Modern Theory of Nuclear Forces. *Rev. Mod. Phys.*, 81:1773–1825, 2009. doi: 10.1103/RevModPhys.81.1773.  
Cited on page 8.
- [18] R. B. Wiringa, V. G. J. Stoks, and R. Schiavilla. Accurate nucleon-nucleon potential with charge-independence breaking. *Phys. Rev. C*, 51:38–51, Jan 1995. doi: 10.1103/PhysRevC.51.38. URL <https://link.aps.org/doi/10.1103/PhysRevC.51.38>.  
Cited on pages 9 and 66.
- [19] Mohammad Naghdi. Nucleon-nucleon interaction: A typical/concise review. *Phys. Part. Nucl.*, 45:924–971, 2014. doi: 10.1134/S1063779614050050.  
Cited on page 9.
- [20] A. Gal, E. V. Hungerford, and D. J. Millener. Strangeness in nuclear physics. *Rev. Mod. Phys.*, 88(3):035004, 2016. doi: 10.1103/RevModPhys.88.035004.  
Cited on page 9.
- [21] Steven Weinberg. Effective chiral Lagrangians for nucleon - pion interactions and nuclear forces. *Nucl. Phys. B*, 363:3–18, 1991. doi: 10.1016/0550-3213(91)90231-L.  
Cited on page 9.

- [22] Steven Weinberg. Nuclear forces from chiral Lagrangians. *Phys. Lett. B*, 251: 288–292, 1990. doi: 10.1016/0370-2693(90)90938-3.  
Cited on page 9.
- [23] R. Machleidt and D. R. Entem. Chiral effective field theory and nuclear forces. *Phys. Rept.*, 503:1–75, 2011. doi: 10.1016/j.physrep.2011.02.001.  
Cited on pages 9, 10, and 14.
- [24] J. Haidenbauer, S. Petschauer, N. Kaiser, U. G. Meißner, A. Nogga, and W. Weise. Hyperon-nucleon interaction at next-to-leading order in chiral effective field theory. *Nucl. Phys. A*, 915:24–58, 2013. doi: 10.1016/j.nuclphysa.2013.06.008.  
Cited on pages 9 and 33.
- [25] J. Haidenbauer, U. G. Meißner, and A. Nogga. Hyperon–nucleon interaction within chiral effective field theory revisited. *Eur. Phys. J. A*, 56(3):91, 2020. doi: 10.1140/epja/s10050-020-00100-4.  
Cited on pages 9, 11, and 67.
- [26] Kenneth G. Wilson. Confinement of Quarks. *Phys. Rev. D*, 10:2445–2459, 1974. doi: 10.1103/PhysRevD.10.2445.  
Cited on page 10.
- [27] Tetsuo Hatsuda. Lattice quantum chromodynamics and baryon-baryon interactions. *Front. Phys. (Beijing)*, 13(6):132105, 2018. doi: 10.1007/s11467-018-0829-4.  
Cited on page 10.
- [28] Sinya Aoki and Takumi Doi. Lattice QCD and baryon-baryon interactions: HAL QCD method. *Front. in Phys.*, 8:307, 2020. doi: 10.3389/fphy.2020.00307.  
Cited on page 10.
- [29] Benoit Blossier, Jochen Heitger, and Matthias Post. Leptonic  $D_s$  decays in two-flavour lattice QCD. *Phys. Rev. D*, 98(5):054506, 2018. doi: 10.1103/PhysRevD.98.054506.  
Cited on page 10.
- [30] S. Acharya et al. Unveiling the strong interaction among hadrons at the LHC. *Nature*, 588(7837):232–238, 2020. doi: 10.1038/s41586-020-3001-6.  
Cited on pages 10, 11, and 35.
- [31] V. G. J. Stoks, R. A. M. Klomp, M. C. M. Rentmeester, and J. J. de Swart. Partial wave analysis of all nucleon-nucleon scattering data below 350-MeV. *Phys. Rev. C*, 48:792–815, 1993. doi: 10.1103/PhysRevC.48.792.  
Cited on page 11.
- [32] J. M. Hauptman, J. A. Kadyk, and G. H. Trilling. Experimental Study of Lambda p and  $\bar{\Lambda} p$  Interactions in the Range 1-GeV/c-10-GeV/c. *Nucl. Phys. B*, 125:29–51, 1977. doi: 10.1016/0550-3213(77)90222-X.  
Cited on page 11.
- [33] B. Sechi-Zorn, B. Kehoe, J. Twitty, and R. A. Burnstein. Low-energy lambda-proton elastic scattering. *Phys. Rev.*, 175:1735–1740, 1968. doi: 10.1103/PhysRev.175.1735.  
Cited on page 11.

- [34] Shreyasi Acharya et al. p-p, p- $\Lambda$  and  $\Lambda$ - $\Lambda$  correlations studied via femtoscopy in pp reactions at  $\sqrt{s} = 7$  TeV. *Phys. Rev. C*, 99:024001, 2019. doi: 10.1103/PhysRevC.99.024001.  
Cited on pages 11, 35, and 73.
- [35] Shreyasi Acharya et al. Exploring the N $\Lambda$ -N $\Sigma$  coupled system with high precision correlation techniques at the LHC. *Phys. Lett. B*, 833:137272, 2022. doi: 10.1016/j.physletb.2022.137272.  
Cited on pages 11, 52, 63, and 66.
- [36] Shreyasi Acharya et al. Scattering studies with low-energy kaon-proton femtoscopy in proton-proton collisions at the LHC. *Phys. Rev. Lett.*, 124:092301, 2020. doi: 10.1103/PhysRevLett.124.092301.  
Cited on pages 11 and 35.
- [37] Shreyasi Acharya et al. Investigation of the p- $\Sigma^0$  interaction via femtoscopy in pp collisions. *Phys. Lett. B*, 805:135419, 2020. doi: 10.1016/j.physletb.2020.135419.  
Cited on pages 11, 66, and 69.
- [38] Shreyasi Acharya et al. Study of the  $\Lambda$ - $\Lambda$  interaction with femtoscopy correlations in pp and p-Pb collisions at the LHC. *Phys. Lett. B*, 797:134822, 2019. doi: 10.1016/j.physletb.2019.134822.  
Cited on page 11.
- [39] Shreyasi Acharya et al. First Observation of an Attractive Interaction between a Proton and a Cascade Baryon. *Phys. Rev. Lett.*, 123:112002, 2019. doi: 10.1103/PhysRevLett.123.112002.  
Cited on page 11.
- [40] Shreyasi Acharya et al. Experimental Evidence for an Attractive p- $\phi$  Interaction. *Phys. Rev. Lett.*, 127(17):172301, 2021. doi: 10.1103/PhysRevLett.127.172301.  
Cited on page 11.
- [41] Shreyasi Acharya et al. Investigating the role of strangeness in baryon-antibaryon annihilation at the LHC. *Phys. Lett. B*, 829:137060, 2022. doi: 10.1016/j.physletb.2022.137060.  
Cited on pages 11, 35, 46, 69, and 70.
- [42] H. Primakoff and T. Holstein. Many-body interactions in atomic and nuclear systems. *Phys. Rev.*, 55:1218–1234, Jun 1939. doi: 10.1103/PhysRev.55.1218. URL <https://link.aps.org/doi/10.1103/PhysRev.55.1218>.  
Cited on page 12.
- [43] Ulf-G. Meissner. The Fujita-Miyazawa force in the light of effective field theory. *AIP Conf. Proc.*, 1011(1):49–58, 2008. doi: 10.1063/1.2932307.  
Cited on page 12.
- [44] Takumi Doi. Few-baryon interactions from lattice QCD. *Few Body Syst.*, 54: 827–833, 2013. doi: 10.1007/s00601-012-0593-x.  
Cited on page 12.
- [45] Takaharu Otsuka, Toshio Suzuki, Jason D. Holt, Achim Schwenk, and Yoshi-nori Akaishi. Three-body forces and the limit of oxygen isotopes. *Phys. Rev.*

- Lett.*, 105:032501, 2010. doi: 10.1103/PhysRevLett.105.032501.  
Cited on page 13.
- [46] A. Kievsky, M. Viviani, and L. E. Marcucci. N - d scattering including electromagnetic forces. *Phys. Rev. C*, 69:014002, 2004. doi: 10.1103/PhysRevC.69.014002.  
Cited on page 13.
- [47] Kimiko Sekiguchi. Experimental Approach to Three Nucleon Forces via Few Nucleon Systems. *Few Body Syst.*, 54(7-10):911–916, 2013. doi: 10.1007/s00601-013-0636-y.  
Cited on page 13.
- [48] Steven C. Pieper and Robert B. Wiringa. Quantum Monte Carlo calculations of light nuclei. *Ann. Rev. Nucl. Part. Sci.*, 51:53–90, 2001. doi: 10.1146/annurev.nucl.51.101701.132506.  
Cited on pages 13 and 14.
- [49] J. Carlson, V. R. Pandharipande, and Robert B. Wiringa. Three-nucleon interaction in 3-body, 4-body, and infinite-body systems. *Nucl. Phys. A*, 401:59–85, 1983. doi: 10.1016/0375-9474(83)90336-6.  
Cited on page 13.
- [50] Steven C. Pieper, V. R. Pandharipande, Robert B. Wiringa, and J. Carlson. Realistic models of pion exchange three nucleon interactions. *Phys. Rev. C*, 64:014001, 2001. doi: 10.1103/PhysRevC.64.014001.  
Cited on page 13.
- [51] Y. Nosyk, D. R. Entem, and R. Machleidt. Nucleon-nucleon potentials from  $\Delta$ -full chiral effective-field-theory and implications. *Phys. Rev. C*, 104(5):054001, 2021. doi: 10.1103/PhysRevC.104.054001.  
Cited on page 14.
- [52] P. Navrátil, V. G. Gueorguiev, J. P. Vary, W. E. Ormand, and A. Nogga. Structure of  $a = 10 - 13$  nuclei with two- plus three-nucleon interactions from chiral effective field theory. *Phys. Rev. Lett.*, 99:042501, Jul 2007. doi: 10.1103/PhysRevLett.99.042501. URL <https://link.aps.org/doi/10.1103/PhysRevLett.99.042501>.  
Cited on page 14.
- [53] G. Hagen, T. Papenbrock, D. J. Dean, A. Schwenk, A. Nogga, M. Włoch, and P. Piecuch. Coupled-cluster theory for three-body hamiltonians. *Phys. Rev. C*, 76:034302, Sep 2007. doi: 10.1103/PhysRevC.76.034302. URL <https://link.aps.org/doi/10.1103/PhysRevC.76.034302>.  
Not cited.
- [54] Takaharu Otsuka, Toshio Suzuki, Jason D. Holt, Achim Schwenk, and Yoshi-nori Akaishi. Three-body forces and the limit of oxygen isotopes. *Phys. Rev. Lett.*, 105:032501, Jul 2010. doi: 10.1103/PhysRevLett.105.032501. URL <https://link.aps.org/doi/10.1103/PhysRevLett.105.032501>.  
Cited on page 14.
- [55] Takumi Doi, Sinya Aoki, Tetsuo Hatsuda, Yoichi Ikeda, Takashi Inoue, Noriyoshi Ishii, Keiko Murano, Hidekatsu Nemura, and Kenji Sasaki. Exploring Three-Nucleon Forces in Lattice QCD. *Prog. Theor. Phys.*, 127:723–738,

2012. doi: 10.1143/PTP.127.723.  
Cited on page 14.
- [56] A. R. Bodmer, Q. N. Usmani, and J. Carlson. Binding energies of hypernuclei and three-body  $\Lambda$ NN forces. *Phys. Rev. C*, 29:684–687, Feb 1984. doi: 10.1103/PhysRevC.29.684. URL <https://link.aps.org/doi/10.1103/PhysRevC.29.684>.  
Cited on pages 15 and 18.
- [57] A. A. Usmani. Three-baryon  $\Lambda$ nn potential. *Phys. Rev. C*, 52:1773–1777, Oct 1995. doi: 10.1103/PhysRevC.52.1773. URL <https://link.aps.org/doi/10.1103/PhysRevC.52.1773>.  
Cited on pages 15, 16, and 18.
- [58] A A Usmani and F C Khanna. Behaviour of the  $\Lambda$ n and  $\Lambda$ nn potential strengths in the  $5\Lambda$ he hypernucleus. *Journal of Physics G: Nuclear and Particle Physics*, 35(2):025105, jan 2008. doi: 10.1088/0954-3899/35/2/025105. URL <https://dx.doi.org/10.1088/0954-3899/35/2/025105>.  
Cited on page 16.
- [59] Dominik Gerstung, Norbert Kaiser, and Wolfram Weise. Hyperon–nucleon three-body forces and strangeness in neutron stars. *Eur. Phys. J. A*, 56(6):175, 2020. doi: 10.1140/epja/s10050-020-00180-2.  
Cited on pages 16 and 19.
- [60] F. Hildenbrand and H.-W. Hammer. Three-body hypernuclei in pionless effective field theory. *Phys. Rev. C*, 100:034002, Sep 2019. doi: 10.1103/PhysRevC.100.034002. URL <https://link.aps.org/doi/10.1103/PhysRevC.100.034002>.  
Cited on page 16.
- [61] Paulo F. Bedaque and Ubirajara van Kolck. Effective field theory for few nucleon systems. *Ann. Rev. Nucl. Part. Sci.*, 52:339–396, 2002. doi: 10.1146/annurev.nucl.52.050102.090637.  
Cited on page 16.
- [62] Sebastian König, Harald W Grießhammer, H-W Hammer, and U van Kolck. Effective theory of 3h and 3he. *Journal of Physics G: Nuclear and Particle Physics*, 43(5):055106, apr 2016. doi: 10.1088/0954-3899/43/5/055106. URL <https://dx.doi.org/10.1088/0954-3899/43/5/055106>.  
Cited on page 16.
- [63] A. Bansal, S. Binder, A. Ekström, G. Hagen, G. R. Jansen, and T. Papenbrock. Pion-less effective field theory for atomic nuclei and lattice nuclei. *Phys. Rev. C*, 98(5):054301, 2018. doi: 10.1103/PhysRevC.98.054301.  
Cited on page 16.
- [64] S. R. Beane, E. Chang, S. D. Cohen, William Detmold, H. W. Lin, T. C. Luu, K. Orginos, A. Parreno, M. J. Savage, and A. Walker-Loud. Light Nuclei and Hypernuclei from Quantum Chromodynamics in the Limit of SU(3) Flavor Symmetry. *Phys. Rev. D*, 87(3):034506, 2013. doi: 10.1103/PhysRevD.87.034506.  
Cited on page 16.

- [65] Isaac Vidaña. A short walk through the physics of neutron stars. *Eur. Phys. J. Plus*, 133(10):445, 2018. doi: 10.1140/epjp/i2018-12329-x.  
Cited on page 16.
- [66] V. A. Ambartsumyan and G. S. Saakyan. The Degenerate Superdense Gas of Elementary Particles. , 4:187, October 1960.  
Cited on page 16.
- [67] J. R. Oppenheimer and G. M. Volkoff. On massive neutron cores. *Phys. Rev.*, 55:374–381, 1939. doi: 10.1103/PhysRev.55.374.  
Cited on page 17.
- [68] R. C. Tolman. *Relativity, Thermodynamics, and Cosmology*. 1934.  
Not cited.
- [69] Richard C. Tolman. Static solutions of einstein’s field equations for spheres of fluid. *Phys. Rev.*, 55:364–373, Feb 1939. doi: 10.1103/PhysRev.55.364. URL <https://link.aps.org/doi/10.1103/PhysRev.55.364>.  
Cited on page 17.
- [70] Laura Tolos and Laura Fabbietti. Strangeness in Nuclei and Neutron Stars. *Prog. Part. Nucl. Phys.*, 112:103770, 2020. doi: 10.1016/j.ppnp.2020.103770.  
Cited on page 17.
- [71] L. Fabbietti, V. Mantovani Sarti, and O. Vazquez Doce. Study of the Strong Interaction Among Hadrons with Correlations at the LHC. *Ann. Rev. Nucl. Part. Sci.*, 71:377–402, 2021. doi: 10.1146/annurev-nucl-102419-034438.  
Cited on pages 17 and 20.
- [72] Diego Lonardoni, Alessandro Lovato, Stefano Gandolfi, and Francesco Pedriva. Hyperon puzzle: Hints from quantum monte carlo calculations. *Phys. Rev. Lett.*, 114:092301, Mar 2015. doi: 10.1103/PhysRevLett.114.092301. URL <https://link.aps.org/doi/10.1103/PhysRevLett.114.092301>.  
Cited on pages 18 and 19.
- [73] D. Lonardoni, F. Pederiva, and S. Gandolfi. Accurate determination of the interaction between  $\Lambda$  hyperons and nucleons from auxiliary field diffusion Monte Carlo calculations. *Phys. Rev. C*, 89(1):014314, 2014. doi: 10.1103/PhysRevC.89.014314.  
Cited on page 18.
- [74] Michael Annan Lisa, Scott Pratt, Ron Soltz, and Urs Wiedemann. Femtoscopy in relativistic heavy ion collisions. *Ann. Rev. Nucl. Part. Sci.*, 55:357–402, 2005. doi: 10.1146/annurev.nucl.55.090704.151533.  
Cited on pages 20, 24, and 55.
- [75] Mihaylov Dimitar. Analysis techniques for femtoscopy and correlation studies in small collision systems and their applications to the investigation of p- $\Lambda$  and  $\Lambda$ - $\Lambda$  interactions with ALICE. *PhD thesis, Technical University of Munich*, 2021.  
Cited on pages 20 and 22.
- [76] R. Lednický and V. L. Lyuboshits. Final State Interaction Effect on Pairing Correlations Between Particles with Small Relative Momenta. *Sov. J. Nucl. Phys.*, 35:770, 1982.  
Cited on pages 20 and 21.

- [77] S. E. Koonin. Proton pictures of high-energy nuclear collisions. *Phys. Lett. B*, 70(1):43–47, 1977.  
Cited on page 20.
- [78] S. Pratt, T. Csörgő, and J. Zimányi. Detailed predictions for two-pion correlations in ultrarelativistic heavy-ion collisions. *Phys. Rev. C*, 42(6):2646, 1990.  
Cited on page 20.
- [79] D. L. Mihaylov, V. Mantovani Sarti, O. W. Arnold, L. Fabbietti, B. Hohlweger, and A. M. Mathis. A femtoscopic Correlation Analysis Tool using the Schrödinger equation (CATS). *Eur. Phys. J. C*, 78(5):394, 2018. doi: 10.1140/epjc/s10052-018-5859-0.  
Cited on pages 22 and 23.
- [80] Andreas Mathis. First Measurement of the Proton– $\Sigma^0$  Interaction via the Femtoscopy Method. *PhD thesis, Technical University of Munich*, 2020.  
Cited on page 22.
- [81] Betty Bezverkhny Abelev et al. Two- and three-pion quantum statistics correlations in Pb–Pb collisions at  $\sqrt{s_{\text{NN}}} = 2.76$  TeV at the CERN Large Hadron Collider. *Phys. Rev. C*, 89(2):024911, 2014. doi: 10.1103/PhysRevC.89.024911.  
Cited on pages 23, 31, and 55.
- [82] L. D. Faddeev. Scattering theory for a three particle system. *Zh. Eksp. Teor. Fiz.*, 39:1459–1467, 1960.  
Cited on page 25.
- [83] L. D. Faddeev. Mathematical aspects of the three-body problem in quantum scattering theory. *New York: Davey (translated from Russian)*, page 443–443, 1965.  
Cited on page 25.
- [84] B. S. Pudliner, V. R. Pandharipande, J. Carlson, and Robert B. Wiringa. Quantum Monte Carlo calculations of  $A \leq 6$  nuclei. *Phys. Rev. Lett.*, 74:4396–4399, 1995. doi: 10.1103/PhysRevLett.74.4396.  
Cited on page 25.
- [85] W. Kohn. Variational methods in nuclear collision problems. *Phys. Rev.*, 74: 1763–1772, Dec 1948. doi: 10.1103/PhysRev.74.1763. URL <https://link.aps.org/doi/10.1103/PhysRev.74.1763>.  
Cited on page 25.
- [86] A. Kievsky, S. Rosati, M. Viviani, L. E. Marcucci, and L. Girlanda. A High-precision variational approach to three- and four-nucleon bound and zero-energy scattering states. *J. Phys. G*, 35:063101, 2008. doi: 10.1088/0954-3899/35/6/063101.  
Cited on pages 25 and 56.
- [87] Ryogo Kubo. Generalized Cumulant Expansion Method. *J. Phys. Soc. Jpn.*, 17(7):1100–1120, 1962. ISSN 0031-9015. doi: 10.1143/JPSJ.17.1100.  
Cited on page 31.
- [88] Nicolas Borghini, Phuong Mai Dinh, and Jean-Yves Ollitrault. A New method for measuring azimuthal distributions in nucleus-nucleus collisions. *Phys. Rev.*

- C, 63:054906, 2001. doi: 10.1103/PhysRevC.63.054906.  
Cited on page 31.
- [89] Vardan Khachatryan et al. Evidence for collectivity in pp collisions at the LHC. *Phys. Lett. B*, 765:193–220, 2017. doi: 10.1016/j.physletb.2016.12.009.  
Not cited.
- [90] Georges Aad et al. Measurement of the distributions of event-by-event flow harmonics in lead-lead collisions at  $\sqrt{s_{\text{NN}}} = 2.76$  TeV with the ATLAS detector at the LHC. *JHEP*, 11:183, 2013. doi: 10.1007/JHEP11(2013)183.  
Not cited.
- [91] Jaroslav Adam et al. Anisotropic flow of charged particles in Pb-Pb collisions at  $\sqrt{s_{\text{NN}}} = 5.02$  TeV. *Phys. Rev. Lett.*, 116(13):132302, 2016. doi: 10.1103/PhysRevLett.116.132302.  
Cited on page 31.
- [92] J. Adam et al. Multipion Bose-Einstein correlations in pp, p-Pb, and Pb-Pb collisions at energies available at the CERN Large Hadron Collider. *Phys. Rev. C*, 93:054908, May 2016. doi: 10.1103/PhysRevC.93.054908.  
Cited on page 31.
- [93] Raffaele Del Grande, Laura Šerkšnytė, Laura Fabbietti, Valentina Mantovani Sarti, and Dimitar Mihaylov. A method to remove lower order contributions in multi-particle femtoscopic correlation functions. *Eur. Phys. J. C*, 82(3):244, 2022. doi: 10.1140/epjc/s10052-022-10209-z.  
Cited on pages 32 and 33.
- [94] Towards the understanding of the genuine three-body interaction for p–p–p and p–p– $\Lambda$ . 6 2022.  
Cited on page 34.
- [95] F. J. Hasert et al. Search for Elastic  $\nu_\mu$  Electron Scattering. *Phys. Lett. B*, 46: 121–124, 1973. doi: 10.1016/0370-2693(73)90494-2.  
Cited on page 35.
- [96] H. Burkhardt et al. First Evidence for Direct CP Violation. *Phys. Lett. B*, 206: 169–176, 1988. doi: 10.1016/0370-2693(88)91282-8.  
Cited on page 35.
- [97] G. D. Barr et al. A New measurement of direct CP violation in the neutral kaon system. *Phys. Lett. B*, 317:233–242, 1993. doi: 10.1016/0370-2693(93)91599-I.  
Not cited.
- [98] A. Lai et al. A Precise measurement of the direct CP violation parameter  $\text{Re}(\epsilon'/\epsilon)$ . *Eur. Phys. J. C*, 22:231–254, 2001. doi: 10.1007/s100520100822.  
Not cited.
- [99] J. R. Batley et al. A Precision measurement of direct CP violation in the decay of neutral kaons into two pions. *Phys. Lett. B*, 544:97–112, 2002. doi: 10.1016/S0370-2693(02)02476-0.  
Cited on page 35.
- [100] Roman Pasechnik and Michal Šumbera. Phenomenological Review on Quark–Gluon Plasma: Concepts vs. Observations. *Universe*, 3(1):7, 2017. doi:

- 10.3390/universe3010007.  
 Cited on page 35.
- [101] Betty Bezverkhny Abelev et al. Elliptic flow of identified hadrons in Pb-Pb collisions at  $\sqrt{s_{NN}} = 2.76$  TeV. *JHEP*, 06:190, 2015. doi: 10.1007/JHEP06(2015)190.  
 Cited on page 35.
- [102] B. Abelev et al. D meson elliptic flow in non-central Pb-Pb collisions at  $\sqrt{s_{NN}} = 2.76$  TeV. *Phys. Rev. Lett.*, 111:102301, 2013. doi: 10.1103/PhysRevLett.111.102301.  
 Cited on page 35.
- [103] B. Abelev et al. Measurement of charged jet suppression in Pb-Pb collisions at  $\sqrt{s_{NN}} = 2.76$  TeV. *JHEP*, 03:013, 2014. doi: 10.1007/JHEP03(2014)013.  
 Cited on page 35.
- [104] Jaroslav Adam et al. Measurement of jet suppression in central Pb-Pb collisions at  $\sqrt{s_{NN}} = 2.76$  TeV. *Phys. Lett. B*, 746:1–14, 2015. doi: 10.1016/j.physletb.2015.04.039.  
 Not cited.
- [105] Jaroslav Adam et al. Measurement of jet quenching with semi-inclusive hadron-jet distributions in central Pb-Pb collisions at  $\sqrt{s_{NN}} = 2.76$  TeV. *JHEP*, 09:170, 2015. doi: 10.1007/JHEP09(2015)170.  
 Cited on page 35.
- [106] Kenneth Aamodt et al. Centrality dependence of the charged-particle multiplicity density at mid-rapidity in Pb-Pb collisions at  $\sqrt{s_{NN}} = 2.76$  TeV. *Phys. Rev. Lett.*, 106:032301, 2011. doi: 10.1103/PhysRevLett.106.032301.  
 Cited on page 35.
- [107] Betty Abelev et al. Centrality dependence of  $\pi$ , K, p production in Pb-Pb collisions at  $\sqrt{s_{NN}} = 2.76$  TeV. *Phys. Rev. C*, 88:044910, 2013. doi: 10.1103/PhysRevC.88.044910.  
 Not cited.
- [108] K. Aamodt et al. Suppression of Charged Particle Production at Large Transverse Momentum in Central Pb-Pb Collisions at  $\sqrt{s_{NN}} = 2.76$  TeV. *Phys. Lett. B*, 696:30–39, 2011. doi: 10.1016/j.physletb.2010.12.020.  
 Cited on page 35.
- [109] Shreyasi Acharya et al. Measurement of the low-energy antideuteron inelastic cross section. *Phys. Rev. Lett.*, 125(16):162001, 2020. doi: 10.1103/PhysRevLett.125.162001.  
 Cited on pages 35, 121, and 122.
- [110] Shreyasi Acharya et al. Measurement of anti- ${}^3\text{He}$  nuclei absorption in matter and impact on their propagation in the Galaxy. *Nature Phys.*, 19(1):61–71, 2023. doi: 10.1038/s41567-022-01804-8.  
 Cited on pages 35, 121, 123, 126, 129, and 139.
- [111] Measurement of the lifetime and  $\Lambda$  separation energy of  ${}^3\text{H}$ . 9 2022.  
 Cited on page 35.

- [112] LHC Machine. *JINST*, 3:S08001, 2008. doi: 10.1088/1748-0221/3/08/S08001.  
Cited on page 36.
- [113] M. Bajko et al. Report of the task force on the incident of 19th September 2008 at the LHC. 3 2009.  
Cited on page 36.
- [114] R. Garoby. Challenges and Plans for the Proton Injectors. *Adv. Ser. Direct. High Energy Phys.*, 24:281–293, 2015. doi: 10.1142/9789814675475\_0016.  
Cited on page 36.
- [115] Esma Mobs. The CERN accelerator complex in 2019. Complexe des accélérateurs du CERN en 2019. 2019. URL <https://cds.cern.ch/record/2684277>. General Photo.  
Cited on page 36.
- [116] Betty Bezverkhny Abelev et al. Performance of the ALICE Experiment at the CERN LHC. *Int. J. Mod. Phys. A*, 29:1430044, 2014. doi: 10.1142/S0217751X14300440.  
Cited on pages 36, 37, 38, and 46.
- [117] K. Aamodt et al. The ALICE experiment at the CERN LHC. *JINST*, 3:S08002, 2008. doi: 10.1088/1748-0221/3/08/S08002.  
Not cited.
- [118] P Cortese et al. ALICE: Physics performance report, volume I. *J. Phys. G*, 30: 1517–1763, 2004. doi: 10.1088/0954-3899/30/11/001.  
Not cited.
- [119] Christian Wolfgang Fabjan et al. ALICE: Physics Performance Report, volume II. *J. Phys. G*, 32:1295–2040, 2006. doi: 10.1088/0954-3899/32/10/001.  
Cited on page 37.
- [120] ALICE Collaboration.  
ALICE Figure repository.  
Accessed 4th December 2020.  
Cited on pages 37, 38, 41, and 42.
- [121] Christian Wolfgang Fabjan, L Jirdén, V Lindestruth, Lodovico Riccati, D Rorich, Pierre Van de Vyvre, O Villalobos Baillie, and Hans de Groot. *ALICE trigger, data-acquisition, high-level trigger and control system: Technical Design Report*. Technical design report. ALICE. CERN, Geneva, 2004. URL <https://cds.cern.ch/record/684651>.  
Cited on page 38.
- [122] Jaroslav Adam et al. Enhanced production of multi-strange hadrons in high-multiplicity proton-proton collisions. *Nature Phys.*, 13:535–539, 2017. doi: 10.1038/nphys4111.  
Cited on page 38.
- [123] K Aamodt et al. Alignment of the ALICE Inner Tracking System with cosmic-ray tracks. *JINST*, 5:P03003. 37 p, 2010. doi: 10.1088/1748-0221/5/03/P03003. URL <https://cds.cern.ch/record/1231809>. Comments: 37 pages, 13 figures, fixed figure appearance.  
Cited on page 39.

- [124] Vito Manzari. The ALICE Inner Tracking System: Commissioning and running experience. *PoS*, VERTEX2009:005, 2009. doi: 10.22323/1.095.0005.  
Cited on page 39.
- [125] Georges Charpak, R. Bouclier, T. Bressani, J. Favier, and C. Zupancic. The Use of Multiwire Proportional Counters to Select and Localize Charged Particles. *Nucl. Instrum. Meth.*, 62:262–268, 1968. doi: 10.1016/0029-554X(68)90371-6.  
Cited on page 40.
- [126] J. Alme et al. The ALICE TPC, a large 3-dimensional tracking device with fast readout for ultra-high multiplicity events. *Nucl. Instrum. Meth. A*, 622:316–367, 2010. doi: 10.1016/j.nima.2010.04.042.  
Cited on pages 40 and 43.
- [127] Christian Lippmann. Performance of the ALICE Time Projection Chamber. *Phys. Procedia*, 37:434–441, 2012. doi: 10.1016/j.phpro.2012.02.390.  
Cited on page 40.
- [128] Walter Blum, Luigi Rolandi, and Werner Riegler. *Particle detection with drift chambers*. Particle Acceleration and Detection. 2008. ISBN 978-3-540-76683-4, 978-3-540-76684-1. doi: 10.1007/978-3-540-76684-1.  
Cited on page 41.
- [129] A. Akindinov et al. Performance of the ALICE Time-Of-Flight detector at the LHC. *Eur. Phys. J. Plus*, 128:44, 2013. doi: 10.1140/epjp/i2013-13044-x.  
Cited on page 41.
- [130] M. Šuljić. ALPIDE: the Monolithic Active Pixel Sensor for the ALICE ITS upgrade. *Nuovo Cim. C*, 41(1-2):91, 2018. doi: 10.1393/ncc/i2018-18091-x.  
Cited on page 42.
- [131] ALICE upgrades during the LHC Long Shutdown 2. 2 2023.  
Cited on page 43.
- [132] J. Adolfsson et al. The upgrade of the ALICE TPC with GEMs and continuous readout. *JINST*, 16(03):P03022, 2021. doi: 10.1088/1748-0221/16/03/P03022.  
Cited on page 43.
- [133] M. Ivanov, I. Belikov, P. Hristov, and K. Safarik. Track reconstruction in high density environment. *Nucl. Instrum. Meth. A*, 566:70–74, 2006. doi: 10.1016/j.nima.2006.05.029.  
Cited on page 44.
- [134] Torbjörn Sjöstrand, Stefan Ask, Jesper R. Christiansen, Richard Corke, Nishita Desai, Philip Ilten, Stephen Mrenna, Stefan Prestel, Christine O. Rasmussen, and Peter Z. Skands. An introduction to PYTHIA 8.2. *Comput. Phys. Commun.*, 191:159–177, 2015. doi: 10.1016/j.cpc.2015.01.024.  
Cited on page 46.
- [135] Stefan Roesler, Ralph Engel, and Johannes Ranft. The Monte Carlo event generator DPMJET-III. In *International Conference on Advanced Monte Carlo for Radiation Physics, Particle Transport Simulation and Applications (MC 2000)*, pages 1033–1038, 12 2000. doi: 10.1007/978-3-642-18211-2\_166.  
Cited on page 46.

- [136] Xin-Nian Wang and Miklos Gyulassy. HIJING: A Monte Carlo model for multiple jet production in p p, p A and A A collisions. *Phys. Rev. D*, 44:3501–3516, 1991. doi: 10.1103/PhysRevD.44.3501.  
Cited on page 46.
- [137] Christian Bierlich et al. A comprehensive guide to the physics and usage of PYTHIA 8.3. 3 2022.  
Cited on page 46.
- [138] B. Andersson, G. Gustafson, and B. Söderberg. A probability measure on parton and string states. *Nuclear Physics B*, 264:29–59, 1986. ISSN 0550-3213. doi: [https://doi.org/10.1016/0550-3213\(86\)90471-2](https://doi.org/10.1016/0550-3213(86)90471-2). URL <https://www.sciencedirect.com/science/article/pii/0550321386904712>.  
Cited on page 46.
- [139] R. Brun, R. Hagelberg, M. Hansroul, and J. C. Lassalle. Geant: Simulation Program for Particle Physics Experiments. User Guide and Reference Manual. 7 1978.  
Cited on page 46.
- [140] Validation of the ALICE material budget between TPC and TOF detectors. 2022. URL <https://cds.cern.ch/record/2800896>.  
Cited on page 46.
- [141] H. Albrecht et al. Observation of Octet and Decuplet Hyperons in  $e^+e^-$  Annihilation at 10-GeV Center-of-mass Energy. *Phys. Lett. B*, 183:419–424, 1987. doi: 10.1016/0370-2693(87)90988-9.  
Cited on page 53.
- [142] Betty Bezverkhny Abelev et al. Long-range angular correlations of  $\ell$ , K and p in p-Pb collisions at  $\sqrt{s_{NN}} = 5.02$  TeV. *Phys. Lett. B*, 726:164–177, 2013. doi: 10.1016/j.physletb.2013.08.024.  
Cited on page 55.
- [143] R. J. Barlow. *Statistics. A Guide to the Use of Statistical Methods in the Physical Sciences*. WILEY, 1997.  
Cited on page 60.
- [144] Towards the understanding of the genuine three-body interaction for p-p-p and p-p- $\Lambda$ . 6 2022.  
Cited on pages 64 and 73.
- [145] R. Kubo. Generalized cumulant expansion method. *Journal of the Physical Society of Japan*, 17(7):1100–1120, 1962.  
Cited on page 64.
- [146] Ling-Yun Dai, Johann Haidenbauer, and Ulf-G Meißner. Antinucleon-nucleon interaction at next-to-next-to-next-to-leading order in chiral effective field theory. *JHEP*, 07:078, 2017. doi: 10.1007/JHEP07(2017)078.  
Cited on page 70.
- [147] EO Alt and AM Mukhamedzhanov. Asymptotic solution of the Schrödinger equation for three charged particles. *Physical Review A*, 47(3):2004, 1993.  
Cited on page 78.

- [148] Future high-energy pp programme with ALICE. 2020. URL <https://cds.cern.ch/record/2724925>.  
Cited on pages 83 and 84.
- [149] Z. Citron et al. Report from Working Group 5: Future physics opportunities for high-density QCD at the LHC with heavy-ion and proton beams. *CERN Yellow Rep. Monogr.*, 7:1159–1410, 2019. doi: 10.23731/CYRM-2019-007.1159.  
Cited on page 84.
- [150] C. D. Anderson. The Positive Electron. *Phys. Rev.*, 43:491–494, 1933. doi: 10.1103/PhysRev.43.491.  
Cited on page 97.
- [151] C. M. G. Lattes, H. Muirhead, G. P. S. Occhialini, and C. F. Powell. PROCESSES INVOLVING CHARGED MESONS. *Nature*, 159:694–697, 1947. doi: 10.1038/159694a0.  
Cited on page 97.
- [152] F. Zwicky. Die Rotverschiebung von extragalaktischen Nebeln. *Helv. Phys. Acta*, 6:110–127, 1933. doi: 10.1007/s10714-008-0707-4.  
Cited on page 97.
- [153] K. G. Begeman, A. H. Broeils, and R. H. Sanders. Extended rotation curves of spiral galaxies: Dark haloes and modified dynamics. *Mon. Not. Roy. Astron. Soc.*, 249:523, 1991. doi: 10.1093/mnras/249.3.523.  
Cited on pages 97 and 100.
- [154] Tommaso Treu and Leon V. E. Koopmans. Massive dark - matter halos and evolution of early - type galaxies to  $z = 1$ . *Astrophys. J.*, 611:739–760, 2004. doi: 10.1086/422245.  
Cited on page 97.
- [155] P. A. R. Ade et al. Planck 2015 results. XIII. Cosmological parameters. *Astron. Astrophys.*, 594:A13, 2016. doi: 10.1051/0004-6361/201525830.  
Cited on page 97.
- [156] Douglas Clowe, Marusa Bradac, Anthony H. Gonzalez, Maxim Markevitch, Scott W. Randall, Christine Jones, and Dennis Zaritsky. A direct empirical proof of the existence of dark matter. *Astrophys. J. Lett.*, 648:L109–L113, 2006. doi: 10.1086/508162.  
Cited on page 97.
- [157] Gianfranco Bertone, Dan Hooper, and Joseph Silk. Particle dark matter: Evidence, candidates and constraints. *Phys. Rept.*, 405:279–390, 2005. doi: 10.1016/j.physrep.2004.08.031.  
Cited on page 97.
- [158] M. Ackermann et al. Detection of the Characteristic Pion-Decay Signature in Supernova Remnants. *Science*, 339:807, 2013. doi: 10.1126/science.1231160.  
Cited on page 97.
- [159] Laura Šerkšnytė et al. Reevaluation of the cosmic antideuteron flux from cosmic-ray interactions and from exotic sources. *Phys. Rev. D*, 105(8):083021, 2022. doi: 10.1103/PhysRevD.105.083021.  
Cited on pages 98, 110, 112, 113, 126, 129, 130, 131, 132, 133, 134, and 135.

- [160] M. Aguilar et al. The Alpha Magnetic Spectrometer (AMS) on the international space station: Part II — Results from the first seven years. *Phys. Rept.*, 894:1–116, 2021. doi: 10.1016/j.physrep.2020.09.003.  
Cited on page 98.
- [161] N. Marcelli. The GAPS experiment: Low-energy antinuclei measurements for dark matter searches. *EPJ Web Conf.*, 280:07002, 2023. doi: 10.1051/epjconf/202328007002.  
Not cited.
- [162] T. Aramaki, C. J. Hailey, S. E. Boggs, P. von Doetinchem, H. Fuke, S. I. Mognet, R. A. Ong, K. Perez, and J. Zweerink. Antideuteron Sensitivity for the GAPS Experiment. *Astropart. Phys.*, 74:6–13, 2016. doi: 10.1016/j.astropartphys.2015.09.001.  
Cited on pages 98 and 108.
- [163] Arno A. Penzias and Robert Woodrow Wilson. A Measurement of excess antenna temperature at 4080-Mc/s. *Astrophys. J.*, 142:419–421, 1965. doi: 10.1086/148307.  
Cited on page 99.
- [164] R. A. Alpher, H. Bethe, and G. Gamow. The origin of chemical elements. *Phys. Rev.*, 73:803–804, 1948. doi: 10.1103/PhysRev.73.803.  
Cited on page 99.
- [165] D. J. Fixsen, E. S. Cheng, J. M. Gales, John C. Mather, R. A. Shafer, and E. L. Wright. The Cosmic Microwave Background spectrum from the full COBE FIRAS data set. *Astrophys. J.*, 473:576, 1996. doi: 10.1086/178173.  
Cited on page 99.
- [166] N. Aghanim et al. Planck 2018 results. I. Overview and the cosmological legacy of Planck. *Astron. Astrophys.*, 641:A1, 2020. doi: 10.1051/0004-6361/201833880.  
Cited on page 99.
- [167] N. Aghanim et al. Planck 2018 results. VI. Cosmological parameters. *Astron. Astrophys.*, 641:A6, 2020. doi: 10.1051/0004-6361/201833910. [Erratum: *Astron. Astrophys.* 652, C4 (2021)].  
Cited on page 100.
- [168] Y. Sofue, M. Honma, and T. Omodaka. Unified Rotation Curve of the Galaxy – Decomposition into de Vaucouleurs Bulge, Disk, Dark Halo, and the 9-kpc Rotation Dip –. *Publ. Astron. Soc. Jap.*, 61:227, 2009. doi: 10.1093/pasj/61.2.227.  
Cited on page 100.
- [169] Julio F. Navarro, Carlos S. Frenk, and Simon D. M. White. A Universal density profile from hierarchical clustering. *Astrophys. J.*, 490:493–508, 1997. doi: 10.1086/304888.  
Cited on page 101.
- [170] Carlos Pérez de los Heros. Status, challenges and directions in indirect dark matter searches. *Symmetry*, 12(10), 2020. ISSN 2073-8994. doi: 10.3390/sym12101648. URL <https://www.mdpi.com/2073-8994/12/10/1648>.  
Cited on pages 101 and 105.

- [171] J. I. Read. The Local Dark Matter Density. *J. Phys. G*, 41:063101, 2014. doi: 10.1088/0954-3899/41/6/063101.  
Cited on page 101.
- [172] Alejandro Ibarra and Sebastian Wild. Prospects of antideuteron detection from dark matter annihilations or decays at AMS-02 and GAPS. *JCAP*, 02:021, 2013. doi: 10.1088/1475-7516/2013/02/021.  
Cited on pages 101, 110, and 130.
- [173] Howard Baer, Ki-Young Choi, Jihn E. Kim, and Leszek Roszkowski. Dark matter production in the early Universe: beyond the thermal WIMP paradigm. *Phys. Rept.*, 555:1–60, 2015. doi: 10.1016/j.physrep.2014.10.002.  
Cited on page 102.
- [174] Giorgio Arcadi, Maíra Dutra, Pradipta Ghosh, Manfred Lindner, Yann Mambrini, Mathias Pierre, Stefano Profumo, and Farinaldo S. Queiroz. The waning of the WIMP? A review of models, searches, and constraints. *Eur. Phys. J. C*, 78(3):203, 2018. doi: 10.1140/epjc/s10052-018-5662-y.  
Cited on page 102.
- [175] Jonathan L. Feng. Dark Matter Candidates from Particle Physics and Methods of Detection. *Ann. Rev. Astron. Astrophys.*, 48:495–545, 2010. doi: 10.1146/annurev-astro-082708-101659.  
Cited on page 102.
- [176] Gerard Jungman, Marc Kamionkowski, and Kim Griest. Supersymmetric dark matter. *Phys. Rept.*, 267:195–373, 1996. doi: 10.1016/0370-1573(95)00058-5.  
Cited on pages 102 and 103.
- [177] Enrico Morgante. *Aspects of WIMP Dark Matter searches at colliders and other probes*. PhD thesis, Geneva U., Dept. Theor. Phys., 9 2016.  
Cited on page 103.
- [178] Yang Bai, Patrick J. Fox, and Roni Harnik. The Tevatron at the Frontier of Dark Matter Direct Detection. *JHEP*, 12:048, 2010. doi: 10.1007/JHEP12(2010)048.  
Cited on page 103.
- [179] Patrick J. Fox, Roni Harnik, Joachim Kopp, and Yuhsin Tsai. LEP Shines Light on Dark Matter. *Phys. Rev. D*, 84:014028, 2011. doi: 10.1103/PhysRevD.84.014028.  
Cited on page 103.
- [180] Oliver Buchmueller, Caterina Doglioni, and Lian Tao Wang. Search for dark matter at colliders. *Nature Phys.*, 13(3):217–223, 2017. doi: 10.1038/nphys4054.  
Cited on page 103.
- [181] Morad Aaboud et al. Search for dark matter and other new phenomena in events with an energetic jet and large missing transverse momentum using the ATLAS detector. *JHEP*, 01:126, 2018. doi: 10.1007/JHEP01(2018)126.  
Cited on pages 103 and 104.
- [182] Vardan Khachatryan et al. Search for dark matter, extra dimensions, and unparticles in monojet events in proton–proton collisions at  $\sqrt{s} = 8$  TeV. *Eur. Phys. J. C*, 75(5):235, 2015. doi: 10.1140/epjc/s10052-015-3451-4.  
Cited on page 104.

- [183] J. Silk et al. *Particle Dark Matter: Observations, Models and Searches*. Cambridge Univ. Press, Cambridge, 2010. ISBN 978-1-107-65392-4. doi: 10.1017/CBO9780511770739.  
Cited on page 104.
- [184] C. Tao. Dark Matter searches: an overview. *JINST*, 15(06):C06054, 2020. doi: 10.1088/1748-0221/15/06/C06054.  
Cited on page 104.
- [185] E. Aprile et al. First Dark Matter Search with Nuclear Recoils from the XENONnT Experiment. 3 2023.  
Cited on page 104.
- [186] M. Ackermann et al. Searching for Dark Matter Annihilation from Milky Way Dwarf Spheroidal Galaxies with Six Years of Fermi Large Area Telescope Data. *Phys. Rev. Lett.*, 115(23):231301, 2015. doi: 10.1103/PhysRevLett.115.231301.  
Cited on pages 104 and 105.
- [187] Dan Hooper and Lisa Goodenough. Dark Matter Annihilation in The Galactic Center As Seen by the Fermi Gamma Ray Space Telescope. *Phys. Lett. B*, 697: 412–428, 2011. doi: 10.1016/j.physletb.2011.02.029.  
Cited on page 105.
- [188] M. Ackermann et al. Constraints on Dark Matter Annihilation in Clusters of Galaxies with the Fermi Large Area Telescope. *JCAP*, 05:025, 2010. doi: 10.1088/1475-7516/2010/05/025.  
Cited on page 105.
- [189] Leanna Dugger, Tesla E. Jeltema, and Stefano Profumo. Constraints on Decaying Dark Matter from Fermi Observations of Nearby Galaxies and Clusters. *JCAP*, 12:015, 2010. doi: 10.1088/1475-7516/2010/12/015.  
Cited on page 105.
- [190] M. Aguilar et al. Towards Understanding the Origin of Cosmic-Ray Positrons. *Phys. Rev. Lett.*, 122(4):041102, 2019. doi: 10.1103/PhysRevLett.122.041102.  
Cited on page 105.
- [191] Oscar Adriani et al. An anomalous positron abundance in cosmic rays with energies 1.5-100 GeV. *Nature*, 458:607–609, 2009. doi: 10.1038/nature07942.  
Cited on page 105.
- [192] M. Ackermann et al. Measurement of separate cosmic-ray electron and positron spectra with the Fermi Large Area Telescope. *Phys. Rev. Lett.*, 108: 011103, 2012. doi: 10.1103/PhysRevLett.108.011103.  
Cited on page 105.
- [193] M. Aguilar et al. First Result from the Alpha Magnetic Spectrometer on the International Space Station: Precision Measurement of the Positron Fraction in Primary Cosmic Rays of 0.5–350 GeV. *Phys. Rev. Lett.*, 110:141102, 2013. doi: 10.1103/PhysRevLett.110.141102.  
Cited on page 105.
- [194] Stefano Gabici, Carmelo Evoli, Daniele Gaggero, Paolo Lipari, Philipp Mertsch, Elena Orlando, Andrew Strong, and Andrea Vittino. The origin of Galactic cosmic rays: challenges to the standard paradigm. *Int. J. Mod. Phys.*

- D*, 28(15):1930022, 2019. doi: 10.1142/S0218271819300222.  
Cited on page 105.
- [195] Agnibha De Sarkar, Sayan Biswas, and Nayantara Gupta. Positron excess from cosmic ray interactions in galactic molecular clouds. *JHEAp*, 29:1–18, 2021. doi: 10.1016/j.jheap.2020.11.001.  
Cited on page 105.
- [196] M. Di Mauro, F. Donato, N. Fornengo, R. Lineros, and A. Vittino. Interpretation of AMS-02 electrons and positrons data. *JCAP*, 04:006, 2014. doi: 10.1088/1475-7516/2014/04/006.  
Not cited.
- [197] Kfir Blum, Boaz Katz, and Eli Waxman. AMS-02 Results Support the Secondary Origin of Cosmic Ray Positrons. *Phys. Rev. Lett.*, 111(21):211101, 2013. doi: 10.1103/PhysRevLett.111.211101.  
Not cited.
- [198] Philipp Mertsch and Subir Sarkar. AMS-02 data confront acceleration of cosmic ray secondaries in nearby sources. *Phys. Rev. D*, 90:061301, 2014. doi: 10.1103/PhysRevD.90.061301.  
Cited on page 105.
- [199] Alessandro Cuoco, Michael Krämer, and Michael Korsmeier. Novel Dark Matter Constraints from Antiprotons in Light of AMS-02. *Phys. Rev. Lett.*, 118(19):191102, 2017. doi: 10.1103/PhysRevLett.118.191102.  
Cited on pages 105, 106, 116, and 125.
- [200] M. Aguilar et al. Antiproton Flux, Antiproton-to-Proton Flux Ratio, and Properties of Elementary Particle Fluxes in Primary Cosmic Rays Measured with the Alpha Magnetic Spectrometer on the International Space Station. *Phys. Rev. Lett.*, 117(9):091103, 2016. doi: 10.1103/PhysRevLett.117.091103.  
Cited on page 105.
- [201] Fiorenza Donato, Nicolao Fornengo, and David Maurin. Antideuteron fluxes from dark matter annihilation in diffusion models. *Phys. Rev. D*, 78:043506, 2008. doi: 10.1103/PhysRevD.78.043506.  
Cited on pages 106 and 107.
- [202] M. Kachelrieß, S. Ostapchenko, and J. Tjemsland. Revisiting cosmic ray antinuclei fluxes with a new coalescence model. *JCAP*, 08:048, 2020. doi: 10.1088/1475-7516/2020/08/048.  
Cited on pages 110, 118, 120, 121, 126, and 127.
- [203] Johannes Herms, Alejandro Ibarra, Andrea Vittino, and Sebastian Wild. Antideuterons in cosmic rays: sources and discovery potential. *JCAP*, 02:018, 2017. doi: 10.1088/1475-7516/2017/02/018.  
Cited on page 130.
- [204] Anirvan Shukla, Amaresh Datta, Philip von Doetinchem, Diego-Mauricio Gomez-Coral, and Carina Kanitz. Large-scale Simulations of Antihelium Production in Cosmic-ray Interactions. *Phys. Rev. D*, 102(6):063004, 2020. doi: 10.1103/PhysRevD.102.063004.  
Cited on pages 118, 119, 126, and 127.

- [205] Michael Korsmeier, Fiorenza Donato, and Nicolao Fornengo. Prospects to verify a possible dark matter hint in cosmic antiprotons with antideuterons and antihelium. *Phys. Rev. D*, 97(10):103011, 2018. doi: 10.1103/PhysRevD.97.103011.  
Cited on pages 106, 130, and 135.
- [206] H. Fuke, T. Maeno, K. Abe, S. Haino, Y. Makida, S. Matsuda, H. Matsumoto, J. W. Mitchell, A. A. Moiseev, J. Nishimura, et al. Search for Cosmic-Ray Antideuterons. *Physical Review Letters*, 95(8):081101, August 2005. doi: 10.1103/PhysRevLett.95.081101.  
Cited on pages 107, 130, and 131.
- [207] Vivian Poulin, Pierre Salati, Ilias Cholis, Marc Kamionkowski, and Joseph Silk. Where do the AMS-02 antihelium events come from? *Phys. Rev. D*, 99:023016, 2019. doi: 10.1103/PhysRevD.99.023016.  
Cited on pages 108 and 110.
- [208] Martin Wolfgang Winkler and Tim Linden. Dark Matter Annihilation Can Produce a Detectable Antihelium Flux through  $\bar{\Lambda}_b$  Decays. *Phys. Rev. Lett.*, 126(10):101101, 2021. doi: 10.1103/PhysRevLett.126.101101.  
Cited on pages 108 and 135.
- [209] T. Aramaki et al. Potential for Precision Measurement of Low-Energy Antiprotons with GAPS for Dark Matter and Primordial Black Hole Physics. *Astropart. Phys.*, 59:12–17, 2014. doi: 10.1016/j.astropartphys.2014.03.011.  
Cited on page 108.
- [210] N. Saffold et al. Cosmic antihelium-3 nuclei sensitivity of the GAPS experiment. *Astropart. Phys.*, 130:102580, 2021. doi: 10.1016/j.astropartphys.2021.102580.  
Cited on pages 108 and 135.
- [211] Thomas K. Gaisser, Ralph Engel, and Elisa Resconi. *Cosmic Rays and Particle Physics: 2nd Edition*. Cambridge University Press, 6 2016. ISBN 978-0-521-01646-9.  
Cited on pages 108 and 113.
- [212] R. D. Blandford and J. P. Ostriker. Particle Acceleration by Astrophysical Shocks. *Astrophys. J. Lett.*, 221:L29–L32, 1978. doi: 10.1086/182658.  
Cited on page 108.
- [213] R. Blandford and D. Eichler. Particle Acceleration at Astrophysical Shocks: A Theory of Cosmic Ray Origin. *Phys. Rept.*, 154:1–75, 1987. doi: 10.1016/0370-1573(87)90134-7.  
Cited on page 108.
- [214] K. Koyama, R. Petre, E. V. Gotthelf, U. Hwang, M. Matsuura, M. Ozaki, and S. S. Holt. Evidence for shock acceleration of high-energy electrons in the supernova remnant SN1006. *Nature*, 378:255–258, 1995. doi: 10.1038/378255a0.  
Cited on page 108.
- [215] Roberta Giuffrida, Marco Miceli, Damiano Caprioli, Anne Decourchelle, Jacco Vink, Salvatore Orlando, Fabrizio Bocchino, Emanuele Greco, and Giovanni

- Peres. The supernova remnant SN 1006 as a Galactic particle accelerator. *Nature Commun.*, 13(1):5098, 2022. doi: 10.1038/s41467-022-32781-4.  
Cited on pages 108 and 109.
- [216] I. Büsching, O. C. de Jager, M. S. Potgieter, and C. Venter. A Cosmic Ray Positron Anisotropy due to Two Middle-Aged, Nearby Pulsars? *Astrophys. J. Lett.*, 678:L39–L42, 2008. doi: 10.1086/588465.  
Cited on page 109.
- [217] Andrew W. Strong, Igor V. Moskalenko, and Vladimir S. Ptuskin. Cosmic-ray propagation and interactions in the Galaxy. *Ann. Rev. Nucl. Part. Sci.*, 57:285–327, 2007. doi: 10.1146/annurev.nucl.57.090506.123011.  
Cited on pages 109 and 111.
- [218] Massimo Persic, Paolo Salucci, and Fulvio Stel. The Universal rotation curve of spiral galaxies: 1. The Dark matter connection. *Mon. Not. Roy. Astron. Soc.*, 281:27, 1996. doi: 10.1093/mnras/278.1.27.  
Cited on page 110.
- [219] Huirong Yan and Alex Lazarian. Cosmic ray scattering and streaming in compressible magnetohydrodynamic turbulence. *Astrophys. J.*, 614:757–769, 2004. doi: 10.1086/423733.  
Cited on page 110.
- [220] Russell Kulsrud and William P. Pearce. The Effect of Wave-Particle Interactions on the Propagation of Cosmic Rays. *Astrophys. J.*, 156:445, 1969. doi: 10.1086/149981.  
Cited on page 110.
- [221] E. A. Dorfi and D. Breitschwerdt. Time-dependent galactic winds I. Structure and evolution of galactic outflows accompanied by cosmic ray acceleration. *Astron. Astrophys.*, 540:A77, 2012. doi: 10.1051/0004-6361/201118082.  
Cited on page 111.
- [222] A. W. Strong and I. V. Moskalenko. Propagation of cosmic-ray nucleons in the galaxy. *Astrophys. J.*, 509:212–228, 1998. doi: 10.1086/306470.  
Cited on pages 111 and 112.
- [223] Andrew W. Strong, Igor V. Moskalenko, and Olaf Reimer. Diffuse continuum gamma-rays from the galaxy. *Astrophys. J.*, 537:763–784, 2000. doi: 10.1086/309038. [Erratum: *Astrophys.J.* 541, 1109 (2000)].  
Cited on page 112.
- [224] Carmelo Evoli, Daniele Gaggero, Andrea Vittino, Giuseppe Di Bernardo, Mattia Di Mauro, Arianna Ligorini, Piero Ullio, and Dario Grasso. Cosmic-ray propagation with DRAGON2: I. numerical solver and astrophysical ingredients. *JCAP*, 02:015, 2017. doi: 10.1088/1475-7516/2017/02/015.  
Cited on page 112.
- [225] Ralf Kissmann. PICARD: A novel code for the Galactic Cosmic Ray propagation problem. *Astropart. Phys.*, 55:37–50, 2014. doi: 10.1016/j.astropartphys.2014.02.002.  
Cited on page 112.

- [226] Igor V. Moskalenko, Andrew W. Strong, Jonathan F. Ormes, and Marius S. Potgieter. Secondary anti-protons and propagation of cosmic rays in the galaxy and heliosphere. *Astrophys. J.*, 565:280–296, 2002. doi: 10.1086/324402.  
Cited on page 113.
- [227] A. W. Strong, I. V. Moskalenko, O. Reimer, S. Digel, and R. Diehl. The distribution of cosmic-ray sources in the galaxy, gamma-rays, and the gradient in the co-to-h<sub>2</sub> relation. *Astron. Astrophys.*, 422:L47–L50, 2004. doi: 10.1051/0004-6361:20040172.  
Cited on page 113.
- [228] E.N. Parker. The passage of energetic charged particles through interplanetary space. *Planetary and Space Science*, 13(1):9–49, 1965. ISSN 0032-0633. doi: [https://doi.org/10.1016/0032-0633\(65\)90131-5](https://doi.org/10.1016/0032-0633(65)90131-5). URL <https://www.sciencedirect.com/science/article/pii/0032063365901315>.  
Cited on page 114.
- [229] M. J. Boschini, S. Della Torre, M. Gervasi, G. La Vacca, and P. G. Rancoita. Propagation of cosmic rays in heliosphere: The HELMOD model. *Adv. Space Res.*, 62:2859–2879, 2018. doi: 10.1016/j.asr.2017.04.017.  
Cited on page 114.
- [230] L. J. Gleeson and W. I. Axford. Solar Modulation of Galactic Cosmic Rays. *Astrophys. J.*, 154:1011, 1968. doi: 10.1086/149822.  
Cited on page 114.
- [231] A. C. Cummings, E. C. Stone, B. C. Heikkila, N. Lal, W. R. Webber, G. Jóhannesson, I. V. Moskalenko, E. Orlando, and T. A. Porter. Galactic cosmic rays in the local interstellar medium: Voyager 1 observations and model results. *The Astrophysical Journal*, 831(1):18, oct 2016. doi: 10.3847/0004-637X/831/1/18. URL <https://dx.doi.org/10.3847/0004-637X/831/1/18>.  
Cited on page 114.
- [232] M. Aguilar et al. Precision Measurement of the Proton Flux in Primary Cosmic Rays from Rigidity 1 GV to 1.8 TV with the Alpha Magnetic Spectrometer on the International Space Station. *Phys. Rev. Lett.*, 114:171103, 2015. doi: 10.1103/PhysRevLett.114.171103.  
Cited on page 115.
- [233] M. Aguilar et al. Precision Measurement of the Helium Flux in Primary Cosmic Rays of Rigidities 1.9 GV to 3 TV with the Alpha Magnetic Spectrometer on the International Space Station. *Phys. Rev. Lett.*, 115(21):211101, 2015. doi: 10.1103/PhysRevLett.115.211101.  
Not cited.
- [234] M. Aguilar et al. Observation of the Identical Rigidity Dependence of He, C, and O Cosmic Rays at High Rigidities by the Alpha Magnetic Spectrometer on the International Space Station. *Phys. Rev. Lett.*, 119(25):251101, 2017. doi: 10.1103/PhysRevLett.119.251101.  
Not cited.
- [235] M. Aguilar et al. Observation of New Properties of Secondary Cosmic Rays Lithium, Beryllium, and Boron by the Alpha Magnetic Spectrometer on the International Space Station. *Phys. Rev. Lett.*, 120(2):021101, 2018. doi: 10.1103/

- PhysRevLett.120.021101.  
Not cited.
- [236] M. Aguilar et al. Precision Measurement of Cosmic-Ray Nitrogen and its Primary and Secondary Components with the Alpha Magnetic Spectrometer on the International Space Station. *Phys. Rev. Lett.*, 121(5):051103, 2018. doi: 10.1103/PhysRevLett.121.051103.  
Not cited.
- [237] M. Aguilar et al. Properties of Neon, Magnesium, and Silicon Primary Cosmic Rays Results from the Alpha Magnetic Spectrometer. *Phys. Rev. Lett.*, 124(21): 211102, 2020. doi: 10.1103/PhysRevLett.124.211102.  
Cited on page 115.
- [238] M. J. Boschini et al. Inference of the Local Interstellar Spectra of Cosmic-Ray Nuclei  $Z \leq 28$  with the GalProp-HelMod Framework. *Astrophys. J. Suppl.*, 250 (2):27, 2020. doi: 10.3847/1538-4365/aba901.  
Cited on pages 115, 116, and 125.
- [239] J. J. Engelmann, P. Ferrando, A. Soutoul, P. Goret, and E. Juliusson. Charge composition and energy spectra of cosmic-ray for elements from Be to NI - Results from HEAO-3-C2. *Astron. Astrophys.*, 233:96–111, 1990.  
Cited on page 116.
- [240] H. S. Ahn et al. Discrepant hardening observed in cosmic-ray elemental spectra. *Astrophys. J. Lett.*, 714:L89–L93, 2010. doi: 10.1088/2041-8205/714/1/L89.  
Cited on page 116.
- [241] O. Adriani et al. Time dependence of the proton flux measured by PAMELA during the July 2006 - December 2009 solar minimum. *Astrophys. J.*, 765:91, 2013. doi: 10.1088/0004-637X/765/2/91.  
Cited on page 116.
- [242] Thomas Pöschl. Modeling of the galactic cosmic-ray antiproton flux and development of a multi-purpose active-target particle telescope for cosmic rays, 2022.  
Cited on page 116.
- [243] Anton Andronic, Peter Braun-Munzinger, Krzysztof Redlich, and Johanna Stachel. Decoding the phase structure of QCD via particle production at high energy. *Nature*, 561(7723):321–330, 2018. doi: 10.1038/s41586-018-0491-6.  
Cited on page 117.
- [244] R. Averbeck, R. Holzmann, V. Metag, and R. S. Simon. Neutral pions and eta mesons as probes of the hadronic fireball in nucleus-nucleus collisions around 1-A-GeV. *Phys. Rev. C*, 67:024903, 2003. doi: 10.1103/PhysRevC.67.024903.  
Cited on page 117.
- [245] A. Andronic, P. Braun-Munzinger, and J. Stachel. Hadron production in central nucleus-nucleus collisions at chemical freeze-out. *Nucl. Phys. A*, 772:167–199, 2006. doi: 10.1016/j.nuclphysa.2006.03.012.  
Cited on page 117.
- [246] Shreyasi Acharya et al. Production of  ${}^4\text{He}$  and  ${}^4\overline{\text{He}}$  in Pb-Pb collisions at  $\sqrt{s_{\text{NN}}} = 2.76$  TeV at the LHC. *Nucl. Phys. A*, 971:1–20, 2018. doi: 10.1016/j.nuclphysa.

- 2017.12.004.  
Cited on page 117.
- [247] Volodymyr Vovchenko, Benjamin Dönigus, and Horst Stoecker. Multiplicity dependence of light nuclei production at LHC energies in the canonical statistical model. *Phys. Lett. B*, 785:171–174, 2018. doi: 10.1016/j.physletb.2018.08.041.  
Cited on page 117.
- [248] Jaroslav Adam et al. Production of light nuclei and anti-nuclei in pp and Pb-Pb collisions at energies available at the CERN Large Hadron Collider. *Phys. Rev. C*, 93(2):024917, 2016. doi: 10.1103/PhysRevC.93.024917.  
Cited on page 117.
- [249] Shreyasi Acharya et al. Multiplicity dependence of light (anti-)nuclei production in p-Pb collisions at  $\sqrt{s_{\text{NN}}} = 5.02$  TeV. *Phys. Lett. B*, 800:135043, 2020. doi: 10.1016/j.physletb.2019.135043.  
Cited on page 117.
- [250] Maximilian Horst, Luca Barioglio, Francesca Bellini, Laura Fabbietti, Chiara Pinto, Bhawani Singh, and Sushanta Tripathy. Novel parameter-free coalescence model for deuteron production. 2 2023.  
Cited on page 117.
- [251] Measurement of (anti)nuclei production in p-Pb collisions at  $\sqrt{s_{\text{NN}}} = 8.16$  TeV. 12 2022.  
Cited on page 117.
- [252] First measurement of antideuteron number fluctuations at energies available at the Large Hadron Collider. 4 2022.  
Cited on page 117.
- [253] T. Pierog, Iu. Karpenko, J. M. Katzy, E. Yatsenko, and K. Werner. EPOS LHC: Test of collective hadronization with data measured at the CERN Large Hadron Collider. *Phys. Rev. C*, 92(3):034906, 2015. doi: 10.1103/PhysRevC.92.034906.  
Cited on page 118.
- [254] Diego-Mauricio Gomez-Coral, Arturo Menchaca Rocha, Varlen Grabski, Amaresh Datta, Philip von Doetinchem, and Anirvan Shukla. Deuteron and Antideuteron Production Simulation in Cosmic-Ray Interactions. *Phys. Rev. D*, 98(2):023012, 2018. doi: 10.1103/PhysRevD.98.023012.  
Cited on pages 118 and 127.
- [255] M. Kachelrieß, S. Ostapchenko, and J. Tjemsland. Alternative coalescence model for deuteron, tritium, helium-3 and their antinuclei. *Eur. Phys. J. A*, 56(1):4, 2020. doi: 10.1140/epja/s10050-019-00007-9.  
Cited on page 120.
- [256] S. P. Denisov, S. V. Donskov, Yu. P. Gorin, V. A. Kachanov, V. M. Kutjin, A. I. Petrukhin, Yu. D. Prokoshkin, E. A. Razuvaev, R. S. Shuvalov, and D. A. Stojanova. Measurements of anti-deuteron absorption and stripping cross sections at the momentum 13.3 gev/c. *Nucl. Phys. B*, 31:253–260, 1971. doi: 10.1016/0550-3213(71)90229-X.  
Cited on page 121.

- [257] E. Abbas et al. Mid-rapidity anti-baryon to baryon ratios in pp collisions at  $\sqrt{s} = 0.9, 2.76$  and  $7$  TeV measured by ALICE. *Eur. Phys. J. C*, 73:2496, 2013. doi: 10.1140/epjc/s10052-013-2496-5.  
Cited on page 121.
- [258] M. J. Boschini et al. Solution of heliospheric propagation: unveiling the local interstellar spectra of cosmic ray species. *Astrophys. J.*, 840(2):115, 2017. doi: 10.3847/1538-4357/aa6e4f.  
Cited on page 125.
- [259] Königstorfer Stephan. First measurement of the absorption of and nuclei in matter and its impact on propagation in the galaxy. *PhD thesis, Technical University of Munich*, 2023.  
Cited on pages 126, 129, 130, and 138.
- [260] Modelling of Antihelium-3 Cosmic-Ray Propagation. 2022.  
Cited on pages 126 and 127.
- [261] V.V. Abramov et al. Production of deuterons and antideuterons with large  $p_T$  in pp and pA collisions at 70 GeV. *Soviet Journal of Nuclear Physics*, 45:5:845–851, 1987.  
Cited on page 127.
- [262] A. W. Strong and I. V. Moskalenko. New developments in the galprop cr propagation model. 6 2001.  
Cited on page 127.
- [263] S. Agostinelli et al. GEANT4—a simulation toolkit. *Nucl. Instrum. Meth. A*, 506: 250–303, 2003. doi: 10.1016/S0168-9002(03)01368-8.  
Cited on page 129.
- [264] V. Uzhinsky, J. Apostolakis, A. Galoyan, G. Folger, V. M. Grichine, V. N. Ivanchenko, and D. H. Wright. Antinucleus-nucleus cross sections implemented in Geant4. *Phys. Lett. B*, 705:235–239, 2011. doi: 10.1016/j.physletb.2011.10.010.  
Cited on page 129.
- [265] R. J. Glauber and G. Matthiae. High-energy scattering of protons by nuclei. *Nucl. Phys. B*, 21:135–157, 1970. doi: 10.1016/0550-3213(70)90511-0.  
Cited on page 129.